Molecular level characterisation of apolipoprotein A-I aggregation leading to fibrils comprising of both α-helical and β-sheet structures

Thesis submitted in partial fulfilment of the requirements for the degree of Doctor of Philosophy.

Lancaster University

by

David Townsend

November 2016

Abstract

Molecular level characterisation of apolipoprotein A-I aggregation leading to fibrils comprising of both α-helical and β-sheet structures.

Submitted by David Townsend for the degree of Doctor of Philosophy.

November 2016.

Amyloidosis is defined as the misfolding of native proteins into insoluble fibrils that are deposited within tissues and extracellular organs. 30+ structurally and sequentially unrelated proteins have the ability to form amyloid aggregates, all of which contain characteristic features. ApoA-I, the main component in high-density lipoprotein, aggregates and becomes deposited as amyloid, either full-length apoA-I fibrils within atherosclerotic plaques, or N-terminal fragments of mutant apoA-I within organs. The work here aims to further the understanding of conditions that promote the aggregation of apoA-I *in vitro*, allowing the structural study of aggregated apoA-I at a molecular level.

ApoA-I remains soluble at neutral pH, maintaining a predominantly α-helical conformation. Upon acidification to pH 4, apoA-I readily assembles into aggregates that, despite being responsive to the amyloid characteristic ThT dye, do not have the typical amyloid morphology and do not produce XRD diffraction patterns suggestive of β-sheets. The inclusion of heparin, and chemical oxidation of apoA-I methionine residues, in order to mimic physiological conditions, results in an increased ThT response and aggregated material more characteristic of amyloid.

Solid-state NMR spectroscopy reveals for the first time that all three aggregation inducing conditions produce aggregates that give rise to cross-peaks

corresponding to both α-helical and novel β-sheet structures. This leads to a refinement in the current theory describing apoA-I aggregation. In native apoA-I, the N-terminal 4-helical bundle protects the 3 hot spot regions from self-association into β-sheets. Acidification of apoA-I leads to the destabilisation of this N-terminus, and a conversion of residues 1-90 into β-sheet structures, whilst the C-terminus retains its α-helical structure.

EGCG, an inhibitor of Aβ, α-synuclein and huntingtin amyloidosis, is shown here to bind to apoA-I with micro-molar affinity. However, rather than inhibit amyloidosis, EGCG causes a structural rearrangement of the aggregated material, resulting in a reduced α-helical content.

Contents

List of Figures

List of Tables

Word Count: 55716

Acknowledgements

My first, and greatest thanks go to my supervisor Prof. David Middleton, for suggesting the thesis topic, acquiring the funding and supporting my research as I started out on this academic journey. Your guidance has been imperative and I am looking forward to continue working with you. My next thanks have to go to Dr Eleri Hughes who's constant advice and support proved essential throughout the 3 years I spent at Lancaster, also to Dr Jill Madine, your help with the work that was carried out at Liverpool was greatly appreciated, as was all you did for me during my undergraduate degree. Again, I look forward to working alongside the both of you for the foreseeable future.

Finally, from the academic side I must thank the entire Chemistry department. From its new beginning, I have witnessed how the department has grown, and I really appreciate all of the support I received over the 3 years, from every single member of staff who have made it a pleasure to work here. Particular thanks goes to those that have provided assistance as I bundled my way through as many analytical techniques as I could. And to the current group of PhD students… well it's been fun!

I must also thank all of my friends and family who have provided the motivation to continue through the tough times, in particular to Maria, whose "tough-love" approach to motivational tactics worked every time, and to my Dad for always emphasising the bigger picture. Also to those who do not have the scientific background, but offered essential help with proof reading, I offer my greatest thanks… and apologies, for your invaluable help.

This work was funded from a PhD studentship awarded by the British Heart Foundation.

Abbreviations List

AAAC	Acoustic alternating contact
Aβ	Amyloid beta
ABCA1	ATP-binding cassette protein AI
ABCG1	ATP-binding cassette protein GI
ACAT	Acyl-CoA cholesterol acyltransferase
AFM	Atomic force microscopy
ApoA-I	Apolipoprotein AI
ASCT	Autologous stem cell therapy
ATP	Adenosine triphosphate
B_0	Static magnetic field
B23	Beam line 23 at Diamond Light Source
CCD	Charged coupled device
CD	Circular dichroism
cDNA	Complementary DNA
CETP	Cholesterylesterase transferase protein
CP	Cross-polarisation
ESI	Electrospray ionisation
ΔF	Change in fluorescence intensity
ΔFi	Initial increase in fluorescence intensity
ΔFt	Total increase in fluorescence intensity
Da	Dalton
DARR	Dipole assisted rotational resonance
DP	Direct-polarisation
E.Coli	*Escherichia Coli*
EDTA	Ethylenediaminetetraacetic acid
EGCG	Epigallocathin gallate
FTIR	Fourier transformed infrared spectroscopy
GAG	Glycosaminoglycan
GlcNs-6S	2-deoxy-2-sulfamino D-glucopyranose-6-phosphate
GSK3	Glucose synthase kinase 3
HDL	High density lipoprotein
HIS	Histidine
HPLC	High performance liquid chromatography
IAPP	Islet amyloid polypeptide
IDL	Intermediate density lipoprotein
IdoA2	L-Idopyranosyluronic acid 2-sulphate
IMAC	Immobilised metal ion affinity chromatography
INEPT	insensitive nuclei enhanced by polarisation transfer
IPTG	Isopropyl β-D-thiogalactoside
ISA	international society for amyloidosis
LB	Lysogeny broth
LCAT	Lethicin cholesterol acyltransferase
LCMS	Liquid chromatography mass spectrometry
LDL	Low density lipoprotein
LDL-R	Low density lipoprotein receptor
MAS	Magic angle spinning
MS	Mass spectrometry

MS-IT-TOF	Mass spectrometry ion trap time of flight
NIDDM	Non-insulin dependent diabetes mellitus
NMR	Nuclear magnetic resonance
OD_{600}	Optical density at 600 nm
OxApoA-I	Oxidised apolipoprotein A-I
PAGE	Polyarylamide gel electrophoresis
PCR	Polymerase chain reaction
PDB	Protein data bank (RSCB)
PLB	Phospholamban
POPC	1-Palmitoyl-2-oleoyl-sn-glycero-3-phosphocholine
RCT	Reverse cholesterol transport
RCSB	Research collaboratory for structural bioinformatics
R Max	Maximum rate
RNA	Ribonucleic acid
ROS	Reactive oxygen species
SAP	Serum amyloid A protein
SDS	Sodium dodecyl sulfate
SLIM	Site-directed ligase independent mutagenesis
SOB	Super optimal broth
SRBI	Scavenger receptor BI
SRE	Self recognition elements
SREBP1	Sterol response element binding protein 1
SSNMR	Solid-state nuclear magnetic resonance
T_1	Longitudinal relaxation
T_2	Transverse relaxation
TEM	Transmission electron microscopy
ThT	Thioflavin T
T lag	Lag time
TMS	Tetramethylsilane
TTR	Transrhyretin
UHPLC	Ultra high performance liquid chromatography
VLDL	Very low density lipoprotein
XRD	X-ray diffraction

1. Introduction to amyloid

1.1. Amyloid Background

The term amyloid was first coined by the German physician Rudolph Virchow in 1854, to describe protein abnormalities taken from cerebral corpora amylacea, which stained positively with iodine reactions (Howie and Brewer, 2009; Sipe and Cohen, 2000; Sipe et al., 2012). Virchow initially presumed these "plaques" consisted mainly of starch, until in 1959 when Freidreich and Kekule discovered not only the absence of carbohydrates but the presence of protein, detected by the high nitrogen content of the plaques (Sipe and Cohen, 2000). Initially Virchow used the iodine-sulphuric acid reaction, common practice in 1814, in order to detect starch. However, the positive results from this test were attributed to the accessory components and associated glycosaminoglycans, rather than the core material, which was later shown to be aggregated protein (Aterman, 1976). Due to the development of more advanced techniques, such as polarising light microscopy, it was possible to detect an apple green birefringence when amyloid deposits were stained with Congo-red (Gillam and MacPhee, 2013; Serpell, Blake, et al., 2000; Sipe and Cohen, 2000). This mode of measurement, now a classifying criterion for all 20 plus amyloid species, was first used on amyloid by Missmahl and Hartwig in 1953 (Howie and Brewer, 2009). The exact mechanism by which Congo red binds to amyloid is still unknown, nevertheless, the resultant birefringence when Congo red stained amyloid is visualised under polarised light is similar to the results observed with cellulose fibrils. This also explains why Virchow came to his inaccurate conclusion that the deposited plaques were composed of starch.

Bottiger first developed Congo red dye in 1884 as a dye for starch rich cottons. The dye works by aligning itself against the cellulose structures, stabilised by the hydrogen bonds between the dye and cellulose. These interactions are expected to be similar to the interaction between the dye and the amyloid fibril. This is due to the linear orientation of both amyloid and cellulose fibrils, as opposed to a branched or helical orientation seen in most other tissues (Howie and Brewer, 2009; Puchtler et al., 1962).

1.1.1. ISA defined amyloid

The International Society for Amyloidosis (ISA) defines amyloid as a protein deposited as insoluble fibrils in tissues and extracellular spaces of organs, after a sequence of changes referred to as amyloidosis. Amyloidosis produces non-branching fibrils, approximately 10nm in diameter, which have the ability to bind Congo red dye and exhibit an apple green birefringence when viewed with a polarised lens. Amyloid species must also be identified by their amino acid sequence, meaning it is insufficient for a mutation of an amyloidogenic protein to be automatically classed as amyloid itself (Sipe et al., 2012). ISA recognises 30 human and 9 animal species of amyloid, many of which have a pathological link to a variety of disease states (Sipe et al., 2014).

1.1.2. Amyloid associated diseases

The misfolding of proteins into amyloid species has been shown to be associated with a wide range of human diseases (**Table 1**.). Proteins involved in amyloid disease can be either: biological peptides (amylin and insulin), full-length proteins (α-synuclein and transthyretin (TTR)), fragments of larger peptides (Aβ

and apoA-I), or caused through general protein decay (Stefani, 2007). In order to classify the different types of amyloid, the 30 species are subdivided into several classes, including whether the amyloid deposits are localised or systemic. Localised species affect only singular tissue types, such as β-amyloid, which deposits solely in the basal forebrain, leading to Alzheimer's disease (Chiti and Dobson, 2006; Whitehouse et al., 1982). However, systemic species are able to affect multiple tissue types and organ systems, such as apolipoprotein AI (apoA-I), the protein of interest in this study. ISA recognises apoA-I derived amyloid deposits in the heart, liver, kidney, peripheral nervous system, testes, larynx and skin, the latter two being C-terminal variants (Sipe et al., 2012).

Amyloidosis is split into 2 groups: either acquired through random mutation of the native protein, such as with serum amyloid A, or hereditary, such as Aβ. ApoA-I is linked to both acquired and hereditary forms of amyloidosis. Random mutations in the apoA-I sequence lead to the aggregation of full-length apoA-I (Das et al., 2016; Mucchiano, et al., 2001; Ramella et al., 2011; Ramella et al., 2012; Wong et al., 2010; Chan et al., 2015), whilst hereditary mutations induce the release of an extremely amyloidogenic N-terminal fragment, referred to as familial apoA-I amyloidosis (Raimondi et al., 2011; Das et al., 2016; Andreola et al., 2003; Adachi et al., 2012). ApoA-I amyloidosis will be discussed in more detail in **Chapter 2**.

Table 1.1 ISA recognised amyloid associated human diseases, caused by the deposition of amyloid fibrils. Table taken from Chiti and Dobson (2006).

Disease	Protein/Peptide	Native Structure	Residues
Neurodegerative			
Alzheimer's	Amyloid β Peptide	Unfolded	40/42
Spongiform Encephalopathy	Prion	Unfolded/Helical	253
Parkinson's	α-Synuclein	Unfolded	140
Dementia	α-Synuclein	Unfolded	140
Frontotemporal Dementia Parkinson's	Tau	Unfolded	352-441
Amylotrophic Lateral Sclerosis	Superdioxide dismutase I	All β, Ig like	153
Huntington's	Huntingtin	Mostly Unfolded	3144
Familial British/Danish Dementia	ABri/ADan	Unfolded	23
Spinocerebella Ataxia	Ataxins	All β	816
	TATA box binding Protein	α and β, TBP like	339
Spinal and Bulbal Muscular Atrophy	Androgen Receptor	All α, nuclear receptor	919
Dentatorubal-Pallidoluysian Atrophy	Atrophin I	Unknown	1185
Non Neuropathic Systemic			
AL Amyloidosis	Ig Light Chain	All β, Ig like	90
AA Amyloidosis	Serum Amyloid A Protein	All α	76-104
Senile Systemic Amyloidosis	Wild-typeTransthyretin	All α and β	127
Familial Polyneiropathy	Mutant Transthyretin	All β	127
ApoA-I Amyloidosis	**(N-terminal) Apo AI**	**Mostly α**	**(80-93)**
ApoA-II Amyloidosis	(N-terminal) Apo AII	Unknown	98
ApoA-IV Amyloidosis	(N-terminal) Apo AIV	Unknown	70
Finnish Hereditary Amyloidosis	Gelsolin Mutants	Unknown	71
Lysosome Amyloidosis	Lysozyme Mutants	α and β Lysozyme	130
Fibronogen Amyloidosis	Fibrogen α-Chain	Unknown	27-81
Icelandic Hereditary Cerebral amyloid angiopathy	Cystatin C Mutant	α and β Cystatin	120
Non Neuropathic Localised			
Type II Diabetes	Amylin (IAPP)	Unfolded	37
Thyroid Medullary Carcinoma	Calcitonin	Unfolded	32
Arterial Amyloidosis	Atrial Natriuretic Factor	Unfolded	28
Cerebral Haemorrhage	Mutant Amyloid β	Unfolded	40/42
Pituitary Prolactinoma	Prolactin	All α, 4 helical	199
Injection Localised Amyloidosis	Insulin	All α, insulin like	21+30
Aortic Medial Amyloidosis	Medin	Unknown	50
Hereditary Lattice Corneal Dystrophy	Kerato-epithelin	Unknown	50-200
Corneal Amyloidosis (Trichiasis)	Lactoferrin	α and β	692
Cataract	γ-Crystallins	All β, crystallin like	Variable
Pulmonary Alveolar Proteinosis	Unknown	Unknown	35
Inclusion Body Myositis	Lung Surfactant Protein C	Unfolded	40/42
Cutaneous Lichen Amyloidosis	Amyloid β Peptide	Unknown	Variable
Calcifying Epithelial Odontogenic Tumour	Keratins	Unknown	46

1.1.3. Amyloid disease pathology

Despite the research into the various amyloid associated diseases, detailed in **Table 1**, a definitive pathology of the aetiology of amyloid associated diseases remains unknown. Many amyloid species are formed through the conversion of monomeric proteins, via soluble oligomeric intermediates, into the insoluble amyloid fibril structures. It is still debated whether the fibrillar deposits are the cause of the disease phenotype, or whether they are an end product of the disease progression. This pathology could be initiated by the oligomeric species which, across the different diseases, have a common structure and are often toxic (Gillam and MacPhee, 2013; Janson et al., 1999; Kayed, 2003; Stefani, 2007). It would appear that the causal species varies with each disease.

1.1.4. Oligomer induced pathology

Oligomeric species of amyloidogenic proteins have been shown to be the cause of many disease phenotypes. For example, in non-insulin dependent diabetes mellitus (NIDDM), by selecting for the formation of oligomeric species in the amyloidosis process, rather than the fibril end product, the oligomers have been shown to be toxic and thus the cause of the disease state (Janson et al., 1999; Kayed, 2003). Rifampicin is a drug commonly used to treat bacterial infections by inhibiting the bacterial RNA polymerase. However, Rifampicin has also been shown to have inhibitory effects on the formation of islet amyloid polypeptide (IAPP) fibrils, but not the oligomeric species, as described in **Figure 1.1**. Inhibition of fibril formation still resulted in β-cell apoptosis, confirming that it is the oligomeric species that causes the NIDDM phenotype (Meier et al., 2006).

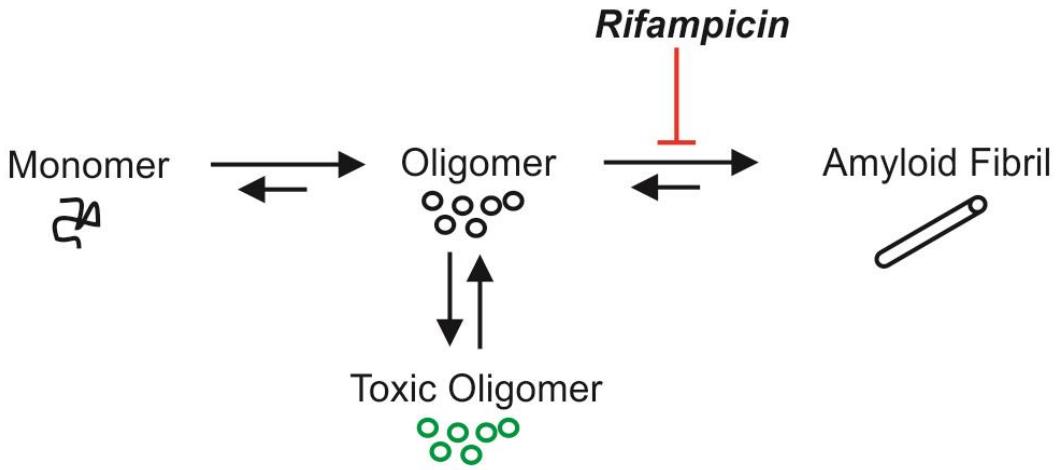

Figure 1.1 Schematic of the amyloidosis of human islet amyloid polypeptide, detailing the conversion from monomeric peptide through oligomeric species into the amyloid fibril. Rifampicin inhibits the formation of fibrils leading to an increased oligomer concentration and subsequent toxic species. Image replicated from Meier *et al.* (2006).

Other examples of oligomer-induced disease pathology include Alzheimer's (Ahmed et al., 2010; Huang et al., 2000; Näslund et al., 2000), Parkinson's, Huntington's, and Familial British dementia (Haass and Selkoe, 2007; Walsh et al., 2002). In Alzheimer's disease, the extent of disease progression is directly correlated to the accumulation of the soluble oligomeric form of the amyloid β protein in the brain, rather than the extent of fibril plaque deposition. This is despite the presence of plaques correlating with the severity of the disease (Berthelot et al., 2013; Kayed, 2003; Näslund et al., 2000). This implies that the amyloid deposits are merely an end product of the disease pathology. This is further confirmed by the presence of plaques many years prior to the disease onset (Perrin et al., 2009).

The structure of the oligomers in amyloidosis varies depending on the particular protein. In Alzheimer's disease, for example, the Aβ (1-42) peptide has the ability to form stable trimeric, tetrameric and pentameric oligomer complexes, in stark contrast to the Aβ (1-40) which does not (Ahmed et al., 2010). This is despite both peptides being able to form full-length amyloid species in the correct conditions.

The proposed mechanism of how oligomeric intermediates manifest into the disease phenotype involves their interaction and disruption of lipid membranes, leading to a loss of selectivity in ion permeability cumulating in cell apoptosis. The oligomeric interactions damage a cell's permeability through a range of methods, described in **Figure 1.2**, including: detergent effects, raft formations, carpeting effects and pore formation. The carpeting and raft-like formations involve the assembly of amyloid fibrils on, or within, the membranes, inhibiting the membrane's normal function (Berthelot et al., 2013), leading to apoptosis. In addition to apoptosis, increased cellular Ca^{2+} levels lead to an increase in reactive oxygen species (ROS), potentially through activation of the citric acid cycle in order to produce excessive ATP, required for the removal of the excess calcium (Stefani, 2007). The exact method of how the oligomers open up the calcium pores is disputed, with two main theories varying in the origin of the oligomers, either outside the cell or after internalisation, prior to interacting with the calcium pores (Demuro et al., 2011). Soluble oligomeric species have also been shown to bind metals, and induce the production of reactive oxygen species (Maynard et al., 2005)

Inhibition of protein aggregation which would retain a protein in its non-toxic monomeric form (Walsh et al., 1997), or its toxic oligomeric form, whilst

enhancement of amyloidosis into full-length fibrils, thus avoiding the toxic oligomeric stage (Madine and Middleton, 2010), are both potential therapeutic techniques. However, not all oligomers in amyloidosis are harmful (Berthelot et al., 2013; Stefani, 2007) and in some cases can be used as potential fibril inhibitors (Uversky, 2010).

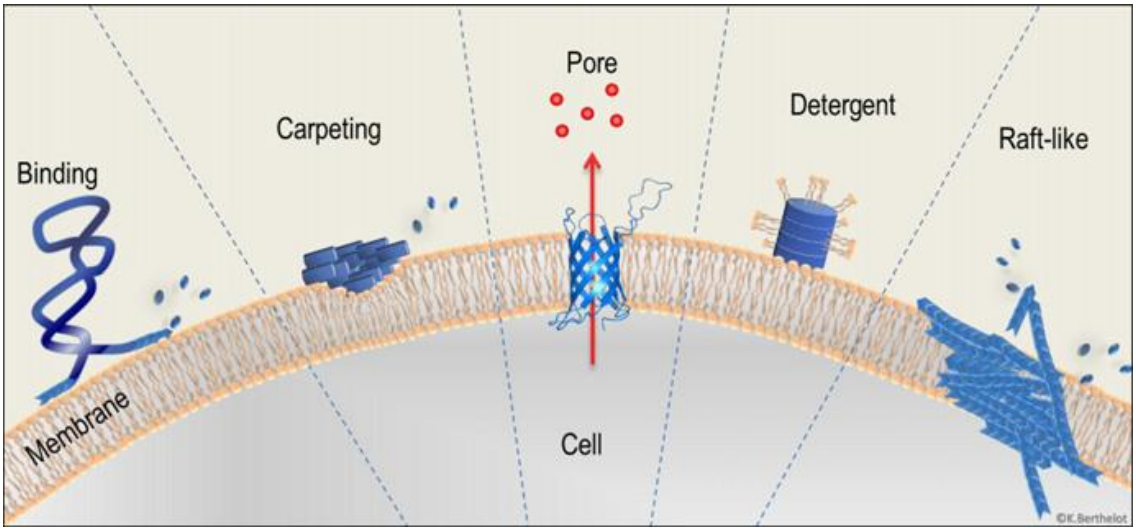

Figure 1.2 Models depicting the interactions between lipid membranes and amyloid that leads to membrane destabilisation and subsequent cell death, via apoptosis. Image taken from Bertheloti (2013).

1.1.5. Amyloid associated components

Amyloid deposits involved in Parkinson's, Alzheimer's and prion associated diseases have all been associated with assemblies that contain non-fibrillar components (Madine et al., 2013) including: other proteins, polysaccharides, proteoglycans and serum amyloid P component (Desai et al., 2010; Chan et al., 2015). There is also evidence for a high concentration of metal ions such as copper, zinc and iron included within the amyloid deposits. These ions have the

ability to induce aggregation via an overall reduction in protein charge or by bridging two peptides. Alternatively, metal ions are also able to inhibit aggregation of amyloidogenic proteins by increasing the net charge of the protein or by interfering with β-sheet stabilising bonds (Alies et al., 2013). The effects of ions are dependent on the specific amino acid sequence.

Proteoglycans, including the long, unbranched glycosaminoglycans (GAG's): heparin, dermatan, keratin and chondroitin sulphates have all been found in amyloid deposits. These GAGs have been shown to initiate the formation of fibrils, in addition to providing stability and resistance to proteolysis (Cohlberg et al., 2002; Madine et al., 2013; Papy-Garcia et al., 2011).

1.1.5.1. Heparin

Heparin, a highly sulphated GAG, is comprised of disaccharide repeats containing an uronic acid, either glucuroinic or iduronic acid, followed by an amino sugar (Casu et al., 2015; Khan et al., 2010). The most common pairing of these involves L-idopyranosyluronic acid 2-sulfate (IdoA2) and 2-deoxy-2-sulfamino-D-glucopyranose-6–phosphate (GlcNS,6S) (**Figure 1.3A**), which accounts for 75–85 % of heparin species within amyloid plaques (Gatti et al., 1979; Casu et al., 2015). The three sulphate groups on this disaccharide repeat highlights the strong charge carried on all heparin molecules, making it one of the most negatively charged molecule in nature. **Figure 1.3B** shows a molecule of heparin consisting of 12 disaccharide repeats of IdoA2-GlcNS,6S (Khan et al., 2010).

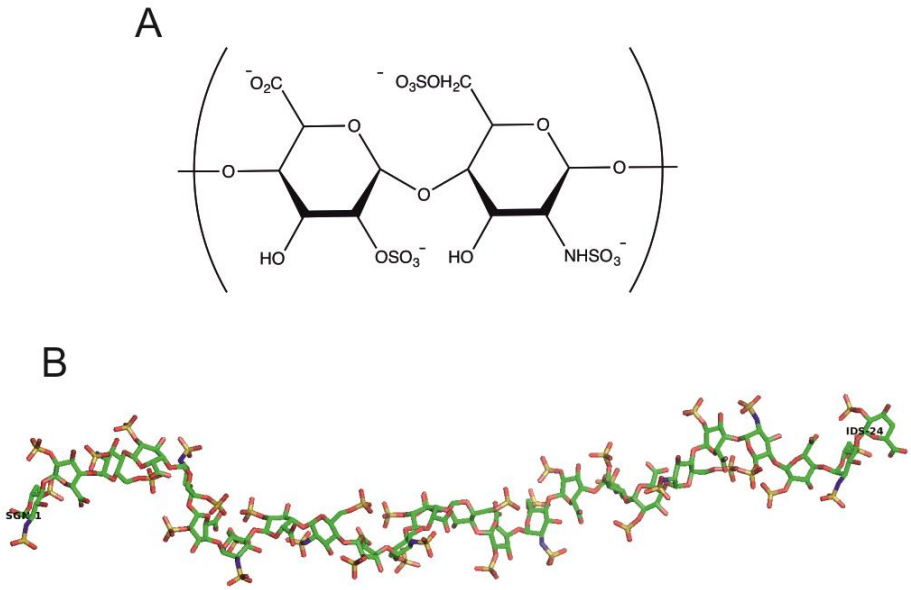

Figure 1.3 (**A**) Disaccharide of IdoA2-GlnNS,6*S* and (**B**) a molecule of heparin consisting of 12 of IdoA2-GlnNS,6*S* repeats (PDB 3IRJ).

Heparin promotes aggregation of the amyloidogenic protein α-synuclein (Cohlberg et al., 2002; Madine et al., 2013), measured both by an increase in fibril yield and rate of aggregation. The ratio of heparin to α-synuclein, and the inclusion of fluorescently labelled heparin within fibrils structures, indicates that the heparin does not merely act as a catalyst for aggregation, but is incorporated into the fibril during its formation (Cohlberg et al., 2002). Heparin is believed to act as a scaffold protein, aligning the α-synuclein monomers in an orientation that favours the formation of β-sheet structures, and promotes stabilising bonds between protein molecules (Madine et al., 2013). Heparin has promoted the formation of ThT responsive fibrillar species in proteins that have no natural propensity to aggregate, such as residues 1-23 of phospholamban (PLB). The peptide PLB (1-23) is predicted to have a low natural propensity to form amyloid. However, in the presence of heparin, a dramatic increase in ThT fluorescence was observed, suggesting amyloid formation (Madine et al., 2013).

1.2. Protein folding and misfolding

Proteins are synthesised as long polypeptide chains with no secondary structure. Consequently, the protein has to determine its own final structure through a specific folding pathway, via intermediates. This leads to the most stable 3D structure (Radford, 2000), with the exception of several unfolded functioning proteins, such as α-synuclein and tau, both of which have increased propensity to aggregate, due to their unfolded nature (Fowler et al., 2007). The 3D structure of each protein is essential to its individual function, in conjunction with the specific amino acid sequence of the protein, and the environment in which the protein is located. All three variables work in co-operation to place the relevant amino acids in the required position, in relation to all other residues, in order for the protein to carry out its biological function.

If the folding pathway becomes disrupted, leading to a novel fold, the protein will usually lose its native function and, in some cases, gain a novel function, according to the new fold. This can lead to a malfunction in a biological process, causing disease pathology (Teoh et al., 2011).

Folding proteins are said to follow an energy landscape mechanism (**Figure 1.4**), whereby the unfolded protein at the top of the funnel samples many different folding conformations, selecting the one with the lowest free energy. This process of trial-by-error continues, forming more stable intermediates, as Van der Waals and hydrogen bonds stabilise the overall structure. Each stabilisation reduces the energy requirements, until the protein finds its native fold, the most stable conformation with the lowest free energy (Radford, 2000).

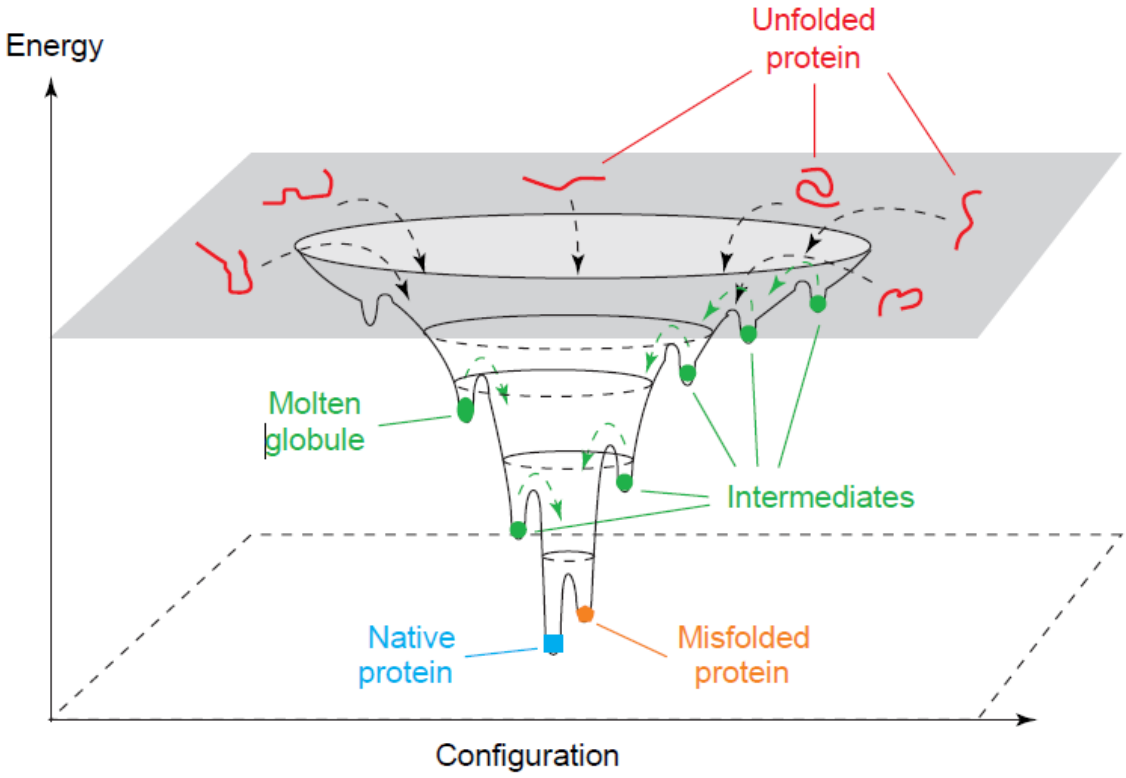

Figure 1.4 Energy landscape schematic indicating the newly synthesised, unfolded proteins entering the top of the funnel (red), the different folding routes a protein can take via intermediate folds (green), resulting in the final natively folded protein (blue). If a particular fold results in a conformation that does not allow further folding into the native structure, and cannot be recovered, the protein has misfolded (orange). Image taken from Radford (2000).

In some circumstances, the intermediate conformation trialled is either less stable or an off-pathway intermediate, leading to the formation of a misfolded protein. This misfolded intermediate can usually be corrected with the help of chaperone proteins. Chaperone proteins allow the reversal of the free-energy driven protein folding, allowing the previous intermediate to select another, more suitable conformation. In some cases, the misfolded intermediate

is too far off the native folding pathway and cannot be recovered, sometimes leading to their aggregation, which can act as precursors for amyloid formation (Dobson, 2003) as shown in **Figure 1.5**.

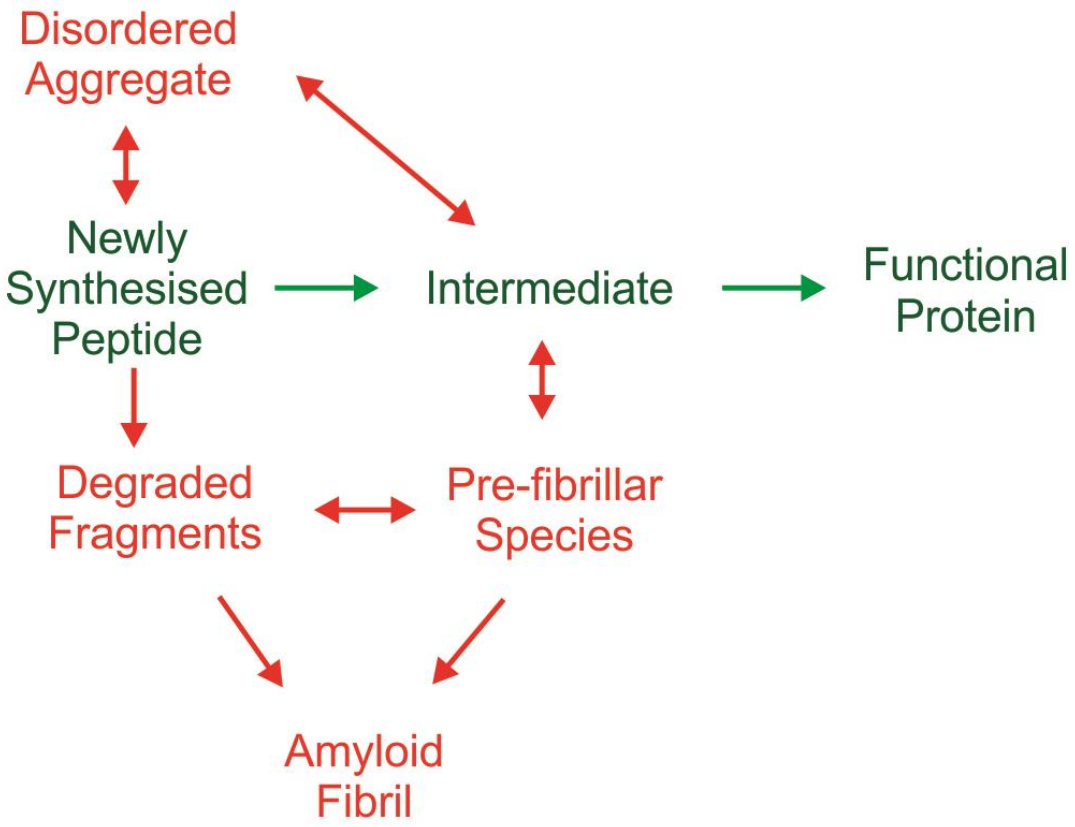

Figure 1.5 Schematic of the protein-folding pathway. The newly synthesised polypeptide chains fold, via intermediates, into the native protein structure, which may be incorporated into larger protein complexes, highlighted by the green arrow pathway. Alternatively, both the unfolded protein and the intermediate folds may form disordered aggregates or prefibrillar species that can promote amyloid formation through seeding.

1.3. Amyloid aggregation

1.3.1. Destabilisation

Amyloid fibres form via the misfolding of proteins into highly ordered β-sheet structures that do not match their native, most stable form, as shown in **Figure 1.5** (Dobson, 2003; Gillam and MacPhee, 2013; Serpell, Sunde, et al., 2000; Teoh et al., 2011). These misfolded proteins then have a higher propensity to aggregate, due to the exposure of aggregation prone regions, which self-assemble into amyloid structures. The aggregation into amyloid is not exclusive to the proteins listed above in **Table 1,** and it is theorised that, under the correct conditions, all proteins have the ability to misfold into an amyloid conformation (Madine et al., 2013; Guijarro et al., 1998).

1.3.2. Nucleation dependent polymerisation

Nucleation dependent aggregation is the leading theory detailing amyloid formation (Chiti and Dobson, 2006; Gillam and MacPhee, 2013). This mechanism is made up of four key stages: a lag phase, a nucleation point, rapid exponential growth, and finally, the accumulation of fully formed fibrils. Although the lag phase appears to have no aggregation kinetics, during this phase the individual protein monomers accumulate into a critical sized homogenous nucleus with a high β-sheet content. This process of aggregation is kinetically unfavourable and is dependent on various conditions, including protein concentration, pH and salt concentration. Once the nucleus has reached a critical state, it passes through the nucleation point and undergoes a thermodynamically favourable elongation process. During this period, protein monomers and oligomers are recruited to the elongating fibre, until the level of monomeric protein in solution is depleted

(Alies et al., 2013; Larsson et al., 2011; Naiki et al., 1997; Serio et al., 2000; Souillac et al., 2002). The most accurate way to measure amyloid formation is through the use of the benzothiazole salt dye, Thioflavin T (ThT). Upon binding to the grooves in the β-sheet structures of amyloid, the ThT molecule experiences a red shift in its fluorescence spectra, resulting in increased emission at 482 nm (LeVine, 1999; Wolfe et al., 2010). By following the increase in fluorescence, the aggregation of proteins into amyloid can be followed in real time, as well as allowing the calculation of the aggregation kinetics, as shown in **Figure 1.6**.

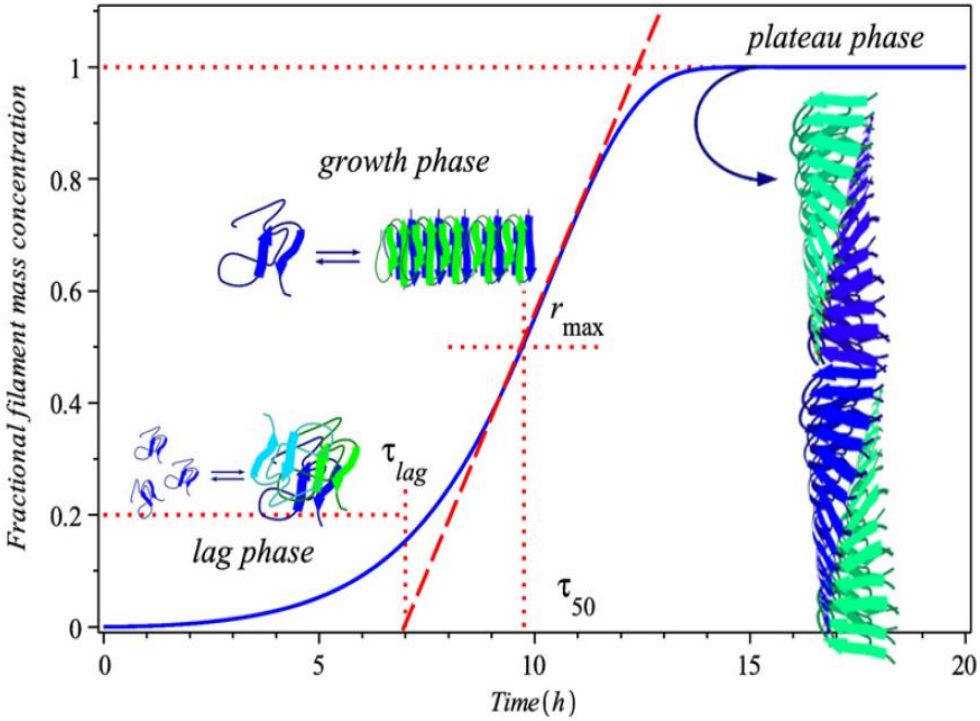

Figure 1.6 Sigmoidal growth curve of amyloid fibrils, via a nucleation dependent polymerisation mechanism. The ThT fluorescence at 482nm depicts a lag phase, a nucleation point, an exponential growth then a plateau phase. From these values, a lag time (τ_{lag}) and a rate of aggregation (r_{max}) can be calculated from the gradient of the slope when it is at its steepest. Image taken from Gillam & MacPhee (2013).

1.3.3. Seeding

The length of the lag phase in amyloid aggregation is highly variable between different amyloid species and conditions. The lag phase length can be reduced through seeding; a process that introduces pre-formed, homogenous aggregated protein fragments to the un-aggregated protein solution. These fragments act as the critical sized nucleus and promote the exponential growth of the fibril, hence reducing the lag phase, as shown in **Figure 1.7** (Larsson et al., 2011; Paravastu et al., 2009).

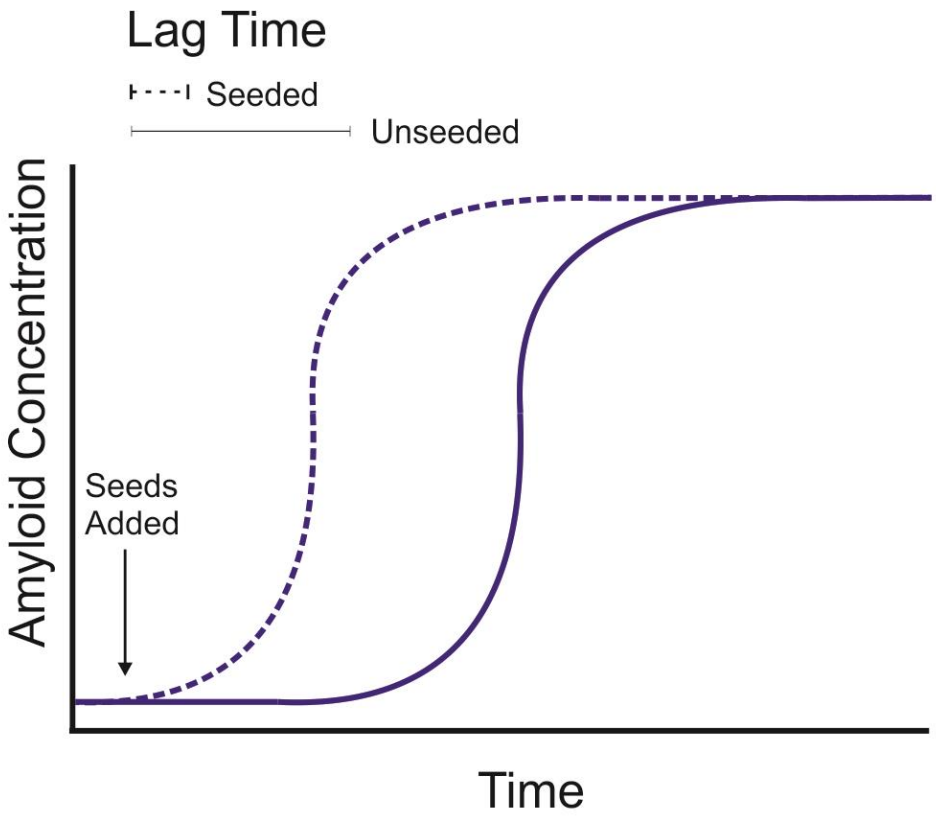

Figure 1.7 Model sigmoidal curve of amyloid formation, via nucleation dependent polymerisation. The blue solid line indicates the natural formation of amyloid, with the length of the lag phase shown above. The blue dotted line indicates the formation of amyloid after seeding (point shown), again with the lag time shown above.

1.3.4. Lipid induced amyloidosis

Many of the proteins that misfold into amyloid species demonstrate increased aggregation upon interaction with lipids, micelles and membranes. For example, the anionic surface induced oligomerisation of α-synuclein in Parkinson's disease (Necula et al., 2003), and islet amyloid polypeptide (IAPP) in diabetes mellitus. In the case of IAPP, the protein interacts with phospholipid membranes, which acts as a catalyst, resulting in the assembly of pre-amyloid structures. These structures can then induce nucleation dependent polymerisation, in a similar manner to seeding aggregation, reducing the lag time and increasing amyloidosis by up to 10 fold (Knight and Miranker, 2004).

In Alzheimer's disease, Aβ peptides interact strongly with GM1-ganglioside containing membranes, leading to the deformation of the C-terminus of Aβ and exposure of hydrophobic regions. These regions then lead to the oligomerisation of 2 Aβ peptides into a β-sheet structure, followed by growth of the fibril (Hoshino et al., 2013). The catalytic effect of membranes on the aggregation of amyloid prone proteins not only exacerbates the disease pathology through fibril formation but, during the interaction, the membranes normal function is often compromised, leading to additional cytotoxicity.

1.3.5. Functional amyloid

Not all amyloid species are inactive aggregates of previously native, functioning proteins. There are many cases where amyloid fibrils have essential functions in humans, bacteria, fungi, and invertebrates, highlighted in **Table 1.2** (Fowler et al., 2007).

Bacteria utilise the high strength of amyloid fibrils, which in some cases have a strength yield similar to steel (Smith et al., 2006), and their immunity to protease degradation is an advantage to their function in mechanical processes within the cells. *Escherichia Coli* for example, contain machinery that actively promotes the formation of the curli amyloid fibril (Cherny et al., 2005), a structural protein used in surface adhesion, colony formation and the promotion of host inflammatory responses (Barnhart and Chapman, 2006; Chapman et al., 2002). In insects and fish, the amyloid species of the chorion proteins are present in the shell of the eggs, protecting it from physical damage, protease degradation and microorganisms (Fowler et al., 2007; Podrabsky et al., 2001).

In humans, a cleaved fragment of the Pmel 17 protein, referred to as Mα, forms amyloid fibrils that act as a template in the synthesis of melanin, accelerating the polymerisation of melanogenic precursors into melanin. Studies have shown that replacing the Mα amyloid with another species of amyloid fibril produces an equal increase in the production of melanin, suggesting that the amyloid structure, rather than the specific protein, is responsible for the enhanced melanin synthesis. Due to the risk of cytotoxic oligomer production as a by-product of these pathways, the formation of amyloid for functional reasons must be highly regulated (Fowler et al., 2007).

Table 1.2 Species of functional amyloid across bacterial, fungal and animal cell lines. The table was produced with data from Fowler *et al.* (2007) and Chiti & Dobson (2006).

Species	Protein	Function
Bacteria:		
E. Coli, Salmonella	Curli	Biofilm and Host Invasion
Streptomyces Coelicolor	Chaplins	Water Surface Tension Modulation
Fungi		
Podospora Anserine	HET-s	Heterokaryon formation
Sacchromyces Cerevisiae	URE2p	Nitrogen Catabolism
	Sup35p	Non Stop Codon Read Through
	Rnq1p	Poorly Understood
Most Fungi	Hydrophobins	Adhesion and Surface Tension
Animalia		
Insects and Fish	Chorion	Eggshell protective and support
Nephila Clavipes	Proteins	Structural, present in Spider silk
Aplisia Californica (Marine snail)	Spidroins Neuron CPEB	Maintenance of synaptic changes in memory
Homo Sapiens	Pmel17	Scaffold and melanin intermediate

1.4. Amyloid characteristics

1.4.1 Amyloid morphology

Amyloid fibrils produce a very characteristic morphology, consisting of long, unbranched fibrils, with a diameter of between 5 and 10 nm and a length of up to 1600 nm when viewed via transmission electron or atomic force microscopy (**Figure 1.8**).

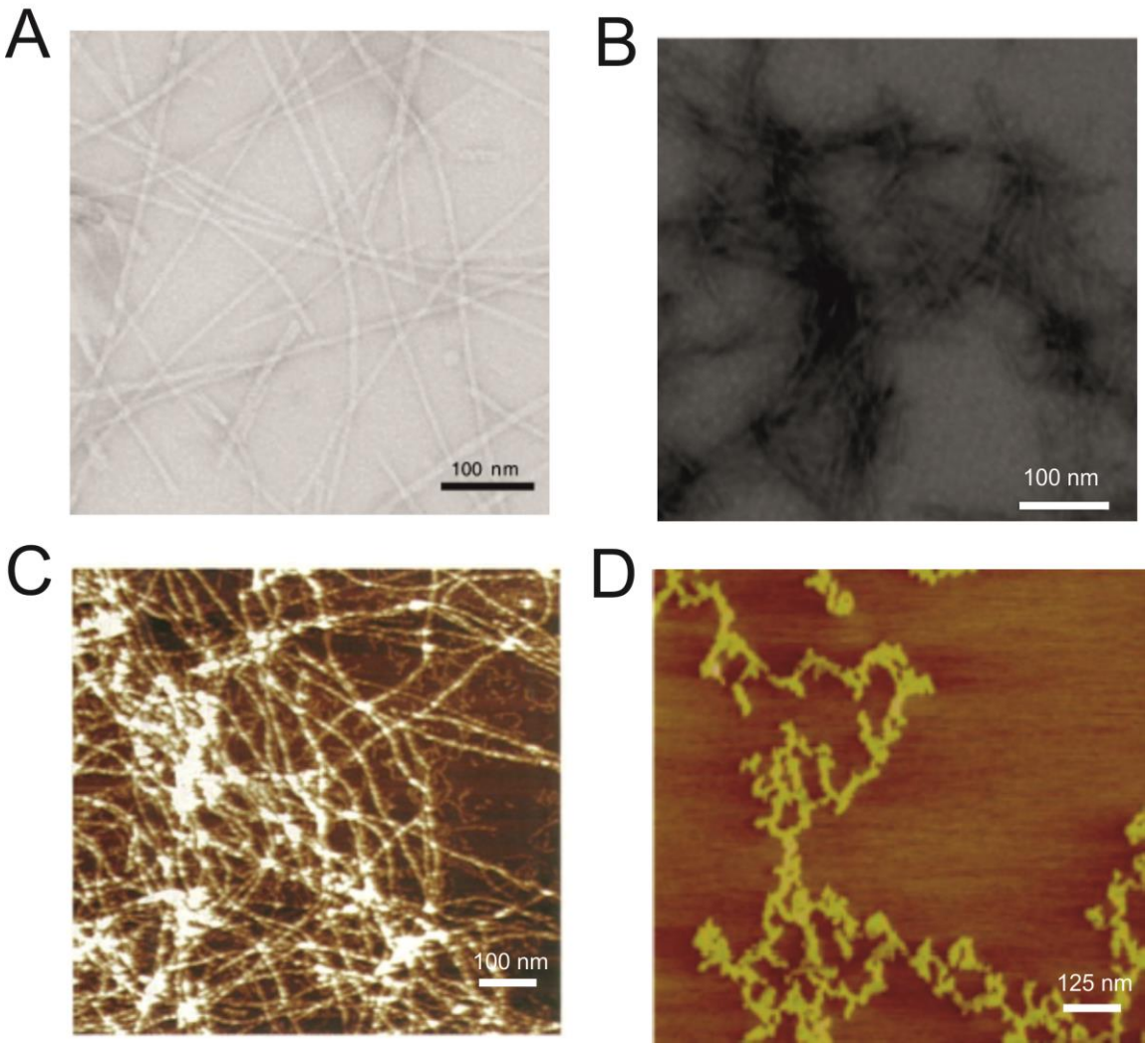

Figure 1.8 Morphology of amyloid fibrils determined by TEM for (**A**) IAPP (Makin and Serpell, 2005) and (**B**) PLB (1-23) in the presence of heparin (Madine et al., 2013) and via AFM for (**C**) Aβ40 (Harper, Lieber, et al., 1997) and (**D**) apoA-I (Ramella et al., 2011).

1.4.2. Amyloid structure

With the development in molecular level biophysical analysis, common themes are being elucidated about amyloid fibrils, regardless of the protein sequence.

There are three levels of structure in amyloid, as shown in **Figure 1.9**. The end product of fully formed fibrils can be visualised as networks of long, un-branched fibres via electron and atomic force microscopy imaging. They have a diameter of approximately 60-120 Å and a length from 1000 to 16,000 Å.

These fibrils can be broken down into 5-8 proto-filaments (not to be confused with proto-fibrils, which represent partially fibrillar aggregates along the aggregation pathway), which arrange parallel to each other, extending in the direction of the fibre, with a diameter of roughly 25-35 Å. Each proto-filament contains an arrangement of β-sheet structural motifs, arranged perpendicular to the fibril axis in a cross-β conformation, typical of all amyloid species (Serpell, Blake, et al., 2000; Serpell, Sunde, et al., 2000; Serpell et al., 1997).

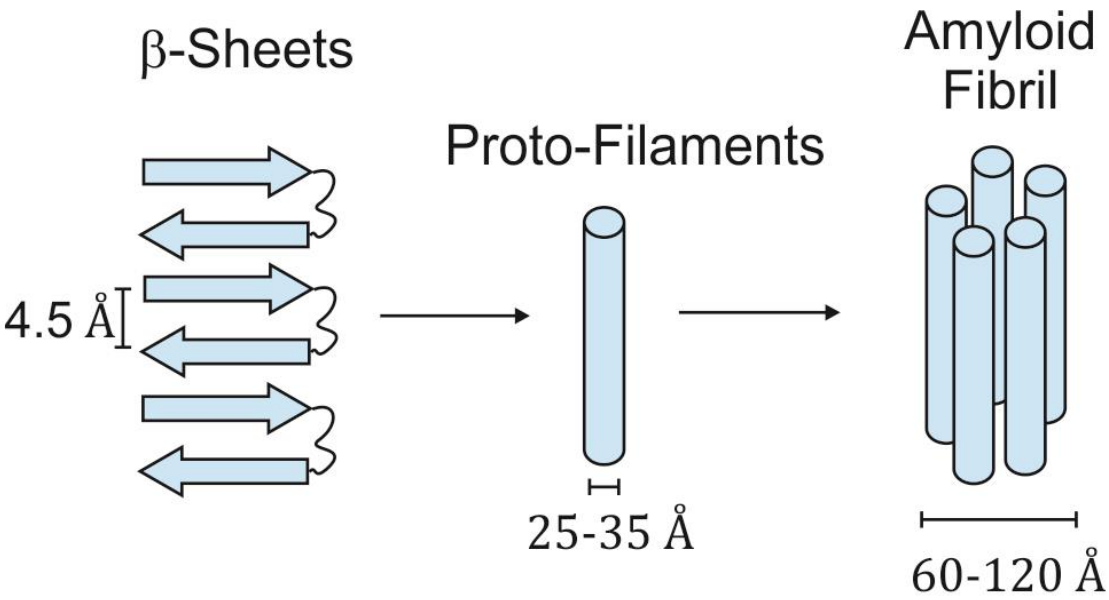

Figure 1.9 Schematic diagram of the 3 levels of amyloid structure, from β-sheets in a cross-β structure, via proto-filaments, into full-length fibrils.

1.4.3. Cross-β structure

Amyloid is highly distinguishable from other forms of insoluble protein aggregates, due to the high proportion of β-sheet secondary structures (Gillam and MacPhee, 2013), which run parallel to the fibril axis (**Figure 1.10B**). X-ray diffraction studies identify a core repeated region with a cross β conformation, containing sharp meridian reflections at 4.7-4.8 Å and less intense equatorial reflections at approximately 10 Å (**Figure 1.10A**). These reflections indicate the distance between the individual β-strands, running perpendicular to the fibril axis, and the multiple β-sheet layers, respectively (**Figure 1.10 C**) (Serpell et al., 2000; Serpell et al., 1997; Jahn et al., 2010; Biancalana and Koide, 2010).

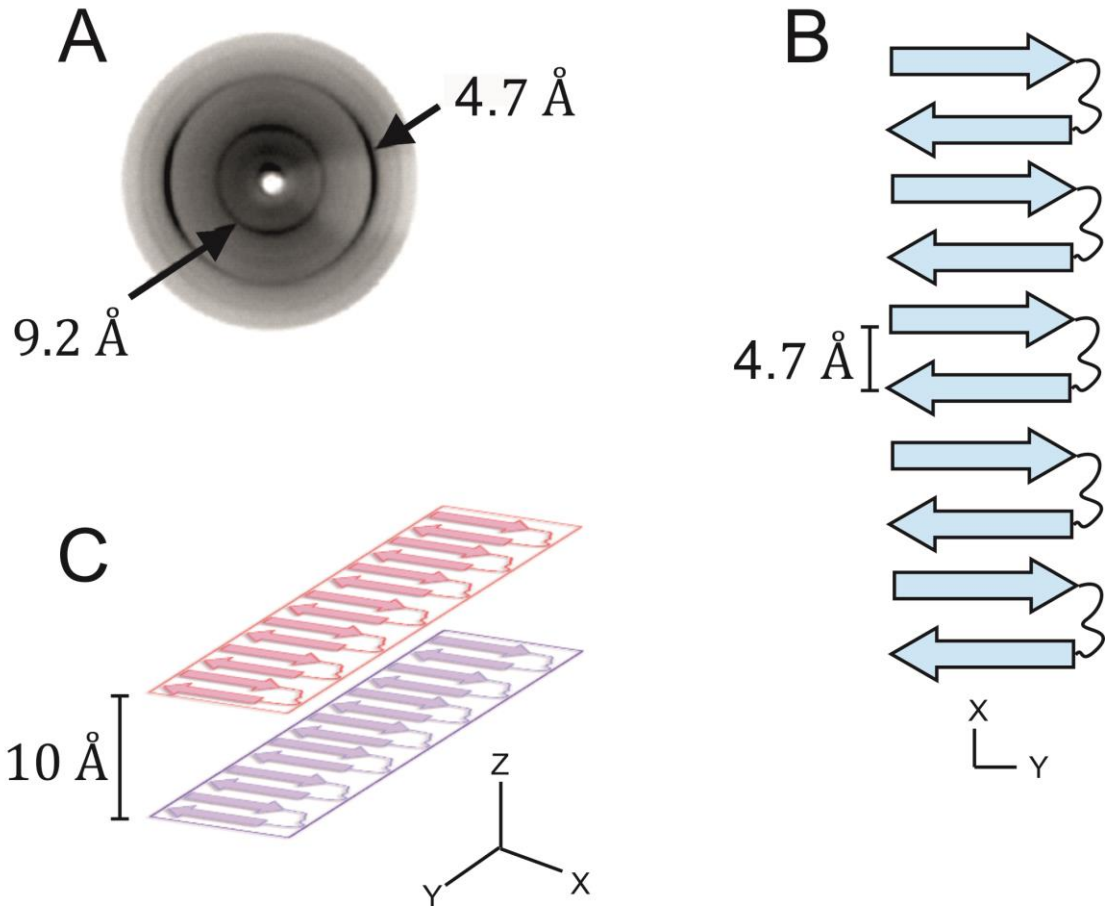

Figure 1.10 (**A**) X-ray fibre diffraction pattern for un-orientated transthyretin (105-115), highlighting reflections at 4.7 Å and roughly 10 Å, consistent with β-sheet spacings. Image taken from Gillam and MacPhee (2013). (**B**) Model of the β strand composition along the fibril axis forming a β-sheet structure in semi-crystalline amyloid species, with the gap between each β strand labelled as 4.7 Å. (**C**) Model of two β-sheets aligning with a 10 Å gap in between.

1.4.4. Tertiary structure

The individual β-sheets that form the cross β structure in **Figure 1.10B** are in an anti-parallel conformation. Nevertheless, they can also be orientated in a parallel form, as shown in **Figure 1.11A**. These β-strands are formed through backbone amide group interactions that are stabilised through hydrogen bonding. In the majority of amyloid structures, the β-sheet lie in-register, with the same side chains stacking on top of each other, a formation described as a steric zipper (**Figure 1.11B**). Other models including a β-helix conformation were originally proposed as the structure of amyloid, due to the high β-strand content measured by circular dichroism (CD) and morphology deduced by TEM. However, these were disproved when X-ray diffraction (XRD) patterns of amyloid lacked the required internal and external radii of 6 and 16 Å, respectively.

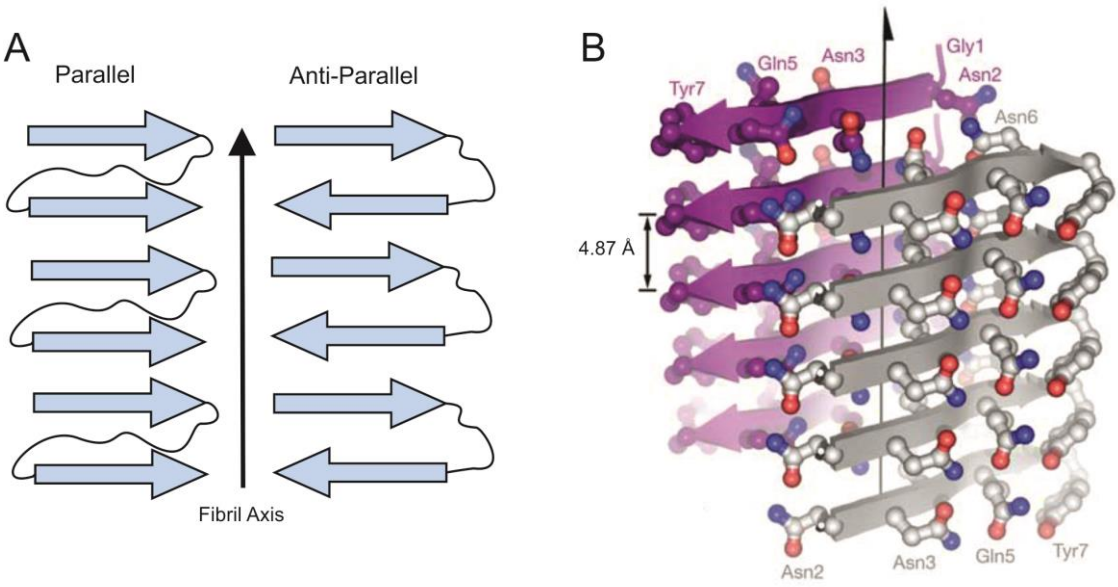

Figure 1.11 (**A**) Models of β-sheets formed through the parallel and anti-parallel orientation of individual β-strands. (**B**) Steric zipper conformation in amyloid, where equivalent side chains stack vertically along the fibril axis. Image taken from (Nelson et al., 2005).

1.4.5. Quaternary structure of amyloid

Despite the common structures mentioned above, which make up the amyloid fibre and are uniform across all thirty plus species of amyloidogenic proteins, variation in the protein sequence can lead to changes in the overall quaternary structure of the amyloid. Specific amino acid side chains extending out from the β-sheets can promote intra-molecular interactions, which lead to variation in the overall conformation of the many β-sheets in the amyloid (Petkova et al., 2002; Tycko, 2011).

In some species of amyloid, different quaternary structures can be produced *in vitro* by the same protein precursor, depending on the conditions under which the proteins are studied. For example, the Aβ (1-40) peptide associated with Alzheimer's disease has two well-defined quaternary structures for amyloid fibrils: 2A (striated ribbon) and 3Q (twisted pair) (Tycko, 2011). Despite their differences, both models share similar traits, including their overall U shape, caused by two parallel β-strands formed from residues 10-22 and 30-40. Agitation promotes the formation of striated ribbon (2A) fibrils with a straight rod appearance and a diameter of 6nm, formed via lateral association. The proto-filaments of 2A fibrils contain two cross-β structures, in a twofold rotational symmetry along the fibril axis (**Figure 1.12A**), stabilised by a salt bridge between residues D23 and K28 (Petkova et al., 2006). However, when Aβ(1-40) is incubated in quiescent conditions, fibrils with a modulation in their diameter and an apparent lack of lateral association are formed. The proto-filaments of 3Q fibrils contain three cross-β structures in a threefold rotational symmetry (**Figure 1.12B**) with no salt bridge formation (Tycko, 2011).

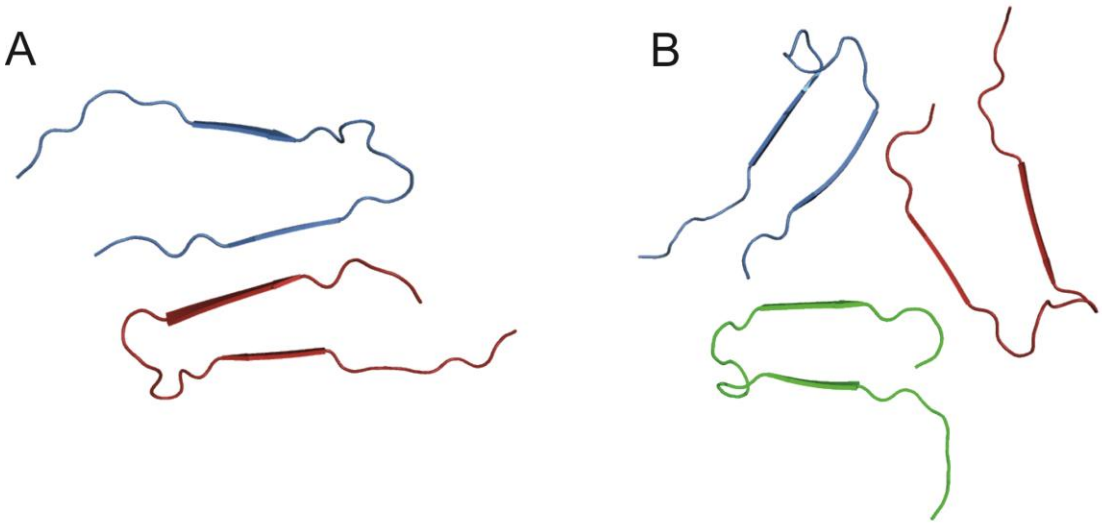

Figure 1.12 Aβ structures viewed along the fibrils axis formed under (**A**) agitated (2A) (PDB 2LMN) and (**B**) quiescent (3Q) conditions (PDB 2LMP) (Paravastu et al., 2008).

1.5. Amyloid Therapies

Despite the large amount of literature on amyloid associated diseases, there is currently no single cure. Available therapies are often invasive and focus around three main areas: targeting the source of the amyloid, inhibiting the toxic oligomeric phase and removing amyloid plaques (**Figure 1.13 and 1.14**).

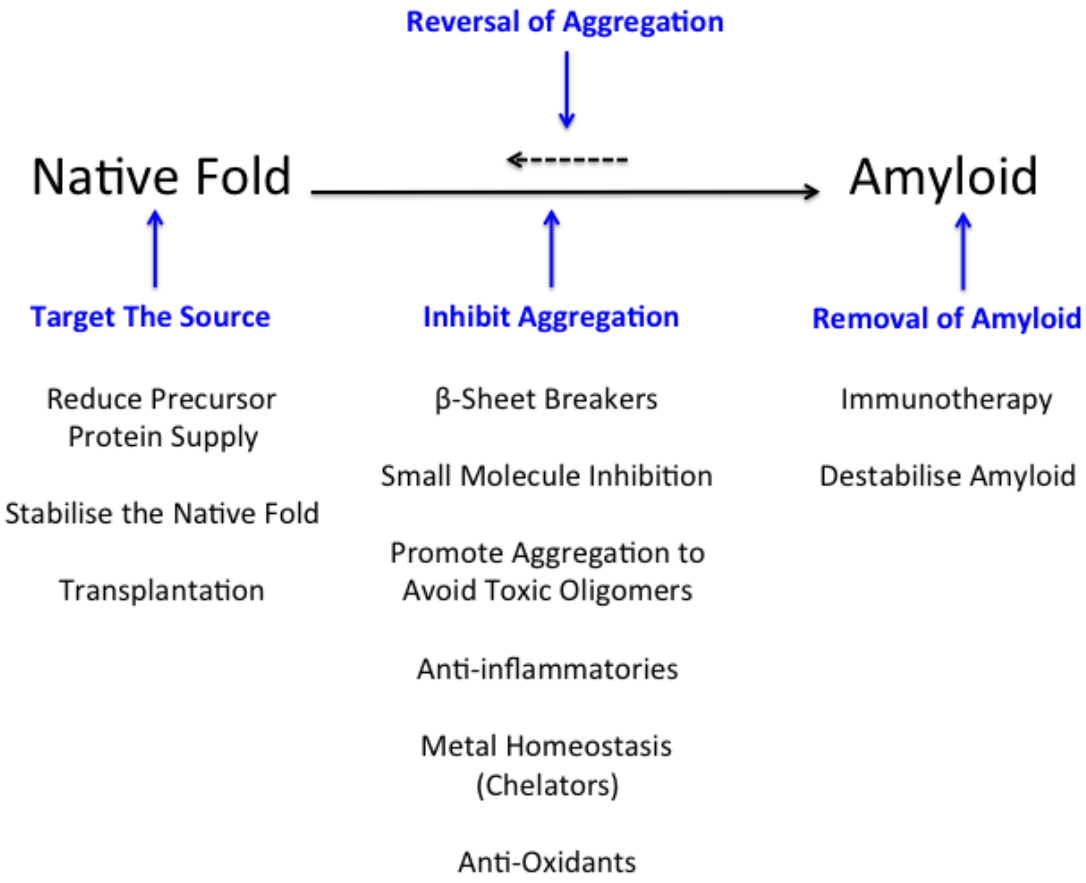

Figure 1.13 Therapeutic strategies to inhibit production, formation and stability of amyloid.

1.5.1. Targeting the source

Current therapies against systemic amyloidosis focus mainly on reducing the supply of precursor protein, in particular at the level of expression, so as to include both wild type and any cleaved amyloidogenic peptides. In AA

amyloidosis, patients are treated with anti-inflammatory drugs to reduce the production of the serum amyloid A (SAP) protein, the expression of which is increased during inflammation. In AL amyloidosis, targeting B-cell dyscrasia with chemotherapy regulates production of the monoclonal immunoglobulin light chain (Gillmore and Hawkins, 2006). In transthyretin (TTR) and Aα-chain amyloidosis, liver transplantation removes the abnormal genetic variant of the protein (Desai et al., 2010). In Alzheimer's disease, drugs targeting the β and γ-secretase enzymes, which cause cleavage of the amyloidogenic Aβ (1-40/42) peptide from the amyloid precursor protein, are currently under investigation (Gillmore and Hawkins, 2006; Kumar et al., 2016). Furthermore, in Alzheimer's disease, hyper-phosphorylation of the tau protein can lead to its aggregation into amyloid-like structures (Sipe et al., 2014) and the production of neurofibrillary tangles (Kumar et al., 2016). Down regulation of glycogen synthase kinase (GSK-3), the main protein involved in the phosphorylation of tau, has been considered as a potential therapy. Chemotherapy can also be used in the case of AL amyloidosis to eliminate the plasma cell clones responsible for the mutant AL secretion. This process involves removal of the patient's own stem cells, followed by autologous stem cell transplantation (ASCT). This procedure can also be combined with heart transplantation (Dubrey et al., 2011).

1.5.2. Stabilising the native fold

Another method to inhibit amyloid formation is through stabilisation of the proteins native fold, since amyloidosis begins with destabilisation of the native fold. In TTR, it has been shown that small molecules can bind to the amyloid fibril precursors, stabilising their fold and reducing the propensity for them to

aggregate (Gillmore and Hawkins, 2006). One such drug in development, Tafamidis™, stabilises the protein in a dimer form, reducing the free monomeric protein, a requirement for amyloidosis (Bulawa et al., 2012). Similarly, the ZAβ3 compound forms a dimer around the Aβ hairpin, inhibiting its self-assembly into amyloid (Hoyer et al., 2008).

1.5.3. Inhibiting amyloidosis

Targeting the amyloidosis step itself is another treatment method for amyloid associated diseases. This can be accomplished via small molecule interactions, or protein based β-sheet breakers.

The development of small molecule inhibitors is most commonly derived from screening of large compound libraries for effects on amyloid formation. Comparing successful compounds can begin to highlight key structures or chemical groups required for effective amyloid inhibition (Pickhardt et al., 2005). The formation of amyloid is often linked to the inclusion of glycosaminoglycans, in particular heparin molecules (**section 1.1.5)**, which promote or stabilise the change in structure from the proteins native fold to amyloid. N-acetylglucosamine analogues, such as Fibrillex™, inhibit the binding of GAGs to the amyloid precursor protein and orally administered sulphated compounds have been shown to substantially reduce amyloid deposition of murine AA amyloid (Gillmore and Hawkins, 2006).

Small peptides, or β-sheet breakers, have also been used as aggregation inhibitors. These can be designed according to the sequence of the target amyloid protein to increase specificity. These peptides arrange themselves against the aggregation "hot spots" of the amyloid precursor protein and inhibit self-

association, which is required for the protein to undergo aggregation (**Figure 1.13**). The selectivity of this treatment means peptides can be used to target a single disease (Gillmore and Hawkins, 2006; Soto et al., 1998). In the case of Alzheimer's disease, a 5-residue peptide iAβ5 (LPFFD) has been shown to not only inhibit amyloidosis, but also disassemble preformed fibrils in vitro (Hard and Lendel, 2012).

Interfering with hydrogen bonds that stabilise the β-sheet structures is another way of inhibiting the formation of amyloid species. The self-recognition elements (SRE) in amyloidogenic proteins can be synthetically produced to include nitrogen methylation on one side. This allows binding of the synthetic SRE sequences to the target on one side, but the methylation on the alternative face inhibits further hydrogen bond interactions and elongation of the β-sheet (**Figure 1.14**). The 25-35 peptide of Aβ, incorporating residues GSNKGAIIGLM, readily forms aggregates typical of amyloid. Incubation of this peptide with N-methylated derivatives leads to a reduction in aggregation and toxicity, since the methylated peptide binds to Aβ(25-35), but inhibits the interaction of additional monomers, thus reducing elongation (Hughes et al., 2000). This technique has also been used to inhibit the amyloidosis of Aβ(1-42) (Amijee et al., 2012). Finally, LMTX, a methylthinium chloride compound recently in phase 3 clinical trials, has been shown to inhibit the aggregation of tau proteins into amyloid-like structures involved with Alzheimer's disease (Kumar et al., 2016).

1.5.4. Amyloid removal

Given the delay in diagnosing amyloid associated diseases, large fibrillar deposits often accumulate within the organs or affected areas before treatment can begin.

As such, the final treatment area involves targeting amyloid's removal. Due to the highly conserved structural characteristics of amyloid, anti-amyloid antibodies have been designed to enhance the removal of amyloid deposits. Antibodies raised against generic fibril epitopes promoted clearance of amyloid in mice with AA amyloidosis (Gillmore and Hawkins, 2006). Antibodies raised against serum amyloid P component, a glycoprotein associated with amyloid deposits, trigger a macrophage driven clearance of amyloid deposits, without adverse effects. Removal of a patients SAP, prior to treatment, allows specific targeting of the amyloid deposits (Bodin et al., 2010).

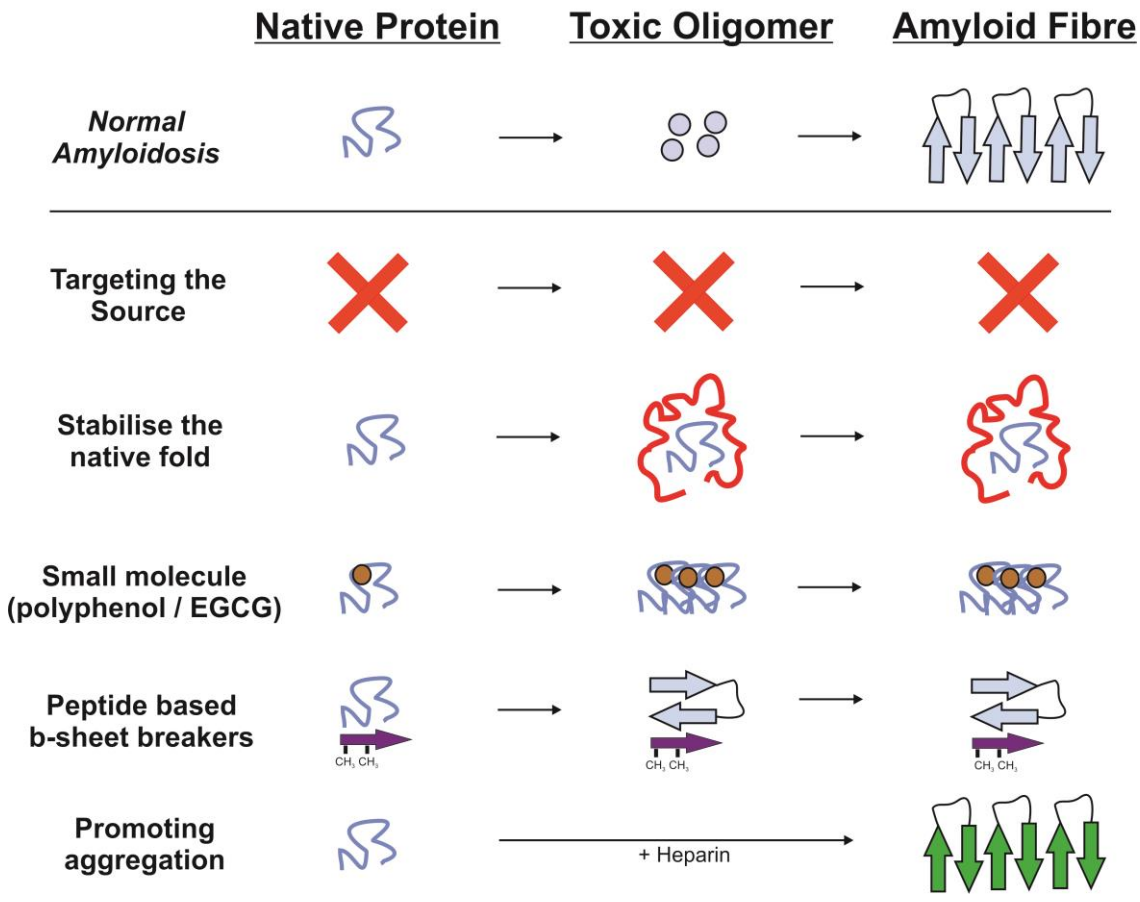

Figure 1.14 Schematic of the various techniques that can be used to inhibit β-sheet elongation or prevention of cytotoxic intermediates.

1.6 Conclusion

This completes an extensive review of the background surrounding amyloidogenic proteins. A detailed list of the proteins known to misfold into amyloid species, along with the associated diseases, is given in **Table 1.1**, and includes the native structure of the amyloidogenic protein. How these aggregates induce a pathological disease state is described, with particular focus on the cytotoxic, intermediate, oligomeric species. Compounds known to localise with amyloid deposits, which can be involved in inducing aggregation, are also detailed.

In order for a protein to aggregate into amyloid species, the native protein must first unfold, and thus, a brief overview of protein folding and unfolding is provided. Following unfolding, amyloid formation commonly follows a nucleation-dependent mechanism, which is outlined here, and this process can be monitored by the amyloid-specific dye ThT. Also provided is a detailed characterisation of amyloid, including the secondary, tertiary and quaternary structures found across all amyloid species.

Finally this introduction describes some of the current techniques utilised to inhibit the development of amyloid associated disease pathology. **Chapter 6** of this thesis will go into more detail regarding the theory behind many of these techniques.

Following on from this introduction, **Chapter 2** will describe the structure and function of apoA-I, and how aggregation of apoA-I into amyloid-like material can be detrimental to cardiovascular health.

2. Cholesterol transport, atherosclerosis and apoA-I amyloidosis

This introductory chapter will describe the human cholesterol transport mechanism, the involvement of apolipoprotein A-I (ApoA-I), and how deregulation of the cholesterol transport mechanism, including the inactivation of apoA-I through amyloidosis, results in atherosclerosis.

2.1. Cholesterol

Cells require cholesterol, and other sterol compounds, for strengthening cell membranes and as a precursor for the biosynthesis of hormones, bile and oxysterols. Since cholesterol is not uniformly distributed among cells and organs, it requires highly regulated transport (Prinz, 2007).

The body acquires cholesterol via two methods, it is either synthesised in the intestine, via the mevalonate pathway, and regulated by the HMG CoA reductase enzyme, or acquired in the gut through dietary intake. These 2 systems are controlled by a feedback mechanism that self-regulates the production of endogenous cholesterol. In a high cholesterol state, such as after consuming a lipid rich meal, low-density lipoprotein (LDL), carrying exogenous cholesterol, binds to the LDL receptor (LDL-R) located on cell membranes. The whole LDL/LDL-R complex is then internalised into the cell, releasing the cholesterol into the cytoplasm (Olson, 1998). When inside the peripheral tissues, cholesterol has 4 main functions: (i) shut off the endogenous production of cholesterol, through inhibition of HMG CoA reductase; (ii) inhibit LDL-R synthesis, through down-regulating the sterol response element binding protein 1 (SREBP1); (iii)

promote acyl-CoA cholesterol acyltransferase (ACAT), and (iv) incorporation into lipid membranes (Wang et al., 1994; Ioannou, 2001).

2.1.1. Mechanism of cholesterol transport

The mechanism of cholesterol transport, via lipoprotein particles is described in **Figure 2.1**. Dietary fats from the gut become incorporated into chylomicron particles, containing 1% protein and 99% lipid content. These enter the bloodstream and lose 75% of their triglyceride content, following interaction with lipoprotein lipase, converting the chylomicrons into chylomicron remnants. The released triglycerides are taken up by adipose tissues for storage or used as a fuel source by cells, whilst the chylomicron remnants are taken up into hepatocytes via B100E receptors. Once inside the liver, the chylomicron remnants are broken down and the cholesterol content is either directly excreted, converted into bile salts or incorporated into very low-density lipoprotein (VLDL), consisting of 92 % lipid and only 8% protein. VLDL is secreted back into the bloodstream, where it is reduced by lipoprotein lipase into intermediate-density lipoprotein (IDL) releasing its triglyceride content. The IDL particle is either taken up by hepatocytes via B100E receptors, or further reduced by hepatic lipase into low-density lipoprotein (LDL). The LDL particle contains 21% protein and 79% lipid, of which only 11% is triglycerides. The LDL particle is transported in the bloodstream to the liver for cholesterol processing, or into peripheral tissues via interaction with the LDL-R. Any residual LDL that is not removed from the bloodstream, due to saturation of the LDL-R, continues circulating and increases the risk of atherosclerosis, following oxidation of the particle (Olson, 1998). LDL can remain in the bloodstream for up to 3 days.

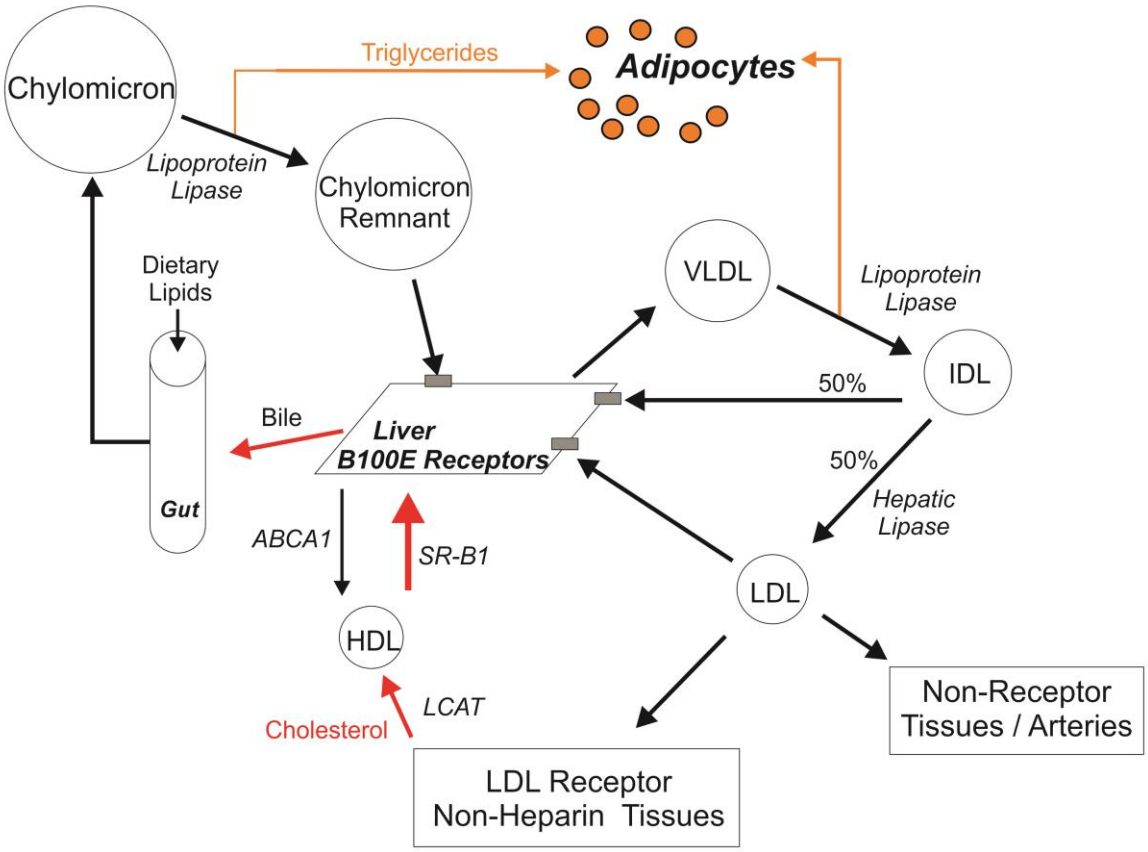

Figure 2.1 Schematic of receptor mediated cholesterol transport mechanism via lipoprotein particles. The black arrows indicate exogenous cholesterol processing, the orange arrows depict the use/storage of triglycerides, and the red arrows show the reverse cholesterol transport mechanism.

2.1.2. Reverse cholesterol transport

In order to maintain a balance of arterial cholesterol, and to remove excess from peripheral tissues, a reverse cholesterol transport (RCT) mechanism is used to counteract the normal cholesterol movement. High-density lipoprotein (HDL), the main facilitator of RCT, consists of apolipoproteins AI (apoA-I), AII (apoA-II) and AIII (apoA-III), phospholipids and cholesterol. The lipoprotein particle is synthesised in the liver or intestine and released into the blood stream. HDL is often referred to as “good cholesterol”, due to its induction of monocyte adhesion

molecules, prevention of LDL modification, but primarily because of its role in the removal of excess cholesterol from the circulatory system, thus protecting against atherosclerosis (Stein and Stein, 1999; Fisher et al., 2012; Lewis, 2005). HDL, via the apoA-I protein, accepts cholesterol from cholesterol-laden cells, including macrophages and endothelial cells lining the arterial wall. This occurs in 4 ways: (i) apoA-I interacts with ATP-binding cassette transporter protein AI (ABCA1), which transfers cholesterol from the cell to the nascent HDL particle (Oram and Vaughan, 2006; Nagao et al., 2014; von Eckardstein et al., 2001), (ii) spontaneous desorption of cholesterol content from the lipid membranes to nascent HDL, (iii) ABCG1 mediates the flux of cholesterol from intracellular organelle to the plasma membrane, prior to desorption to nascent HDL, or, (iv) scavenger receptor BI (SR-B1) promotes a net movement of cholesterol, similar to aqueous diffusion, onto the HDL particle, requiring direct interaction (Annema and von Eckardstein, 2013).

Upon binding to cholesterol, the apoA-I protein co-activates lecithin cholesterol acyltransferase (LCAT). This enzyme transfers fatty acids from lecithin to the cholesterol, forcing its internalisation into the hydrophobic core of the HDL particle. This allows the HDL particle to transfer its cholesterol content through the bloodstream. Upon reaching the liver, the cholesterol content is transferred from the HDL particle into the liver via an interaction between apoA-I and the SR-B1 transporter protein, or endocytosis of the entire HDL-cholesterol particle into the liver, followed by activation of F_0F_1 ATPase. Alternatively, cholesterylester transfer protein (CETP) can promote the exchange of cholesterol for triglycerides with lipoproteins containing apo-B. Apo-B then removes the cholesterol, via LDL receptors on hepatic cells.

Cholesterol in the liver is then excreted as either free cholesterol, following its conversion into bile salts, or eliminated as faeces (Annema and von Eckardstein, 2013). Poor regulation of the cholesterol transport, or the RCT pathway, can lead to an imbalance in the level of LDL within the circulatory system, with a potential to manifest itself into atherosclerotic plaques and pose a serious health risk.

2.2. Atherosclerosis

Atherosclerosis is the leading cause of heart attacks and is responsible for up to 50% of deaths in the USA and Europe. It is caused by an excessive inflammatory response against accumulated fibrous and fibro-fatty plaques within the endothelium of arteries (Ross, 1993). There are many sources of injury to the endothelium that give rise to atherosclerosis. The most common is the endothelium interacting with excess LDL that has become oxidised, due to interaction with nitrous oxide, a product of endothelial cells normally used in the regulation of vascular tone (Matthys and Bult, 1997). Oxidised LDL leads to an inflammatory response, resulting in the recruitment of T-lymphocytes and macrophages. These white blood cells absorb the oxidised LDL, via scavenger receptors, converting the cells to lipid-rich foam cells. The lipid-rich macrophages and T-lymphocytes migrate to the intima, the inner layer of the arterial wall, and become deposited as “fatty streaks”. Over time, the fatty deposits develop into fibrous plaques, forming a core containing lipids and immune cell debris following necrosis, overlain with a fibrous cap of smooth muscle, collagen and connective tissue. These lesions increase in size, though cell proliferation and recruitment of macrophages and immune response cells, resulting in obstruction of blood flow in the lumen. The fibrous caps can rupture,

causing a haemorrhage into the plaque area, or the formation of thrombi. Thrombi travel freely in the circulatory system, which can result in the blocking of arteries. This has the potential to lead to ischemia of the major organs including the heart and brain, manifesting itself as infarction (Ross, 1999a; Ross, 1993; Ross, 1999b). The entire process is summarised in **Figure 2.2.**

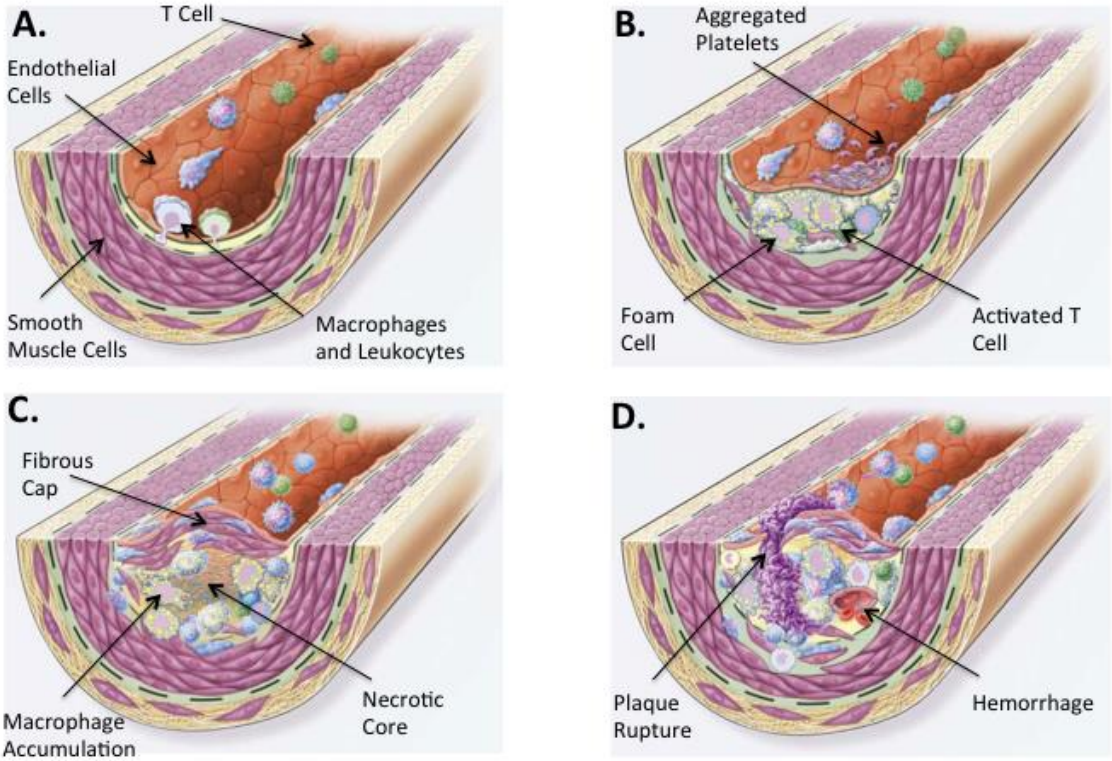

Figure 2.2 Progression of atherosclerosis in an arterial blood vessel. (**A**) Macrophages and leukocytes, having digested oxidised LDL, migrate to the sub endothelial space. (**B**) Formation of fatty steaks after the deposition of foam cells, activation of T-cells and invasion of smooth muscle cells. (**C**) Continued recruitment of macrophages. (**D**) Cracking of the fibrous cap leads to a plaque rupture and the formation of a thrombus. Alternatively, disruption of the plaque may lead to haemorrhaging from the artery. Modified image from Ross (1999a).

2.3. High-density lipoprotein (HDL)

High-density lipoprotein (HDL) was the first of the cholesterol transport plasma proteins to be discovered, followed by low-density lipoprotein (LDL) and subsequently, the LDL receptor on peripheral tissues. This lead to the proposal of the receptor mediated lipid transport mechanism, via lipoprotein particles (**Figure 2.1**). Michael Macheboeuf isolated HDL particles in 1929 which were found to contain 59% protein and 41% lipid, of which 18% was cholesterol and 23% was phospholipids (Olson, 1998). HDL is made up of several forms of apolipoproteins, including A-I, A-II, A-III and A-IV. However, with the exception of apoA-I, not all of these apolipoproteins are present on every HDL molecule. The specific combination of apolipoproteins on each HDL molecule gives them their individual subclass, each of which differs by size, shape, density and charge. HDL particles can include upwards of 80 proteins, 200 species of lipids and low copies of various micro-RNA molecules (Annema and von Eckardstein, 2013). The requirement for apoA-I on every HDL molecule further highlights its necessity in the RCT mechanism.

2.3.1. HDL biogenesis

Formation of the HDL molecule begins with the synthesis of apoA-I in the liver and intestine. ApoA-I acquires cholesterol and phospholipids, the rate limiting step in HDL production, from either hepatic or peripheral cells, including macrophages. For this to occur, the lipid donor cells need to express the ATP-binding cassette protein AI (ABCA1), an integral membrane transporter protein. This protein actively effluxes free cholesterol and phospholipids from cells, creating lipid-rich domains on the plasma membrane that apoA-I can interact

with (Oram and Vaughan, 2006). In this form, nascent HDL particles are disc shaped, due to the un-esterified cholesterol content. Once in circulation, the nascent HDL particle interacts with lecithin cholesterol acyltransferase (LCAT). LCAT esterifies the free cholesterol, producing cholesterol-esters, which migrate into the centre of the particle. This internalisation of the cholesterol produces the overall spherical shape of mature HDL (Fisher et al., 2012; Aguilar-Espinosa et al., 2013; Oram and Vaughan, 2006).

2.3.2. Role of HDL as "good cholesterol"

HDL is commonly referred to as "good cholesterol", given its main role in the reverse cholesterol transport mechanism, described above in **section 2.1.2**. In addition to this function, HDL also has anti-oxidant and anti-inflammatory properties (Fisher et al., 2012), as well as acting as an inhibitor of monocyte adhesion molecules and LDL modifications (Stein and Stein, 1999). Although the role of HDL in the reverse cholesterol transport mechanism is only a small percentage of the overall cholesterol transport, efflux from the engulfed macrophages back to the liver for processing is most crucial, with regard to atherosclerosis (Lewis, 2005). Any reduction in the anti-atherosclerotic properties of HDL, whether it is a reduction in HDL production, its maturation, or its effectiveness in the cholesterol transport mechanism, would lead to an increase in atherosclerosis and enhanced health risk, hence the interest within the medical field.

2.4. Apolipoprotein AI

Apo-AI, as mentioned previously, is the main constituent of HDL, making up 70-75 % of the total protein content, and gives the lipoprotein its main cholesterol binding function (Oram and Vaughan, 2006). ApoA-I has a concentration in the plasma of approximately 0.2 mg/ml (Tate et al., 2006).

2.4.1. ApoA-I sequence

Prepro-apoA-I is a 267-residue peptide containing the 243-residue apoA-I, an 18-residue signal sequence and a 6-residue linker region (Sharpe et al., 1984). Removal of the signal sequence releases pro-apoA-I and allows secretion into the plasma. The 6-residue linker sequence is cleaved by an unknown protease, forming apoA-I (McGuire et al., 1996). The native prepro-apoA-I sequence is shown in **Figure 2.3**, with a predicted mass of 28078 Da (Pankhurst et al., 2003).

-24 -6

MKAAVLTLAVLFLTGSQARHFWQQ	0
DEPPQSPWDRVKDLATVYVDVLKDS	25
GRDYVSQFEGSALGKQLNLKLLDNW	50
DSVTSTFSKLREQLGPVTQEFWDNL	75
EKETEGLRQEMSKDLEEVKAKVQPY	100
LDDFQKKWQEEMELYRQKVEPLRAE	125
LQEGARQKLHELQEKLSPLGEEMRD	150
RARAHVDALRTHLAPYSDELRQRLA	175
ARLEALKENGGARLAEYHAKATEHL	200
STLSEKAKPALEDLRQGLLPVLESF	225
KVSFLSALEEYTKKLNTQ	243

Figure 2.3 Prepro apoA-I sequence containing the 18-residue signal peptide (green) a 6-residue linker (red) and the 243-residue apoA-I peptide (black). Hot spot regions 14-22, 53-58, 69-72 and 227-232 are underlined.

A modified plasmid vector allowing optimisation for bacterial expression has been produced by Oda (2001) and detailed in Ryan (2003). This plasmid will be utilised in **Chapter 3** for the expression of recombinant apoA-I.

2.4.2. Delipidation of apoA-I

Dissociation of lipids from apoA-I, resulting in the lipid-free structure of apoA-I, is required for recycling of the HDL particle and subsequent interaction with ABC AI transporter proteins (Davidson and Thompson, 2007). Delipidation is also a key stage in the transition between the soluble native protein and its amyloid species (Obici et al., 2006). It has previously been shown that increased apoA-I expression coincides with increased levels of amyloidogenic apoA-I species deposited within atherosclerotic plaques. Despite apoA-I's native role in reversing atherosclerosis, this suggests that when the lipid-free apoA-I concentration exceeds the level required for effective removal of cholesterol, it leads to a misassembled amyloid species (Mucchiano, et al., 2001).

2.4.3. Structural studies of apoA-I

ApoA-I exists in multiple native structures, due to its conversion between lipid-free, partially lipidated and fully lipid associated forms (Ajees et al., 2006; Mei and Atkinson, 2011). The research collaboratory for structural bioinformatics protein data bank (RCSB PDB) website currently has 4 structural models, covering the majority of the apoA-I peptide sequence (**Figure 2.4**), and 5 structural models for shorter segments of the peptide.

A model produced by Ajees *et al*. (2006)(PDB 2A01) represents the crystal structure of full-length, lipid-free apoA-I at a resolution of 2.4 Å (**Figure 2.4A**).

However, this model has since been discredited by various authors, who present more accurate model structures (Tate et al., 2006). This model appears to show a high degree of similarity to the model for mouse apoA-I (PDB 2LEM).

A crystal structure for the N-terminally truncated apoA-I (Δ 1-43), thought to be in its lipidated state, was proposed by Borhani et al (1997), consisting of a mainly α-helical structure in a looped belt conformation that facilitated lipid binding (**Figure 2.4B**).

The most complete model for lipid-free apoA-I, described in detail below, comes from Mei and Atkinson (2011), deposited as PDB 3R2P. This structure of a C-terminally truncated apoA-I (Δ185-243) dimer was deduced via x-ray crystallography at a resolution of 2.2 Å (**Figure 2.4C**). The ability of this peptide to form functional HDL complexes, along with having strong similarities to the N-terminally truncated, lipid-bound apoA-I (Δ1-43) described above, indicates that this model is a good representation of full-length apoA-I. It also contains many of the functional aspects in relation to lipid binding and the role of apoA-I in HDL.

A model based on small angle neutron scattering for the full-length, lipid-bound apoA-I in a reconstituted HDL nanoparticle, incorporating lipids and cholesterol, was presented by Wu et al., (2009). However, this had a much lower resolution compared to the other structures, due to the methods used (**Figure 2.4D**). This is the structure that will be used throughout this thesis when referring to lipid-bound apoA-I.

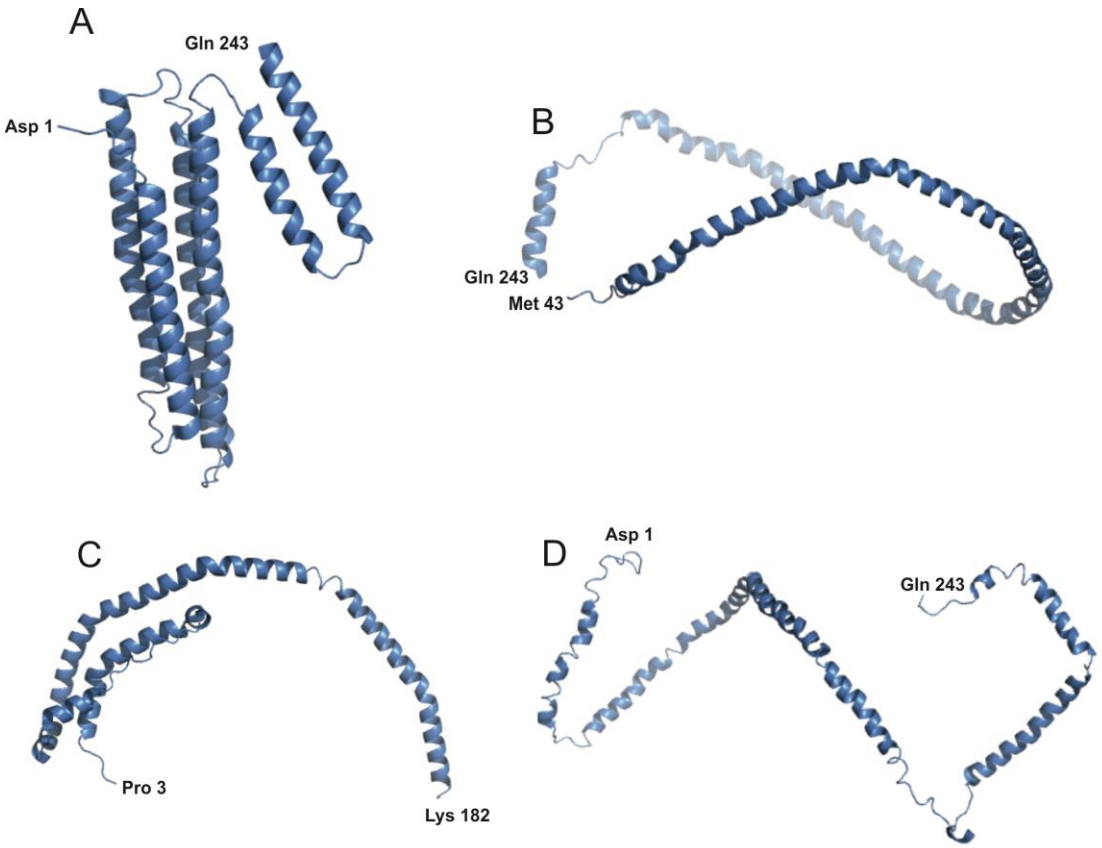

Figure 2.4 Structural models of apoA-I deposited within the protein databank. (**A**) Lipid-free apoA-I (PDB 2A01) proposed by Ajees *et al.* (2006), (**B**) N-terminally truncated apoA-I (Δ1-43) deduced by Borhani *et al.* (1997), (**C**) lipid-free apoA-I (Δ185-243) proposed by Mei and Atkinson (2011), (**D**) lipid-bound apoA-I in a HDL nanoparticle presented by Wu *et al.* (2009).

2.4.4. Lipid-free apoA-I

ApoA-I is synthesised in its lipid-free form, and binds cholesterol and other lipids as part of its inclusion into a HDL particle. *In vivo*, given the strong affinity of apoA-I for lipids, the concentration of lipid-free apoA-I remains very low. In fact, less than 5 % of circulating apoA-I is lipid-free (Das et al., 2016). Lipid-free apoA-I can be split into 3 regions: the N-terminus stabilises the protein structure, the central region offers flexibility, facilitating the conversion from monomer to dimers, whilst the C-terminus gives apoA-I its lipid binding ability.

2.4.4.1. Lipid-free apoA-I structure

The most complete, widely accepted structural model for lipid-free apoA-I comes from Mei and Atkinson (2011) and represents the C-terminally truncated (Δ185-243) apoA-I peptide, with the structural model consisting of residues 3-182 (**Figure 2.5**). This removes much of the lipid binding C-terminus, due to problems of self-association within this region, but retains the N-terminus. This region is of particular relevance in this study, due to its increased propensity to form amyloid-like structures.

The (Δ185-243) apoA-I peptide contains 9 helical regions in total: two well defined helices and seven semi-continuous helices formed with conserved AB sequence repeats. The two well defined helices are located in the N-terminus: the major helix (residues 7-34) containing a valine kink at residue 21, and a minor helix (37-41) running parallel to the major helix. This minor helix forms a connecting turn into the first of the 11-residue repeated regions associated with H1. H1 consists of two 11-residue B repeats (residues 44-54 and 55-65) before termination by a proline kink at residue 66. The A repeat of H2 produces a turn,

which extends into a second A repeat in H2 and, due to the lack of a proline, this helix continues into a B repeat of H3. The A/B repeat in H2/H3 is followed by 4 consecutive A/B repeats (H4-H7), which form an almost continuous helix, with proline residues forming a kink at the start of each A segment of the next helix.

2.4.4.1.1. Lipid-free apoA-I dimer

Lipid-free apoA-I was shown to form a symmetrical homo-dimer in an approximate semi-circle, measuring roughly 17 Å in height and 110 Å in diameter, coinciding with the width of HDL particles (Mei and Atkinson, 2011). The backbone of the dimer contains 2 long antiparallel helices, one from each monomer, with an exact AB repeat pairing of the H5 region. At each end of the backbone, a 4 helical bundle is formed with 3 helices from the N-terminus of 1 monomer and a single helix in the C-terminus from the second monomer, internalising the hydrophobic residues and stabilising the bundle (**Figure 2.5A**).

2.4.4.1.2. Lipid-free apoA-I monomer

The H5 helical region (residues 121-143) that holds the apoA-I dimer together via anti-parallel helices is the most flexible AB repeat, in particular residues 136-141 which has little helical conformation, when in isolation. It is believed that in monomeric apoA-I this region acts as a hinge, with the final two AB repeats (H6 and H7) folding back on the rest of the molecule to self-associate with its own N-terminus rather than the N-terminus of its dimeric partner (Mei and Atkinson, 2011; Gursky et al., 2012), as shown in **Figure 2.5B**. Therefore, the 4 helical bundle remains, but unlike the dimeric apoA-I, all 4 helices belong to the same molecule. It is predicted that the remaining peptide, residues 185-243, is largely

unstructured in the monomeric species (Gursky et al., 2012), suggesting that this model is a good representation of the full-length monomeric apoA-I.

Figure 2.5A was produced using the PDB file 3R2D and generating symmetry mates within 6 Å, in order to produce the dimer interactions between the H5 regions, which are separated by approximately 5 Å (Mei and Atkinson, 2011).

Figure 2.5B was produced by Professor D. Middleton using the MODELLER programme and switching the residues 143-182 of H6 and H7 in the second molecule to the first molecule, before re-introducing residues 121- 143 of H5 in order to form the hinge region and link the domain swapped region to the rest of the apoA-I peptide.

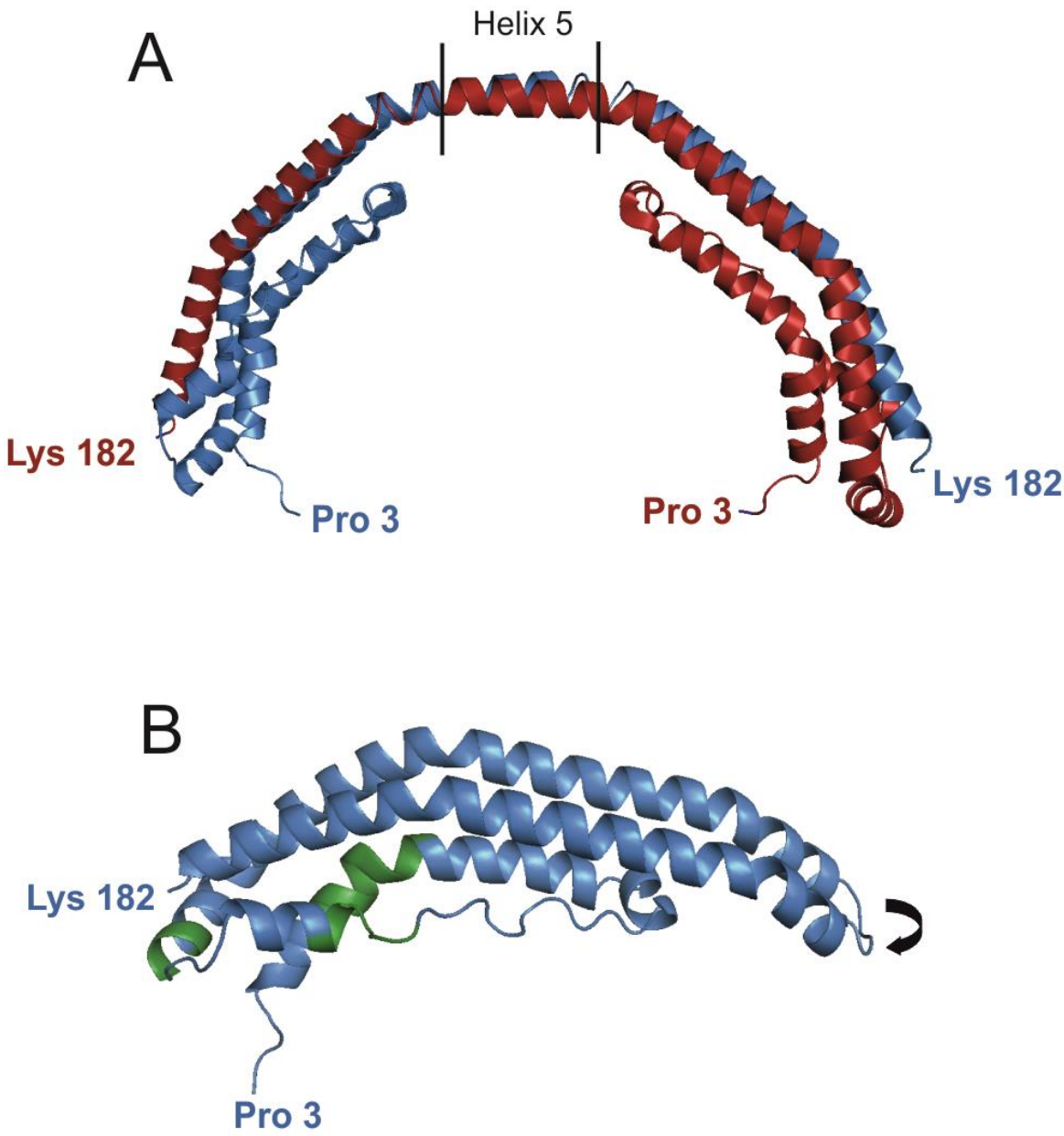

Figure 2.5 Crystal structure of lipid-free apoA-I (Δ185-243) at 2.2 Å, deduced by Mei and Atkinson (2011). (**A**) Dimeric apoA-I linked via an anti-parallel H5-H5 interaction (PDB 3R2D) and (**B**) Monomeric apoA-I model formed via domain swapping of the H6 and H7 regions and conversion of the H5 helix into a hinge, produced by D. Middleton. Hot spot regions are highlighted in green.

2.4.5. Lipid-bound apoA-I

Lipid-bound apoA-I accounts for 90-95% of all circulating apoA-I, indicating apoA-I's high affinity for cholesterol lipids (Ajees et al., 2006; Das et al., 2016; Tate et al., 2006).

2.4.5.1. Lipid-bound apoA-I structure

The structure of the lipid-free peptide is highly conserved upon binding lipids, with the sequence prediction for the 11 and 22 residue α-helical A and B repeats remaining the same (Gursky et al., 2012).

It is proposed that upon lipid interaction, mediated by the C-terminus, the N-terminus of monomeric apoA-I unhinges, and opens itself to the formation of intermediate dimeric apoA-I. The N-terminus then continues to unfold, exposing hydrophobic interiors that then allow insertion of lipids. The N-terminus then interacts with the C-terminus of its opposing dimer, forming a double belt discoidal HDL particle. It is proposed that the N-terminal H1 and H2 repeat regions interact with the H8 and H9 of the C-terminus, regions that are not shown on the apoA-I (Δ185-243) model (Mei and Atkinson, 2011). This model agrees with the lipidated apoA-I (Δ1-43) structure of a figure of 8 bundle with 4 helices deduced by Borhani *et al.* (1997) as shown in **Figure 2.6A**.

The structure of reconstituted HDL associated full-length apoA-I is described in Wu et al. (2009) and shows similarities to the Borhani structure with the overall figure of 8 conformation and an anti-parallel helical dimer (**Figure 2.6B**), despite being deduced at a lower resolution. This structure is based on the apoA-I associated into the HDL complex, with cholesterol and POPC lipids at 10 and 100 times the molar concentration of apoA-I (**Figure 2.6C**).

Figure 2.6D gives better insight into the 3D structure of apoA-I dimer wrapped around a reconstituted HDL particle. Helices 1 and 10 show the highest affinity for cholesterol and phospholipids, whilst an 11-residue sequence in helix 9 is essential for ABC AI interaction, highlighting the importance of the C-terminus in the role of apoA-I (Oram and Vaughan, 2006).

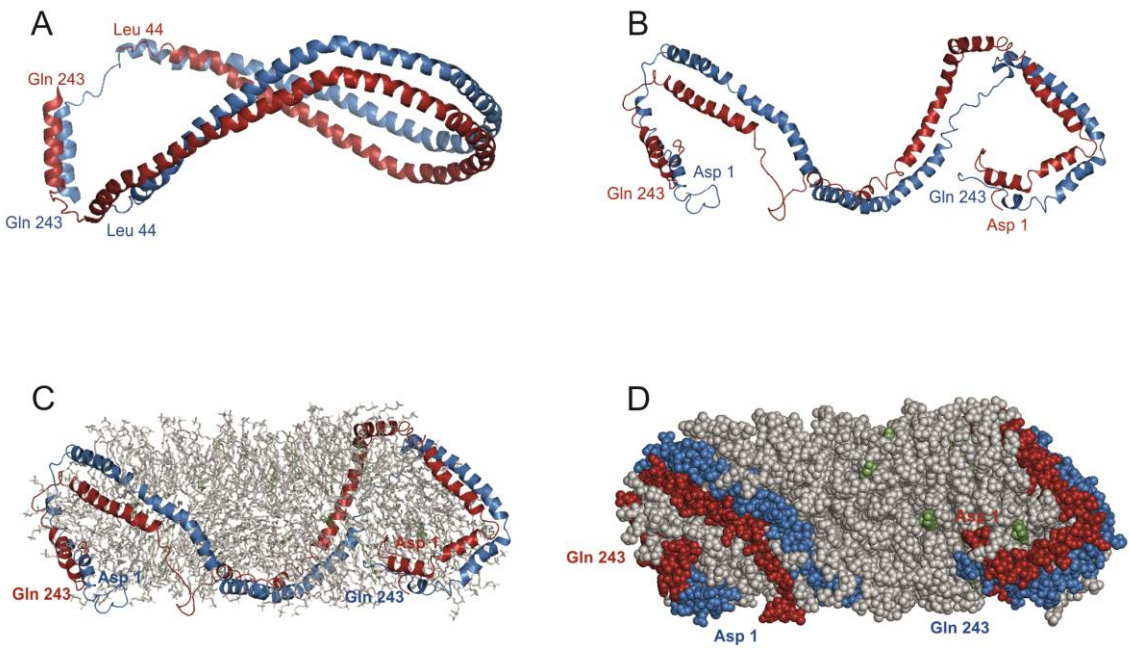

Figure 2.6 Structure of lipid-bound apoA-I. Figure of 8 dimer deduced by (**A**) Borhani *et al.* (1997) and (**B**) Wu *et al.* (2009). The Wu *et al.* structure was produced in the presence of 10 and 100-fold molar excess cholesterol and POPC lipid, compared to apoA-I (**C**), which gives a full 3D structure of apoA-I wrapped around the HDL particle (**D**).

2.4.6. NMR studies of apoA-I

Section 2.4.3 details the current models of apoA-I, based on either full-length apoA-I, or shortened peptides, such as the apoA-I (Δ1-43) and apoA-I (Δ185-243). All 4 of these models were produced using data from X-ray crystallography studies, highlighting a lack of high-resolution solid-state NMR data in this area of study. This is due to issues with the insolubility of the aggregates, and the difficulty in assigning NMR residues of apoA-I. This arises because of the broad line widths, which are common in peptides with a flexible, open structure, such as apoA-I. NMR has been used to study the structure of small peptide sequences from the full-length apoA-I, including: residues 142-187 (PDB 1GW3/1GW3) (Wang et al., 1997), 166-185 (PDB 1ODP/1ODQ/1ODR) (Wang et al., 1996) and 1-93 (Mangione et al., 2001).

The 142-187 peptide studied by Wang (1997) in lipid environments, was found to include 2 amphipathic helical regions, consisting of residues 146-162 and 168-182, which are believed to be involved in lipid binding. These 2 helices form a helix-hinge-helix confirmation, the formation of which is driven by lipid interaction. When compared to the full-length, lipid-bound structure of apoA-I in a reconstituted HDL particle, deduced by Wu *et al*. (2009), the 142-187 peptide shows a relatively high degree of similarity, in particular the presence of 2 helical regions, separated by an unstructured region (**Figure 2.7A/B**). The 166-185 peptide corresponds to the second helix of the aforementioned 142-187 peptide, and again matches the helix formed in the Wu *et al.* structure of lipid-bound, full –length apoA-I in a reconstituted HDL particle (**Figure 2.7C/D**).

The 1-93 peptide studied by Mangione *et al.* (2001) is predicted to consist of primarily random coil structures, due to the C-terminus in this peptide driving

the formation of a coiled-coil conformation. This was confirmed with far UV circular dichroism that suggested 44 % of the peptide consisted of random coils, 32 % β-sheets, 5 % α-helices and 19 % turns. However, both 1D and 2D solution NMR spectra failed to identify the random coiled structures. Instead, the resonances were clustered around statistically random chemical shifts, concluding that the apoA-I (1-93) peptide remained unfolded and highly flexible, under the conditions studied. The lack of a methodology for producing ^{13}C and ^{15}N labelled apoA-I (1-93) hindered any further NMR analysis of this region.

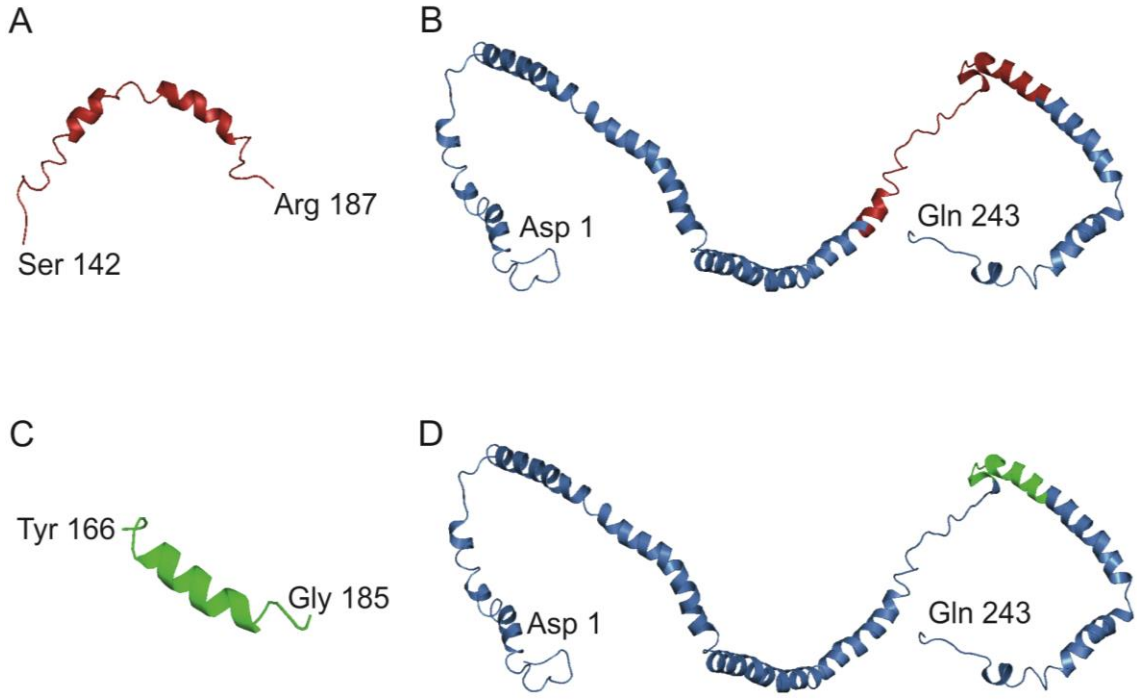

Figure 2.7 NMR derived structural models for (**A**) apoA-I (142-187) and (**C**) apoA-I (166-185) taken from PBD 1GW3 and 10DR, respectively. Figures **B** and **D** highlights the corresponding regions on the full-length, lipid-bound apoA-I structure deduced by Wu *et al.* (2009).

2.4.7. ApoA-I interactions

ApoA-I interacts primarily with 3 proteins in its function within HDL: ABCA1 on peripheral tissues, for localising with free cholesterol; LCAT, to esterify and internalise the cholesterol into the HDL particle interior; and SR-B1 on hepatic cells, to transfer cholesterol to the liver for removal.

2.4.7.1. ATP-binding cassette protein A1

The ATP-binding cassette protein A1 (ABC A1), a member of the ABC superfamily, is a transporter protein that utilises ATP in order to transport cholesterol and phospholipids from cells, including macrophages, into the HDL reverse cholesterol transport pathway. Excess cholesterol in cells can lead to disruption of the membrane and eventually cell apoptosis, hence the requirement for its efficient removal. ABC A1, an integral membrane protein, forms a channel through the membrane that allows "flopping" of lipids from the inner to the outer surface of the membrane. Upon externalisation, the lipids can then associate with apoA-I (Oram and Vaughan, 2006). Lipidation of apoA-I via ABC A1 is the rate-limiting step in the production of HDL, and subsequently the entire reverse cholesterol transport mechanism. Despite, in theory, the overexpression of ABC A1 increasing reverse cholesterol transport, doing so can lead to cell viability issues, manifesting itself in unregulated release of cholesterol (Liu et al., 2014). The interaction between ABCA1 and apoA-I is promoted by the apolipoprotein A-I binding protein (AIBP), which stabilises the interaction, as well as reducing ABCAI degradation (M. Zhang et al., 2016).

2.4.7.2. Lecithin cholesterol acyltransferase

LCAT is the primary enzyme responsible for esterification of cholesterol bound to nascent HDL, and hence, for the maturation of HDL. LCAT cleaves fatty acids from lecithin and transfers it onto serine 181 of LCAT, before releasing the fatty acid to the hydroxyl group of cholesterol through its acyltransferase activity.

ApoA-I activates the LCAT enzyme in order to esterify its bound cholesterol and promote internalisation of the cholesterol-ester, resulting in HDL maturation (Ossoli et al., 2015). Residues 145-185 of apoA-I are believed to be involved with LCAT activation, since deletion of residues within this region resulted in reduced LCAT activity (Minnich et al., 1992).

2.4.7.3. Scavenger receptor B1

The scavenger receptor B1 (SR-B1) is a receptor for the HDL molecule, located on hepatic tissues (Acton et al., 1996). SR-B1 can bind to a host of ligands, including HDL, and selectively uptakes lipids into hepatic cells, with its highest affinity for cholesterol esters and free cholesterol, and a lower affinity for phospholipids and triglycerides. This process occurs via 2 definitive stages: the binding of HDL to the SR-B1 via the apoA-I protein, followed by the diffusion of lipid content into the plasma membrane. This all occurs without the breakdown of HDL, regenerating the lipid-free apoA-I, and reinitiating the RCT cycle (Lewis, 2005; Annema and von Eckardstein, 2013; Tate et al., 2006).

2.4.8. ApoA-I amyloid

ApoA-I, due to its lipid binding function, possesses a naturally high hydrophobicity and a low structural stability, in order to facilitate the binding of lipids, which induces a structural conversion. This also makes the protein susceptible to aggregation, in particular into β-sheet structures, bearing the hallmarks of amyloid (**Figure 2.8**).

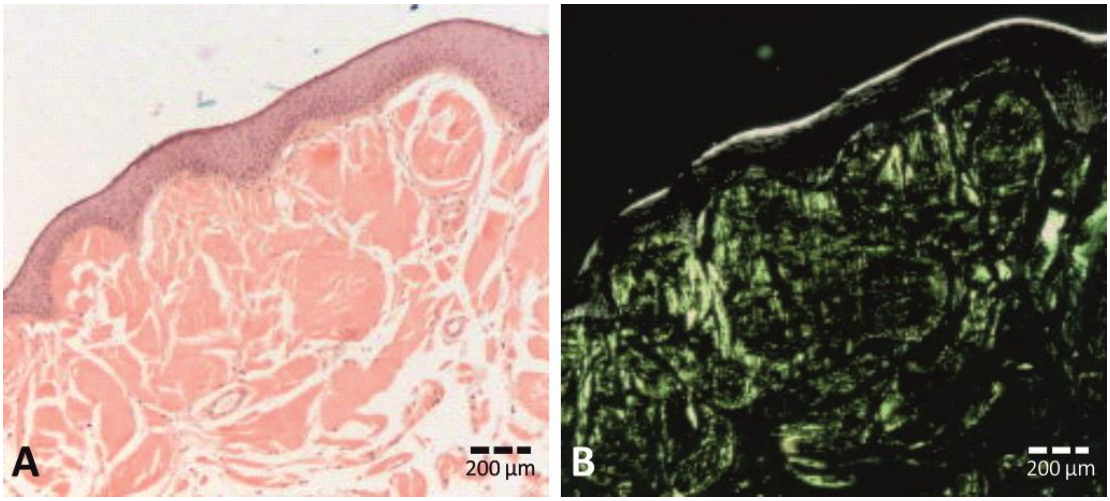

Figure 2.8 Congo red stained vocal fold biopsy of apoA-I amyloid (**A**), and visualised under cross polarised light (**B**), image from Hazenberg *et al.*, (2009)

ApoA-I associated amyloid deposition has been associated with two forms of human disease: (i) acquired amyloidosis, linked to the deposition of full-length apoA-I fibrils within atherosclerotic plaques (Das et al., 2016; Ramella et al., 2012; Ramella et al., 2011; Mucchiano, Häggqvist, et al., 2001; Wong et al., 2010; Chan et al., 2015) and (ii) familial apoA-I amyloidosis (AApoAI), where N-terminal fragments of mutant apoA-I species become deposited within major organs (Raimondi et al., 2011; Das et al., 2016; Andreola et al., 2003; Adachi et al., 2014; Vigushin et al., 1994).

Natively folded apoA-I avoids aggregation into amyloid species by sequestering the aggregation hot spot region, residues 14-22, in the middle of the 4-helix bundle. Mutations in the N-terminus, or cleavage of fragments consisting of residues 1-100, results in destabilisation of the helical bundle, allowing the formation of β-sheet structures in the 14-22 and 53-58 hot spot regions. It is proposed that these β-sheets organise into layers, with side chain interactions stabilising a "β-zipper" conformation (**Figure 1.11B**), propagating through the N terminus, or the full peptide (Das et al., 2016; Das et al., 2014). However, the exact mechanism for the conversion of apoA-I into amyloid is unknown.

2.4.8.1. Detrimental effects of apoA-I aggregation

A reduction in the function of the HDL particle would result in a decrease in the reverse cholesterol transport mechanism and lead to an enhanced progression of atherosclerosis. Therefore, any change in the activity of apoA-I that could affect the formation of the HDL particle, or the effectiveness of its reverse cholesterol transport function, would also be detrimental to health.

Aggregation of apoA-I into amyloid species leads to the inactivation of the HDL molecule, in particular its ability to interact with ABCA1, LCAT, SRB1 and lipids. Amyloidosis of apoA-I manifests itself as three driving forces for atherosclerosis: (i) a reduction in reverse cholesterol transport, (ii) deposition of the aggregated apoA-I or inactive HDL molecules within vessels, leading to increased plaque loading, and (iii) cytotoxicity of the apoA-I aggregates, or aggregation intermediates on endothelial tissue, thus enhancing the inflammatory response (Stein and Stein, 1999; Annema and von Eckardstein, 2013; Baglioni et al., 2006). An increase in apoA-I expression, and a subsequent

increase in vascular HDL concentration, results in a reduction in free cholesterol and the associated risk of plaque formation, in addition to the removal of cholesterol that has already been deposited within plaques (Annema and von Eckardstein, 2013).

Oxidation of apoA-I, via myeloperoxidase, particularly on residue W72, leads to an inhibition of the apoA-I's ability to bind to ABCAI, thus reducing the cholesterol absorption ability of the protein, halting the maturation of HDL. ApoA-I with the oxidised tryptophan residue is present in only low concentrations within the plasma, but accounts for 20% of all apoA-I in vessels with atherosclerotic plaques (Huang et al., 2014).

2.4.9. ApoA-I mutants

ApoA-I is known to have many naturally occurring mutants. Most of the research focuses on the atheroprotective R173C "Milano" mutant (Mahley et al., 1983) or the amyloidogenic mutants that lead to the release of the apoA-I N terminus, resulting in familial apoA-I amyloidosis (Gursky et al., 2012). These include G26R, W50R, L60R, L64P, L75P, and L90P (Raimondi et al., 2011).

2.4.9.1. Aggregation inducing mutants

Raimondi (2011) studied a range of mutations (G26R, W50R, L60R, L64P, L75P and L90P) within the N-terminus of apoA-I. Reduction in pH resulted in aggregation of all mutants into amyloid species. Fourier transformed infrared spectroscopy (FTIR) showed a conversion from primarily unstructured regions, to β-sheet structures, characteristic of amyloid. The L90P mutant showed the largest increase in amyloidosis, followed by the W50R and L75P mutants,

whereas the G26R and L60R had no significant difference in the aggregation propensity, compared to the wild type apoA-I (1-93) peptide. Despite this, the full-length apoA-I G26R mutant and the N-terminus of the L90P mutant (Soutar, 1992) have been detected as amyloid deposits within arterial plaques. The naturally occurring Iowa G26R mutant is thought to induce amyloidosis of apoA-I via destabilisation of the N-terminal region.

As well as mutations within the 1-93 N-terminus, mutations outside of the N-terminus region can lead to increased cleavage and release of the 1-93 peptide, which then has an increased propensity to aggregate (Gursky et al., 2012).

2.4.9.2. Atheroprotective mutants

The R173C "Milano" mutant was the first known natural apoA-I mutant, which introduces a cysteine into the native sequence, allowing the increased formation of apoA-I homo and heterodimers. Individuals with the Milano variant of apoA-I have decreased expression of apoA-I, and subsequent HDL, which normally coincides with increased risk of cardiovascular disease. However, the inverse is observed, whereby apoA-I Milano has an additional atheroprotective function. It is thought that this function is caused by a change in the structure of apoA-I Milano compared to the wild type. Removal of the positively charged arginine from position 173, and replacement with a cysteine inhibits the salt bridge formation between residues 173 and 169, leading to decreased stability of the monomeric apoA-I Milano. These changes to the apoA-I Milano structure affect its ability to bind lipids, resulting in a lower concentration of the cholesterol-bound HDL complexes in the plasma. How this results in better cardiac health is still unknown (Alexander et al., 2009).

2.5. Aims

The aims of this work were to understand the biophysical and structural changes that apoA-I undergoes when aggregating into amyloid species. Secondly, the work aims to identify modulators of aggregation as potential therapies. The objectives were to:

- Establish a working protocol for the large-scale production of apoA-I, with the ability to modify the expression system to facilitate the production of ^{13}C and ^{15}N isotopically labelled apoA-I for analysis by solid-state NMR (SSNMR), and insertion of single amino acid mutations. This will be described in **Chapter 3**.
- Establish suitable conditions for promoting the aggregation of apoA-I into amyloid species. This will focus on the effects of pH, heparin and methionine oxidation. It will be essential to confirm that scaling up of amyloid production can facilitate structural studies of apoA-I aggregates using circular dichroism, X-ray diffraction and SSNMR. This will be described in **Chapter 4.**
- Use biophysical techniques (CD, X-ray diffraction and SSNMR) to propose a detailed model for apoA-I aggregation into amyloid species. This will be discussed in **Chapter 5**.
- Examine the effect of green tea polyphenols on apoA-I aggregation. In particular, epigallocatechin gallate (EGCG), which has been shown to inhibit aggregation of other amyloidogenic proteins. This will be discussed in **Chapter 6**.

3. Recombinant expression of apoA-I and apoA-I mutants

3.1. Introduction

3.1.1. Protein expression

Throughout the duration of this study, apoA-I was required in large quantities for use in a range of measurements to determine suitable conditions that promote its aggregation, and for structural studies, including SSNMR, to study the structure of the aggregated material. SSNMR analysis additionally required the production of uniformly labelled ^{13}C and ^{15}N apoA-I. Furthermore, the production of natural mutants of apoA-I, and mutants that included the introduction of a novel cysteine residue into the sequence for fluorescence tagging purposes were investigated. Recombinant expression of apoA-I in *Escherichia Coli* (*E.Coli*) was carried out in order to facilitate these requirements. The size of apoA-I, at 243 residues, meant that purchasing synthetic protein in the quantities required would not be feasible. The cost of labelling the synthetically produced peptide would also rule out SSNMR analysis of the protein, due to the cost implications. The objectives of this section were to establish a suitable recombinant expression and purification system for apoA-I, which would also facilitate site-directed ligase independent mutagenesis (SLIM) (Chiu, 2004) and expression of ^{13}C and ^{15}N labelled apoA-I .

An N-terminally hexa-histidine tagged recombinant protein construct for apoA-I, including an E2D mutation, facilitating formic acid cleavage of the his-tag via the introduction of a novel acid labile Asp-Pro peptide bond, has been successfully expressed in *E.Coli* cells (Oda et al., 2001). This methodology

produced a suitably high yield of apoA-I (3-243) protein, which is referred to as apoA-I, or wild type apoA-I to distinguish it from the mutant apoA-I proteins throughout the remainder of this thesis. This protocol forms the basis of the expression methods used throughout this work and uses the plasmid construct kindly provided by Dr. M. Oda (Oakland Children's Hospital Research Institute). A plasmid map is supplied in **Appendix 1**. Given the success of this methodology, it was utilised not only for the production of the apoA-I (3-243) wild type, but also the production of mutant apoA-I (3-234) species via SLIM based PCR methods, and modified to allow isotopic labelling of the wild type protein.

3.1.2. Labelled protein production

Recombinant protein expression allows the inclusion of stable isotope labels, in particular, ^{13}C and ^{15}N, uniformly or sparsely distributed through the protein sequence. These are essential for SSNMR studies, as they allow an increase in sensitivity and resolution and can simplify the complexities of the spectra. There are several ways to label proteins, depending on the information that is required from the solid-state NMR experiments. Selectively labelling individual amino acids, such as Ile, Leu and Val, gives insight into the proteins global fold, due to their location within hydrophobic cores. However, this requires the purchasing of synthetic protein, which was too costly due to the size of apoA-I, or acquiring one of the auxotrophic strains of *E.Coli*. Uniform labelling of apoA-I with ^{13}C and ^{15}N is more cost effective and a good starting point to assess the resolution achieved. Uniform labelling also increases the accuracy of residue assignment, when facilitated by multi-dimensional triple resonance experiments (Lian and Middleton, 2001).

3.1.3. ApoA-I mutants

The production of mutant apoA-I proteins was investigated for two reasons: (i) the comparison of aggregation kinetics of naturally occuring mutant apoA-I to native apoA-I, and (ii) to introduce a novel cysteine residue into the apoA-I sequence. This cysteine residue will facilitate fluorescently labelled tagging of the protein, in order to allow the visualisation of apoA-I uptake and distribution within human endothelial cells. Four single amino acid mutations have been selected and will be produced via SLIM.

1. A naturally occurring mutant, apoA-I Iowa, substitutes the glycine in position 26 with an arginine, and has been found deposited as amyloid aggregates within arterial plaques. The mutant also increases the formation of amyloid-like species in apoA-I (1-83), albeit at a slower rate (Adachi et al., 2012). This is thought to be caused by destabilisation of the N-terminus region (Adachi et al., 2014). The destabilising effects of G26R on full-length apoA-I correspond to its location within the major helix of the N-terminus (**Figure 3.1A**). It is proposed that the introduction of basic charge, carried by the arginine, into the hydrophobic face of the helix, increases the solvent exposure of the helix bundle, leading to its destabilisation (Adachi et al., 2012).
2. A mutant corresponding to the replacement of the leucine in position 90 with a proline residue, has been shown to enhance the rate of aggregation of the apoA-I (1-93) peptide into insoluble material, characteristic of amyloid (Raimondi et al., 2011; Monti et al., 2011). This mutation is located within the N-terminal 1-100 residues (**Figure 3.1B**), and its increased propensity to aggregate could be linked to destabilisation of the N-terminus, as with the G26R mutant.

3. A mutant with leucine 44 replaced by a stop codon should facilitate the production of apoA-I (3-43). The N-terminal 1-80/100 residues of apoA-I have a strong propensity to form amyloid when isolated from the remaining apoA-I sequence. Proteolytic cleavage and release of N-terminal fragments occurs naturally, leading to increased deposition of these short peptides as amyloid species. A peptide corresponding to residues 1-43 has been shown to readily form amyloid-like species in isolation (Adachi et al., 2014).
4. Two cysteine mutants were produced in order to facilitate tagging of the free thiol group on the cysteine residue with luminescent tags, since apoA-I lacks native cysteine residues. Lysine and arginine in positions 96 and 173, respectively, were each replaced with a cysteine residue, producing the K96C and R173C mutant (**Figure 3.1 C** and **D**, respectively). The R173C mutant is the naturally occurring apoA-I Milano mutant, which is of increasing significance in the study of lipid-bound apoA-I, due to its reduced concentration in carriers of the R173C gene, despite having lower incidence of atherosclerosis and associated cardiac disease (Alexander et al., 2009). Both of these cysteine mutants have previously been produced, using the same expression and purification methods as the wild type protein (Oda et al., 2001). The K96C mutant is located in the extended helix repeats along domain 4/5 but appears internally located, meaning that its ability to be tagged is reduced (**Figure 3.1C**). However, the cysteine introduced into position R173C, lies in the domain swapped C-terminus and is exposed to the exterior of the protein (**Figure 3.1D**). This C-terminal region is involved in dimerisation, and introduction of a free thiol group into this region could lead to the formation of more stable apoA-I dimers via disulfide cross bridges.

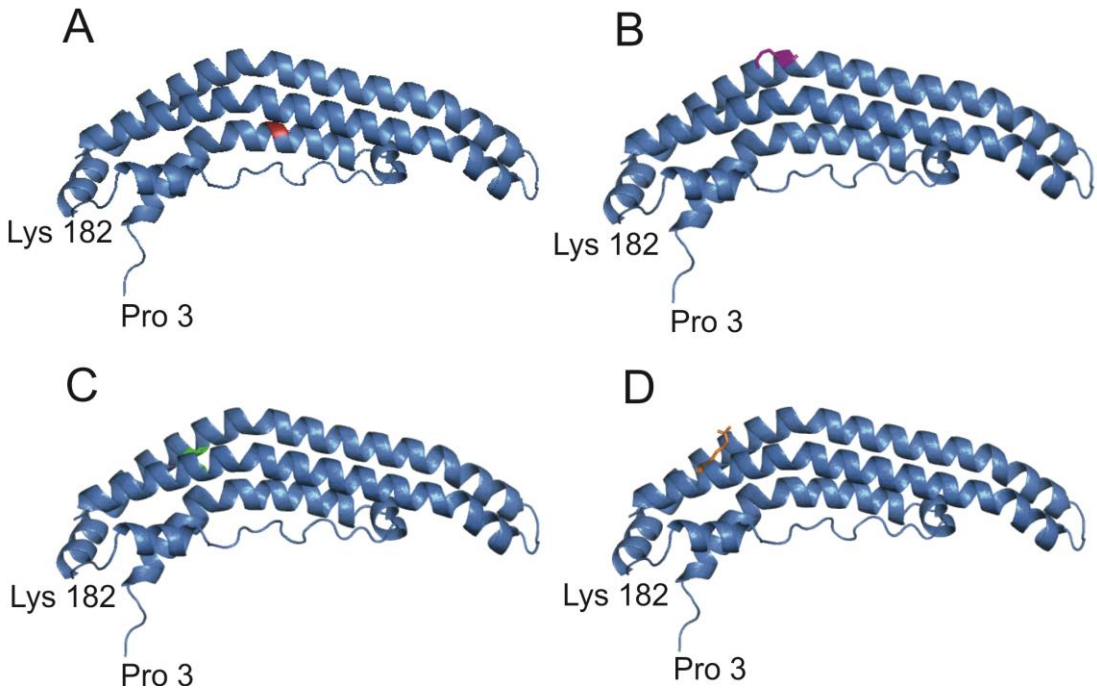

Figure 3.1 Structure of monomeric apoA-I (Δ185-243) highlighting the native residue to be removed for the apoA-I mutants (**A**) G26R in red, (**B**) L90P in purple, (**C**) K96C in green and (**D**) R173C in orange.

3.1.4. SLIM PCR mutagenesis

Site-directed ligase independent mutagenesis (SLIM) is a PCR based mutagenesis method that allows the rapid insertion, deletion or substitution of single amino acids (Chiu, 2004). This method utilises an inverse PCR amplification of the template sequence by 4 primers: 2 long-tailed primers, containing the desired mutation, and 2 short-tailed, complementary primers.

3.1.5. Formic acid cleavage

The Asp-X bond is readily hydrolysed under acidic conditions. The nucleophilic attack of the ionised carboxylate of the aspartic acid side chain on the peptide carbonyl group releases the Asp-C-terminal peptide. The reactive N-terminal aspartic anhydride is then hydrolysed, releasing the N-terminal peptide, ending with aspartic acid residue ta its C-terminus (**Figure 3.2**).

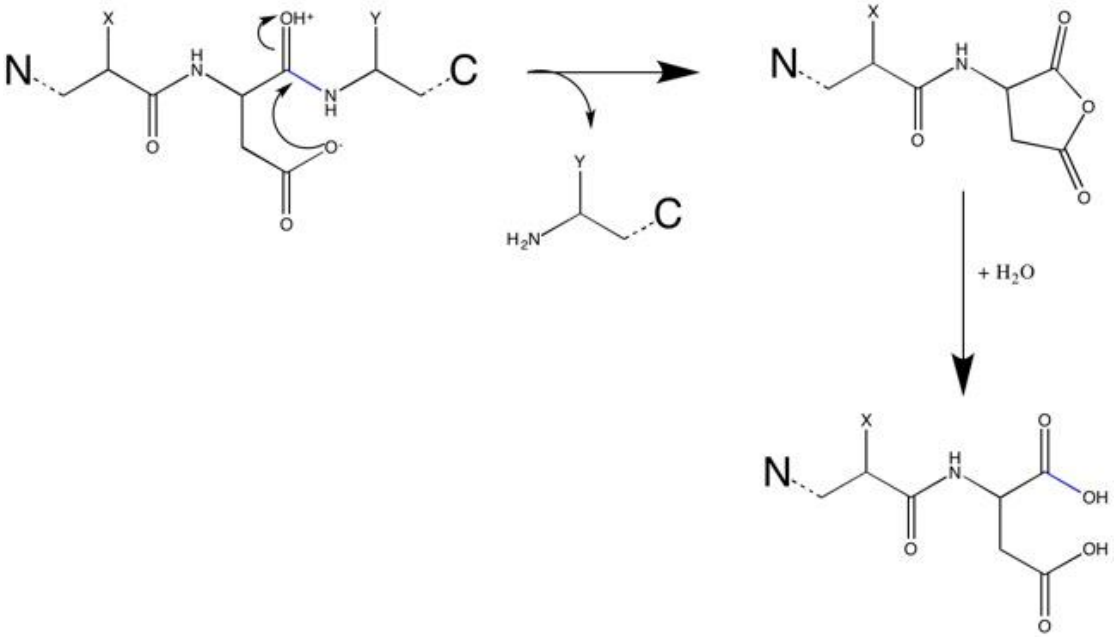

Figure 3.2 Peptide hydrolysis following incubation of the asp-X peptide bond in acidic conditions.

3.1.6. Aims

The main aim of this chapter of research was to establish a working protocol for the large-scale production of apoA-I. This expression system must have the ability to be modified, in order to allow expression of ^{13}C and ^{15}N uniformly labelled apoA-I for analysis by solid-state NMR. Finally, the procedure should be able to facilitate the expression and purification of the apoA-I mutants listed in **section 3.1.3**, following mutagenesis of the apoA-I DNA.

3.2. Materials and methods

3.2.1. Construct design

3.2.1.1. ApoA-I E2D Construct

A pNFXex expression vector containing the E2D mutated and codon optimised human apoA-I gene with an N-terminal hexa-histidine tag, was kindly provided by Dr M. Oda of Oakland Research Institute, USA. Also provided were expression vectors for the human apoA-I (G26R) mutant.

Oda *et al.* (2001) and Ryan *et al.* (2003) conducted studies on apoA-I that required expression of recombinant apoA-I, and started with a pBluescript K+ plasmid, containing the gene for apoA-I (**Figure 2.3**). The cDNA of human apoA-I has a distinctive lack of useful restriction endonuclease sites, required for sub-cloning and DNA manipulation. As such, several silent mutations were introduced into the apoA-I DNA to produce 13 new restriction endonuclease sites (**Table 3.1**). The pBluescript K+ plasmid is suitable for the manipulation of DNA and is commonly used for sub-cloning, sequencing and site-directed mutagenesis (Mayer, 1995). In the work by Oda *et al.* and Ryan *et al.*, the plasmid allowed (i) attachment of a hexa-histidine tag to the N-terminus of apoA-I (ii) insertion of the E2D mutation into the apoA-I sequence, creating an Asp-Pro acid labile bond to facilitate formic acid cleavage of the N-terminal histidine-tag and linker region, and (iii) 18 individual codon optimisations (**Table 3.2**), which removed codons that utilise tRNA molecules of low abundance in *E.coli*. Changing the codons in the human apoA-I DNA sequence to those corresponding to the same residue, but with increased use in bacterial cells, leads to a 5-fold increase in protein yield. This recombinant gene was then sub-cloned into the highly expressive pET20b+ plasmid, producing the expression vector pNFXex, containing the sequence

shown in **Figure 3.3**, and a gene corresponding to ampicillin resistance (Ryan et al., 2003).

Table 3.1 Codon changes made in apoA-I cDNA to introduce 13 new endonuclease sites (Ryan et al., 2003).

Amino acid	**Codon change**	**Restriction site**
Asp 1	GAT to GAC	ClaI
Pro 7	CCC to CCA	Nco
Gyl 35	GGC to GGA	BamHI
Gln 41	CAG to CAA	MfeI
Leu 42	CTA to TTG	
Leu 44	CTA to CTT	AflII
Thr 54	ACC to ACG	AatII
Glu 70	GAG to GAA	EcoRI
Leu 126	CTC to CTG	PstI
Gln 127	CAA to CAG	
Val 156	GTG to GTC	SalI
Ala 164	GCC to GCG	KasI/NarI
Ala 175	GCC to GCG	AscI
Gly 186	GGC to GGG	
Arg 188	AGA to CGG	ApaI
Glu 234	GAG to GAA	DXhoI
Leu 240	CTC to CTT	HindIII

Table 3.2 Codon optimisations made in human apoA-I cDNA, and the codon frequency per 1000 in *E.coli* cells. Red letters indicate the altered nucleotide. Information taken from Ryan et al, (2003).

Residue	Original Sequence	Original Frequency	Modified Sequence	Modified Frequency
Pro 3	CCC	5.4	CCG	22.3
Pro 4	CCC	5.4	CCG	22.3
Pro 7	CCC	5.4	CCA	8.5
Pro 99	CCC	5.4	CCG	22.3
Pro 165	CCC	5.4	CCG	22.3
Pro 209	CCC	5.4	CCG	22.3
Pro 220	CCC	5.4	CCG	22.3
Arg 10	CGA	3.7	CGC	21.1
Arg 83	AGG	1.6	CGC	21.1
Arg 188	AGA	2.7	CGC	21.1
Leu 42	CTA	4.0	TTG	11.3
Leu 44	CTA	4.0	CTT	11.3
Leu 46	CTC	10.6	CTG	50.9
Leu 47	CTT	11.3	CTG	50.9
Leu 126	CTC	10.6	CTG	50.9
Leu 214	CTC	10.6	CTG	50.9
Leu 233	CTC	10.6	CTG	50.9
Gly 39	GGA	8.6	GGC	28.6

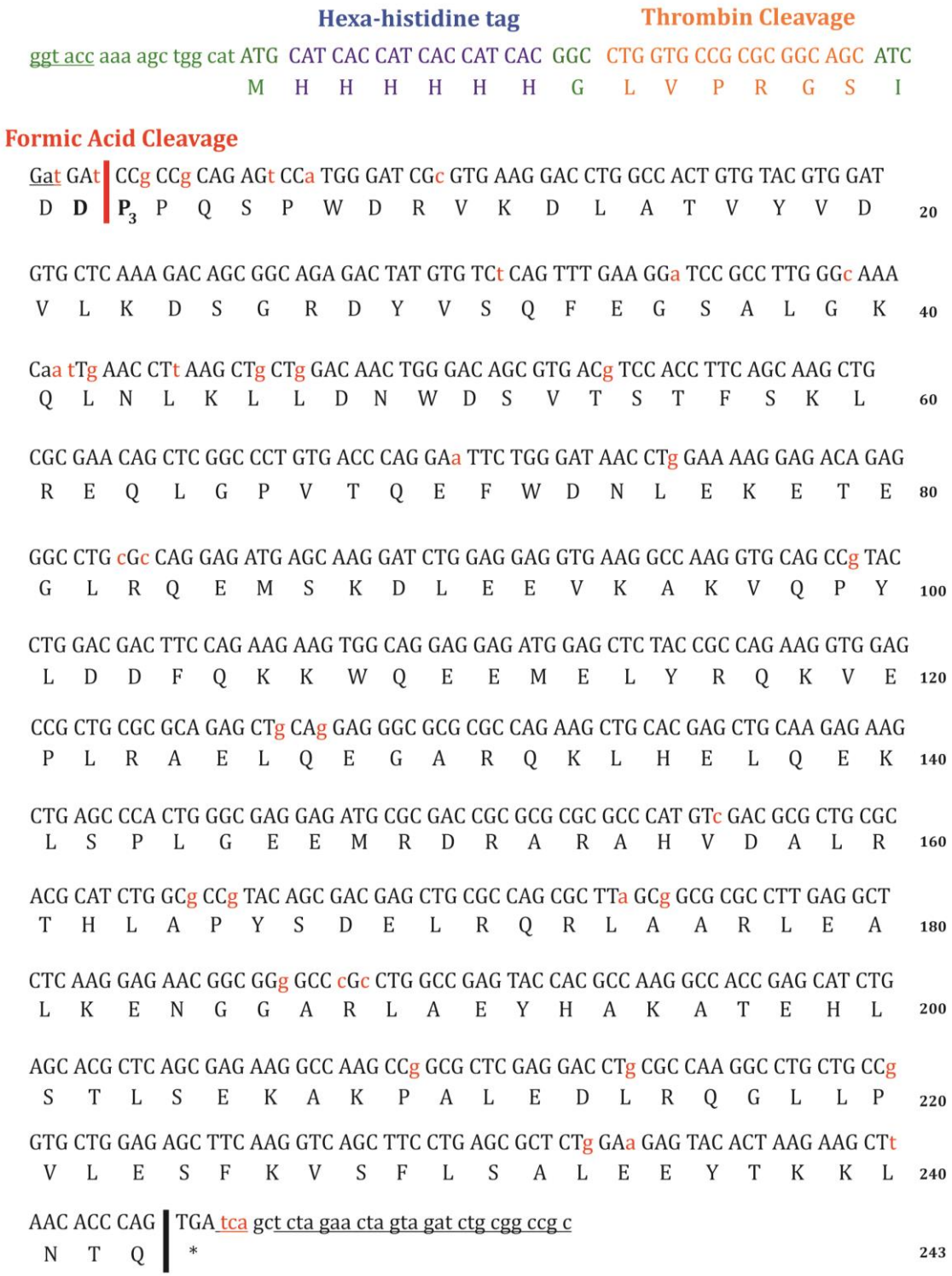

Figure 3.3. N-terminally his-tagged apoA-I (E2D) sequence in the pNFXex expression vector. The red lowercase letters represent the nucleotides that were altered in the codon optimisation step (listed in **Table 3.2**). The sequences highlighted in blue, orange and red are the hexa-histidine tag, thrombin cleavage site and formic acid cleavage site, respectively.

3.2.1.2. Production of mutant constructs via SLIM PCR

As described in **Section 3.1.4**, the SLIM PCR method of mutagenesis utilises 4 primers to amplify the template DNA: 2 long tailed primers, containing the desired mutation; and 2 short primers. These are detailed in **Appendix 2**. Amplification of the template DNA by the 4 primers in complementary pairs result in the formation of 4 PCR products. Following denaturation and subsequent re-hybridisation, 16 hybrid products are formed, 2 of which able to form plasmids spontaneously. The entire procedure is simplified in **Figure 3.4**.

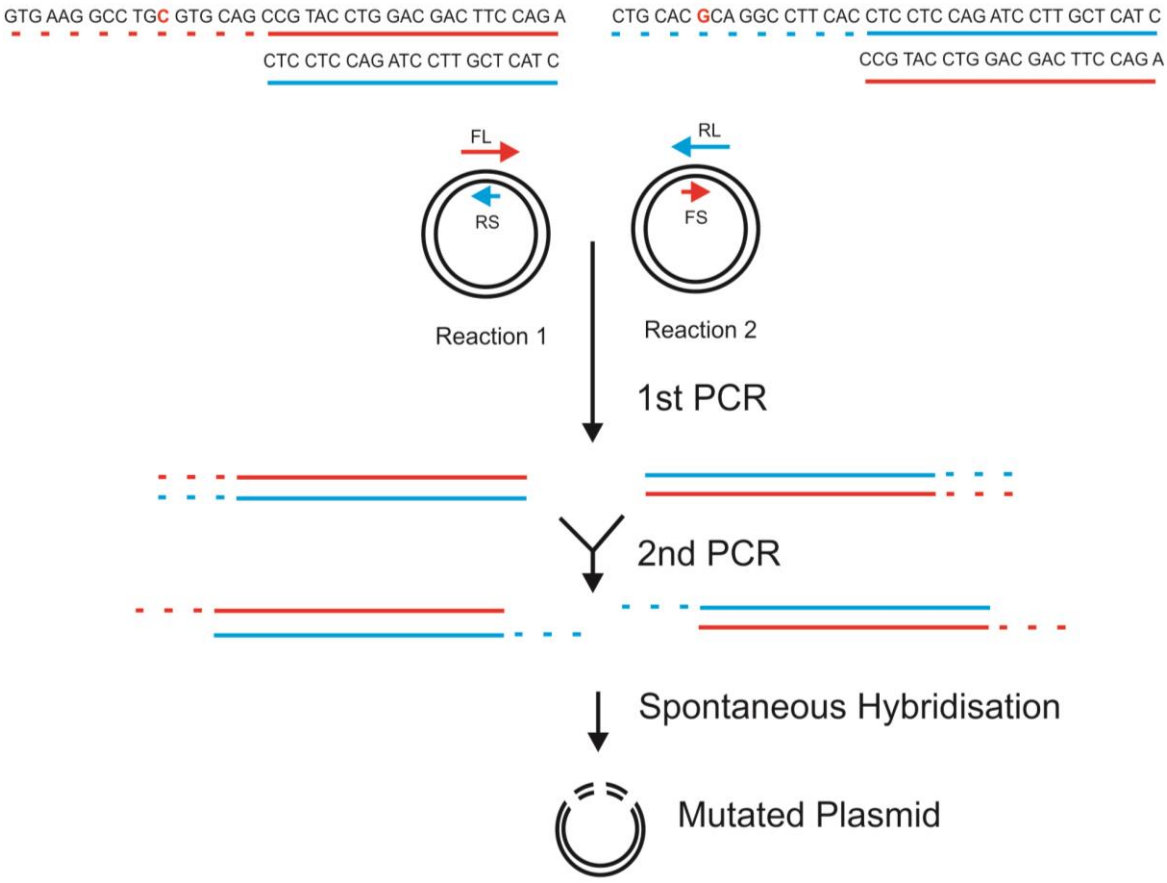

Figure 3.4 Schematic of the SLIM PCR protocol adapted from Chiu et al., (2004). This example includes the primers used to create the K96C mutation in apoA-I.

SLIM PCR mutagenesis followed the same procedure for all 4 mutants, utilising the Novagen KOD Hot Start DNA Polymerase Kit.

To each of the 3 PCR tubes: reaction 1, reaction 2 and the control sample, 12.5 µL water, 5 µL Phusion HF buffer (ThermoFisher), 2.5 µL DTNPs (Novagen), 2.5 µL betamine, 0.5 µL Phusion Hot Start II DNa Polymerase (ThermoFisher) and 1 µL of template apoA-I E2D DNA were added. 0.5 µL of the forward-long and 0.5 µL of reverse-short primers were added to reaction 1, whilst 0.5 µL of forward-short and 0.5 µL of reverse-long primers were added to reaction 2. No primers were added to the control sample.

After pre-warming all 3 samples at 98 °C for 2 minutes, each reaction underwent the first round of PCR. This consisted of 30 cycles of: 95 °C for 30 seconds, 50 °C for 30 seconds and 68 °C for 8 minutes, prior to holding at 4 °C.

Samples of 5 µL were removed from each reaction for analysis by agarose gel electrophoresis, in order to determine whether the DNA had been amplified. The control reaction was then discarded following the gel electrophoresis stage. To degrade the original methylated template DNA, 1 µL of Dpn1 restriction enzyme (New England BioLabs) was added to reactions 1 and 2 and incubated at 37 °C for 1 hour. 30 µL of hybridisation buffer was added to each reaction, prior to combining the two. After denaturing the DNA at 98 °C for 3 minutes, the combined reactions underwent a second round of PCR. This involved 2 cycles of heating to 65 °C for 5 minutes and then cooling to 30 °C for 15 minutes. After holding at 4 °C the mutated plasmid DNA was then removed and stored at -80 °C.

3.2.1.3. Confirmation of PCR products via agarose gel

After the first round of PCR, 5 µL samples of DNA taken from reactions 1, 2 and the control to confirm the amplification of DNA on a 0.8 % agarose gel.

0.8 g of agarose was dissolved in 100 mL Tris acetate EDTA (TAE) buffer, along with 10 µL SYBR Safe DNA Gel Stain (Invotrogen). The gel solution was poured into a gel cast and allowed to set.

5 µL of each of sample (reaction1, reaction 2 and the control sample) were combined with 1 µL of Gel Loading Buffer (ThermoFisher) and loaded onto the gel, along with 6 µL Quick Load 1Kb DNA Ladder (New England BioLabs). The gel was run at 100V for 60 minutes, before imaging under UV light using a Chemidoc XRS+ imaging system, running the Image Lab 4 programme. The pre-set programme for SYBR Safe stain, and automatic exposure were selected, to detect the highest intensity bands.

3.2.2. Transformation into *E.coli*

Transformation involves the incorporation of an engineered plasmid vector into the genomes of competent cells. For this study, 2 separate *E.coli* cell lines were used, XL1Blue and BL21 (DE3), to allow plasmid vector storage and recombinant expression, respectively.

3.2.2.1. Transformation into XL1Blue cells

DNA from each of the apoA-I species, apoA-I E2D, G26R, L90P, K96C, R173C and L44Stop, required transformation into an *E.coli* XL1Blue strain for long-term storage.

50 µL of *E.coli* XL1Blue cells (Agilent Technologies) for each of the 6 apoA-I species (apoA-I E2D, G26R, L90P, K96C R173C and L44Stop) were thawed on ice, prior to the addition of 1.7 µL of β-mercaptoethanol (BioRad). After 10 minutes, 5 µL of plasmid DNA (provided by Oda or produced via SLIM PCR, as described in **section 3.2.1.2**) was added, gently mixed, and left on ice for 30 minutes. The cells were then heat-shocked at 45 °C for 45 seconds before returning to ice for 2 minutes. 900 µL of SOB media was slowly added and incubated for 1 hour at 37 °C with shaking.

Following incubation, 200 µL of culture was plated out on LB agar plates, containing 200 µM ampicillin. The plates were then returned to incubation at 37°C overnight. Growth on the plates, in the presence of ampicillin, indicated that the cells had taken up the plasmid vector containing the gene for ampicillin resistance and the apoA-I fusion peptide. Individual colonies were selected and grown in overnight cultures of LB media containing 200 µM ampicillin at 37 °C. Overnight cultures were used to create 50 % glycerol stocks and frozen at -80 °C.

3.2.2.2. Transformation into *E.coli* Bl21 (DE3) cells

In addition to the long-term storage of the plasmid vectors in the *E.coli* XL1Blue cell line, the vectors were also transformed into an *E.coli* BL21 (DE3) expressing cell line (Agilent Technologies) to increase protein expression yields. This allows the formation of expressing cell line glycerol stocks, meaning that repeated DNA isolation from the XL1Blue cell line and transformation into the BL21 (DE3) cell line, prior to protein expression, can be avoided.

The method for the transformation of DNA into BL21 (DE3) cells was identical to the transformation into the XL1Blue cell line (**Section 3.2.2.1**).

3.2.3. Production of apoA-I

3.2.3.1. Recombinant protein expression

Small overnight cultures of *E.coli* BL21 (DE3) cells, containing each of the apoA-I mutant plasmids, were prepared in LB media, containing 0.1 % ampicillin (Melford Biolabs), from the glycerol stocks produced in **Section 3.2.2.2**. The cultures were incubated at 37 °C overnight, with shaking. These cultures were then used to inoculate 2 L of LB media.

The 2L cell culture was incubated at 37 °C until an OD_{600} of 0.6 had been reached. Once the OD_{600} was sufficient, a 1 mL sample of culture was removed, for analysis by gel electrophoresis.

Protein expression was induced by addition of 1mM isopropyl β-D-thiogalactoside (IPTG) (Melford Biolabs). Incubation continued at 37 °C, with shaking, for a further 5 hours following induction. Samples of the induced cells were taken every hour from the second hour-point for gel electrophoresis.

3.2.3.2. Minimal media growth

Transformed cells were also induced in minimal media, enriched with labelled glucose and ammonium chloride (CortecNet), as the sole ^{13}C and ^{15}N sources. The cells were grown as previously described in **Section 3.2.3.1**. Briefly, overnight cultures of the BL21 (DE3) cells, containing the desired apoA-I plasmid were prepared and used to inoculate 2 L of LB media, which was grown at 37 °C until an OD_{600} of 0.6 was reached.

The cells were then pelleted by centrifugation at 5000 g and re-suspended in 1 L pre-warmed minimal media (88 mM Na_2PO_4, 55 mM KH_2PO_4, 1 mM $MgSO_4$, 0.3 mM ampicillin, 0.1 mM $CaCl_2$, 0.03 mM thiamine HCl, 22 mM glucose, 19 mM

NH_4Cl). The cells were left to adjust to the new media for 30 minutes, before induction with 1mM IPTG. Cells were incubated for a further 5 hours, to allow protein expression.

3.2.3.3. Cell harvest and lysis

Following the 5-hour induction, cells were harvested through centrifugation at 5,000 g for 20 minutes. The cells were then re-suspended in 6 M guanidine hydrochloride cell lysis buffer (6 M GnHCl, 20 mM $NaPO_4$ pH 7.4) and frozen at -20°C to aid lysis. The re-suspended cells were further lysed through sonication at 20 microns of power, for 5 cycles of 15 seconds on, 45 seconds off. The cells were kept on ice during this time to avoid overheating. Cell debris was removed through centrifugation at 43,000 g for 30 minutes, and the supernatant was collected.

3.2.3.4. Immobilised metal ion affinity chromatography (IMAC)

The fusion protein, containing the apoA-I (E2D) gene and the hexa-histidine tag, can be isolated from the other cell proteins via immobilised metal ion affinity chromatography (IMAC). The hexa-histidine tag binds with high affinity to a nickel sepharose resin, whilst the remaining cell proteins pass through the column in the flow-through. The his-tagged protein can then be washed and eluted with increasing concentrations of imidazole, which out-competes the hexa-histidine tag for nickel binding.

A 20 mL HisTrap FF™ pre-packed Nickel Sepharose column (GE Healthcare) was set up on an AKTA Start system (GE Healthcare) running the UNICORN control software. The column was equilibrated with guanidine lysis

buffer until the conductivity and UV readings were constant, which was roughly 5 column volumes.

The cell lysis supernatant was loaded onto the column at a flow rate of 1 mL/min and the flow-through was collected. The column was sequentially washed with (I) guanidine lysis buffer (II) 20mM $NaPO_4$, 0.5M NaCl, pH 7.5 (III) 20mM $NaPO_4$, 0.5M NaCl, 25mM imidazole, pH 7.5 (IV) 20mM $NaPO_4$ 0.5M NaCl, 50mM imidazole, pH 7.5, each at a flow rate of 5 mL/min, until the UV remained constant, roughly 3-4 column volumes of each. 10 mL fractions were collected at each stage for analysis by SDS-PAGE. The fusion protein was then eluted with 20mM $NaPO_4$, 0.5M NaCl 0.5M imidazole pH 7.5, running at 1 mL/min with 1 mL fractions collected.

The concentration of elution fractions were measured using a Nanodrop 2000 (Thermo Scientific) and those with high UV absorbance and protein concentration were pooled. A 50 µL sample of the eluted fractions was taken for analysis by gel electrophoresis.

3.2.3.5. Dialysis and cleavage

The elution fractions with the highest UV and concentrations were pooled in a cellulose dialysis membrane and dialysed against 50 mM Tris HCl, 1 mM benzamidine, 1 mM EDTA, pH 7.4 at 4 °C overnight.

The dialysed protein was then filtered through a 0.2 µm syringe filter (Corning) to remove a white precipitate that had developed during dialysis. The filtered protein was then incubated in 45 % v/v formic acid (Sigma) at 55 °C for 5 hours to cleave the hexa-histidine tag from the apoA-I, via the acid labile Asp-Pro sequence, introduced with the E2D mutation.

Following cleavage with formic acid, the protein was dialysed a further 2 times into 50 mM Tris HCl, 1 mM benzamidine, 1 mM EDTA pH 7.4 at 4 °C for 16 hours to remove the residual formic acid. A second filtration through a 0.2 μm membrane removed any precipitate that formed during the dialysis. Finally, the protein was dialysed into McIlvaine buffer (165 mM Na_2HPO_4, 17.6 mM citrate, at pH 7.0) overnight. This step was incorporated to enable apoA-I aggregation to be monitored over a large pH range (pH 2.2-8). The final protein product was then frozen at -20 °C.

3.2.4. Characterisation of recombinant apoA-I

3.2.4.1. SDS poly-acrylamide gel electrophoresis (PAGE)

SDS-PAGE gels were run in order to determine the expression level and purity of apoA-I at various stages of the procedure. The proteins were separated using a 15 or 17.5 % polyacrylamide gel in a Bio-Rad gel electrophoresis system. 18 μL of protein samples were added to 2 μL of 10x sample buffer (20 % 1 M Tris HCl, 40 % glycerol, 2 % mercaptoethanol, 5 % 0.5 M EDTA, 4 % SDS and 29 % water). The samples were heated at 95 °C to aid denaturing, and loaded into a 5 % stacking gel, along with 5 μL of PageRuler™ Low Range Unstained Protein Ladder (Thermo Scientific). All gels were run at 200 V for roughly 60 minutes, prior to fixing with 25 % isopropanol and 10 % acetic acid in water. Gels were then stained with 10 % acetic acid and 6 % Coomassie Brilliant Blue G-250 overnight. The excess stain was removed with 10 % acetic acid.

3.2.4.2. Native poly-acrylamide gel electrophoresis (PAGE)

Native PAGE gels were run in order to determine the native fold of apoA-I, in particular the oligomeric state of the wild type and cysteine mutants (K96C and R173C) in non-reducing conditions. The introduction of the cysteine residue into the apoA-I sequence gives rise to a free thiol group, which has the ability to form apoA-I dimers via disulphide cross links.

The proteins were run on a NativePAGE™ 4-16% Bis-Tris gel (Life Technologies) with the NativePAGE gel running system. Protein samples of 7.5 µL were added to 2.5 µL of NativePAGE™ sample buffer and loaded onto the gel. The gel was run using NativePAGE™ Anode Buffer and NativePAGE™ Dark Blue Cathode Buffer at 150 V for 120 minutes with a NativeMark Unstained Protein Standard (Thermo Fisher).

3.2.4.3. Mass spectrometry

Electrospray ionisation mass spectrometry of apoA-I and apoA-I mutants was carried out in order to determine the identity of the proteins. This analysis was undertaken at the Institute of Integrative Biology at Liverpool University, assisted by Mr Mark Prescott. ApoA-I samples, in 30 % acetonitrile, were loaded into the nano-electrospray source of the mass spectrometer (Waters Q-ToF micro) at a rate of 250 µL/hour, via syringe. The positive ion mass spectrum was collected, containing multiply-charged ions, and analysed by applying MaxEnt to the data, in order to determine a single mass for the peptide.

3.2.4.4. Gene sequencing

Following transformation of the plasmid into *E.coli* XL1Blue cells for long-term storage, as described in **section 3.2.2.1**, it was necessary to isolate the DNA from the cells in order to sequence the plasmid. This was done using the GenElute™ Plasmid DNA Mini-Prep system (Sigma Aldrich). Overnight cultures of 5 mL were spun down at 12,000 g into a pellet. The pellet was then re-suspended in 200 µL re-suspension solution, prior to lysing the cells, using 200 µL of the GenElute alkaline-SDS based lysis solution. This was gently mixed before the lysis was stopped with 350 µL neutralisation solution. The solution was mixed again before centrifugation at 12,000 g for 10 minutes to pellet the cell debris. The cell lysis was then loaded onto a GenElute MiniPrep Binding Column and centrifuged at 12,000 g for 1 minute to remove any non-DNA material in the flow-through. The DNA bound to the column was washed with 750 µL of the diluted wash solution, prior to another centrifugation at 12,000 g. This removed any residual salts and other contaminants. Excess ethanol from the lysis buffer was removed by repeating the centrifugation step. DNA was eluted with 100 µL of molecular biology reagent water by centrifugation at 12,000 g. DNA samples were sent to Source-Bioscience for sequencing, followed by translation into amino acid sequence using the ExPASy Translate online server. The sequences for each of the five apoA-I species are shown in **Appendix 3**.

3.3. Results

3.3.1. SLIM PCR mutagenesis

3.3.1.1. PCR amplification of the DNA by the mutated primers

SLIM PCR was used to introduce a series of single amino acid mutations into the apoA-I E2D sequence: G26R, L44Stop, L90P, K96C and R173C. Following the incubation of the paired primers in two separate reactions, and the first round of the PCR amplification, DNA samples of the two separate reactions for each mutant were taken.

Agarose gel electrophoresis confirmed the PCR amplification of the DNA for the L44Stop, L90P and R173C in both reactions, as seen in **Figure 3.5**. The K96C mutant samples show amplification of the DNA in reaction 1, but not in reaction 2. The two reaction samples were combined, regardless of the lack of PCR product in reaction 2, and taken forward into transformations and subsequent DNA sequencing. This was due to the successful amplification of the other 3 mutants and presence of a band in reaction 1.

3.3.1.2. Confirmation of mutation by gene sequencing

Sequencing of the DNA from all apoA-I species was performed by Source-Bioscience (Nottingham, UK), the sequences determined are shown in **Appendix 3**. The sequence for apoA-I E2D, L44Stop, K96C and R173C came back as expected, confirming successful substitution of the desired nucleotides. However, the G26R and L90P mutant contained undistinguishable nucleotides, resulting in an incomplete amino acid conversion (**Appendix 3**, blue X). However, these indistinguishable codons are away from site of mutation, suggesting that the cause is due to a sequencing error, rather than an issue with the mutation.

Moreover, the G26R sequence contained codons that could not be distinguished in the linker region between the his-tag and the formic acid cleavage site, in particular, the Glu 2 residue that should have been mutated into an Asp residue to facilitate the formic acid cleavage.

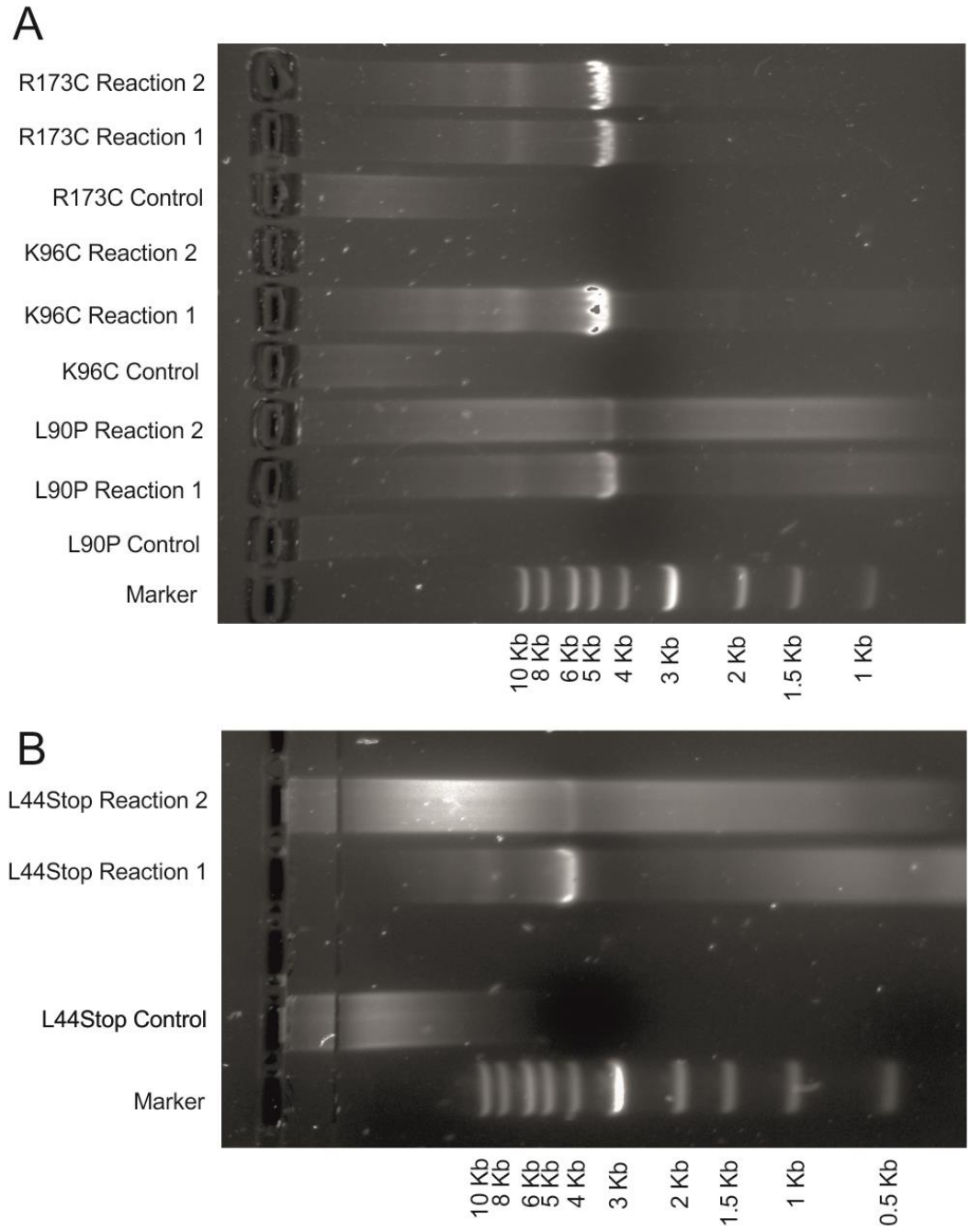

Figure 3.5 Agarose gel electrophoresis of apoA-I (**A**) L90P, K96C, R173C and (**B**) L44Stop DNA, after the first round of SLIM PCR.

3.3.2. ApoA-I expression and purification

3.3.2.1. Expression of apoA-I

Once the pNFX expression plasmid, containing the apoA-I E2D gene, had been successfully transformed into the *E.coli* BL21 (DE3) expressing cell line, the next stage involved large-scale expression in LB media, enriched with ampicillin. The methods outlined in Oda *et al*., (2001) and Ryan *et al*., (2003) had already been optimised to produce yields of up to 100 mg/L culture, which used an incubation temperature of 37 °C, and induction with 1mM IPTG at an OD_{600} of 0.6, for 3 hours.

Incubation times from 2 to 5 hours were monitored to determine if longer incubation after induction would lead to a further increase in apoA-I yield. This enhancement may be required when it comes to expressing apoA-I in minimal media. A sample of the cell culture taken prior to induction with IPTG (pre-induction) and was run on an SDS PAGE gel to highlight the low level of apoA-I expression (**Figure 3.6**). This is essential as it confirms that cell growth can be carried out in LB media without expressing apoA-I fusion protein, prior to transfer into minimal media for induction of labelled protein expression. This will result in a negligible amount of unlabelled apoA-I being produced, whilst simultaneously maximising labelled apoA-I expression.

The gel in **Figure 3.6** also included samples of the cell culture taken at various time points after induction with IPTG and activation of the T7 promoter, controlling the expression of the apoA-I fusion peptide. Expression of a protein that migrates to the 25-30 kDa region of the gel, and consistent with the apoA-I fusion peptide (29642 Da), is dramatically increased after 2, 3, 4 and 5 hours of induction. The yield of apoA-I fusion peptide was sufficient for further work after

induction for 3 hours. However, induction for 5 hours led to a slightly denser band in the apoA-I fusion peptide region, suggesting an increase in yield, without increasing the expression of cellular proteins not under the LAC operon control. As such, it was decided that expression would continue with incubation for 5 hours after induction.

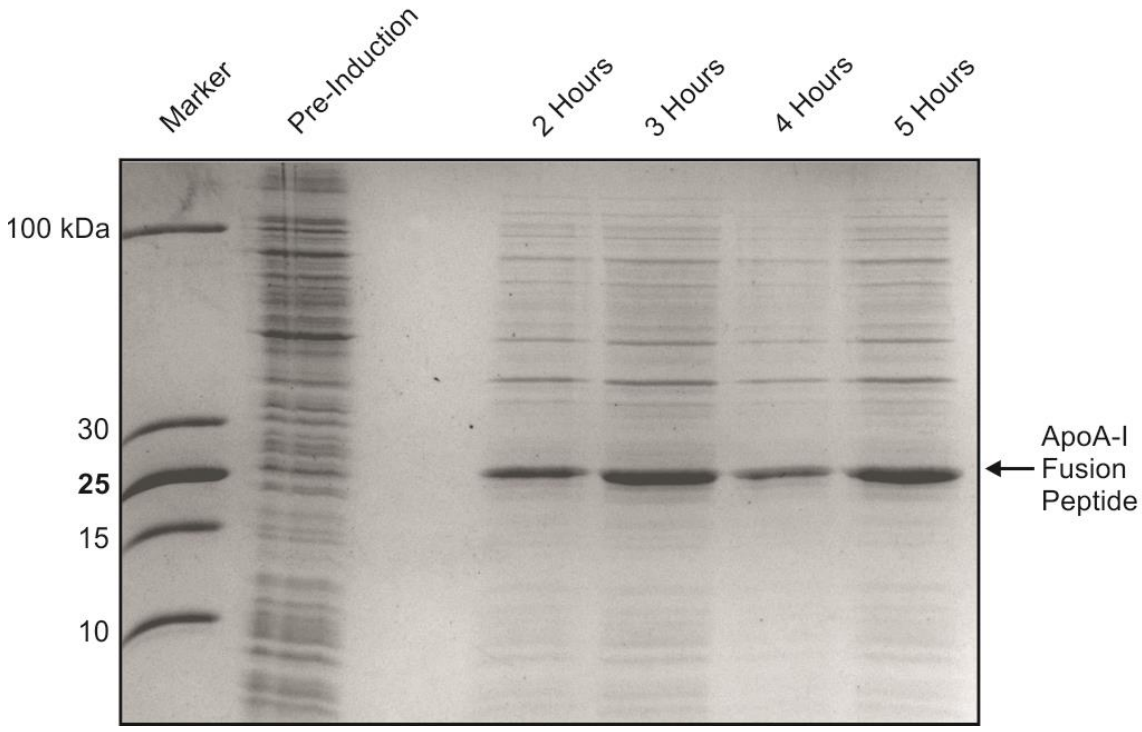

Figure 3.6 15% SDS PAGE gel of apoA-I fusion peptide expression prior to, and after induction for 2, 3, 4 and 5 hours with 1 mM IPTG.

Following optimisation of the length of induction, expression of apoA-I was trialled using a range of IPTG concentrations, and at a reduced temperature. **Figure 3.7** shows that at 30 °C, the lowest maintainable incubator temperature available in the lab, expression of apoA-I was still accomplished, albeit at a reduced level, compared to expression at 37 °C, across all IPTG concentrations and regardless of the induction time. This concluded that, if necessary, induction

of apoA-I expression could be carried out at a lower temperature but would result in a decreased yield. At 37 °C, the concentration of IPTG added made no difference to the protein yield.

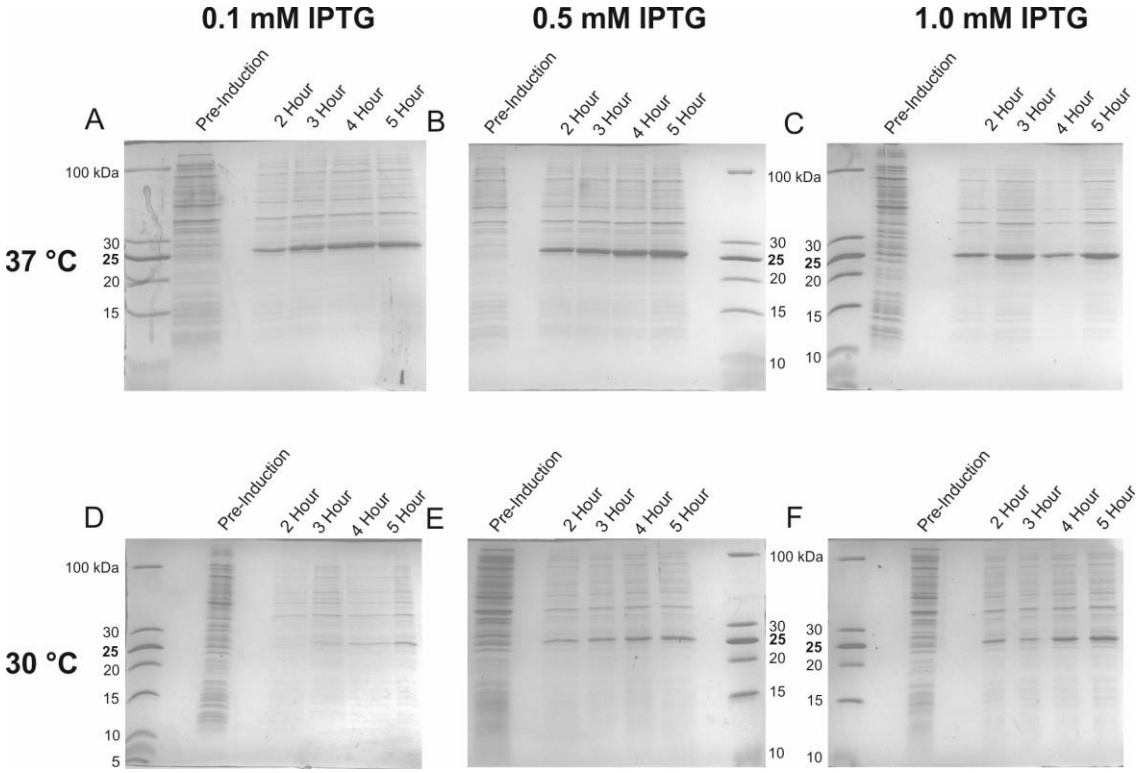

Figure 3.7 15 % SDS PAGE gel of the expression tests for apoA-I at 37 °C (**A-C**) and 30 °C (**D-F**) following induction with 0.1 mM (**A/D**), 0.5 mM (**B/E**) or 1 mM (**C/E**) IPTG and left to express protein for up to 5 hours.

Next, expression of apoA-I in minimal media was investigated. Expression was induced at 37 °C with 0.5 or 1 mM IPTG. Expression was monitored overnight, in order to deduce whether leaving cells in minimal media overnight would affect the protein yield. Due to the slow growth of *E.coli* cells in labelled media, it is often common to leave expressing cells to grow overnight at reduced temperatures. **Figure 3.8** shows the expression of apoA-I is induced with both

0.5 and 1 mM IPTG, independent of the concentration. As with **Figure 3.6**, incubation for 5 hours or longer resulted in a slightly higher concentration of protein expressed. This gel also confirms that if need be, cells can be induced in minimal media overnight without effecting the protein yield, or resulting in protein fragmentation.

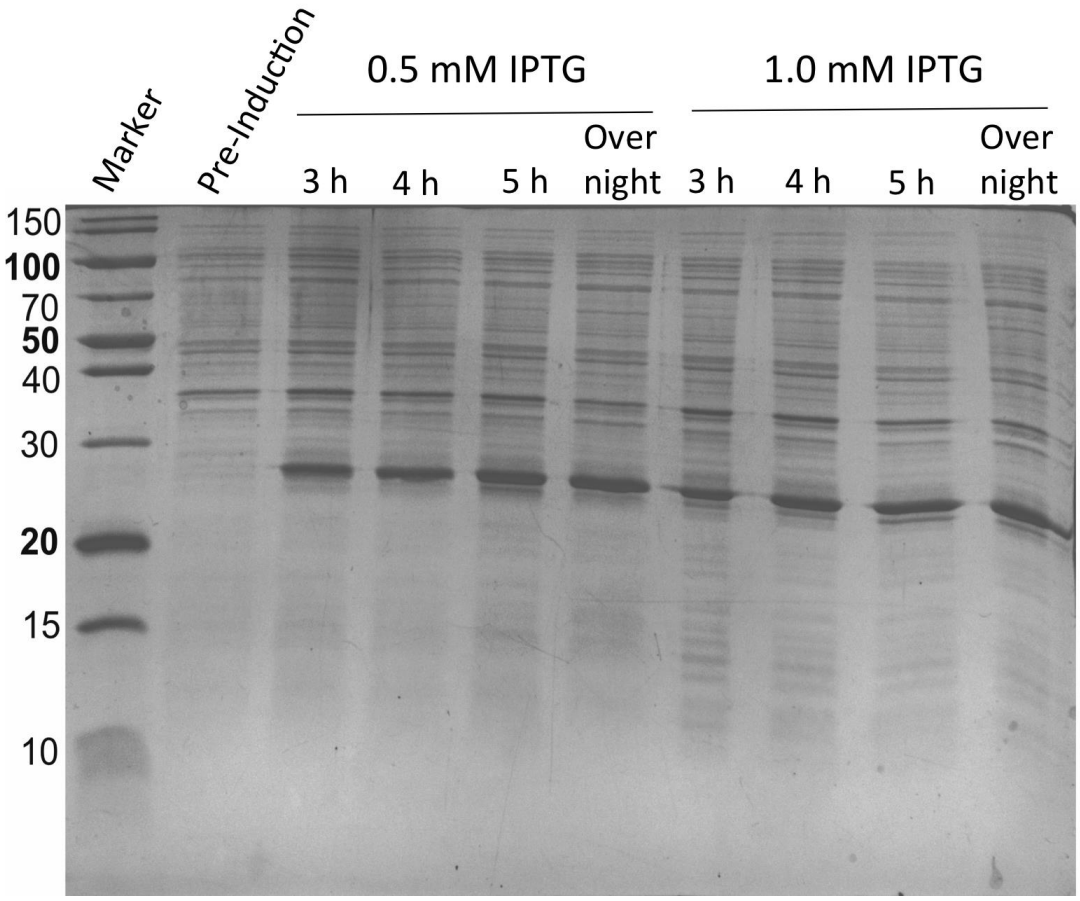

Figure 3.8 15 % SDS PAGE gel of the expression tests for apoA-I production in minimal media at 37 °C, monitored overnight following induction of protein expression with 0.5 or 1 mM IPTG.

3.3.2.2. Expression of apoA-I mutants

The methodology for the apoA-I mutant fusion peptide expression, followed that of the apoA-I E2D procedure outlined in Oda et al., (2001) and Ryan et al., (2003), with an increased induction time of 5 hours.

Upon induction with IPTG, the L90P, K96C and R173C mutants all experienced increased expression of a protein, which migrated to the expected regions on an SDS gel for the mutated apoA-I fusion peptide, (**Figure 3.9**). However, the expression level of the mutants was considerably less compared to the native protein.

No increase in expression of a protein corresponding to the apoA-I L44Stop was observed following induction (**Figure 3.9 lanes 2/3**). This could have been due to the small size of the apoA-I (1-43) fusion peptide (roughly 7,300 Da), running poorly on the 15 % gel, or a poor staining result, again due to its small size in comparison to the remainder of the proteins stained in the gel. **Figure 3.9** shows that any proteins running below 10 kDa, including the protein marker, are poorly resolved. Expression of this mutant did not go any further, due to time restraints on the project. However, if this were to continue, a full expression test would be required to determine suitable conditions for expressing short recombinant peptides, or attempt an alternative expression system.

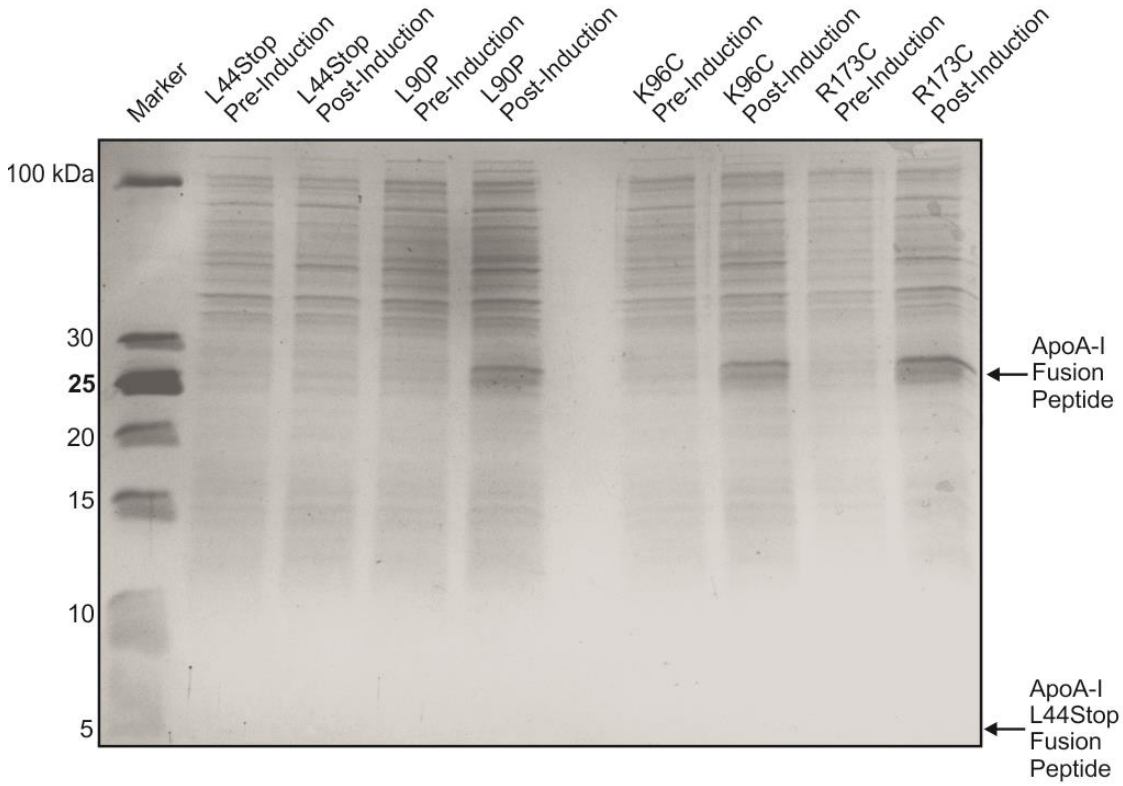

Figure 3.9 15% SDS PAGE of apoA-I L44Stop, L90P, K96C and R173C mutants prior to induction and after 5 hours incubation, following induction with 1 mM IPTG.

3.3.2.3. Immobilised metal ion affinity chromatography

Following expression, cell harvesting, lysis and the removal of cell debris, the lysis supernatant was loaded onto a hisTrap column, using an AKTA Start™ purification system. This system allows the UV monitoring of the material leaving the column at 280 nm, which is roughly proportional to the protein concentration.

After collecting the flow-through, which produced a high UV absorbance, consistent with the elution of large quantities of non-binding cellular proteins (**Figure 3.10: Flow-through**), an initial wash stage with the guanidine lysis

buffer removed a large concentration of impurities (**Figure 3.10: Wash 1**). The subsequent wash stages with sodium phosphate buffer, containing 0 %, 5 % and 10 % of a 500mM imidazole buffer (0, 25 and 55 mM, respectively), removed additional non-specific binding proteins, shown by peaks in the UV absorbance (**Figure 3.10: Wash 2, 3 and 4**).

Elution with 500 mM imidazole buffer resulted in a large spike in UV, consistent with the elution of the his-tagged apoA-I (**Figure 3.10 Elution**). This was collected in 1 mL fractions and the fractions containing the highest protein concentration were pooled. Combined fractions underwent dialysis into Tris buffer, in order to remove the imidazole.

Samples of fractions 3, 5, 10, 17 and 22 coinciding with the flow-through, wash 1, wash 2, wash 3 and wash 4, were taken and underwent ethanol precipitation to remove guanidine, prior to analysis by SDS-PAGE (**Figure 3.11**).

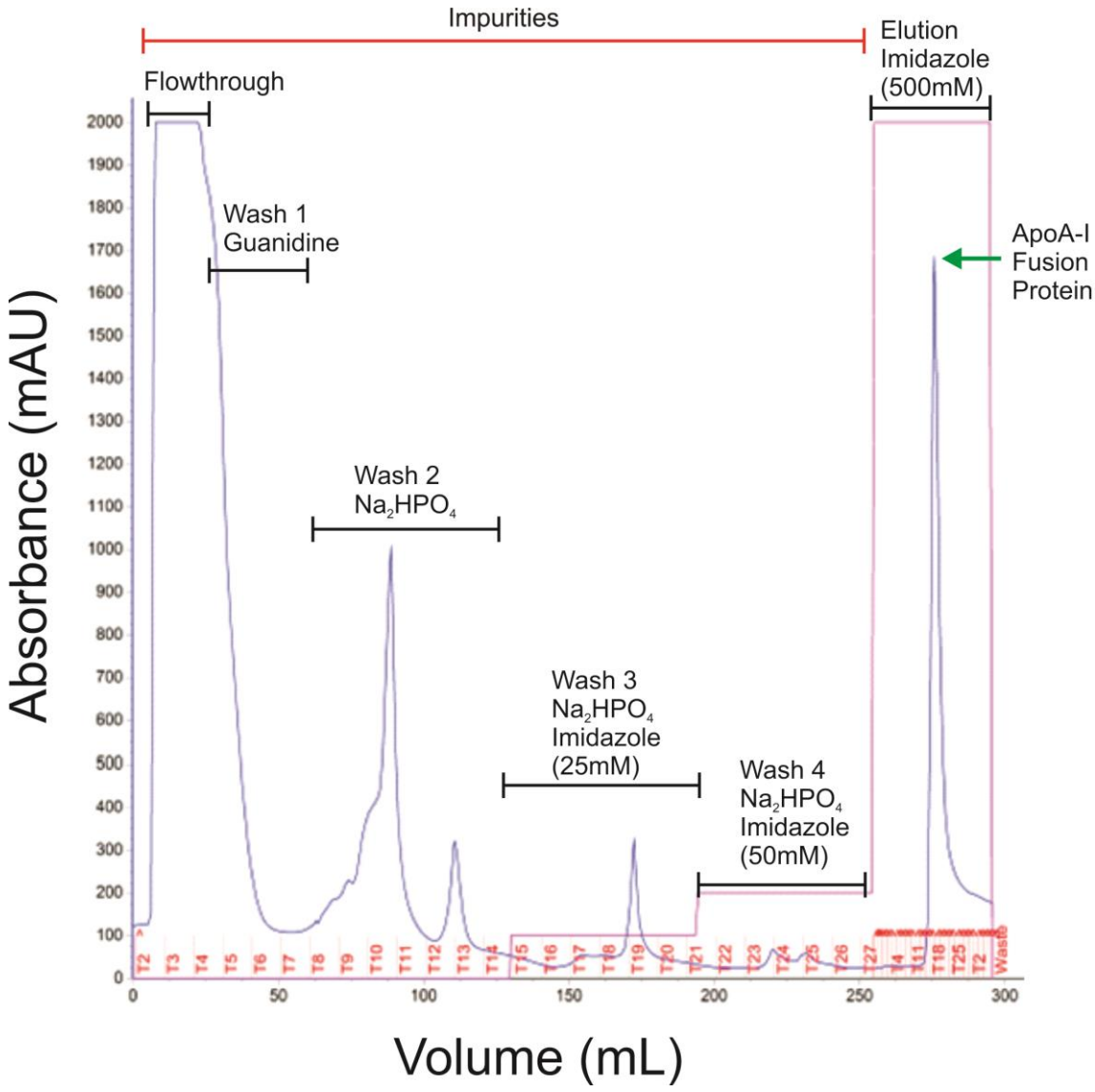

Figure 3.10 Chromatograph of the labelled apoA-I fusion peptide purification using a nickel IMAC his-trap column. The UV absorbance (blue), 500mM imidazole buffer ratio (pink), and fraction numbers (red) are included in this diagram, along with a description of each step.

Samples of the flow-through and various wash stages for the labelled apoA-I purification were run on SDS PAGE gel electrophoresis to determine what protein content was being removed from the column at each step.

Figure 3.11 indicates a high level of impurities present in the flow-through, as expected, due to the high UV absorbance seen in **Figure 3.10**. Wash 1, with guanidine, removes non-specifically binding proteins, associated with the apoA-I fusion protein, whilst wash 3 and 4, containing low concentrations of imidazole, remove proteins that are bound weakly to the column, presumably via the proteins native histidine residues. This results in a much purer elution profile.

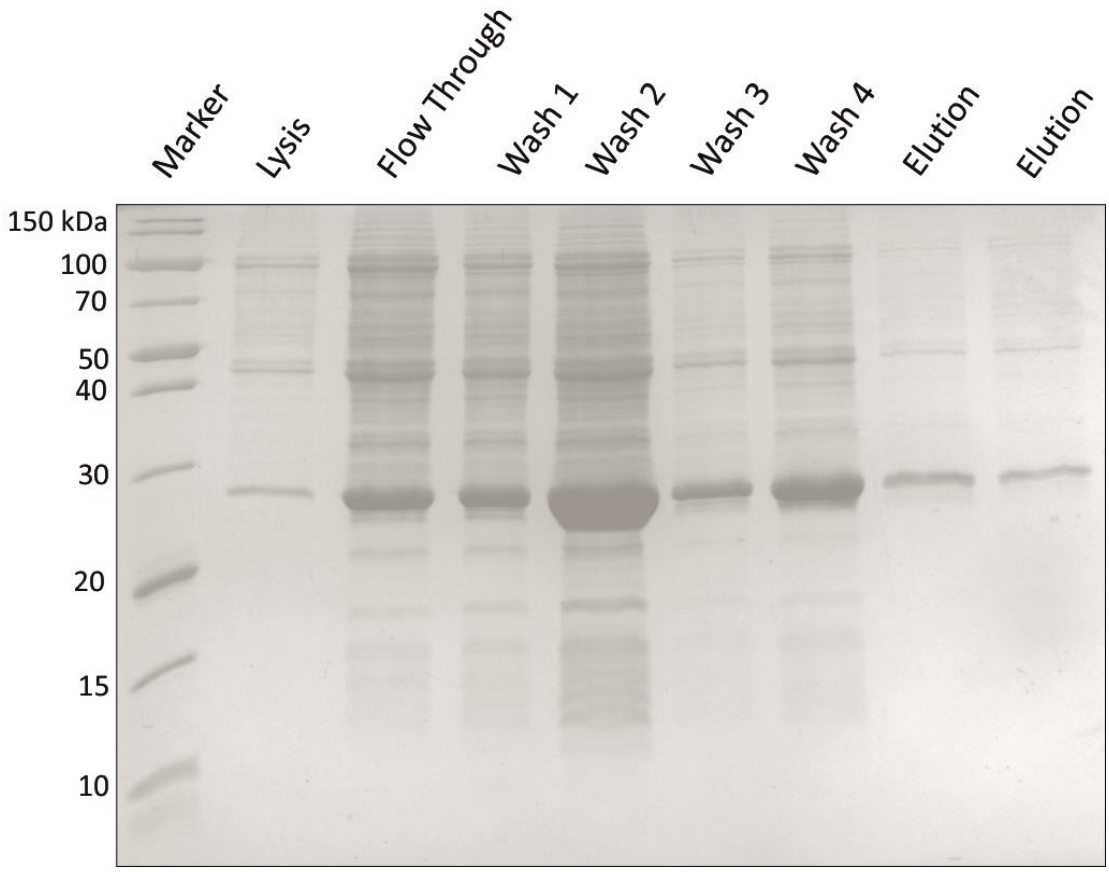

Figure 3.11 15% SDS PAGE of samples from each of the stages of the his-Trap purification of labelled apoA-I. Samples of the lysis, flow-through, wash 1, wash 2, wash 3, wash 4 and the 2 elution peaks with the highest UV absorbance were selected.

3.3.2.4. Cleavage of the fusion peptide

Following incubation with formic acid for 3 hours, gels of the cleavage products identified 2 bands in close proximity (gel not shown), similar to that shown in **Figure 3.12** for the 2.5 hour sample. These 2 species were believed to be the isolated apoA-I (2-243) product, and the fusion peptide that has not undergone cleavage of the his-tag. It was unclear at this time whether the formic acid concentration, incubation time or temperature was leading to incomplete cleavage. Initially, samples were incubated in 45 % formic acid at 55 °C overnight, with samples taken at various time points. This experiment confirmed that the length of the incubation period was the cause of the incomplete cleavge. 3 hours was shown not sufficient to cleave all of the fusion peptide. After 2.5 hours, 2 species of protein are detected, presumed to be the fusion peptide and cleaved apoA-I. However, beyond 5 hours, only a single product with the smaller molecular weight is detected without any additional protein degradation. As such, all future formic acid treatment steps were carried out for 5 hours.

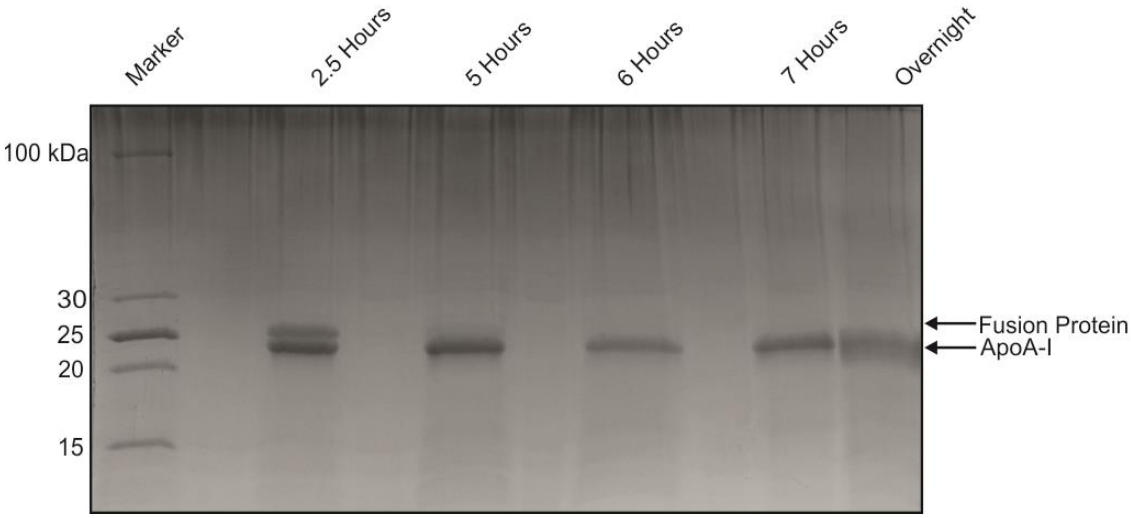

Figure 3.12 15 % SDS PAGE of samples taken at various time points, during the incubation of the apoA-I fusion peptide in 45 % formic acid.

3.3.3. ApoA-I characterisation

Incubation of proteins in 45 % formic acid leads to the cleavage of peptides following aspartic acid residues, in particular, between the aspartic acid and proline residues, introduced into the apoA-I N-terminus via the E2D mutation. This results in the release of the hexa-histidine tag connected to the linker region and the apoA-I peptide, minus the first 2 residues. The sequence apoA-I (3-243) will be referred to as apoA-I or the wild type protein for the remainder of this thesis, unless stated otherwise. All additional mutants produced, such as G26R, L44Stop, L90P, K96C and R173C all carried the same E2D mutation to promote formic acid cleavage.

3.3.3.1. SDS PAGE

SDS PAGE analysis of the purified apoA-I, labelled apoA-I, apoA-I K96C and apoA-I R173C mutants confirmed a single protein product for each mutant, which migrated to a region on the gel with a molecular weight of approximately 25 kDa (**Figure 3.13**). This is in agreement with the predicted molecular weight of 27834 Da, 27809 Da and 27781 Da for the wild type apoA-I, the K96C and R173C mutants, respectively. The gel appears to show multiple faint bands for each protein product. However, since the same occurs for the protein marker, and individual gels confirm the purity of each species, this increased bandwidth is presumed to be caused by uneven running of the gel, or poor staining.

The apoA-I L90P mutant was also run on an SDS PAGE gel as shown in **Figure 3.14**. The apoA-I (L90P) mutant produced a band in the 25 kDa region corresponding to full-length apoA-I, consistent with the predicted mass of the peptide (27817 Da). However, unlike the other mutants, apoA-I L90P also

produced two additional bands in the 15 and 10 kDa regions (**Figure 3.14**). At this point, it was noticed that the introduction of the L90P mutation produced a second Asp-Pro acid labile bond. Upon incubation with formic acid to cleave the N-terminal his-tag, an additional cleavage of the peptide between residues Asp 89 and Pro 90 would result in the production of 2 apoA-I fragments, 3-89 and 90-243, with masses of 10005 and 17847, respectively, corresponding to the 2 additional bands on the apoA-I L90P gel. Despite the interest in the N-terminal region of apoA-I, the purification of the apoA-I (3-89) peptide was not continued, due to time restraints on the project.

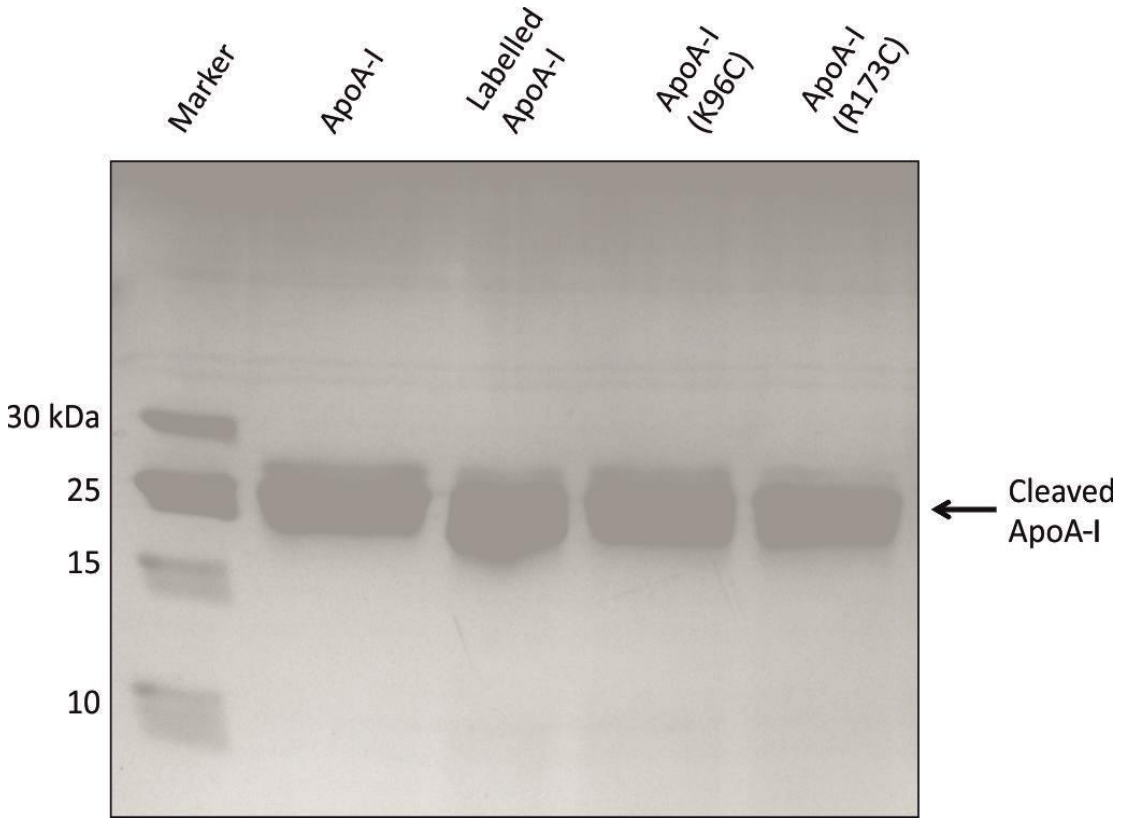

Figure 3.13 SDS PAGE analysis of apoA-I and apoA-I mutants, showing the protein purity following immobilised metal-ion chromatography and cleavage of the hexa-histidine tag with formic acid.

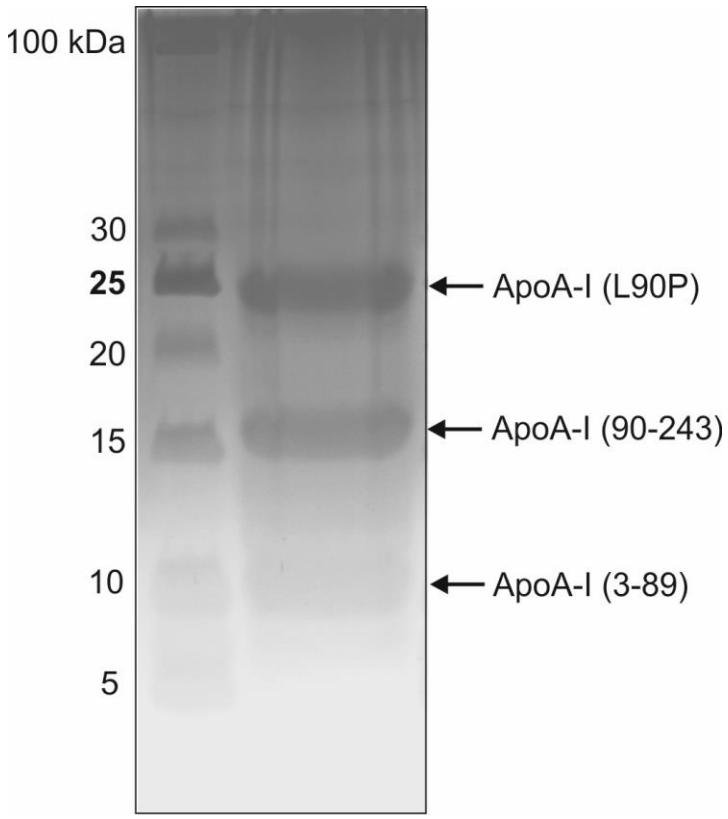

Figure 3.14 17.5 % SDS PAGE of apoA-I (L90P), highlighting the region associated with full-length apoA-I L90P, and fragments in the 15 and 10 kDa regions corresponding to apoA-I (3-89) and (90-243).

3.3.3.2. Native PAGE

Native PAGE gels of apoA-I, and the cysteine K96C and R173C mutants were run in order to determine the oligomeric state of the proteins. Native apoA-I produces a single band in the 25-30 kDa region, confirming the protein is in its monomeric state (**Figure 3.15**). Introducing a novel cysteine residue into the apoA-I sequence could lead to the formation of apoA-I disulphide-linked homo-dimers. ApoA-I K96C appears to remain monomeric, showing a similar banding pattern to wild type apoA-I. In the apoA-I R173C sample, a main band in the 25-30 kDa region is present and suggests that the majority of the protein is in the monomeric state. However, unlike the wild type and apoA-I K96C species, the

R173C mutant also produces an additional band in the 66 kDa region, which is likely caused by partial dimerisation of apoA-I (**Figure 3.15**).

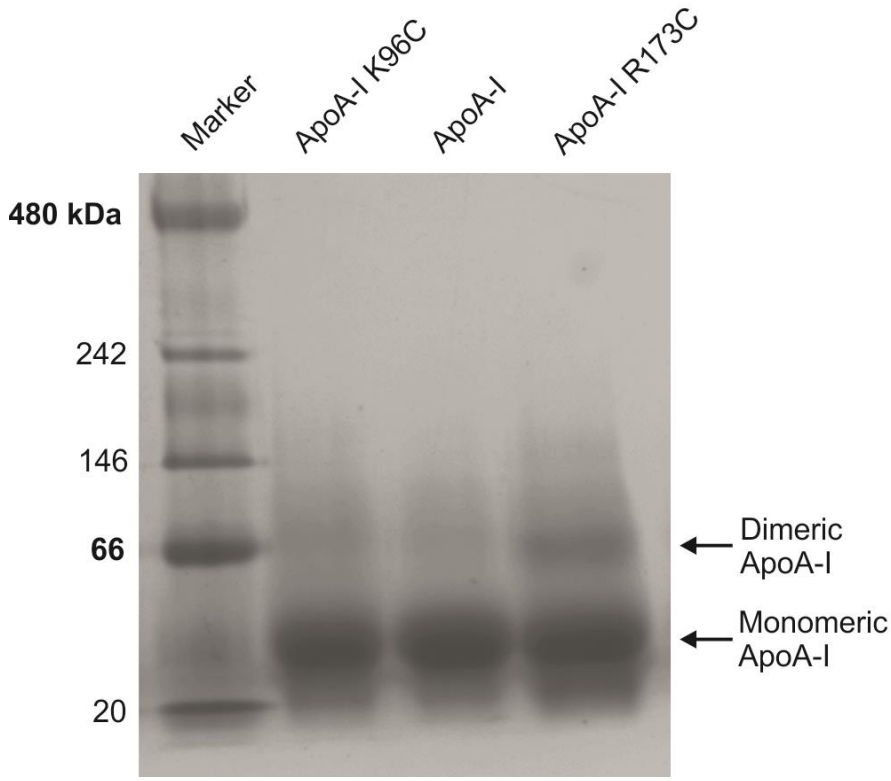

Figure 3.15 4-16 % Native PAGE gel of wild type apoA-I and the apoA-I K96C and R173C cysteine mutants.

3.3.3.3. Mass spectrometry

In order to confirm the identity of the purified product as apoA-I, samples were analysed by electrospray ionising mass spectrometry. ApoA-I (2-243) has a predicted intact mass of 27834 Da. **Figure 3.16** shows an intact peak of 27837 Da for apoA-I, in concurrence with the predicted masses and sufficient to confirm the identity of the protein as apoA-I. Despite not matching with the predicted mass exactly, it is closer than the mass published in Ryan *et al.*, (2003) of 27816 Da.

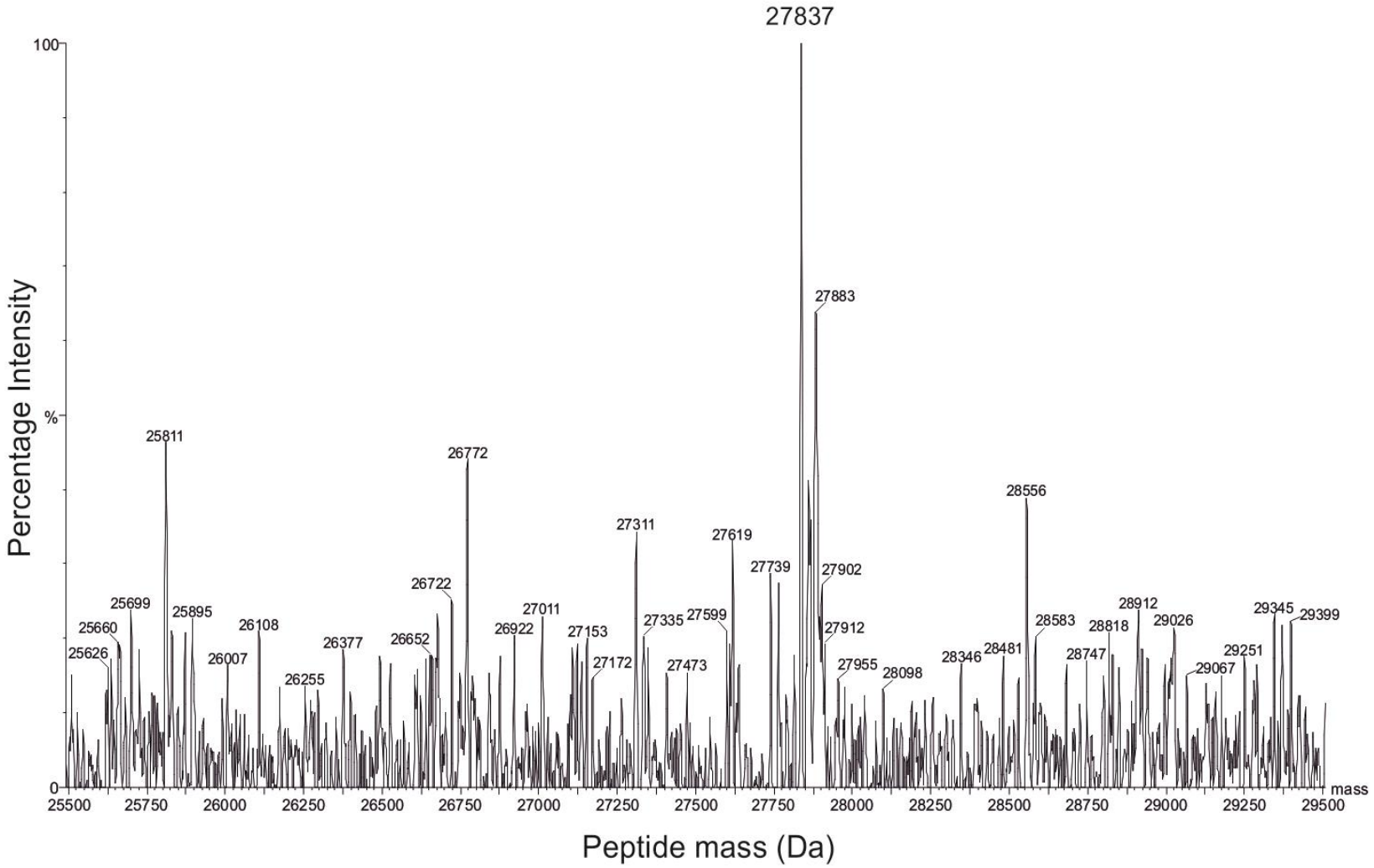

Figure 3.16 Electrospray ionisation mass spectroscopy of apoA-I, with an intact mass of 27837 Da.

Although the gene sequence of the mutant apoA-I species confirmed successful mutation, none of the mutant plasmids produced here could be expressed as proteins corresponding with the intact predicted masses, according to electrospray ionisation mass spectrometry. ApoA-I G26R has a predicted mass of 27933 Da, but the mass spectrometry detected a peak mass of 28557 Da (**Figure 3.17**). The gene sequencing for this mutant did highlight 6 codons that it could not detect as amino acids, due to missed nucleotides, 5 of which would be present in the cleaved 3-243 residue peptide. It is possible that these undistinguishable amino acids do not match up to the native sequence, and as such have resulted in a mass higher than predicted.

ApoA-I K96C peptide has a predicted mass of 27809 Da. However, the mass spectrometry detected a main peak at 27888 Da (**Figure 3.18**). ApoA-I R173C has a predicted average mass of 27781 Da, but the mass spectrometry returned a peak mass of 18207 Da (**Figure 3.19**). Despite a much lower mass than expected, there is no reason to suggest that cleavage of the apoA-I (R173C) peptide occurred. Both the K96C and R173C mutant plasmid DNA returned a gene sequence consistent with only the intended single amino acid mutation into the native apoA-I species.

ApoA-I L90P has a predicted mass of 27818 Da for the intact peptide, but as discussed in **section 3.3.3.1**, this mutation leads to the cleavage of the peptide into fragments 3-89 and 90-243. These fragments have intact masses of 10005 Da and 17847 Da, respectively. The smaller of these fragments was detected via mass spectrometry as a major peak (10005 Da), whilst only a small contribution came from a mass of 17849 Da (**Figure 3.20**). Cleavage of the apoA-I L90P would result in equal ratios of the 3-89 and 90-243 peptide present in solution.

However, despite a band appearing on the SDS gel, the low intensity of the peak corresponding to the apoA-I (90-243) peptide suggests that the majority of the peptide is no longer in solution.

3.3.3.4. Detection of labelled apoA-I.

Uniformly labelled apoA-I was produced to enable solid-state NMR analysis of the structure of apoA-I. The expression of a peptide consistent with apoA-I was successful, as shown in **Figure 3.16**, although the only way to determine the protein produced had incorporated the ^{13}C was to run a 1D spectrum of the lyophilised labelled apoA-I at pH 7. **Figure 3.21** confirms the intensity of the ^{13}C signal is sufficient to allow structural studies to be carried out, thus confirming that the expression in minimal media was successful.

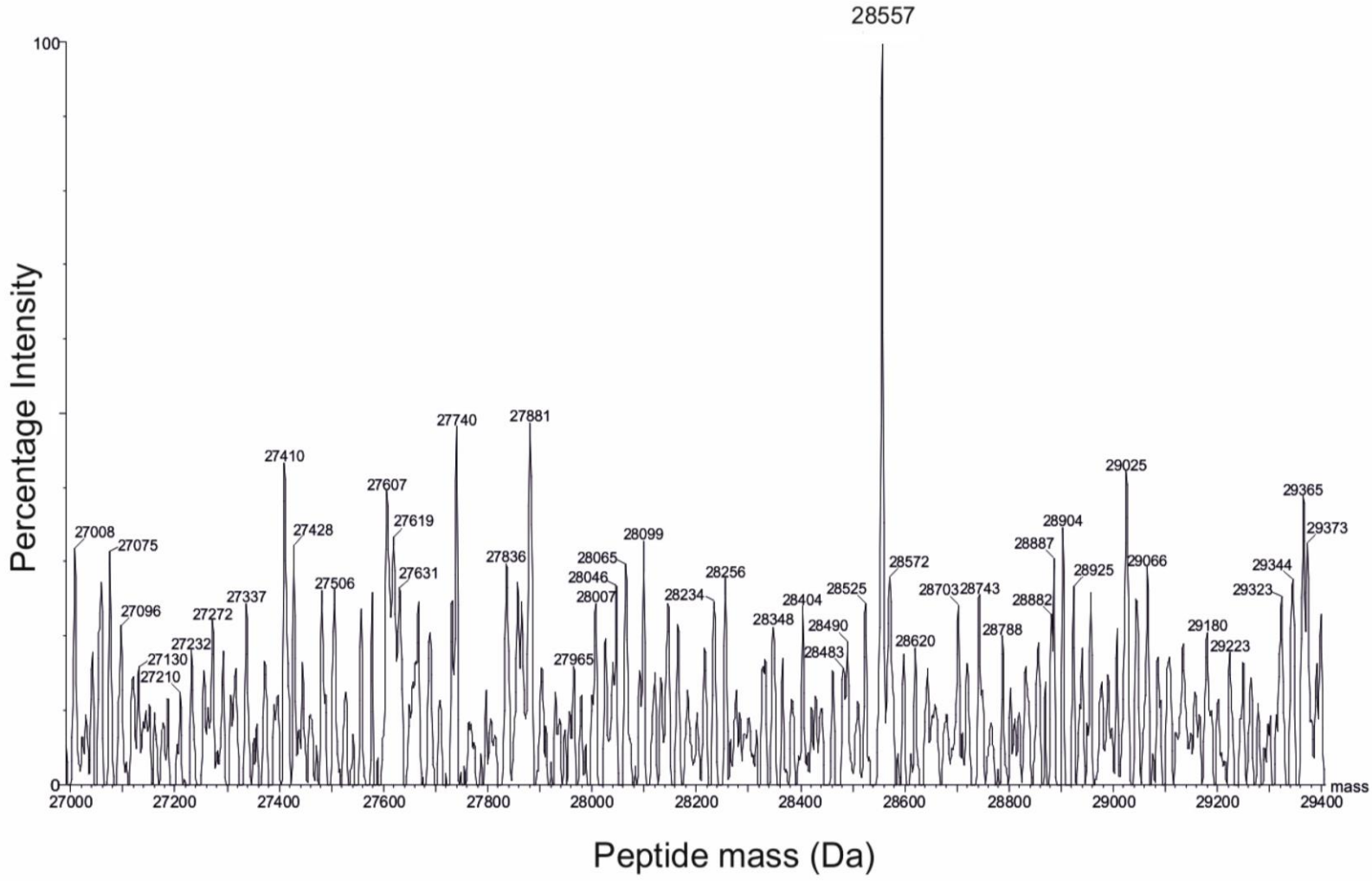

Figure 3.17 Electrospray ionisation mass spectroscopy of apoA-I G26R, with an intact mass of 28557 Da.

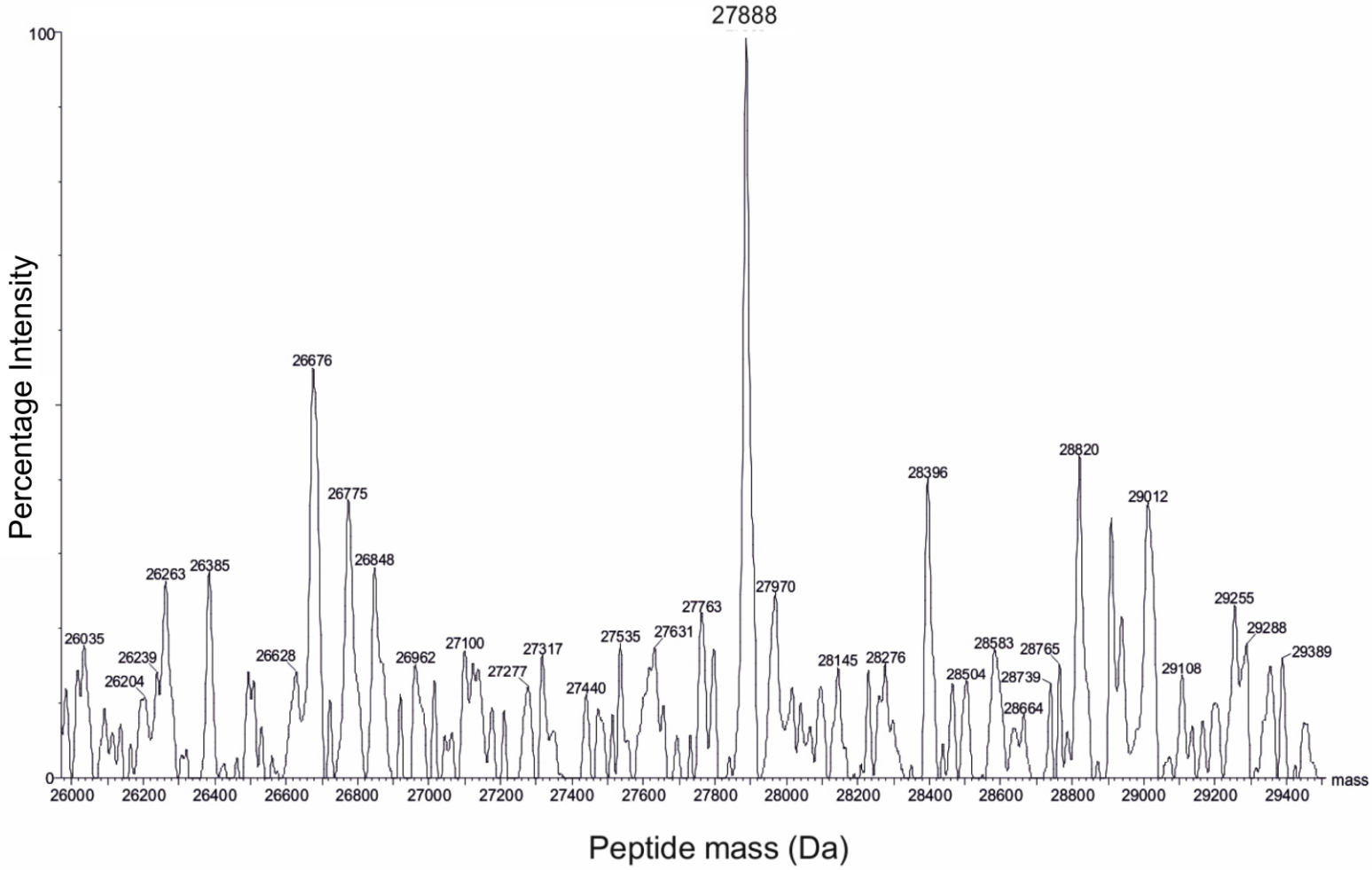

Figure 3.18 Elecrospray ionisation mass spectroscopy of apoA-I K96C, with a mass of 27888 Da

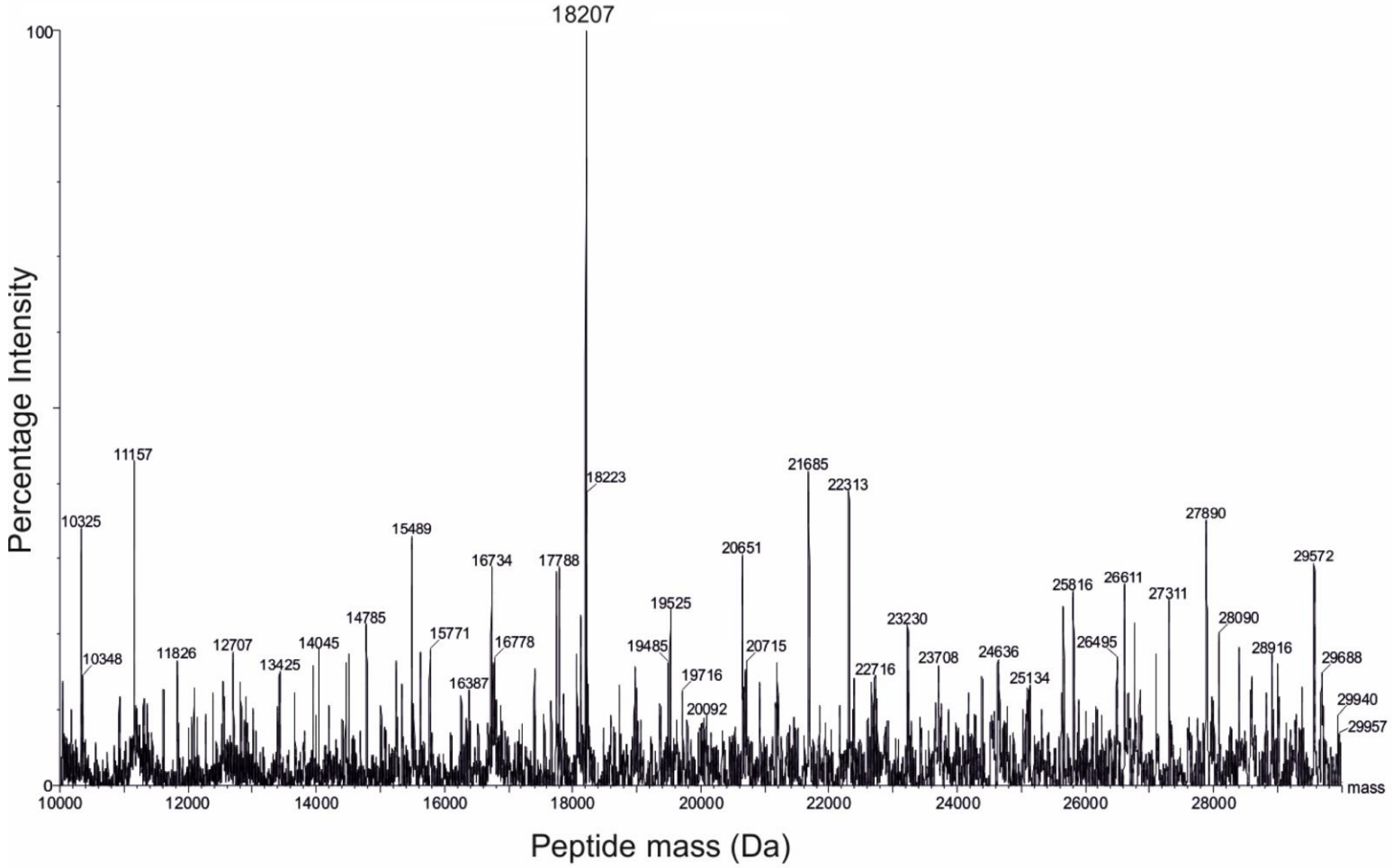

Figure 3.19 Electrospray ionisation mass spectroscopy of apoA-I R173C, with a mass of 18207 Da.

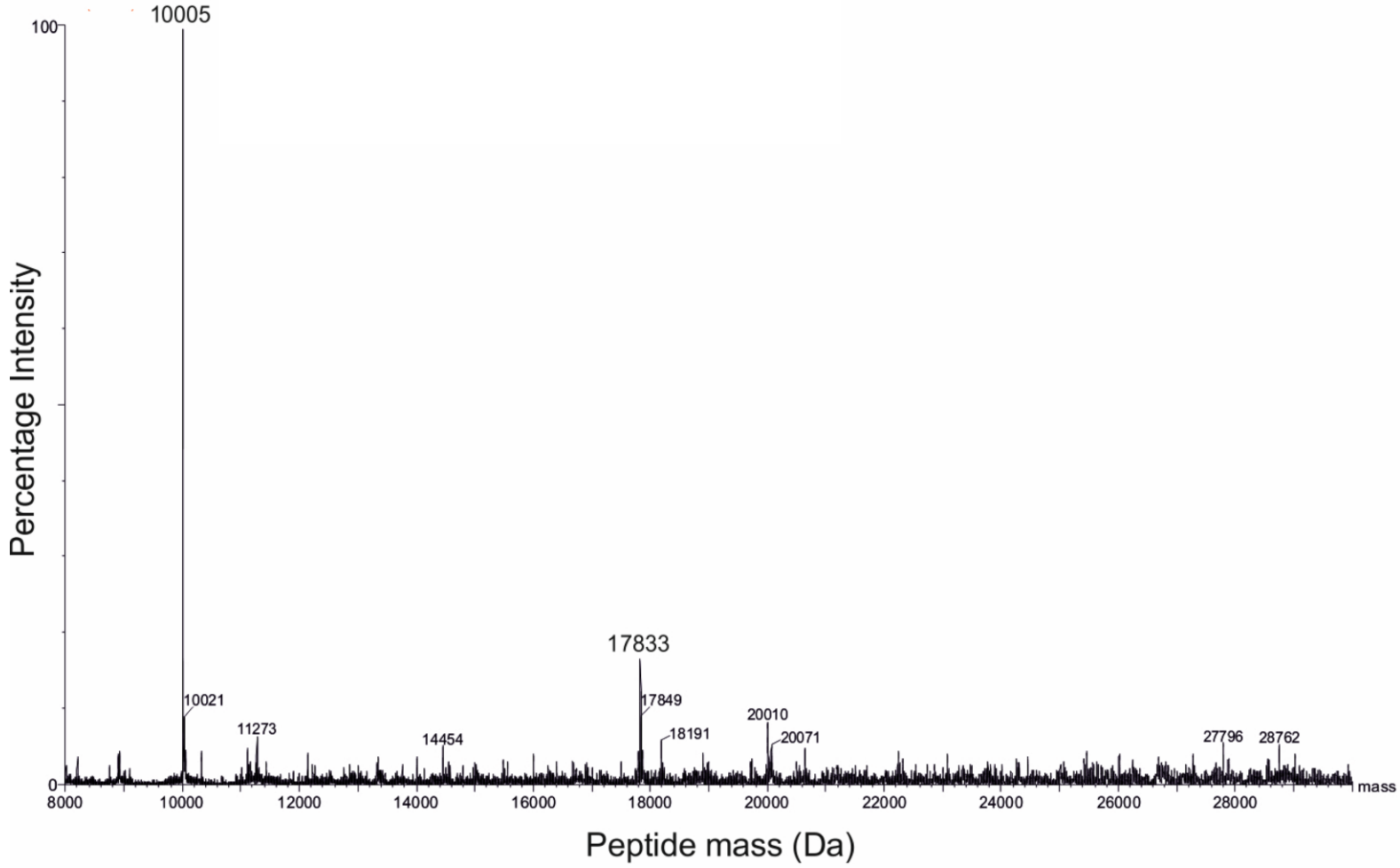

Figure 3.20 Electrospray ionisation mass spectroscopy of apoA-I L90P with a mass of 10005 Da corresponding to residues 3-89.

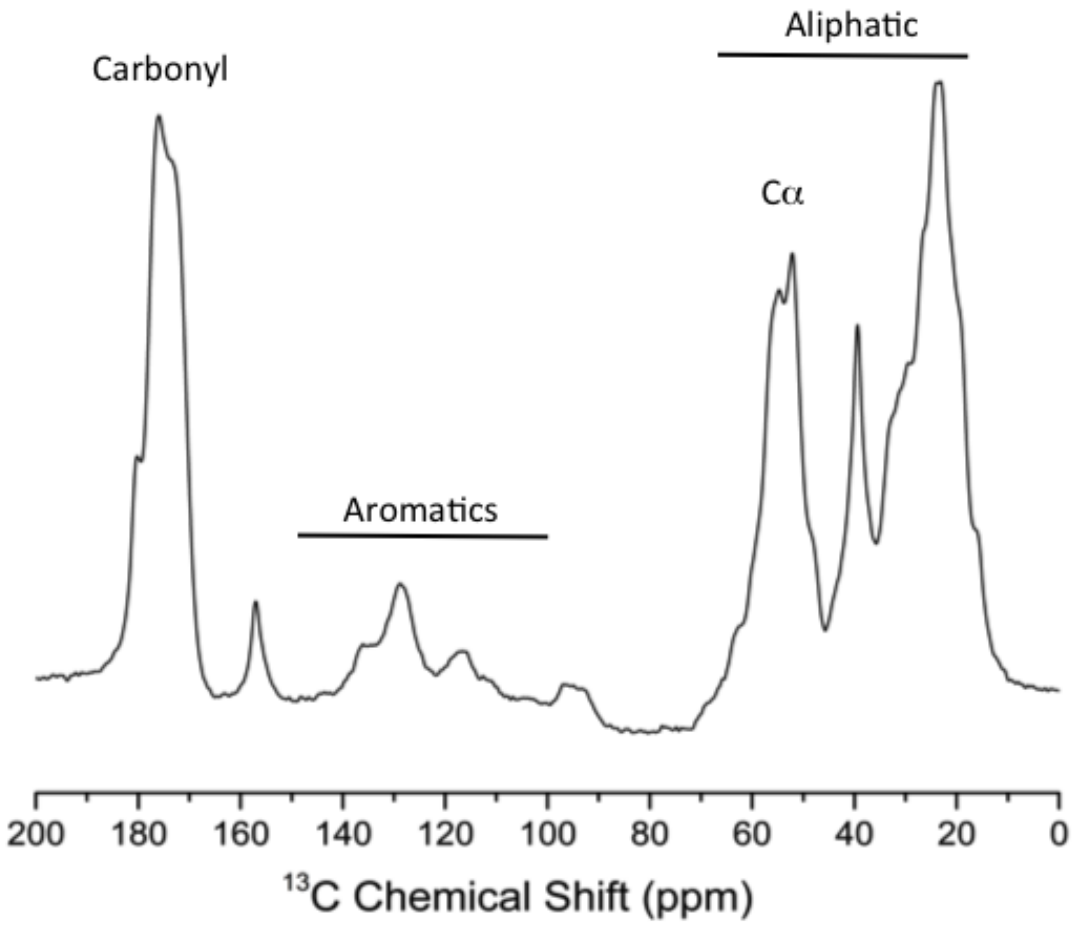

Figure 3.21 Preliminary 1D ^{13}C DP MAS spectrum of labelled apoA-I, confirming the expression of apoA-I in minimal media enriched with ^{13}C glucose produced a uniformly labelled protein.

3.4. Discussion

The research carried out in this thesis required large quantities of apoA-I in order to allow characterisation of conditions that promoted the aggregation of apoA-I into insoluble, amyloid-like aggregates. Isotopically labelled apoA-I was also required for structural studies by SSNMR. There is also evidence to suggest that chemically synthesised proteins can behave differently to those produced via recombinant expression methods, in particular in their aggregation potential (Finder et al., 2010). As such, expression of apoA-I, adapting the previously published methods of Oda *et al*., (2001) and Ryan *et al.,* (2003) was utilised and modified to allow production of ^{13}C and ^{15}N uniformly labelled apoA-I.

This chapter aimed to ensure that sufficient apoA-I could be produced via a bacterial expression system to enable large-scale production of apoA-I. **Figure 3.13** confirms the purity of the final apoA-I product that was produced with a yield of roughly 80 mg per litre of culture. This system was successfully modified to incorporate protein induction in minimal media solution, containing ^{13}C glucose and ^{15}N ammonium chloride as sole carbon and nitrogen sources. This resulted in the production of uniformly labelled ^{13}C and ^{15}N apoA-I with a yield of 22 and 29 mg per litre of culture respectively, which is suitable for NMR studies. Manipulation of the gene DNA, through SLIM PCR meant that mutant plasmids corresponding to L44Stop, L90P, K96C and R173C could be produced and used for protein expression. Despite all mutants forming plasmids with the correct amino acid sequence (**Appendix 3**), only the apoA-I G26R, L90P, K96C and R173C were expressed under the same experimental procedure as the wild type apoA-I. From those that were expressed, only the G26R, K96C and R173C mutant were able to be isolated as pure protein. The introduction of the L90P mutant

produces an Asp-Pro sequence at residues 89-90, which is acid labile. The use of formic acid cleavage, in order to cleave the apoA-I mutant protein from the bound his-tag, degrades the apoA-I L90P protein into fragments, corresponding to residues 2-89 and 90-243. These fragments were detectable in a 17.5 % SDS PAGE gel (**Figure 3.14**) and a peptide with a mass corresponding to residues 3-89 was detected in the mass spectrometry.

Despite the apoA-I G26R, K96C and R173C mutant plasmids containing the correct DNA sequence, and the expression of a protein, which migrated to the area associated with apoA-I on an SDS page gel, mass spectrometry failed to identify any of the mutant apoA-I species by their mass. The use of the apoA-I mutants in the remainder of this project was limited, with only their aggregation propensities compared to the wild type protein, and structural characterisation was not attempted, due to a lack of time.

Future work would need to focus on modifying the expression and purification procedure, in order to facilitate the production of the mutants listed. SLIM PCR successfully produced the mutant plasmids, as determined by DNA sequencing, and uptake of the plasmids into *E.Coli* cells was confirmed, via selection of colonies that were resistant to ampicillin. This implies that somewhere between the expression procedure and the final dialysis of the purified and cleaved apoA-I mutants into McIlvaine buffer, there has been an error that did not occur in expression of the wild type apoA-I and labelled apoA-I.

3.4.1. Production of N-terminal apoA-I peptides

For the N-terminal 1-43 peptide, expression of the full-length peptide with a cleavage site mutated into the sequence may be more successful than introducing

a stop codon into the apoA-I sequence. Given the serendipitous observation that the introduction of the proline residue in position 90 lead to the cleavage of the intended L90P mutant peptide into apoA-I (3- 89) and (90-243), the arginine in position 49 could be mutated into a proline residue, creating an Asp-Pro formic acid cleavage site at residues 48-49. After treatment with formic acid, a step that would still be necessary to remove the his-tag, apoA-I peptides corresponding to residues 3-48 and 49-243 would be produced. The apoA-I (3-48) peptide could then be separated from the his-tag and the remainder of the apoA-I 90-243 sequence by size exclusion chromatography, avoiding the loss of the short peptide through the dialysis membrane, which has a molecular weight cut-off of 14 kDa.

Following on from the L90P mutant, looking into the ability of the apoA-I (3-89) peptide to form amyloid and its structure upon aggregation would be interesting, given the increased propensity of the first 100 residues in the N-terminus to aggregate into amyloid species. Here is presented a method by which a peptide corresponding to the majority of the apoA-I N-terminus can easily be produced, in an expression system that can be modified to produce uniformly labelled protein. Alternatively, cleavage of the N-terminal tag could be carried out with thrombin protease, in order to avoid the addition of formic acid, since the apoA-I pNFX plasmid also contains a thrombin cleavage sequence. This would also result in the production of the entire apoA-I (1-243) peptide, rather than the 3-243 sequence.

Successful expression and purification of apoA-I facilitated the analysis of apoA-I aggregation in chapter 3, the structural studies of the amyloid-like material in chapter 4 and preliminary inhibition experiments in chapter 5.

4. Determination of the factors responsible for apoA-I aggregation

4.1. Introduction

4.1.1. ApoA-I amyloid

Current understanding of the aggregation of apoA-I into amyloid is that the protein can become deposited within human arteries as either N-terminal fragments of apoA-I, or as the full-length protein. Familial apoA-I amyloidosis is associated with N-terminal fragments of mutant apoA-I, which become deposited within major organs (Ramella et al., 2012; Das et al., 2016; Rosú et al., 2015; Sipe et al., 2014; Monti et al., 2011; Chan et al., 2015). Alternatively, acquired amyloidosis is linked to the deposition of full-length protein as amyloid within atherosclerotic plaques (Ramella et al., 2011; Chan et al., 2015; Mucchiano, Häggqvist, et al., 2001). Deposition of full-length apoA-I as insoluble aggregates reduces its ability to form functioning HDL, leading to a reduced atheroprotective function and a potential increased pathogenic fibril load (Ramella et al., 2011). Cleavage of the N-terminus of apoA-I can occur when the protein undergoes a transition from its lipid-bound to lipid-free structure (Mucchiano, Jonasson, et al., 2001), but may also occur after the deposition of full-length protein.

The presence of myeloperoxidase-oxidised lipid-free, full-length apoA-I in atherosclerotic plaques has been reported (Chan et al., 2015; Sigalov and Stern, 2001). This may be significant because oxidation of methionine residues, in particular Met-86 and Met-148, promotes the aggregation of lipid-free apoA-I into amyloid. In serum, oxidised apoA-I can account for up to 25 % of circulating apoA-I, although the extent of oxidation of each individual protein can vary from

1 to all 3 methionine residues (Wong et al., 2010). Even though oxidative cleavage of apoA-I has been reported, the chemical oxidation methods described by Chan *et al.* (2015) and Sigalov and Stern (2001) avoid oxidative cleavage.

Amyloid formation by apoA-I *in vitro* occurs under conditions that reflect environments experienced by lipid-free apoA-I at the pro-inflammatory sites of atherosclerotic plaques (Ramella et al., 2012). Such conditions include oxidation, either chemically or enzymatically (Chan et al., 2015); interaction with GAGs, in particular heparin in the circulatory system, as discussed in **section 1.1.5.1** (Ramella et al., 2012; Madine et al., 2013); and acidic pH (Ramella et al., 2011; Raimondi et al., 2011), caused by the release of arachidonic acid during platelet activation in an immune response against atherosclerotic plaques (Ross, 1999a).

The aim here is to produce a more detailed description of the factors that influence apoA-I aggregation than work previously published, and to identify suitable conditions to produce aggregates for structural analysis in **Chapter 5**. Here follows a brief description of the techniques used in this study, also summarised in **Table 4.1** for each of the amyloid structures.

Table 4.1 Analytical techniques used to study amyloid proteins (Li et al., 2009).

<table>
<tr><th></th><th>Native Monomer</th><th>Small Oligomers</th><th>Intermediate Protofibril</th><th>Amyloid Fibril</th></tr>
<tr><td>Atomic Structure</td><td colspan="2">Solution-state NMR</td><td></td><td>Solid-state NMR</td></tr>
<tr><td rowspan="3">Secondary Structure</td><td colspan="3">Circular Dichroism</td><td>Thin Film CD</td></tr>
<tr><td></td><td></td><td colspan="2">X-ray Fibre Diffraction</td></tr>
<tr><td></td><td></td><td colspan="2">Thioflavin T Assay</td></tr>
<tr><td rowspan="3">Fibril Morphology</td><td></td><td colspan="3">Transmission Electron Microscopy</td></tr>
<tr><td></td><td colspan="3">Atomic Force Microscopy</td></tr>
<tr><td colspan="3">Intrinsic Fluorescence</td><td></td></tr>
<tr><td rowspan="3">Assembly Size</td><td colspan="2">Gel electrophoresis</td><td></td><td></td></tr>
<tr><td colspan="3">Dynamic Light Scattering</td><td></td></tr>
<tr><td colspan="2">Mass spectrometry</td><td></td><td></td></tr>
</table>

4.1.2. Biophysical Techniques

4.1.2.1. Thioflavin T

A technique widely used to study the aggregation of proteins into amyloid species *in vitro* is Thioflavin T (ThT) fluorescence. ThT is a benzothiazole salt dye that selectively stains amyloid fibrils, due to its high affinity binding to cross-β strand ladders, the solvent exposed grooves between parallel β-sheet structures (Biancalana and Koide, 2010; Coelho-Cerqueira et al., 2014; Nelson et al., 2005). The restricted oscillations of the benzothiazole and aminobenzoyl rings, upon binding to consecutive β-strands, causes rotation of the bond outlined in **Figure 4.1** (Girych et al., 2014; Chan et al., 2015). This causes a red shift in the fluorescent properties of the molecule with increased emission at 482 nm, when excited at 450 nm (Wolfe et al., 2010; LeVine, 1999; Girych et al., 2014). This allows quantification of the extent of amyloid formation, and measurement of aggregation kinetics.

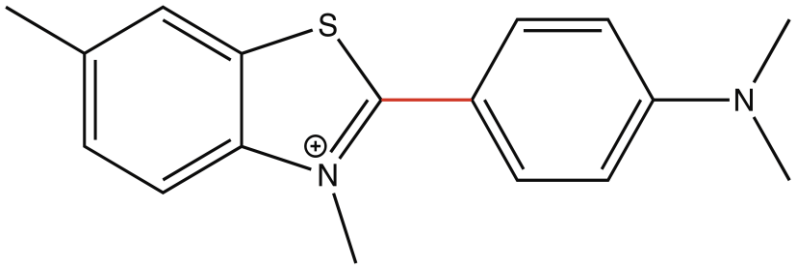

Figure 4.1 Chemical structure of Thioflavin T, highlighting the bond that rotates upon binding to β-sheet structures (red), causing a red shift in the compound's fluorescent properties, with enhanced emission at 482nm when excited at 450nm.

Figure 4.2 gives a typical ThT fluorescence curve in the presence of amyloid forming peptides, derived from incubation of ThT with the amyloidogenic N-terminal apoA-I G26R mutant (Girych et al., 2014). This curve shows the main stages in the nucleation-dependent polymerisation mechanism, which is common among most amyloid species. The process shown below does not include any secondary nucleation stages, which would produce an additional increase, similar to the elongation phase (Cohen et al., 2013).

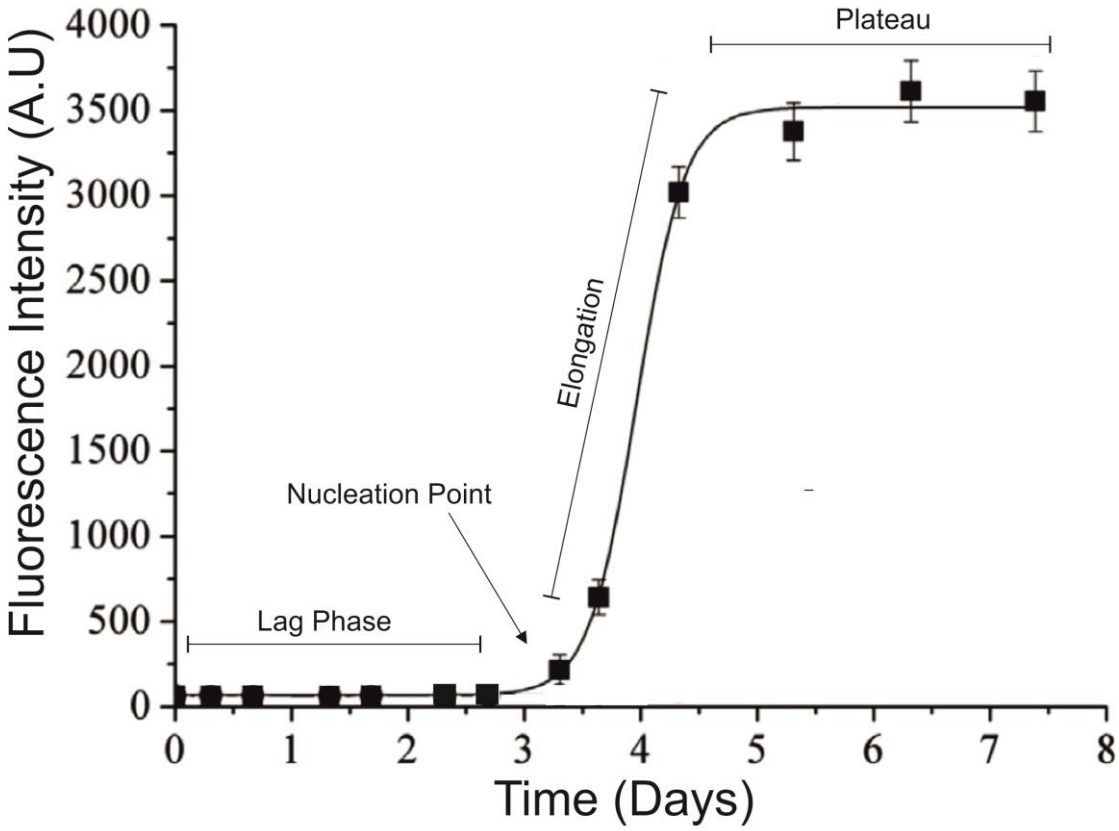

Figure 4.2 ThT fluorescence increase upon incubation with amyloidogenic apoA-I 1-83 (G26R) at 0.9 μM. Image modified from Girych (2014) to highlight the nucleation-dependent growth mechanism.

Using ThT does have its disadvantages, including its reduced binding to β-sheets at acidic pH (Li et al., 2009) and the ability to promote the aggregation of amyloid species, as shown for α-synuclein (Coelho-Cerqueira et al., 2014). As such, studies of apoA-I incubated in the presence of ThT, allowing real-time changes in the ThT fluorescence to be monitored, may not be reliable and should be complemented with single point measurements. In single point experiments ThT is added after the aggregation end point, so as not to interfere with the aggregation process. Doing so will also allow assays with longer incubation periods to be measured, as real-time measurements are limited to approximately 6-7 hours at 37 °C, before solvent evaporation affects the fluorescence signal.

4.1.2.2. Congo red

Congo red is a dye which selectively binds to the β-sheets of amyloid species (Puchtler et al., 1962) with high affinity. The exact interaction between Congo red and amyloid is currently unknown. Nevertheless, it is assumed that the dye binds to the cross-β structures, similar to how ThT interacts with amyloid. Upon binding to amyloid, Congo red's absorbance spectrum changes, with a shift in the maximum absorbance from 490 nm to 540 nm, causing the amyloid species to be stained red when visualised under a microscope. This can be measured both qualitatively, for determining the presence of amyloid in tissue samples; and quantitatively, in order to determine the amount of amyloid formed using *in vitro* experiments (Klunk et al., 1999b; Li et al., 2009). Upon cross-polarisation of microscope lenses, the Congo red stained amyloid exhibits a green birefringence, an example of which is shown in **Figure 4.3**.

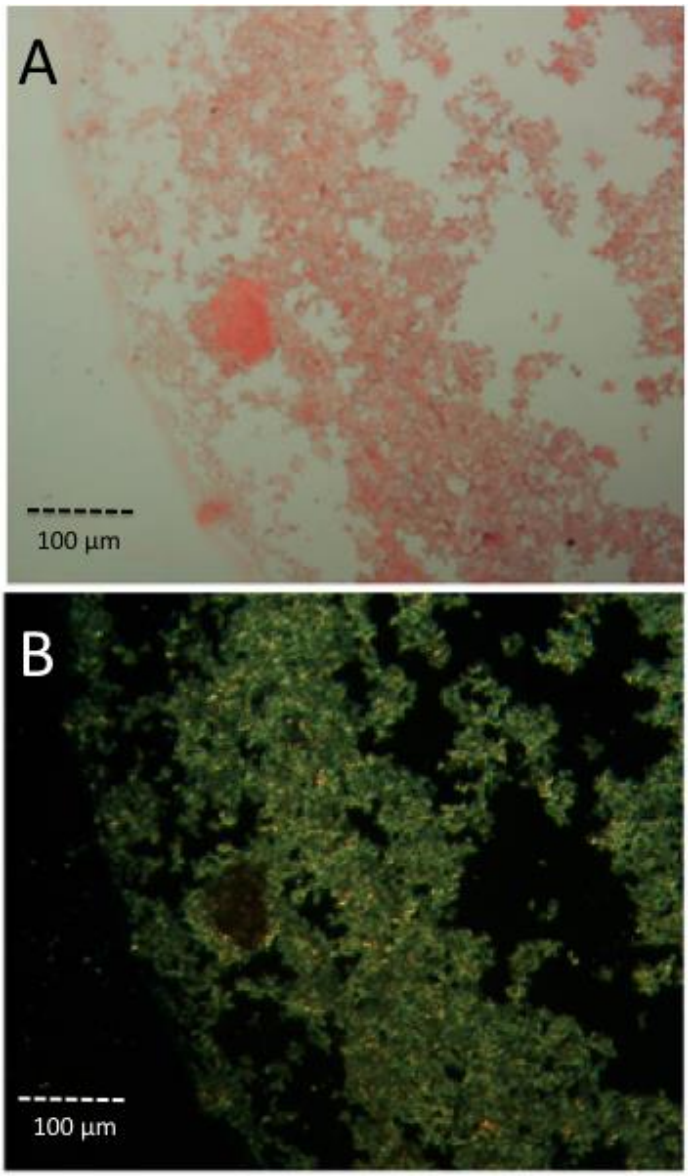

Figure 4.3 Methionine oxidized apoA-I aggregates stained with congo red and visualised with an uncrossed polariser (A) and after crossing by 90 ° Image taken from Wong et al., (Wong et al., 2010)wong.

4.1.2.3. Intrinsic Fluorescence

Intrinsic fluorescence of specific amino acids within a protein, namely tryptophan, phenylalanine, and tyrosine, have been used to determine whether or not a change in the environment of these residues occurs during self-assembly of the peptide (Vivian and Callis, 2001; Andrews and Forster, 1972).

Internalisation of residues to a less polar environment within the β-sheet structures of amyloid can give rise to a blue shift in the spectrum, whereas the inverse results in a red shift. Fluorescence excitation of tryptophan residues at 280 nm gives rise to emission maximum at around 355 and 335 nm for solvent exposed and hydrophobic environments, respectively (Das et al., 2016; Touchette et al., 2010). The location of tryptophan residues, in close proximity to either acidic or basic residues, can also alter the maximum emission wavelength. An acidic residue near the pyrrole end or a basic residue near the benzene end of tryptophan will result in a red shift of the fluorescence spectrum, with the inverse configuration producing a blue shift (Vivian and Callis, 2001). Acidic and basic residues surrounding tryptophan residues can also result in the quenching of fluorescence signals.

4.1.2.4. Morphology of amyloid

Amyloid fibrils have a highly characteristic morphology on the nano-scale, consisting of networks of long un-branched fibrils, roughly 10 nm in diameter (Serpell, 2000; Serpell, Sunde, et al., 2000), described in detail in **section 1.4.1.** TEM is the most commonly used microscopic technique for studying the morphology of amyloid fibrils and intermediate oligomeric species. In addition, AFM is unique in its ability to detect and measure dimensions of substrates adsorbed onto mica surfaces. By detecting how far the cantilever deflects as it is traced across the surface, the height of the sample from the mica surface can be measured, and the topography determined (Harper, Wong, et al., 1997). A combination of these techniques can be used to determine the morphology of insoluble protein aggregates, including their length, width and height.

4.1.2.5. X-ray diffraction

X-ray diffraction patterns can be used to study the secondary structural content of amyloid deposits, without the requirement for high-quality crystal structures that can make x-ray crystallography difficult. All X-ray diffraction patterns of amyloid contain broad reflections at roughly 10 Å for the equatorial region and 5 Å for the meridional reflections. These values are characteristic of the spacing between the β-sheet layers (**Figure 1.11B**) and individual β-sheet motifs (**Figure 1.11A**), respectively, as discussed in **Section 1.4.3** and shown in **Figure 1.10**. These values can vary, depending on the protein sequence, due to the side chain interactions (Jahn et al., 2010; Li et al., 2009), but are present in all amyloid species.

4.1.3. Aims

The main aim of this chapter of research was to establish suitable conditions for promoting the aggregation of apoA-I into amyloid species, focusing on the effects of pH, heparin, and methionine oxidation.

Previous reports have observed that acidification of full-length apoA-I induces amyloid formation, which is enhanced in the presence of heparin, as well as noting the aggregation-inducing effects of methionine oxidation on apoA-I. Here, these conditions are examined in further detail, with the aim to determine whether any differences can be detected between the aggregates formed in the absence and presence of heparin. Upon confirmation of amyloid formation under these conditions, it will be essential to confirm that scaling up of the amyloid formation can be achieved, allowing structural studies using circular dichroism and solid-state NMR.

4.2. Methods

Unless otherwise stated, all samples are solubilised in a phosphate/citrate (McIlvaine) buffer, containing 165 mM Na_2HPO_4 and 17.6 mM citrate and adjusted to the correct pH, using concentrated HCl (37%) or 5M NaOH, giving a buffer range of pH 2.2 to pH 8.0 (McIlvaine, 1921). This buffer was used by Ramella (2011) in the study of apoA-I across a pH range of 4 to 8. This work showed that, when apoA-I was incubated in McIlvaine buffer at neutral pH, the protein was stable and avoided aggregation. However, at acidic conditions, in particular pH 4, the protein readily aggregated into insoluble material (Ramella et al., 2011). Throughout this thesis, apoA-I was routinely assayed at 36 μM, equivalent to 1.0 mg/ml, whenever possible. Lower concentrations of apoA-I were used in some of the ThT experiments, in order to reduce the quantity of protein required.

4.2.1. Quantification of protein solubility

ApoA-I at 1 mg/ml (36 μM) was incubated in the absence and presence of a 2-fold molar excess (72 μM) of heparin (14-15 kDa, Iduron), over a range of pH 4 to pH 8, at 37 °C for 3 days. Samples were then centrifuged at 13,400 rpm in a bench top centrifuge and the supernatant removed. The soluble protein concentration of the supernatant was measured in triplicate on a Thermo Scientific Nanodrop 2000, which takes absorbance measurements at 260 nm (RNA contribution) and 280 nm (protein contribution). These measurements were then used to calculate the percentage of starting material that had converted to insoluble aggregates and been removed by sedimentation.

4.2.2. Thioflavin T fluorescence

For all assays, the fluorescence of ThT (Sigma-Aldrich) was measured using a Flexstation 3 Microplate Reader (Molecular Devices Ltd.) in a 96-well clear-bottomed, black-walled microplate (Nunc), with the fluorescence read from below the plate, taking an average of 6 reads. ThT was excited at 450 nm and the emission signal recorded at 482 nm (Wolfe et al., 2010). The assay was conducted at 37 °C with agitation of the sample, regardless of whether it was a continual read or end-point measurement (see below).

Continual read experiments were carried out on apoA-I, in the presence of ThT at all times. Fluorescence measurements were taken from triplicate samples of 20 μM ThT incubated with apoA-I at 7.2 μM every 30 s for 10 minutes prior to a change of conditions (see results section for specific details on each experiment). Measurements were then taken every 30 seconds for 10 hours, or until evaporation occurred. All experiments were carried out at 37 °C, with agitation of the plate for the duration of the experiment.

In end-point experiments, 1 mL of apoA-I (36 μM) was incubated in sealed eppendorf tubes at 37 °C with agitation for 3 days, in the absence of ThT. After this time, 196 μL of the sample was removed and added to 4 μL of ThT (1 mM stock in McIlvaine buffer), to give a final ThT concentration of 20 μM, and total fluorescence was measured from triplicate samples and recorded as the total fluorescence (F_T). The remaining ThT-free sample was centrifuged and the supernatant removed. Protein concentration of the supernatant was measured, according to **Section 4.2.1,** and 196 μL was added to 4 μL (20 μM final concentration) ThT. Fluorescence measurements were taken in triplicate and recorded as the supernatant fluorescence (F_S).

The above procedure was adapted to examine apoA-I under various conditions. These included determining the effects of pH over a range of pH 4 – 8, determining the effects of apoA-I concentration, the role of heparin, oxidation of apoA-I methionine residues, and mutations in the apoA-I sequence. The protein concentration used, the measurement type (continual or end point), and the change of conditions administered during the continual read experiments will be described in the results section.

4.2.3. ApoA-I methionine oxidation

Approximately 25 % of circulating apoA-I contains at least one of its three native methionine residues oxidised, as a result of myeloperoxidase induced oxidation, or interacting with oxidised lipids (Wong et al., 2010). Oxidative modifications to apoA-I have been shown to induce amyloid formation. ApoA-I was dialysed into 10 mM NaH_2PO_4 pH 7.5 overnight, before incubation with H_2O_2 (1000 fold molar excess), overnight, at 37 °C. The sample was then dialysed back into 10 mM NaH_2PO_4 at pH 7.5 twice, in order to remove any excess hydrogen peroxide.

4.2.4. Congo red

ApoA-I at 18 μM was incubated at pH 4 and pH 7 alone and in the presence of 36 μM heparin (14-15 kDa, Iduron), for 3 days with agitation at 37 °C. Samples were mixed with 90 μM Congo red dye and left for 24 hours at room temperature. Single drops were placed onto glass slides and allowed to dry at room temperature, before viewing with a Zeiss axioscope A1 microscope in transmission mode, with 10x objective lens and polarised lenses at 0 ° for the uncrossed measurements, and 90 ° for the crossed measurements.

4.2.5. Intrinsic fluorescence of tryptophan residues

Wild type apoA-I contains 4 tryptophan residues at positions 8, 50, 72 and 108. ApoA-I (18 μM) at pH 4 and pH 7, in the absence and presence of heparin (36 μM), and oxidised apoA-I (18 μM) at pH 7.5 and pH 6 (10mM Na_2HP04), were incubated at 37 °C, with agitation. Fluorescence spectra from 300 to 400 nm were collected on a Cary Eclipse spectrometer, with excitation at 279 nm and a band pass of 1 nm, immediately and 1 hour after preparation of the samples.

4.2.6. Transmission electron microscopy

ApoA-I (36 μM) at pH 4 and pH 5, in the absence and presence of heparin (72 μM); oxidised apoA-I (36 μM) at pH 6, and apoA-I (46-59) at pH 4, were incubated at 37 °C, with agitation for 3 days. Samples were centrifuged and the pellets washed several times with distilled water to remove buffer salts. Pellets were then diluted to 18 μM, before 10 μL was loaded onto carbon-coated copper grids and left for 2 minutes. Excess sample was removed by blotting. The grid was then stained by inverting it onto a droplet of 0.2 % uranyl acetate. After 30 seconds of staining, the grids were blotted and left to dry for 1 hour. The sample was then visualised on a Tecnai 10 electron microscope at 100 kV.

4.2.7. Atomic force microscopy

ApoA-I (36 μM) at pH 4, in the absence and presence of heparin (72 μM), was incubated at 37 °C, with agitation for 3 days. Samples were diluted to 18 μM and loaded onto freshly cleaved mica, prepared through the removal of a single layer of tape from the mica surface. The sample was left to adhere to the membrane overnight, followed by washing with distilled water to remove any buffer salts.

AFM was performed with a Keysight Technologies (Santa Rosa, Ca, USA) 5500 series instrument fitted with a 90x90 μm scanner. All images were acquired in acoustic alternating contact (AAC or "tapping") mode, using etched silicon probes (PPP-NCL, Keysight), with nominal fundamental resonance frequencies of 190 kHz. These 225 μm long cantilevers have a nominal force constant (k) of 48 N/m, a top height of 10-15 nm, and a tip radius of <10 nm. PicoView (V1.2, Keysight) was used to control the AFM and capture the images. Height (topographic), amplitude, and phase shift images were recorded simultaneously over an area of 0.5 x 0.5 μm, at a frequency of 160 kHz, a scan rate of 0.5 lines/sec, and a setpoint (Asp) of 2.2 V. Analysis of images was performed using Gwyddian V2.44.

4.2.8. X-ray diffraction

ApoA-I (36 μM) at pH 4, both in the presence and absence of heparin (72 μM), was incubated at 37 °C, with agitation for several days. The fibrils were pelleted through centrifugation at 5,000 rpm into a glass capillary using a bench top centrifuge. The sample was irradiated, using a Cu-Kα radiation (1.54 Å wavelength), and images were collected using a charged coupled device (CCD) detector (Atlas-S2). Using CrysAlis software, plots of intensity against 2θ were taken from the image and d spacings were calculated using Bragg's law (**Equation 4.1**). The order (n) is set to 1, and wavelength (λ) set to 1.54 Å for this experiment.

$$n\lambda = 2dsin\theta \qquad [4.1]$$

4.3. Results

As highlighted previously, the main aim of this chapter was to determine suitable conditions, in the context of the pro-inflammatory environment of atherosclerosis, for promoting the aggregation of apoA-I into amyloid, allowing structural studies. The effects of each factor are described below.

4.3.1. Effect of pH on apoA-I aggregation

ApoA-I at 36 μM was incubated for 3 days, over a range of pH conditions. During this time, a white precipitate formed in the acidic samples, which was removed through centrifugation. The concentration of the remaining soluble protein was then measured, in order to quantify the amount of protein that had converted into insoluble material. Previous studies reported that acidic environments promote the aggregation of soluble apoA-I into insoluble material (Ramella et al., 2012). Here, at neutral and mildly basic pH conditions (pH 8) the percentage of protein that had converted to insoluble material remained negligible. This percentage increased to roughly 35 % at pH 6, and was considerably higher in the extreme acidic conditions, with 80 and 95 % of material converting into insoluble material at pH 5 and pH 4, respectively (**Figure 4.4A**).

It was next investigated whether the insoluble aggregates produced at acidic pH were typical of amyloid species. This was initially done using the amyloid specific binding characteristics of the ThT dye. At neutral and mildly basic pH conditions, the total fluorescence of the ThT (F_T in **Figure 4.4B**), after 3 days incubation, was consistent with ThT and buffer control samples, and showed no significant increase in fluorescence intensity. This indicates that no amyloid-like material is formed at neutral and basic pH.

Experiments also determined that incubation of ThT across the entire pH range 4-8 did not induce a change in the control ThT fluorescence (F_C). This confirms that any difference in the ThT fluorescence intensity is caused by aggregation of the protein, not protonation of the ThT compound. Previous work by Hackl et al., (2015) and Sabatè et al., (2008) identified a decrease in fluorescence intensity when ThT was incubated below pH 3 and above pH 8. In the pH range studied here (pH 4-8) the molecule is predicted to be in its mono-ionised form, allowing comparative study (Sabaté et al., 2008).

However, when incubated in acidic conditions, the total fluorescence (F_T) increased for all 3 pH conditions, with enhanced intensity at pH 4 and pH 5, compared to pH 6.

After centrifugation and removal of any insoluble material, the ThT fluorescence of the supernatant (F_S) at all 5 pH conditions are equal, and have similar intensities to the control samples. This suggests the absence of any amyloid-like material remaining in the supernatant.

This implies that the insoluble material that is formed at low pH, which is removed through centrifugation, gives rise to the ThT response observed during incubation at acidic pH. This is characteristic of amyloid, and infers that the majority of the amyloid-like species, which bind to the ThT, are confined within the insoluble material.

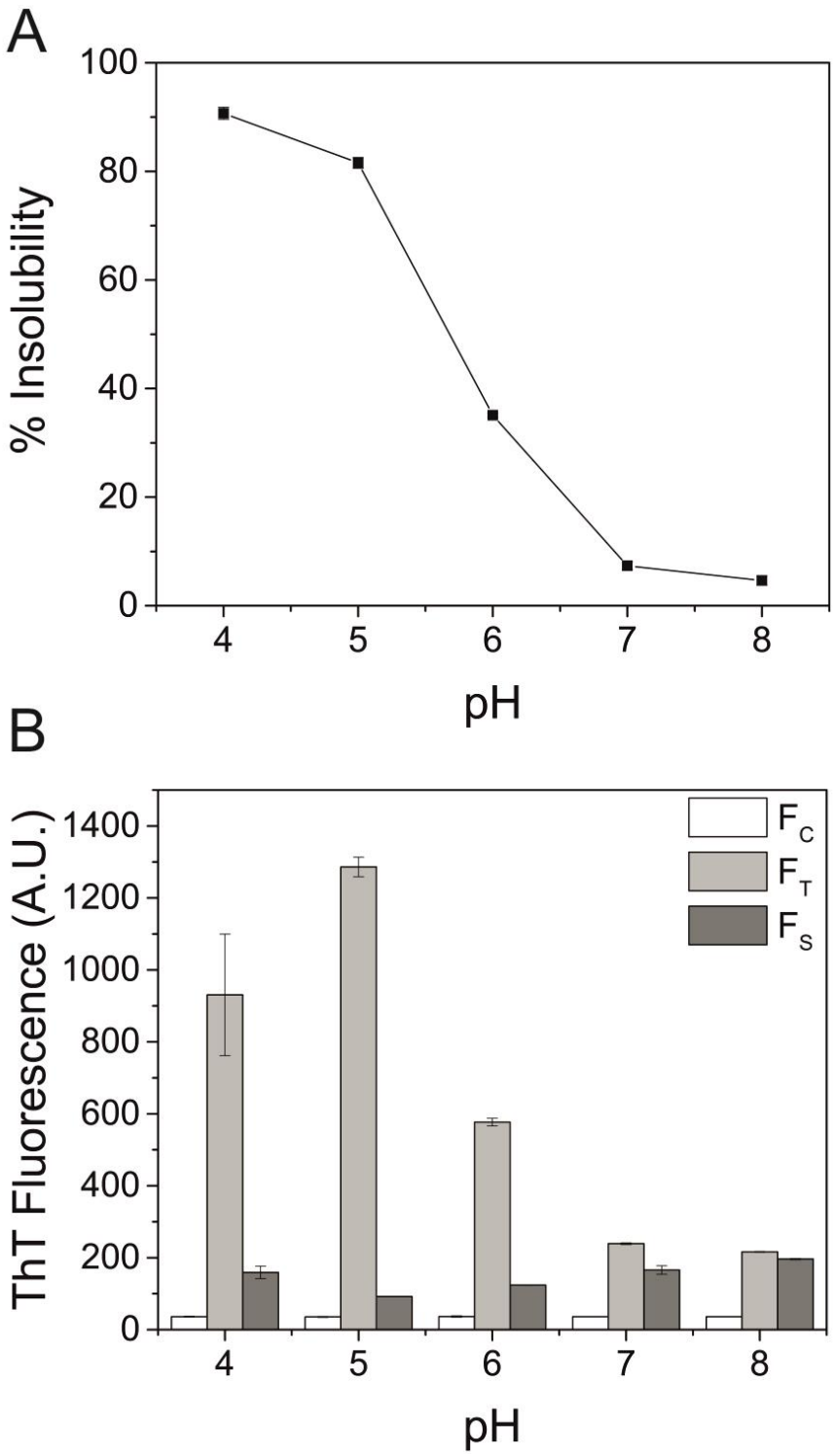

Figure 4.4 (**A**) Percentage of apoA-I that is converted into insoluble material across a range of pH conditions. (**B**) ThT fluorescence of apoA-I (36 μM) after 3 days' incubation at a range of pH conditions, showing the ThT controls at each pH condition (F_C) total increase (F_T) and remaining fluorescence after centrifugation (F_S). Data shown is the mean of 3 samples with ± standard error.

4.3.2. Measuring the time course of aggregation

ThT fluorescence was used to monitor the kinetics of apoA-I aggregation in real time. ApoA-I at 36 μM (1 mg/ml) was incubated at neutral pH for 10 minutes, prior to the addition of a sufficient volume of concentrated HCl to acidify the samples to pH 4. This was confirmed using a narrow Mettler Toledo pH probe.

Previous work suggests that heparin enhances the propensity for apoA-I to aggregate at acidic conditions (Ramella et al., 2011). **Figure 4.5** shows the ThT fluorescence of apoA-I, in the absence and presence of 2-fold molar excess of heparin, following the addition of HCl. Fluorescence at pH 7, before acidification, remained at the baseline level, consistent with the absence of amyloid-like species. This remained the case for the pH 7 sample throughout the experiment.

However, following acidification to pH 4, an instantaneous increase in ThT fluorescence intensity is observed, both in the absence and presence of heparin. This initial ThT intensity will be referred to as F_I. The rapid increase in ThT fluorescence at pH 4 was observed within the time taken to add the HCl to the sample, mix it thoroughly, return the plate to the plate reader, and take the next measurement. The ThT fluorescence continues to increase after this initial jump in fluorescence until it reaches a plateau, referred to here as the total fluorescence intensity (F_T).

Due to the rapid increase in ThT fluorescence upon acidification of apoA-I, parameters that are commonly used to compare aggregation kinetics, such as rate and lag time, were unable to be calculated. As such, the total ThT fluorescence after the intensity leveled off (F_T) and the initial ThT fluorescence (F_I), were the two main parameters used to compare ThT fluorescence in the continual read experiments.

ApoA-I at pH 7 has an F_I intensity consistent with the buffer and ThT controls, and a similarly low F_T value, consistent with the absence of any amyloid-like species. However, acidification of apoA-I to pH 4 causes an increase in both F_I and F_T fluorescence, the intensity of which is dramatically enhanced in the presence of heparin. The effects of heparin will be studied in more detail later in this chapter. Controls of ThT and heparin alone did not show any increase in fluorescence upon acidification (**Figure 4.5B**).

Previous studies of amyloid have shown that agitation of the peptide during fibril formation can significantly increase the rate of fibril formation, by reducing the lag time (Nielsen et al., 2001). This occurs because mechanical agitation promotes the fragmentation of the peptide, leading to an increased number of fibril-free ends, each of which can promote fibril extension, via a secondary nucleation mechanism (Xue et al., 2008). Here, apoA-I was agitated throughout the incubation period for all experimental procedures. It was not possible to thoroughly mix the samples with the concentrated HCl, without agitating the peptide. Since the aggregation of apoA-I was so rapid, by the time the mixing of HCl into the solution had ceased, insoluble material had already begun to appear in the sample. Therefore, it was decided agitation was to continue, in order to produce homogenous aggregates. With the high levels of precipitate formed during the incubation (>90 %), agitation also facilitated mixing of the sample during incubation, rather than letting the insoluble material sediment out of solution. This could have inhibited the interaction of the insoluble fibril with soluble, monomeric species, thus halting elongation.

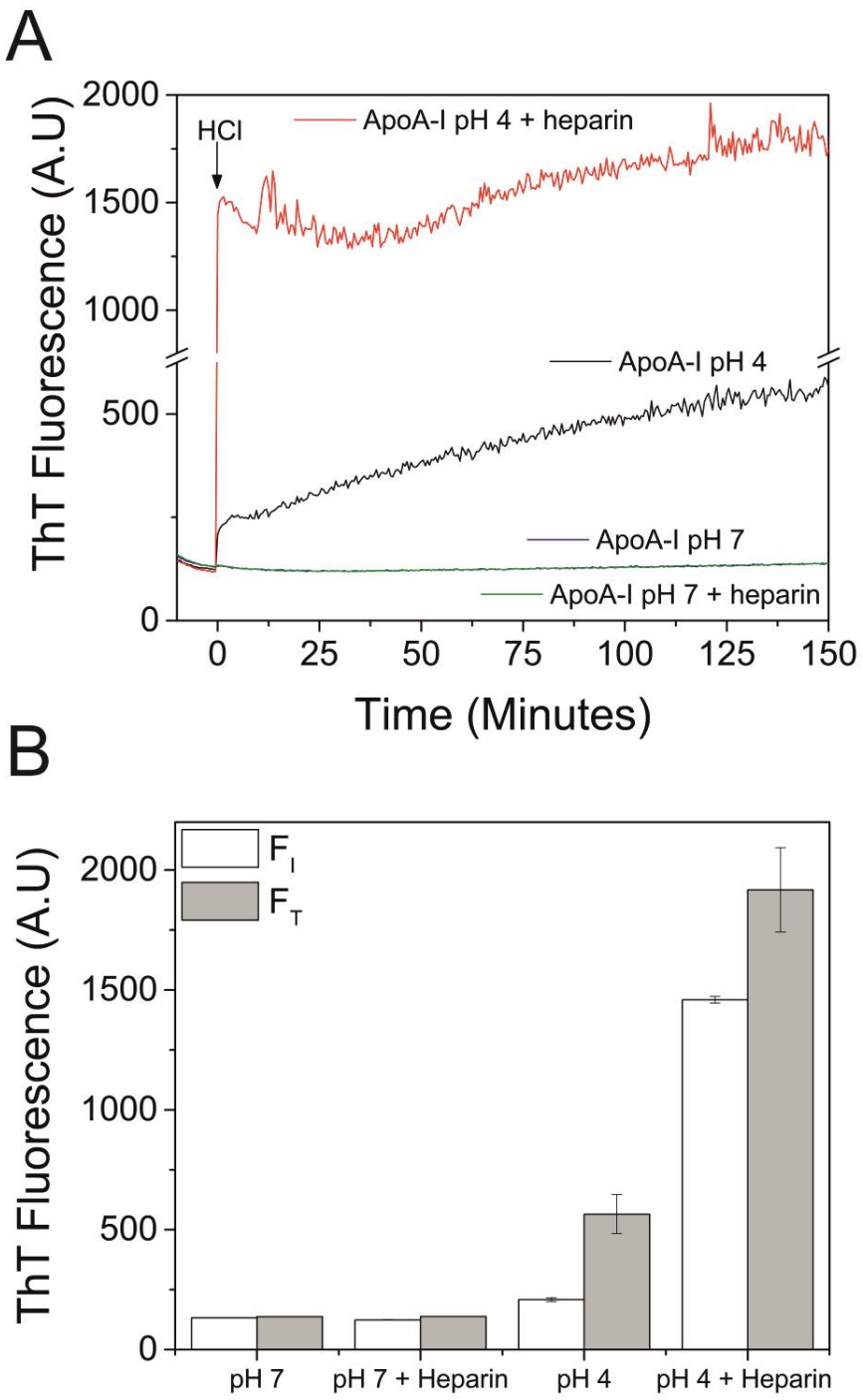

Figure 4.5 (**A**) ThT fluorescence of apoA-I (36 μM) in the absence and presence of heparin at pH 7, and at acidic pH following the addition of concentrated HCl (arrow points to the time point when HCl was added) (**B**) F_I and F_T values for apoA-I at pH 7 and 4, in the absence and presence of heparin. Data shown is the mean of 3 samples, with ± standard error bars shown in Figure **B**.

4.3.3. Effects of heparin on apoA-I aggregation

As described in **section 1.1.5.1**, GAGs, in particular heparin, have been shown to influence the aggregation and deposition of amyloidogenic proteins *in vitro*, and are commonly found co-localised with amyloid deposits (Cohlberg et al., 2002). GAGs have been shown to enhance the rate of amyloid formation in amyloid-associated proteins, as well as induce the formation of amyloid in proteins with no natural propensity to aggregate (Madine et al., 2013). The percentage sedimentation and end-point ThT experiments, described in **Figure 4.4,** were repeated with the inclusion of 15 kDa heparin at a 2-fold molar excess to the apoA-I (36 μM).

The presence of heparin has no significant effect on the amount of insoluble material produced after 3 days, over the entire pH range of 4 to 8, compared to the protein alone (**Figure 4.6A**). At neutral and basic pH, the percentage of insoluble material formed remains negligible, as was the case for apoA-I incubated alone. At pH 6, approximately 35 % of protein is converted to insoluble material, whilst at more acidic conditions this percentage increases to roughly 80 and 95 % for pH 5 and pH 4, respectively. These percentages are similar to those in **Figure 4.4,** when apoA-I was incubated alone.

Conversely, ThT fluorescence was dramatically enhanced at acidic pH in the presence of heparin, compared to the protein alone (**Figure 4.6B**). At neutral and basic pH, the ThT fluorescence produced after 3 days' incubation was consistent with control samples, showing no increase in ThT fluorescence intensity (F_T) and suggesting that no amyloid-like material was formed. This is the same as when apoA-I was incubated in the absence of heparin under the

same conditions. Upon centrifugation, no change in fluorescence intensity was observed (F_S).

However, after incubation for 3 days in acidic conditions, the 3 acidic samples, pH 6, pH 5 and pH 4, all showed an increase in ThT fluorescence. Furthermore, this increase in intensity was greatly enhanced by the presence of heparin, as shown by comparing the F_T values in **Figures 4.6B**. Similar to the samples of apoA-I without heparin, pH 4 and pH 5 produced a much higher F_T intensity than the pH 6 sample. Upon centrifugation and removal of the insoluble material, the F_S values at acidic conditions were reduced to the level associated with no amyloid formation.

This confirms, as with the un-heparinated samples, that the insoluble material that is formed from the incubation of apoA-I in the presence of heparin at acidic conditions is the source of the ThT fluorescence. Therefore, this also confirms that the majority of the amyloid-like species are confined to the insoluble aggregates.

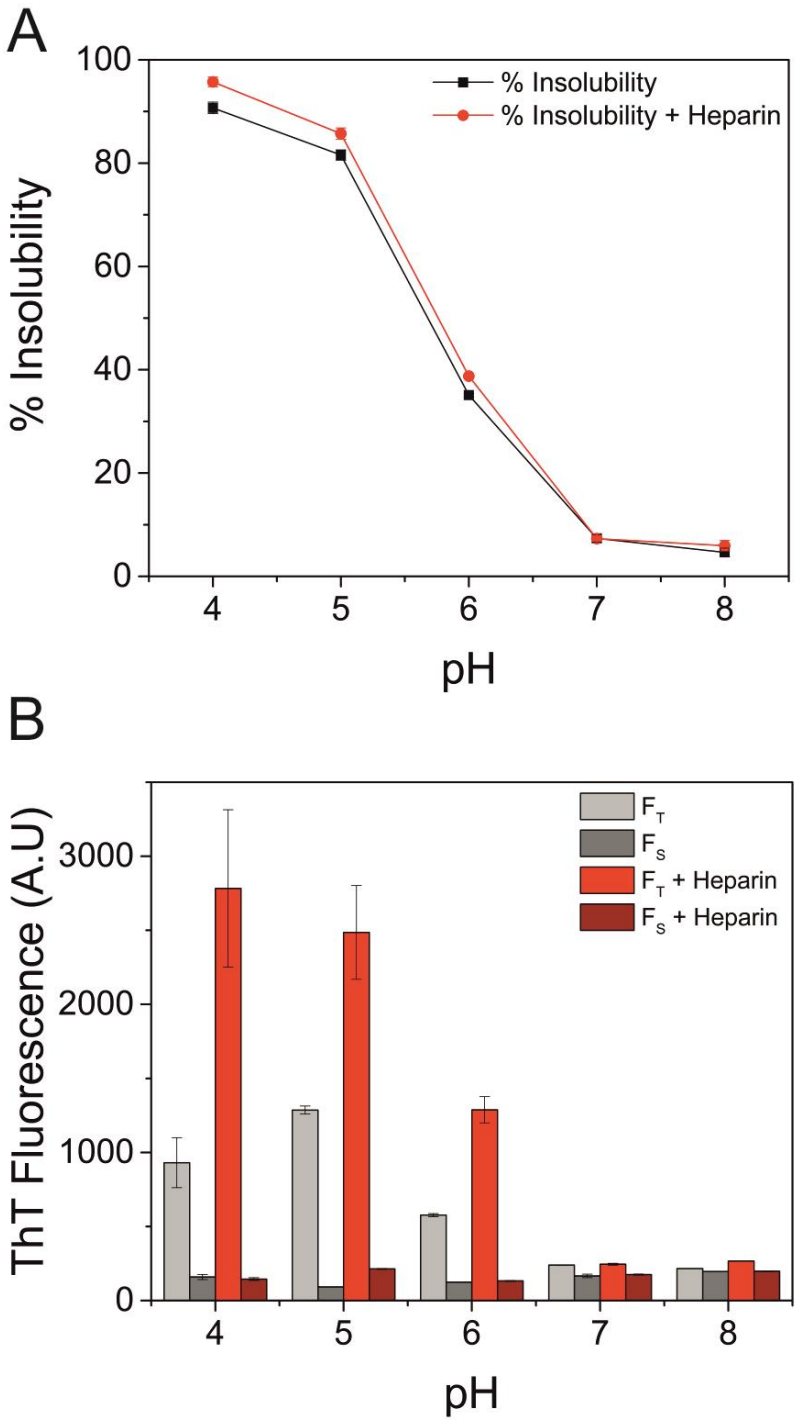

Figure 4.6 (**A**) Percentage of apoA-I that is converted into insoluble material across a range of pH conditions, in the absence and presence of 2-fold molar excess of heparin. (**B**) ThT fluorescence of apoA-I (36 μM) after 3 days incubation in the absence and presence of heparin (72 μM), at a range of pH conditions, showing the total (F_T) and remaining fluorescence after centrifugation (F_S). Data shown is the mean of 3 samples with ± standard error bars.

In order to quantify the effect heparin has on the ability for apoA-I to form amyloid-like insoluble material, apoA-I at 7.2 μM (0.2 mg/ml) was incubated with increasing concentrations of heparin, in molar ratios of apoA-I to heparin of 1:0.25, 1:0.5, 1:1, 1:2 and 1:5. After incubation at pH 7 for 10 minutes, concentrated HCl was added to reduce the sample to pH 4.

Upon addition of HCl, an instantaneous increase in ThT fluorescence was observed for all heparin concentrations (**Figure 4.7A**). The intensity of this initial jump in ThT fluorescence (F_I) was dependent on the concentration of heparin, with higher concentrations resulting in a larger F_I values (**Figure 4.7B**). Following the initial increase, the ThT fluorescence intensity continued to rise at a roughly equal rate, regardless of heparin concentration (**Figure 4.7C**), resulting in a final F_T value that appeared dependent on the F_I intensity, and thus, the heparin concentration. The ThT response of the control sample of apoA-I alone at pH 4 is negligible, due to the low protein concentration used in the experiment.

In Tris buffer, apoA-I remained soluble at pH 4 and aggregation into insoluble material only occurred in the presence of heparin. **Figure 4.8A** shows the ThT response of apoA-I incubated in Tris buffer at pH 4, in the absence of heparin for 10 minutes, and then upon addition of increasing concentrations of heparin. In the absence of heparin there was no increase in ThT fluorescence over the course of the incubation. However, upon addition of heparin, an instant increase in ThT was observed for all heparin concentrations. The F_I intensity was dependent on the concentration of heparin, as observed previously in **Figure 4.7B**. Again, following the initial increase the ThT intensity continued to increase at a similar rate (**Figure 4.8C**), independent of heparin concentration, until the total fluorescence (F_T) was reached.

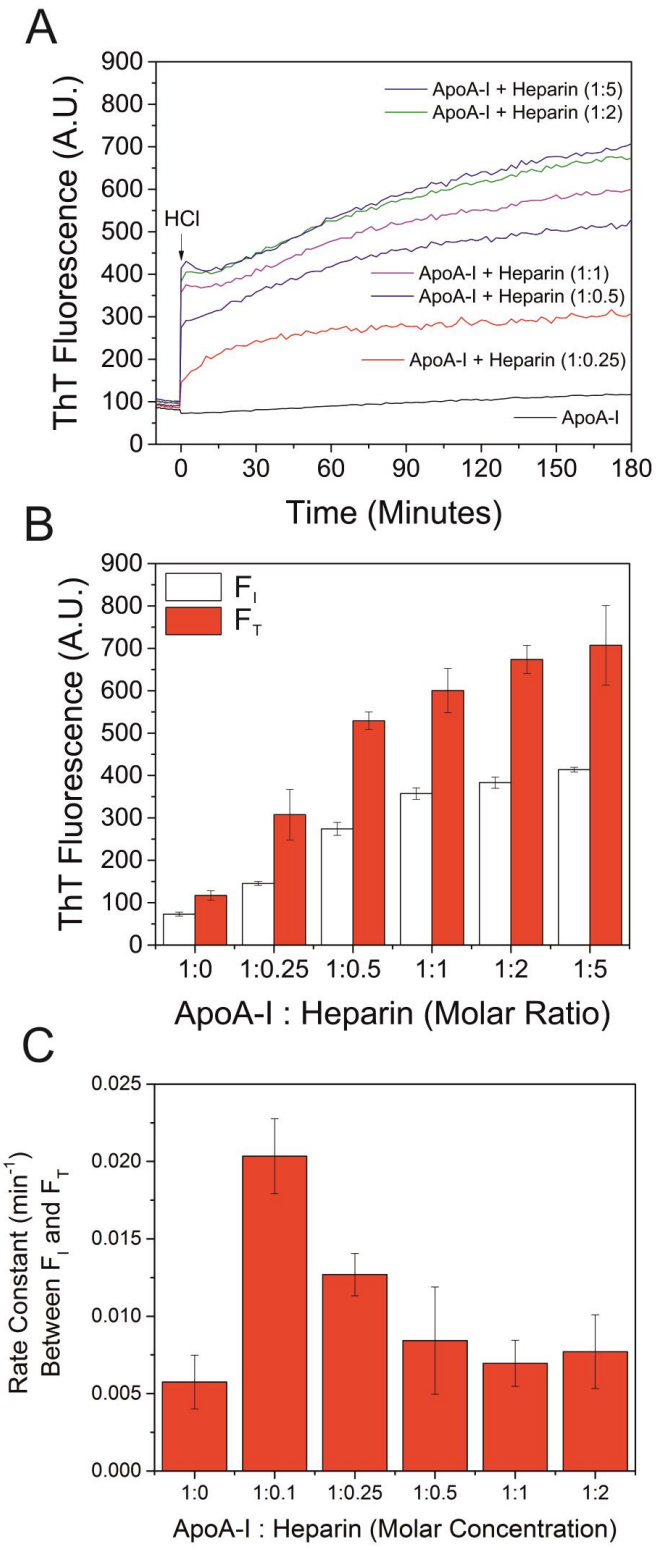

Figure 4.7 (**A**) ThT fluorescence of apoA-I (7.2 μM) in McIlvaine buffer at pH 4 with increasing concentrations of heparin, following acidification. (**B**) F_I and F_T parameters taken from the continual ThT data in **A**. (**C**) Rate of increase between F_I and F_T. Data shown is the mean of 3 samples with ± standard error bars.

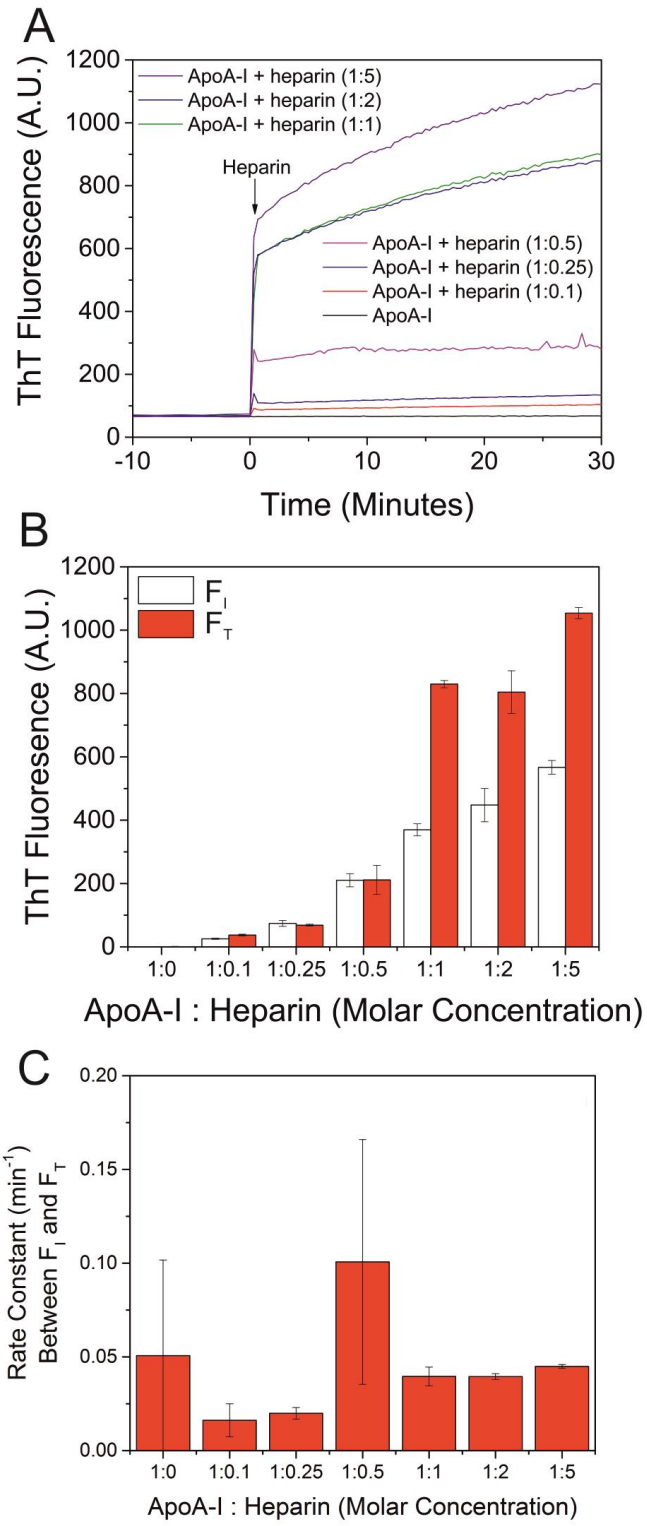

Figure 4.8 (**A**) ThT fluorescence of apoA-I (7.2 μM) in Tris buffer at pH 4 following the addition of increasing concentrations of heparin. (**B**) F_I and F_T parameters taken from the continual ThT data in **A**. (**C**) Rate of increase between F_I and F_T. Data shown is the mean of 3 samples with ± standard error bars.

The rate of aggregation was determined by fitting the fluorescence intensity between the F_I and F_T points with the exponential **equation 4.2,** where k is the rate constant, y is the fluorescence intensity, a is the intercept and x is the time in minutes. The fittings are shown in **Appendix 4**.

$$\boldsymbol{Y = a + b * exp^{(-kx)}} \qquad \textbf{[4.2]}$$

Heparin is thought to act as a scaffold for stabilising proteins in a conformation that promotes the formation of β-sheet structures (Madine et al., 2013; Iannuzzi et al., 2015). In order for this to occur, apoA-I has to bind to heparin. Heparin, the structure of which is shown in **Figure 1.3**, carries a highly negative charge. It is assumed that heparin binds ionically to apoA-I, carrying a positive charge on its basic residues, when incubated at a pH lower than the PI value of 5.6 for apoA-I, hence the increased ThT response only at acidic pH (**Figure 4.6**).

The F_I enhancement observed in **Figures 4.7B** and **4.8B** following the addition of HCl and heparin, respectively, could be modelled using the Hill equation (**Equation 4.3**) and Origin Pro software. Where the fluorescence (V) is dependent on the maximum fluorescence (V_{Max}), the concentration of heparin (S), the Hill co-efficient (n) and the dissociation constant (K_D).

$$\mathbf{V = V_{Max}\,[S]^n \,/\, K_D + [S]^n} \qquad \textbf{[4.3]}$$

This produced apparent dissociation constants for heparin of 2.6 (±1.1) μM and 5.1 (±1.5) μM at pH 4 (**Figure 4.9**), with a free enthalpy change of -31.8 kJ/mol and 30.2 kJ/mol, based on the addition of HCl and heparin, respectively. This value is the mean of 3 samples. These 2 dissociation constants are similar, and suggest a strong affinity of apoA-I for heparin.

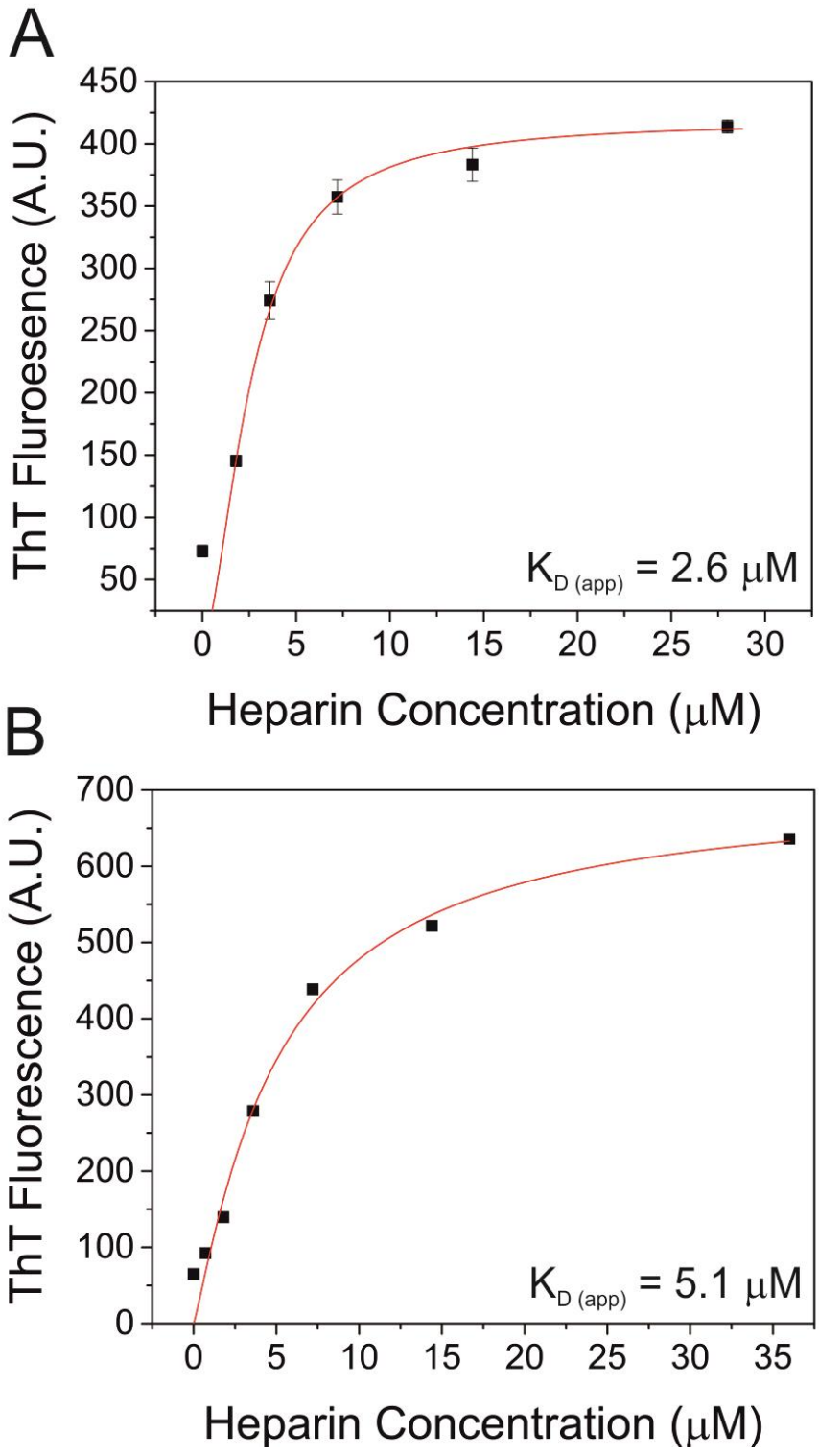

Figure 4.9 Heparin concentration dependence of apoA-I aggregation, measured by ThT fluorescence (F_I) and modelled by the Hill equation. F_I values were used following acidification of apoA-I incubated in the presence of heparin (**A**) and addition of heparin to apoA-I, already incubated at pH 4 (**B**).

ApoA-I was incubated at pH 4 in Tris buffer, with increasing concentrations of NaCl salt, prior to the addition of a 2-fold molar excess of heparin. This was in order to determine whether NaCl was able to interfere with the ionic interaction between heparin and apoA-I.

A control for apoA-I incubated in the presence of heparin but no NaCl is the baseline for this experiment, and any ThT intensity decrease in comparison, is suggestive of inhibition of the heparin-mediated aggregation. No decrease in fluorescence intensity was observed as a result of increasing the concentration of NaCl when added to apoA-I alone, (data not shown) confirming that the presence of NaCl does not affect the natural propensity of apoA-I to aggregate.

However, when apoA-I is incubated with a 2-fold molar excess of heparin, a decrease in ThT fluorescence intensity in the presence of NaCl is observed. Increasing the concentration of NaCl leads to a further decrease in both the F_I and F_T fluorescence measurements (**Figure 4.10**). This suggests that NaCl can inhibit the pro-amyloidogenic properties heparin exhibits on apoA-I aggregation into amyloid-like material. Thus confirming an ionic interaction between heparin and apoA-I.

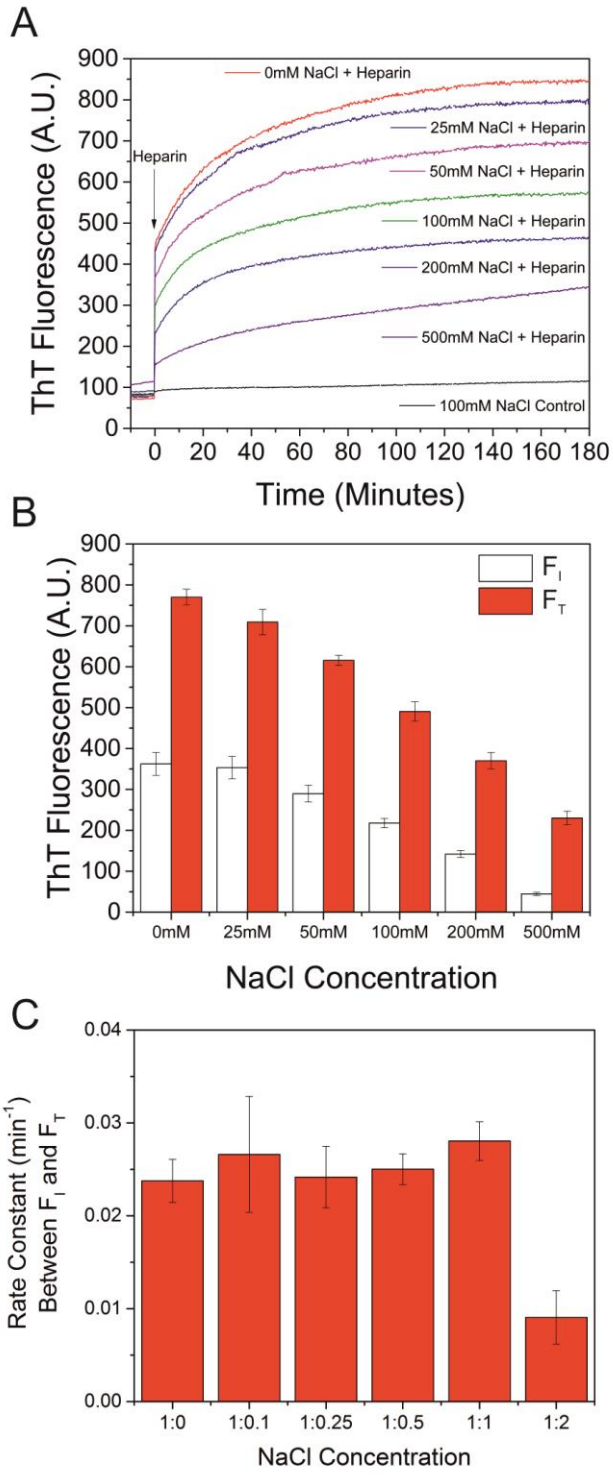

Figure 4.10 Effects of salt on heparin induced apoA-I aggregation. (**A**) ThT response of apoA-I (7.2 μM) incubated at pH 4 with increasing concentrations of NaCl, following the addition of heparin (14.4 μM). (**B**) Initial increase in ThT upon addition of heparin (F_I), and the total increase in ThT fluorescence (F_T). Data shown is the mean of 3 samples with ± standard error bars.

4.3.4. Effects of concentration of apoA-I aggregation

ApoA-I was incubated at pH 4 at increasing concentrations (7.2, 18 and 36 μM), alone and in the presence of a two-fold molar excess of heparin for 3 days. After this time, end point ThT measurements were taken. All three concentrations gave rise to an increase in ThT fluorescence (**Figure 4.11**), with higher concentrations of protein leading to higher fluorescence intensity, with an enhancement of fluorescence in the presence of heparin at each of the three concentrations. This shows that the formation of ThT reactive material increased with protein concentration. Following removal of the insoluble material by centrifugation, the F_S value of all 3 concentrations decreased to levels associated with no amyloid-like material. This shows that the soluble ThT reactive element remains small and constant, regardless of the protein concentration.

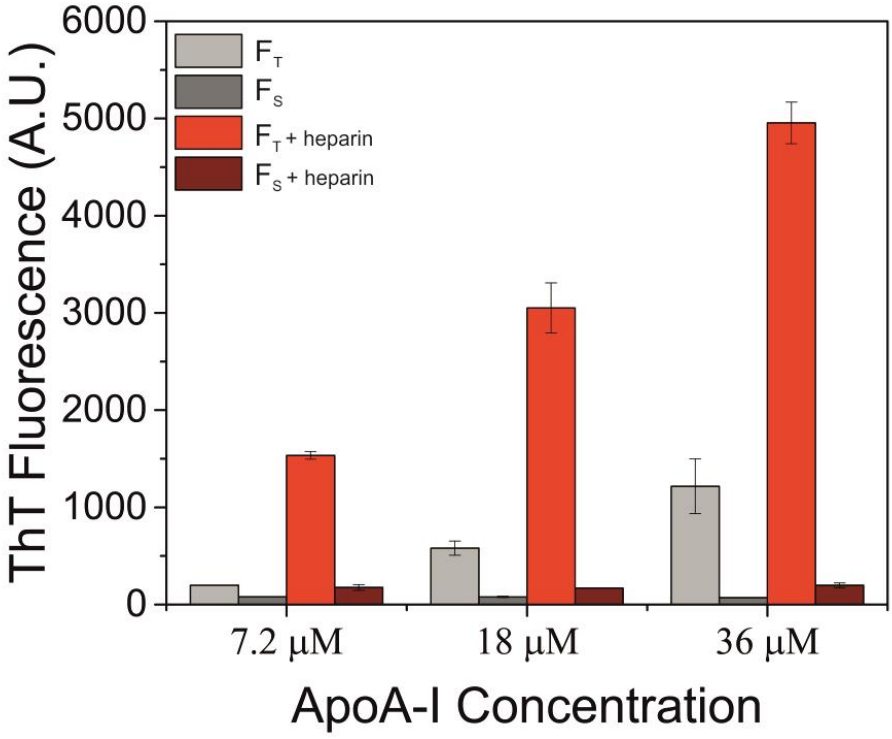

Figure 4.11 ThT fluorescence of apoA-I at 0.2, 0.5 and 1 mg/ml (7.2, 18 and 36 μM) in the absence and presence heparin, following acidification to pH 4. Data shown is the mean of 3 samples with ± standard error bars.

4.3.5. Ability of apoA-I mutants to aggregate

ApoA-I has many naturally occurring mutants, as outlined in **section 2.4.9** of this thesis. Mutants corresponding with single amino acid changes were produced, as described in **section 3.3.2.2**, for two reasons: i) in order to compare the differences in aggregation propensity between wild type apoA-I and the mutant apoA-I G26R species, and ii) to incorporate a unique cysteine residue into the apoA-I sequence, in order to attach a fluorescent tag for cellular imaging purposes (K96C and R173C). All mutants were subject to end-point ThT analysis to determine their propensity to aggregate, compared to the wild type apoA-I.

4.3.5.1. ThT responsiveness of apoA-I G26R

The naturally occurring G26R Iowa mutant of full-length apoA-I has been found deposited as amyloid-like aggregates within arterial plaques. This mutation also induces aggregation of the apoA-I (1-83) peptide, the mechanism of which is thought to be linked to the destabilisation of the N-terminus of apoA-I (Adachi et al., 2012; Adachi et al., 2014). However, the mutation has been shown to have no effect on the ability of full-length apoA-I to form amyloid-like aggregates (Raimondi et al., 2011).

Here, putative apoA-I G26R produces a similar ThT response to the wild type protein after 3 days of incubation at pH 4. However, unlike the wild type, the G26R mutant gives rise to an enhanced F_T value at neutral pH (**Figure 4.12 A** and **B**). The ThT response of the protein remaining in solution (F_S) was minimal, following centrifugation. This is consistent with no amyloid formation. This confirms that the ThT responsive material is confined to the insoluble material, formed at both pH 4 and pH 7.

4.3.5.2. ThT responsiveness of apoA-I K96C and R173C

The putative apoA-I K96C and R173C peptides were produced, in order to allow tagging of the novel cysteine residue for cell imaging purposes. Therefore, it was preferable that both mutants had similar amyloidogenic properties to the wild type apoA-I peptide, allowing direct comparison of their cellular uptake and distribution.

Figures 4.12 C and **D** show that at pH 7 neither mutant produced a significant increase in the F_T, consistent with control samples and the absence of amyloid-like material.

At acidic pH, wild type apoA-I is shown to produce an increase in the F_T value, which is greatly enhanced in the presence of heparin. However, the K96C and R173C mutants produce an increase in F_T, only in the presence of heparin at pH 4. This fluorescence increase is shown to be caused by the insoluble material produced during incubation at pH 4 in the presence of heparin, since the F_S value returns to the baseline level, following its sedimentation.

4.3.5.3. Quantification of apoA-I mutant solubility

Quantification of the conversion from soluble apoA-I to insoluble material for the wild type protein is discussed in section **4.2.1** and **4.3.1**. At neutral and basic pH, less than 10 % of apoA-I becomes incorporated into insoluble material and removed through centrifugation. This percentage increases dramatically at acidic pH, with almost 95 % of the protein having been converted into insoluble material. This is the case for samples both in the absence and presence of heparin.

The G26R mutant produces a similar percentage conversion into insoluble material at acidic pH to the wild type apoA-I. However, at pH 7, the G26R mutant loses ≈ 60 % of its soluble protein, following centrifugation (**Figure 4.13 red**).

ApoA-I K96C and R173C mutants produce very similar sedimentation data. Neither mutation leads to the conversion of insoluble material at neutral pH, consistent with the wild type apoA-I. At pH 4 alone, no insoluble material is formed, unlike the wild type apoA-I. Conversion from soluble apoA-I to insoluble aggregates only occurs at pH 4 in the presence of heparin (**Figure 4.13 blue** and **green**). This mirrors the ThT findings for the cysteine mutants, discussed in **Section 4.3.5.2.**

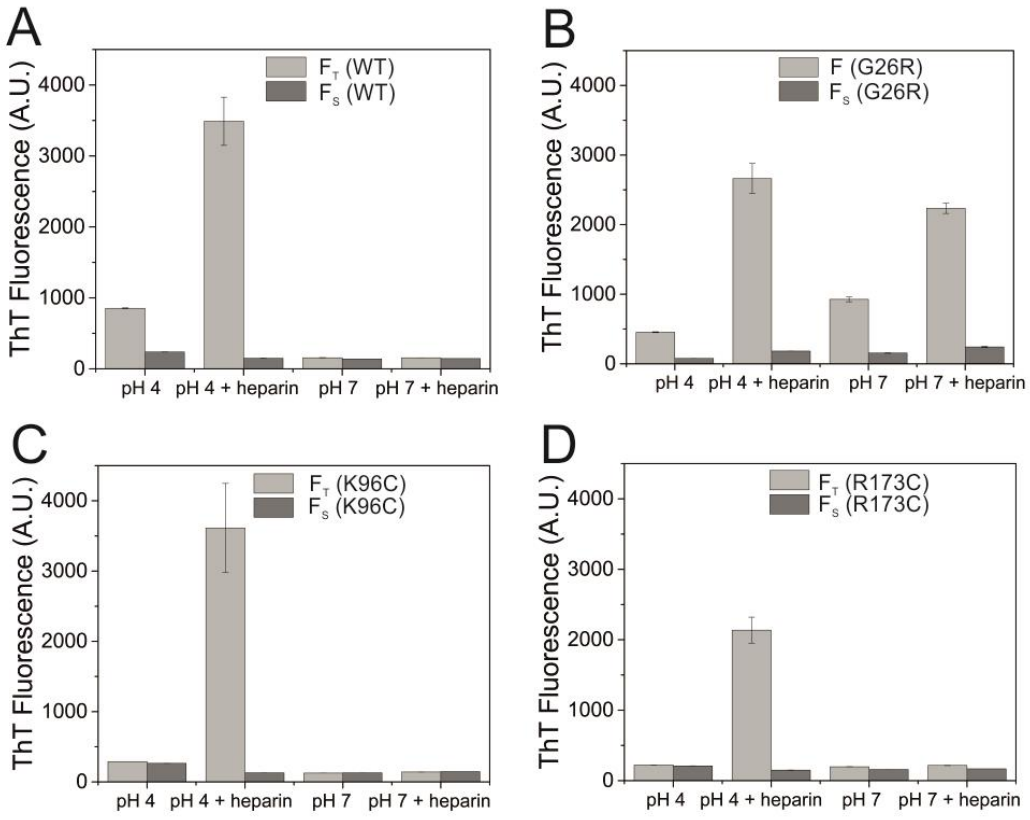

Figure 4.12 End-point ThT fluorescence of apoA-I wild type (**A**), G26R (**B**), K96C (**C**) and R173C (**D**). Data shown is the average of 3 samples with ± standard error bars.

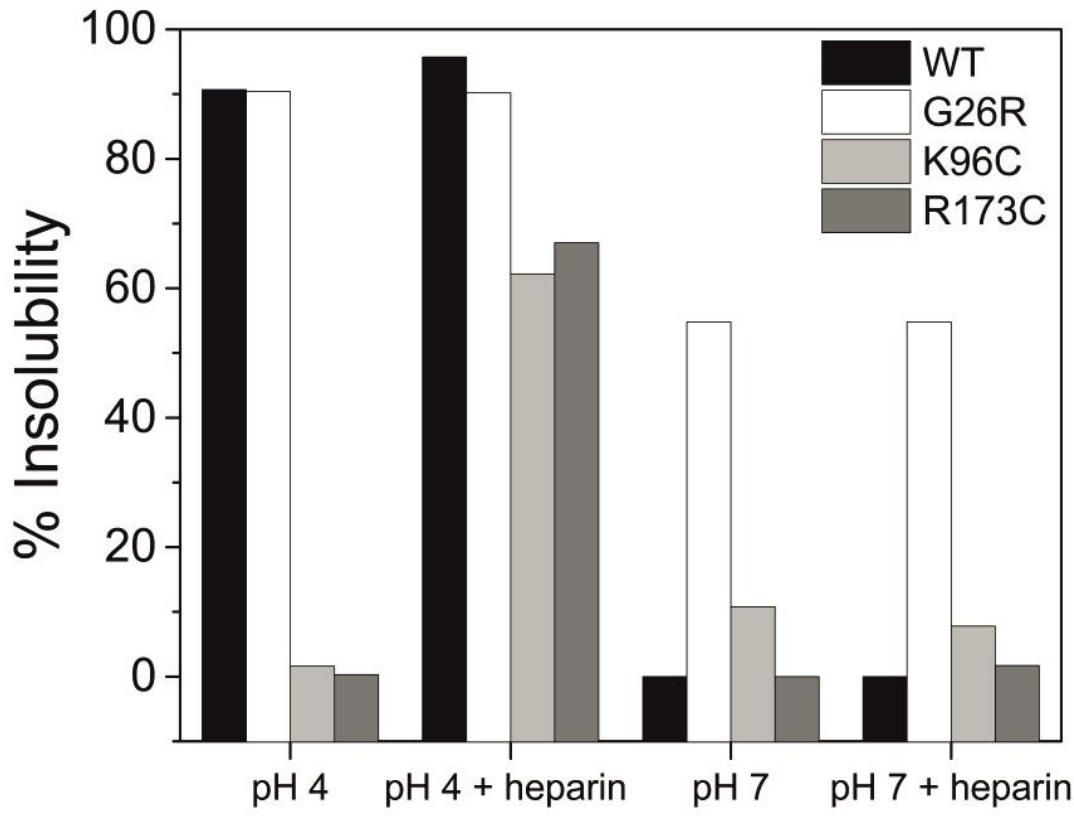

Figure 4.13 Percentage of starting material converted into insoluble material for apoA-I wild type (black) G26R (red), K96C (blue) and R173C (green).

4.3.6. Ability of oxidised apoA-I to aggregate

4.3.6.1. Characterisation of oxidised apoA-I

ApoA-I was oxidised, following procedures outlined by Chan (2015). After incubation with H_2O_2 and dialysis back into 10 mM phosphate at pH 6, oxidised apoA-I produced a white precipitate. As such, dialysis into phosphate buffer at pH 7.5 was attempted instead, resulting in a clear protein sample. The oxidised product was shown to be slightly heavier than the wild type apoA-I when run on an SDS gel (**Figure 4.14**), consistent with oxidation of at least one of the three native methionine residues.

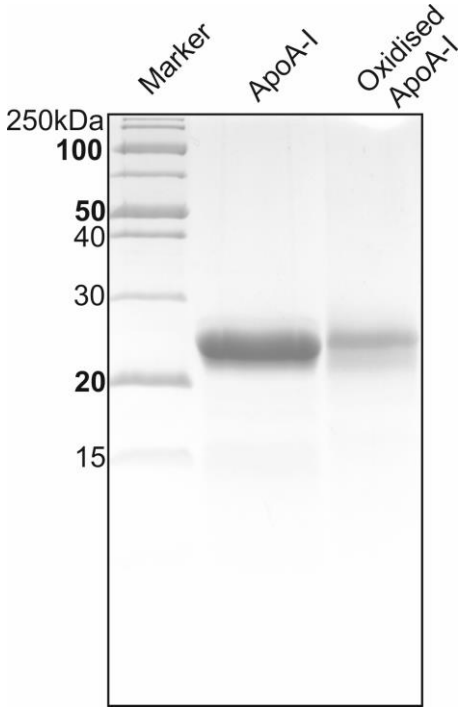

Figure 4.14 15 % SDS PAGE gel of chemically oxidised apoA-I and untreated, wild type apoA-I.

In order to determine the extent at which incubation in hydrogen peroxide oxidised the methionine residues of apoA-I, oxidised apoA-I underwent mass spectrometry analysis**.** Oxidation of apoA-I at all three methionine residues results in a predicted mass of 27882 Da, compared to the predicted mass of 27834 Da for the un-oxidised apoA-I. **Figure 3.16** indicates a mass for the intact un-oxidised apoA-I of 27837 Da, whilst **Figure 4.15** shows that oxidised apoA-I has an intact mass of 27891 Da, 54 Daltons higher than the un-oxidised apoA-I. Oxidation of three methionine residues would result in a mass increase of 48 Daltons but, given the variance between the detected mass and the predicted mass for the un-oxidised apoA-I, the difference of 4 Daltons is deemed negligible. As such, the putative oxidised apoA-I is considered oxidised at all three methionine residues, as expected following the methods outlined by Chan *et al.* (2015).

4.3.6.2 Oxidised apoA-I aggregation

Oxidation of 3 methionine residues (86, 112, 148) in apoA-I has been shown to induce aggregation of apoA-I into amyloid species at pH 6 (Wong et al., 2010; Chan et al., 2015). Here, the effect of chemical oxidation of apoA-I on the ability to form amyloid-like aggregates will be determined across a more physiologically relevant pH range (pH 6–7.5), and used to produce aggregates for structural analysis by solid-state NMR.

Here, **Figure 4.16A** indicates that at neutral pH, a negligible amount (<10 %) of oxidised apoA-I becomes converted into insoluble material, consistent with the percentage conversion of wild type apoA-I at pH 7. The ThT fluorescence (F_T) of the oxidised apoA-I at neutral pH also remains negligible and is consistent with control samples, suggesting that oxidised apoA-I does not form amyloid-like material under these conditions.

At pH 6, the percentage of apoA-I converted to insoluble material increases to roughly 40 %, similar to the wild type protein at this pH. This is despite the formation of a large white precipitate upon acidification of oxidised apoA-I to pH 6. The formation of a visible precipitate was only seen for the wild type protein at pH 4 and 5, where upwards of 90 % of the protein was converted into insoluble material.

Oxidised apoA-I produced a significant increase in ThT fluorescence (F_T) at pH 6, which was reduced upon centrifugation and removal of the insoluble material to F_S, consistent with no amyloid-like material. This suggests that the amyloid-like material was confined solely to the insoluble material and not the remaining soluble oxidised apoA-I.

These results suggest that oxidised apoA-I has an increased propensity to aggregate, compared to wild type apoA-I.

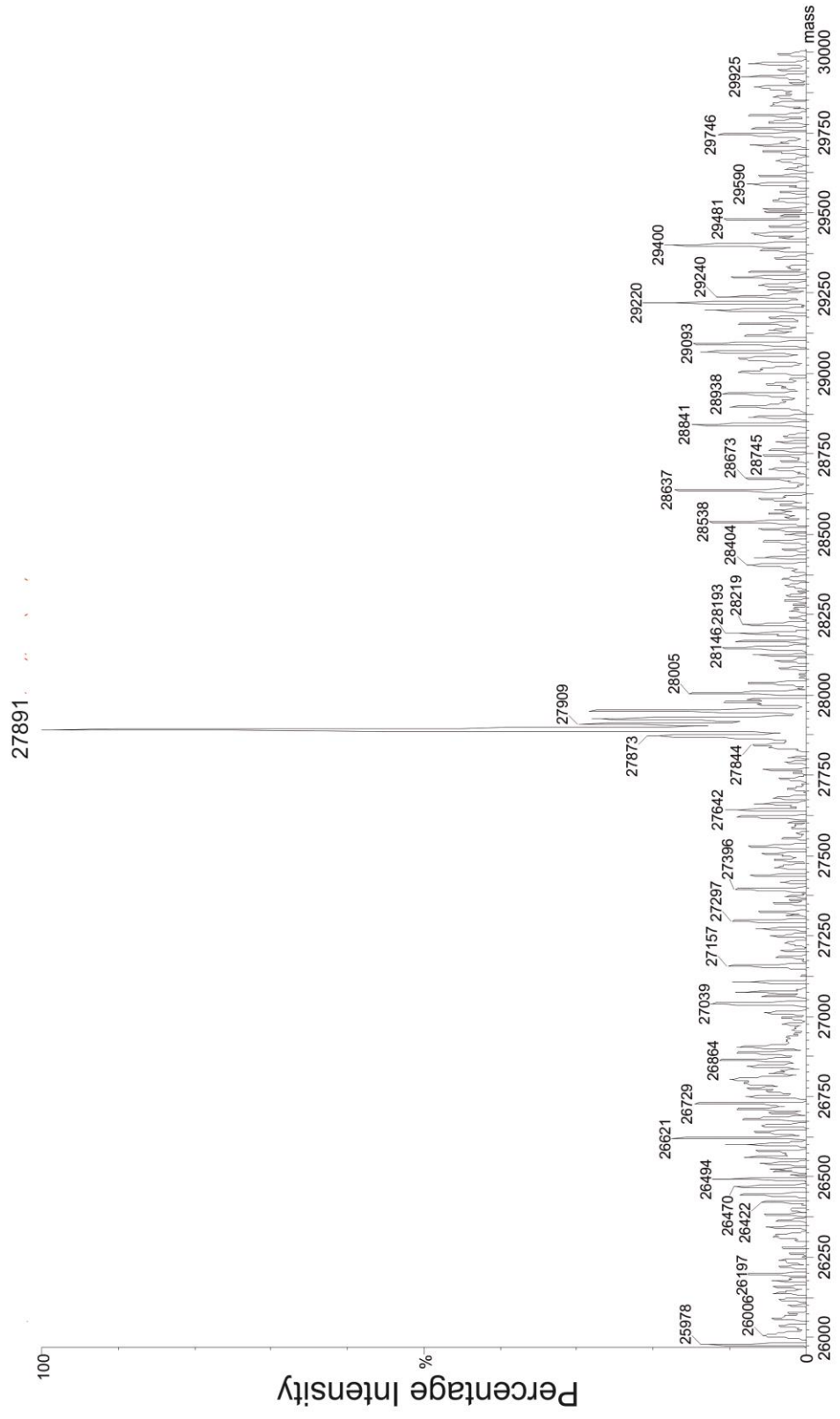

Figure 4.15 Electrospray ionisation mass spectroscopy of oxidised apoA-I with an intactv mass of 27891 Da.

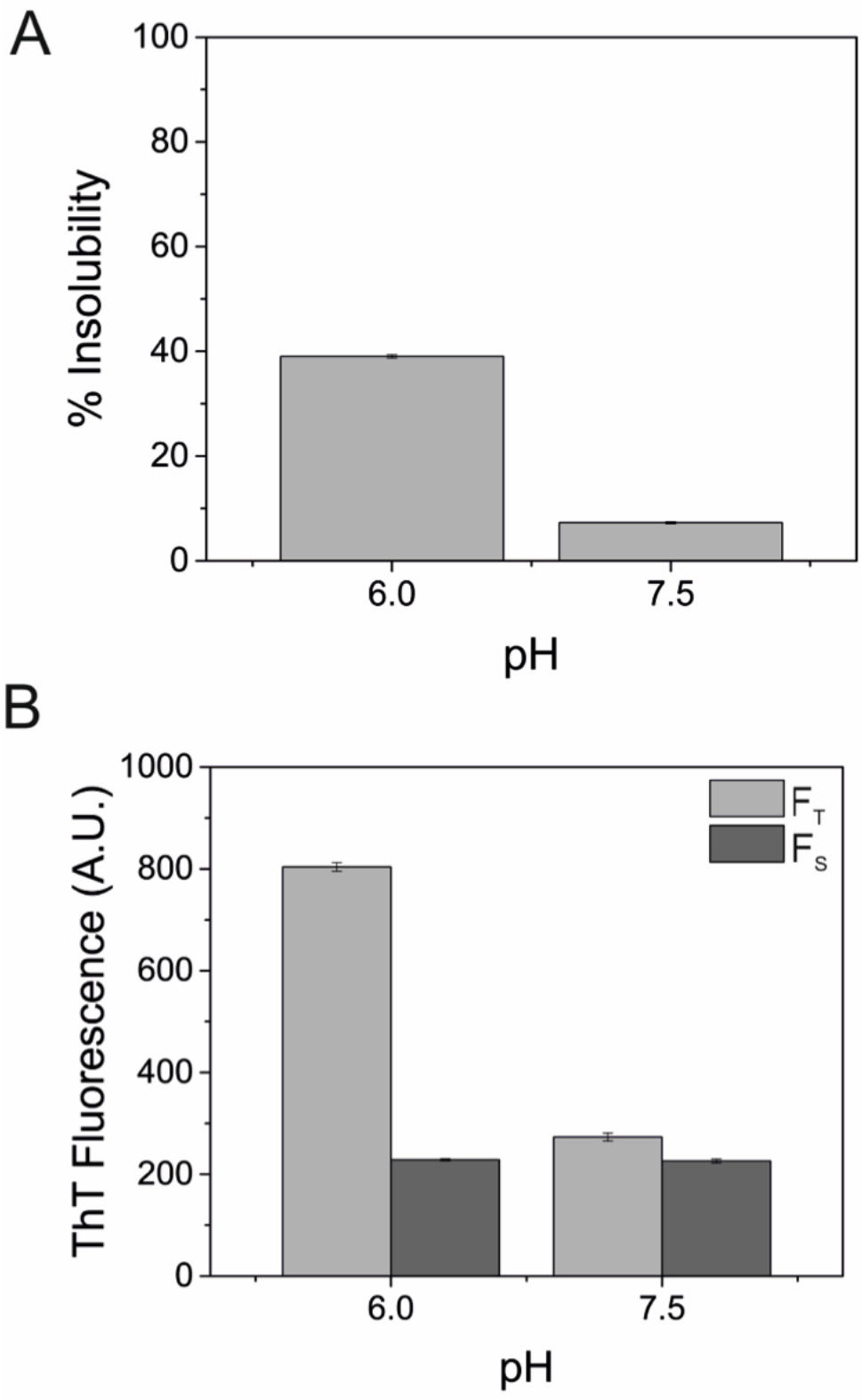

Figure 4.16 Percentage insolubility (**A**) and ThT fluorescence (**B**) of oxidised apoA-I at pH 7.5 and pH 6. Data shown is the mean of 3 samples with ± standard error bars.

4.3.7. Ability of apoA-I (46-59) to aggregate

As mentioned earlier, several groups have reported the amyloidogenic properties of peptides comprising the first 90/100 residues from the N-terminus of apoA-I (Rosú et al., 2015; Sipe et al., 2012; Mucchiano, Häggqvist, et al., 2001; Adachi et al., 2012). In particular, the peptide comprising of residues 46-59 has been shown to bind ThT, form fibrils with a typical amyloid morphology, and produce an XRD reflection pattern, consistent with the formation of amyloid at neutral pH (Wong et al., 2012). Here, the ability of apoA-I (46-59) to seed, and be seeded, by full-length apoA-I into amyloid-like aggregates was studied, as well as the effect heparin has on apoA-I (46-59) aggregation.

ThT fluorescence data shown in **Figure 4.17,** suggests that apoA-I (46-59) does not form amyloid-like material at neutral pH, neither in the absence nor the presence of heparin. However, at acidic pH, apoA-I (46-59) produces a large increase in ThT fluorescence, both in the absence and presence of heparin, but not in a similar manner to the full-length apoA-I. Full-length apoA-I undergoes a dramatic increase in ThT fluorescence, following acidification, measured as the ΔF_I parameter. However, apoA-I (46-59) has a much slower increase in ThT fluorescence following acidification, which is more common of amyloid-like aggregates (Wong et al., 2012). Wild type apoA-I showed a dramatic enhancement in the presence of heparin, whereas no significant difference is observed when heparin is incubated with the apoA-I (46-59) peptide. This suggests that heparin has no effect on the aggregation of apoA-I (46-59) at acidic pH.

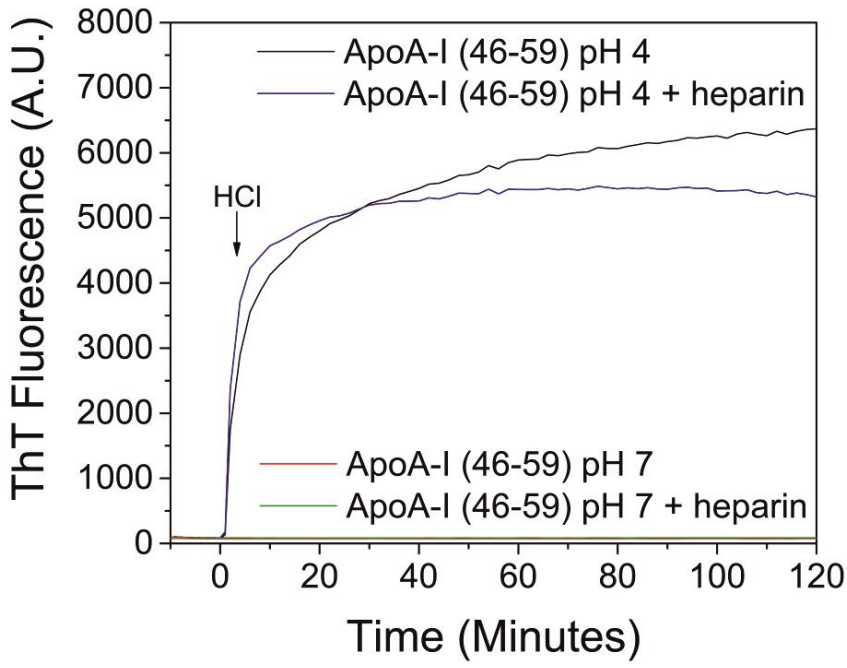

Figure 4.17 ThT fluorescence of apoA-I (46-59) at pH 4 and pH 7 alone, and in the presence of heparin, following acidification by addition of concentrated HCl. Data shown is the mean of 3 samples.

4.3.7.1. Ability of full-length apoA-I to seed apoA-I (46-59)

The ability of amyloid aggregates formed by full-length, wild type apoA-I in the presence of 2-fold molar excess of heparin, to seed apoA-I (46-59) aggregation was studied. At pH 4, apoA-I (46-59) was shown to aggregate spontaneously (**Figure 4.17**), with a less dramatic F_I increase compared to full-length apoA-I.

The incubation of full-length seeds with apoA-I (46-59), prior to acidification, results in a similar F_I increase upon addition of HCl. However, the presence of seeds results in a lower F_T intensity (**Figure 4.18**). This is more consistent with the ThT response of full-length apoA-I at pH 4 (**Figure 4.5**), rather than the ThT response of apoA-I (46-59) alone.

At pH 7, apoA-I (46-59) shows no ThT response when incubated alone, but an F_I increase following addition of full-length apoA-I seeds. However, this

increase in ThT intensity is similar to the ThT response of the full-length apoA-I seeds controls (**Figure 4.18B**). This suggests that full-length seeds cannot promote the aggregation of apoA-I (46-59) at neutral pH. However, at acidic pH, the seeds affect the ThT response of the aggregates formed. The reduction in ThT fluorescence, following the initial increase in **Figure 4.18B,** could be caused by sedimentation of the insoluble apoA-I seeds out of solution.

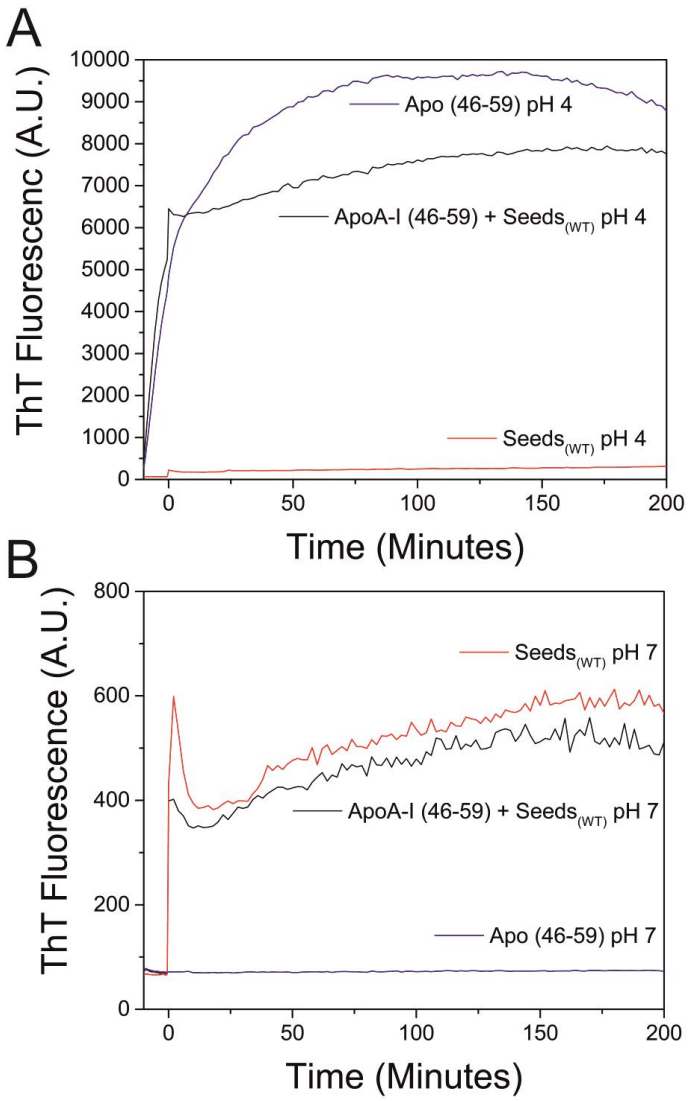

Figure 4.18 ThT fluorescence of apoA-I at pH 4 and 7 in the absence and presence of seeds formed from full-length aggregates.

4.3.8. Congo red binding ability of apoA-I

Congo red is an amyloid specific dye that binds selectively to β-sheet structures of amyloid, staining the deposited, insoluble material red. Upon visualisation under polarised light, a green birefringence is observed, indicating a positive result for amyloid (Puchtler et al., 1962; Klunk et al., 1999a; Li et al., 2009).

ApoA-I, both in the absence and presence of heparin, does not produce any aggregated material at pH 7, thus there is no insoluble material to which the Congo red dye can bind. This is shown in the images taken with uncrossed polarising lenses, where no red material is visible (**Figure 4.19**). When the polarising lens is rotated 90 degrees, a lack of green birefringence confirms amyloid is not formed under these conditions.

Upon acidification of apoA-I to pH 4, both in the absence and presence of heparin, apoA-I forms insoluble material (as defined above in **section 4.3.1** and **4.3.3**) that binds to the Congo red dye and is visualised as a red deposit with uncrossed lenses. Upon cross polarisation of the lenses, the dye produces a yellow-green birefringence, confirming the insoluble material is characteristic of amyloid.

This data suggests that, despite a large difference in the ThT response produced by aggregates formed in the absence and presence of heparin at pH 4, both aggregates bind to Congo red, which is a characteristic trait of all amyloid species.

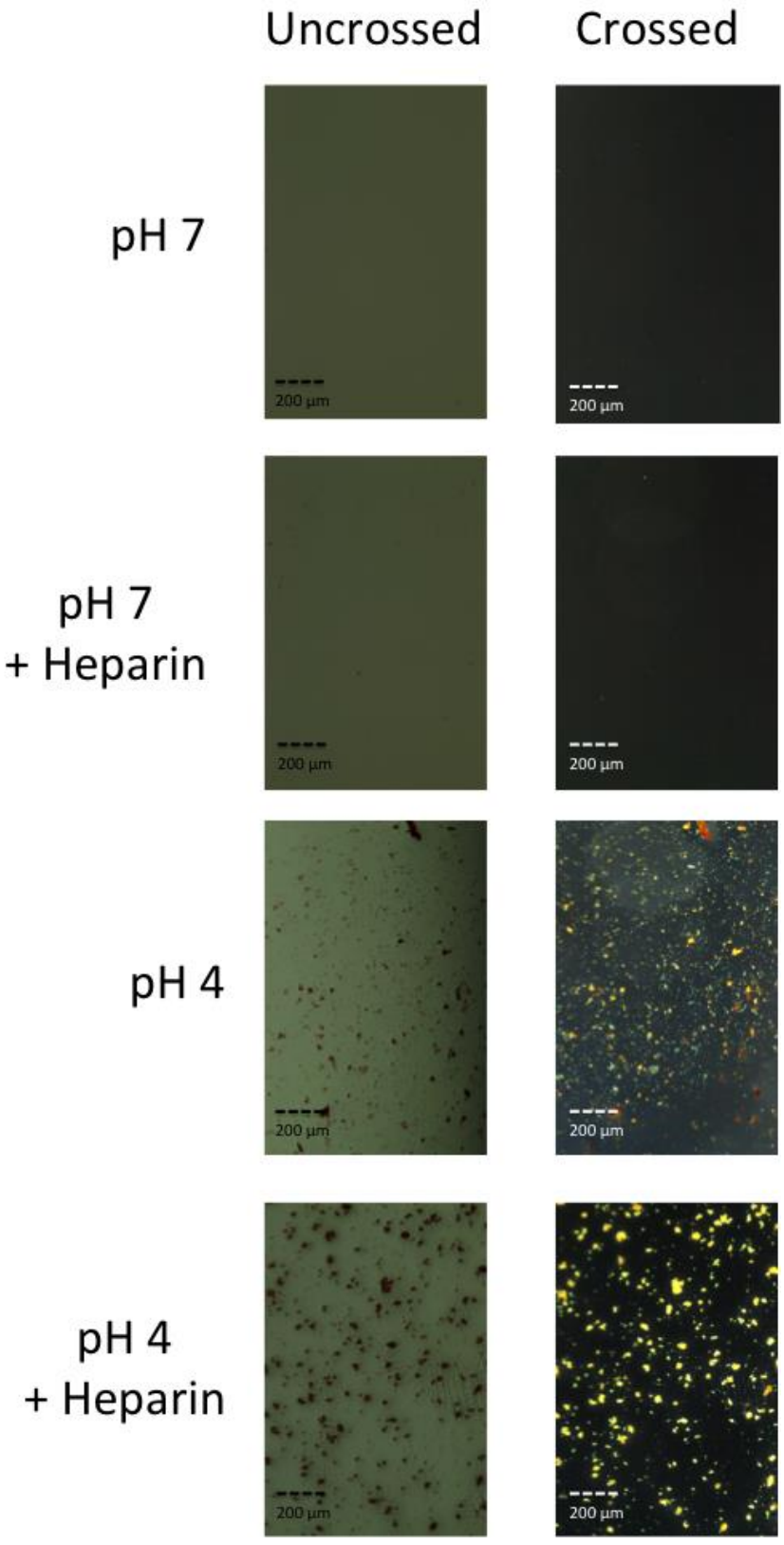

Figure 4.19 Congo red-stained apoA-I samples at pH 7 and pH 4 in the absence and presence of heparin, following incubation for 3 days. Lenses were at 0 and 90° for the uncrossed and crossed images, respectively.

4.3.9. Intrinsic fluorescence of tryptophan residues

Intrinsic fluorescence studies of apoA-I were carried out to determine whether any significant change in the environment surrounding the aromatic residues, in particular tryptophan (8, 50, 72 and 108) occurred. A change of environment could give insights into a structural rearrangement occurring during the aggregation of apoA-I. Solvent-exposed tryptophan residues have a peak emission at roughly 355 nm, with slight variance for the specific environment, upon excitation at 279 nm. However, tryptophan residues in hydrophobic environments, such as those experienced when the residues are buried within secondary structural elements, undergo a blue shift in the spectrum and have their peak emission centred around 335 nm (Touchette et al., 2010). ApoA-I consists of a majority α-helical content in the native structure, and all four of the tryptophan residues are located within helical structures, as shown in **Figure 4.20A** (Das et al., 2016).

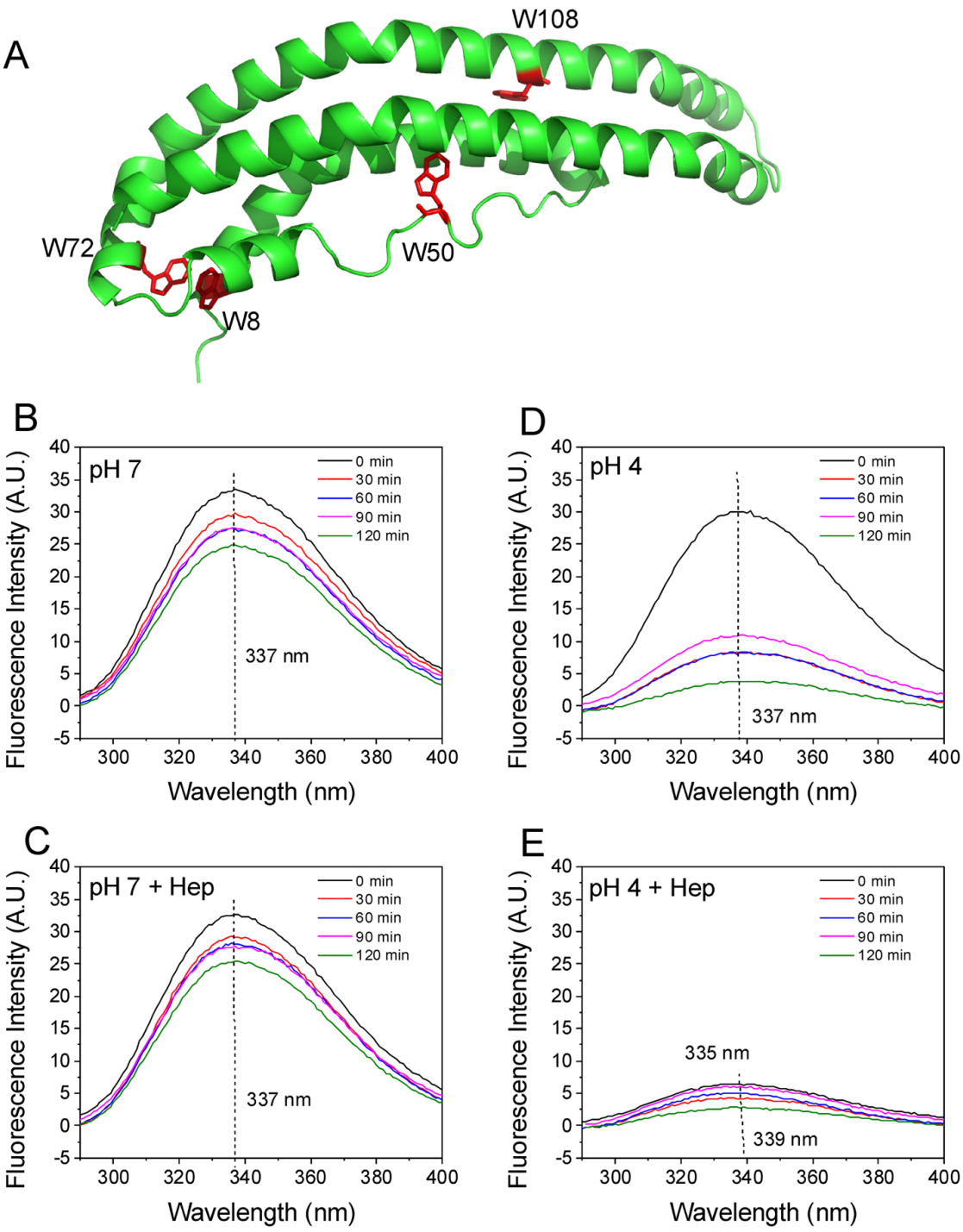

Figure 4.20 (**A**) Structure of monomeric apoA-I (Δ185-243), highlighting the tryptophan residues in the native sequence. Tryptophan fluorescence emission spectra for apoA-I samples at pH 7 (**B/C**) and pH 4 (**D/E**), after excitation of tryptophan residues at 279 nm. Peak emission wavelengths are highlighted for each spectrum.

At pH 7, the emission maximum occurs at 337 nm in both the absence and presence of heparin (**Figure 4.20 B** and **C**), which remains unchanged after 2 hours incubation, despite a small decrease in intensity. These emission maximum are consistent with hydrophobic environments (Touchette et al., 2010). This was expected, given that many of the tryptophan residues are located at the hydrophobic interface of monomeric apoA-I.

Incubation of apoA-I at pH 4 in the absence of heparin produces a similar spectrum to the pH 7 sample, with a maximum fluorescence of 337, although the decrease in fluorescence intensity is considerably higher, consistent with increased protein precipitation at acidic pH (**Figure 4.20 D**). In the presence of heparin at pH 4, the fluorescence intensity is reduced considerably compared to the other 3 samples, suggesting a faster aggregation and precipitation. A blue shift in the spectrum also occurs, resulting in a maximum fluorescence peak of 334 nm for the fresh solution (**Figure 4.20 E**). This shift suggests that heparin causes a change in the environment surrounding one or more of the tryptophan residues, and a blue shift in particular is consistent with movement to a less polar environment.

In summary, heparin appears to induce a different aggregation pathway. Oxidation of methionine residues within apoA-I causes a red shift in the peak emission wavelength, compared to the native apoA-I at pH 7.4, towards 345 nm (**Figure 4.21**). This red shift suggests that apoA-I undergoes unfolding, following oxidation of the three methionine residues, consistent with previous studies that oxidation leads to the destabilisation of the native apoA-I structure (Wong et al., 2010). Upon incubation for 1 hour at pH 6, a slight decrease in signal intensity is observed, due to the formation of insoluble material. A blue shift in the

spectrum's peak emission, from 345 nm at pH 7.4 to 340 nm at pH 6, also occurs, suggesting that the tryptophan residues become incorporated into more hydrophobic regions following acidification, consistent with amyloidosis.

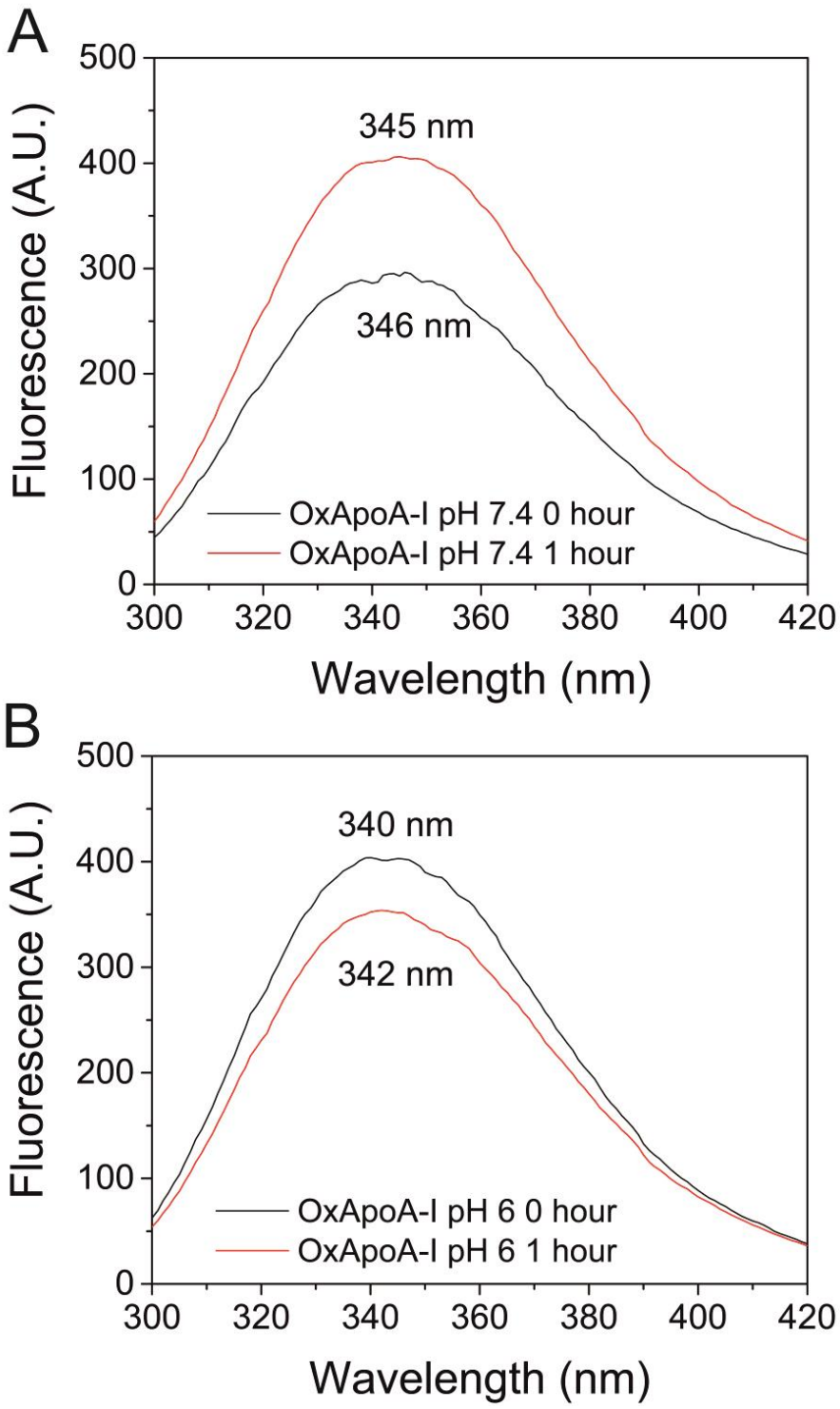

Figure 4.21 Tryptophan fluorescence emission spectra for oxidised apoA-I at pH 7.4 (**A**) and pH 6 (**B**). Peak emission wavelengths are highlighted.

4.3.10. Morphology of apoA-I aggregates

4.3.10.1. Transmission electron microscopy

Insoluble aggregates produced during incubation of apoA-I at acidic pH were visualised via TEM. **Figure 4.22** shows negatively-stained apoA-I aggregates formed at pH 4 and pH 5, in both the absence and presence of heparin; oxidised apoA-I at pH 6 and apoA-I (46-59) at pH 4.

In the absence of heparin, large quantities of amorphous aggregates are deposited at pH 4 and pH 5, which do not resemble amyloid species (**Figure 4.22 A** and **C**). However, in the presence of heparin, apoA-I forms dense networks of long, un-branched fibrils that are more characteristic of amyloid, at both pH 4 and pH 5 (**Figure 4.22 B** and **D**).

Oxidised apoA-I at pH 6 produced long, thin fibrils (**Figure 4.22E**), characteristic of amyloid and consistent with previous TEM images, observed under the same conditions (Wong et al., 2010). Large quantities of smaller spherical structures also appeared, which could potentially be oligomeric species.

Finally, apoA-I (46-59) incubated at pH 4 also produced fibrils characteristic of amyloid species (**Figure 4.22 F**).

In summary, aggregates with a highly conserved amyloid morphology are only observed following the aggregation of oxidised apoA-I or apoA-I (46-59). Although the aggregates formed at pH 4 and pH 5 do not resemble true amyloid fibrils, the inclusion of heparin leads to a network of more fibrillar material.

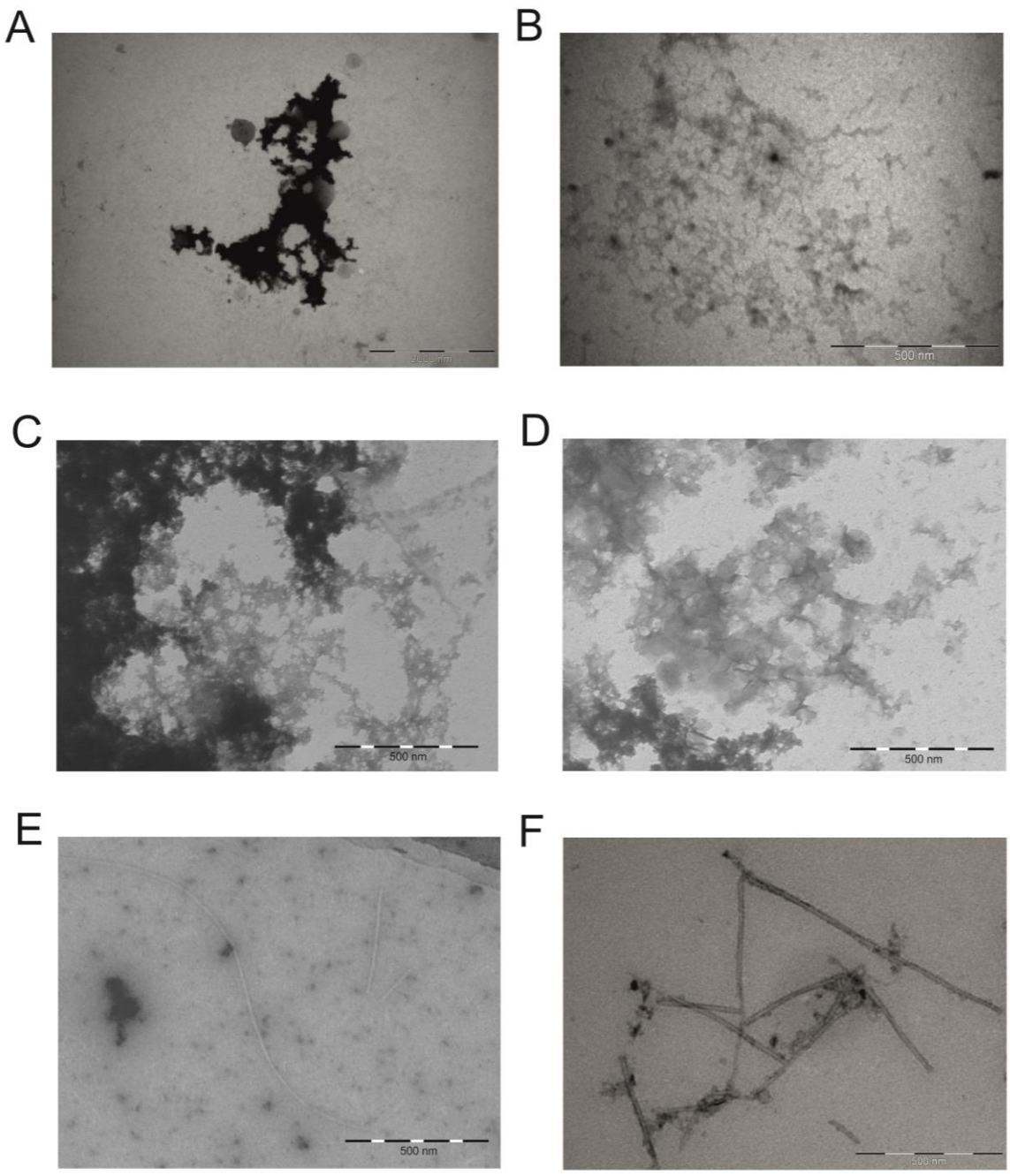

Figure 4.22 TEM images of apoA-I (36 μM) after 3 days' incubation at pH 4 (**A/B**) and pH 5 (**C/D**) in the absence (**A/C**) and presence (**B/D**) of heparin, oxidised apoA-I at pH 6 (**E**) and apoA-I (46-59) at pH 4 (**F**).

4.3.10.2. Atomic force microscopy

ApoA-I aggregates formed at pH 4 in the presence of heparin for 3 days were loaded onto mica sheets and visualised using AFM. **Figure 4.23** shows networks of thin, un-branched fibrils are formed, similar to the TEM results. Furthermore, AFM allows a height calculation of approximately 5 nm, which is an additional characteristic of amyloid fibrils (Serpell et al., 1997). This technique was also attempted for apoA-I aggregates formed in the absence of heparin, however, no material was detected on the mica surface.

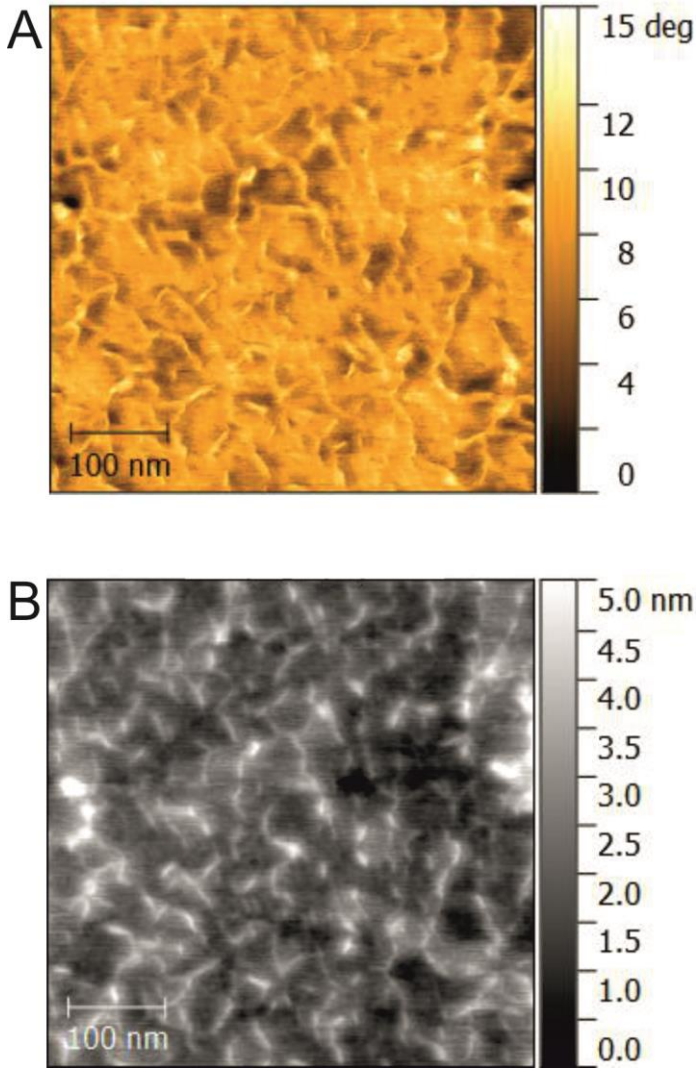

Figure 4.23 AFM phase (**A**) and topography (**B**) images of apoA-I (36 µM) after several days' incubation at pH 4 in the presence of heparin (72 µM).

4.3.11 X-ray diffraction

Samples of insoluble material formed following incubation of apoA-I at pH 4, in the absence and presence of heparin, were analysed by X-ray diffraction, in order to determine if any reflections consistent with β-sheet spacings were detectable. In the absence of heparin, the diffraction pattern of apoA-I suggests that the aggregates are amorphous, with no deducible secondary structural content. A large reflection at 3.27 Å, does not coincide with β-sheet spacing. Thus, it does not suggest that the formation of amyloid occurs under these conditions (**Figure 4.24A** and **B**).

However, in the presence of heparin, 2 distinct reflections are detected with d-spacings of 4.47 Å and 9.7 Å (**Figure 4.24C** and **D**). These both coincide with the predicted spacings for β-sheet structures, approximately 4.7 Å and 10 Å for equatorial and meridional reflections, respectively (Li et al., 2009). These reflections coincide with the spacings between the individual β-strands, running perpendicular to the fibril axis; and the distance between the multiple β-sheet layers, as described in **Figure 1.10**. Separation of the equatorial and meridional reflections was not possible, due to the inability to align the fibrils in the capillary tube.

In summary, despite both the aggregates formed alone and in presence of heparin exhibiting a ThT response and binding to Congo red, only the aggregates formed in the presence of heparin produce X-ray diffraction reflections, consistent with the presence of β-sheets.

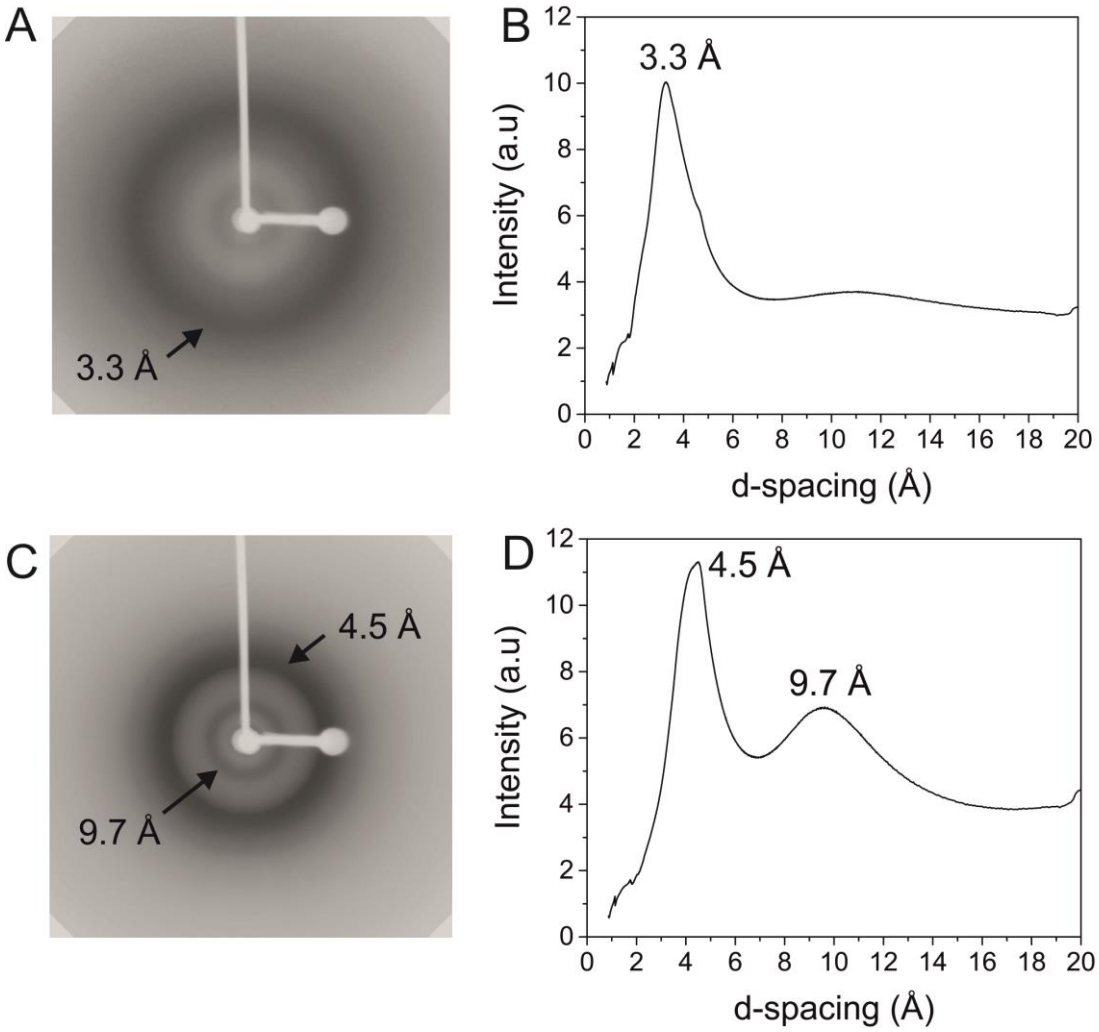

Figure 4.24. X-ray diffraction pattern of apoA-I (36 μM), after incubation at pH 4 in the absence (**A and B**) and presence (**C and D**) of heparin for several days. Arrows in **A** and **C** highlight the reflections detected as peak intensities in the 1D spectra.

4.4. Discussion

Much of the current literature on apoA-I aggregation *in vitro* focuses on the first 90-100 residues of the N-terminus, which become cleaved from the full peptide and deposited as amyloid, leading to familial apoA-I amyloidosis (Raimondi et al., 2011; Girych et al., 2014; Das et al., 2016; Monti et al., 2011; Sipe et al., 2014). Studies into the aggregation of full-length apoA-I have determined that acidification or oxidation of the protein can induce misfolding, which leads to a structural rearrangement, resulting in the formation of insoluble material, with many amyloid characteristics (Ramella et al., 2011; Chan et al., 2015; Mucchiano, Jonasson, et al., 2001).

The aim of this chapter of research is to provide a more detailed description of the factors that influence apoA-I aggregation, and to identify physiologically suitable conditions for promoting the aggregation of full-length apoA-I into amyloid species. These conditions will then be used to produce large quantities of apoA-I derived amyloid, allowing structural analysis of the insoluble material.

4.4.1. Acidic pH induces apoA-I aggregation

Initial experiments repeated the work by Ramella (2011) and looked at the effect of pH on apoA-I aggregation. By incubating apoA-I over a pH range of 4-8 for 3 days, it was shown that apoA-I readily forms insoluble aggregates at acidic pH, in particular, pH 4 and pH 5. This experiment also confirmed that apoA-I was not converted into insoluble material at neutral and basic pH, suggesting the protein is stable in these conditions.

The insoluble material at acidic pH also produced an increase in ThT fluorescence at 482 nm. Upon sedimentation of the insoluble protein through centrifugation, a large decrease in ThT fluorescence in the supernatant was observed. This confirms that the insoluble aggregates were the source of the ThT response, and that the majority of the ThT responsive material is retained in the insoluble material. At neutral and basic pH, no increase in ThT fluorescence was observed, confirming the stability of apoA-I under these conditions. ThT fluorescence response was shown to be dependent on protein concentration, suggesting a nucleation-based growth mechanism of apoA-I in the absence of heparin. The amount of amyloid formed, and thus the ThT response, is a linear function of the free monomeric protein available (Cabriolu et al., 2010).

ApoA-I aggregates formed at pH 4 in the absence of heparin were able to bind to Congo red and exhibited a green birefringence upon cross-polarisation, suggesting the aggregates are amyloid-like. However, when visualised by TEM, large amorphous aggregates became deposited as clumps of non-fibrillar material. These aggregates did not produce X-ray diffraction patterns consistent with β-sheet structures, although a broad reflection at 3.3 Å may mask any β-sheet contributions.

Maximum fluorescence emission of the 4-tryptophan residues in apoA-I at 337 nm suggests they are located within hydrophobic regions, which is consistent with natively folded apoA-I at neutral pH. The reduction in intensity results from the high percentage of material that becomes converted into insoluble aggregates at pH 4, but the emission peak remains mostly unchanged.

These findings are physiologically relevant. In normal circulation, where the pH of serum is roughly neutral, lipid-free apoA-I avoids aggregation, in order

to carry out its role in cholesterol clearance. However, at acidic pH, such as those experienced at sites of inflammation or atherosclerotic plaques (Ross, 1999a; Thijssen and Mensink, 2005), the protein readily undergoes aggregation into insoluble material. This is significant, since it is at atherosclerotic sites where full-length apoA-I has been found deposited as amyloid. This material gives rise to a ThT response and a green birefringence when stained with Congo red, both of which are suggestive of amyloid. However, these aggregates lack many of the amyloid hallmarks, including their morphology, XRD patterns and the fluorescence of tryptophan residues suggesting the environments remain similar to the natively folded apoA-I.

4.4.2. Heparin induced apoA-I aggregation

Glycosaminoglycans, as described in **section 1.1.5**, have been shown to associate with amyloid deposits (Cohlberg et al., 2002; Iannuzzi et al., 2015), and are involved in promoting amyloidosis in protein species with no natural propensity to form amyloid (Madine et al., 2013). Sedimentation experiments deduced that the percentage of starting material that was converted into insoluble material remained the same in both the absence and presence of heparin, across the entire pH range studied.

However, the insoluble material formed at acidic pH in the presence of heparin showed enhanced ThT fluorescence, compared to the material formed in its absence. The enhanced ThT response in the presence of heparin is not observed at neutral and basic pH, suggesting that the binding of heparin to apoA-I is dependent on ionic interactions (Stewart et al., 2016). Heparin only induces an aggregation response in apoA-I when incubated at acidic pH, with a dramatic

enhancement in ThT fluorescence at pH 4 and pH 5. These two pH conditions are both below the isoelectric point of apoA-I, which was predicted by the online Expasy server to be 5.4 (Gasteiger et al., 2003). At pH 4 and 5, apoA-I carries net positive charges, which can bind ionically to the heparin molecule. The addition of sodium chloride systematically reduces the ThT enhancement caused by the introduction of heparin, further confirming the interaction between apoA-I and heparin is electrostatic.

ApoA-I was shown to bind heparin with micromolar affinity, and induce aggregation in a concentration-dependent manner. The addition of increasing concentrations of heparin led to a rapid increase in ThT fluorescence, which was dependent on the heparin concentration and not consistent with a nucleation-dependent mechanism. This initial increase was followed by a slower increase in ThT fluorescence, the rate of which was independent of heparin concentration, consistent with a secondary nucleation event.

ApoA-I aggregates formed in the presence of heparin bind to Congo red, and exhibit a green birefringence upon cross-polarisation. Unlike the insoluble aggregates formed from apoA-I alone, apoA-I aggregates formed in the presence of heparin also have a morphology more consistent with amyloid-like fibrils, and produce XRD patterns that suggest the presence of β-sheet structures. Intrinsic fluorescence spectra suggest that aggregation of apoA-I in the presence of heparin results in a less polar environment surrounding the tryptophan residues, consistent with amyloid formation.

4.4.3. Oxidation induced apoA-I aggregation

Oxidation of methionine residues in apoA-I has been shown to promote aggregation of the apoA-I at pH 6 (Wong et al., 2010). Here, upon acidification to pH 6, the oxidised apoA-I produced large quantities of white precipitate. This insoluble material gave rise to a ThT response, a morphology consistent with both amyloid fibrils and oligomeric species, and a blue shift in the fluorescence maximum of tryptophan residues. This blue shift suggests the conversion to a less polar structure, consistent with amyloid formation. This data suggests that oxidised apoA-I is more susceptible to amyloidosis than un-oxidised apoA-I.

4.4.4. Aggregation of apoA-I mutants

ThT fluorescence and the percentage insolubility of mutant apoA-I species were used to determine the aggregation propensity of apoA-I mutants, compared to wild type apoA-I. The G26R mutant was shown to have similar propensity to aggregate as the wild type at acidic pH but unlike the wild type, G26R had an increased ThT fluorescence and percentage insolubility at neutral pH. Both of the cysteine mutants, the K96C and R173C, showed no increased propensity to aggregate when compared to the wild type apoA-I. This makes them both suitable candidates for fluorescent tagging, in order to study cellular internalisation and distribution of apoA-I models. The apoA-I (46-59) peptide was monitored, via ThT and sedimentation experiments, in order to determine suitable conditions to allow structural comparisons to the wild type, full-length apoA-I. ApoA-I (46-59) at pH 4 in the absence of heparin produced a ThT response and morphology consisting of amyloid fibrils. However, the addition of heparin showed no increase in ThT fluorescence, unlike the full-length peptide.

4.4.5. Conclusion

In conclusion, the data presented here confirm that the acidification of apoA-I induces at least a partial conversion from the native structure of apoA-I into insoluble aggregates that, despite giving rise to a ThT response and Congo red birefringence, lack many of the hallmarks of amyloid.

However, upon inclusion of heparin, more ordered aggregates are formed with an enhanced ThT response. These aggregates produce a birefringence when stained with Congo red, have a more fibrillar morphology, and produce an X-ray diffraction pattern, suggestive of β-sheet structures. Intrinsic fluorescence suggests a difference in the aggregation mechanism of apoA-I in the presence of heparin, resulting in a more amyloid-like structure.

Oxidation of apoA-I gives rise to insoluble aggregates that match all of the amyloid characteristics of the apoA-I aggregates formed at pH 4 in the presence of heparin, but produce fibrils with a typical amyloid morphology, including potential oligomeric species.

Work in Chapter 5 will look into whether the inclusion of heparin or oxidiation of apoA-I results in a structural difference between the insoluble aggregates, compared to apoA-I alone. The conditions determined here that will be taken forward for the structural analysis of apoA-I include: a concentration of 36 μM wherever possible, an apoA-I: heparin molar ratio of 1:2 and incubation at pH 4 with agitation for 3 days.

5. Structural analysis of apoA-I aggregates

5.1. Introduction

Characterising the structure of apoA-I derived amyloid is essential for understanding the mechanism of apoA-I aggregation. With this knowledge, advancing the design of apoA-I amyloid inhibitors is possible, as is determining whether any intermediate aggregates are formed during the aggregation mechanism that could be cytotoxic (Amijee et al., 2012; Walsh et al., 2002; Uversky, 2010). Given the insolubility of amyloid, and the rate at which apoA-I readily aggregates into insoluble material upon acidification, the aggregates prove difficult to study using standard structural techniques. X-ray crystallographic analysis of amyloid fibrils has proved difficult, due to the large and heterogeneous nature of the aggregates (Toyama and Weissman, 2011). Eisenberg's group were able to produce micro-crystals, 6-7 residues in length, for the yeast Sup35 amyloidogenic protein, and acquire adequate diffraction data (Nelson et al., 2005). However, the limitations on the size of these amyloid fragments, and the inability of all peptides to form micro-crystals still restrict the use of X-ray crystallography (Toyama and Weissman, 2011). Studying amyloid is also not amenable to solution NMR and therefore, solid-state NMR is required.

Currently, there are no structural models for apoA-I derived amyloid deposited within the protein databank. In fact, there are only full-length models for the most studied amyloidogenic proteins, in particular: Aβ (Tycko, 2011; Madine et al., 2012; Paravastu et al., 2009; Paravastu et al., 2008; Serpell, Blake, et al., 2000), α–synuclein (Tuttle et al., 2016), IAPP (Soriaga et al., 2015) and AL amyloidosis (Brumshtein et al., 2015; Brumshtein et al., 2014).

Many studies get around the challenges in studying the structure of amyloid by utilising model systems consisting of peptide regions from within the full-length amyloid-associated protein (Nelson et al., 2005; Petrlova et al., 2014; Serpell, Blake, et al., 2000; Gursky et al., 2012; Borhani et al., 1997). However, the structure of the aggregated material is very sensitive to the protein sequence, thus, truncation or mutation of amino acid residues can dramatically change the overall structure of the amyloid deposited, compared to the parent protein. For example, full-length Aβ (1-40), forms parallel β-sheets (Petkova et al., 2002), whilst fragments of the peptide, including the 16-22 and 11-25 residues, form anti-parallel β-sheets (Petkova et al., 2004).

5.1.1. Structure of natively folded apoA-I

As described in **section 2.4.3,** and shown in **Figure 2.4** of this thesis, only 4 structural models for soluble, native apoA-I exist in the protein databank, all of which are derived from soluble apoA-I. The 3 models corresponding to the most complete protein are of (i) lipid-free apoA-I (Δ185-234) at 2.2 Å resolution, deduced by X-ray crystallography (Mei and Atkinson, 2011); (ii) the full-length, lipid-bound apoA-I at a much lower resolution, using small angle neutron scattering (Wu et al., 2009); and (iii) lipid-bound apoA-I (44-243) at a resolution of 4 Å, using X-ray crystallography (Borhani et al., 1997). Crucially, there are no structural details for the insoluble apoA-I aggregates. Here, structural analysis via circular dichroism and nuclear magnetic resonance will be acquired for the lipid-free apoA-I aggregated material. As such, all future comparisons to the native apoA-I will refer to the PDB 3R2P (Mei and Atkinson, 2011) lipid-free structure.

5.1.2. Secondary structural content

The structure of apoA-I (Δ185-243), described in **section 2.4.4.1**, contains approximately 60-80 % α-helical content (Mei and Atkinson, 2011), and is in good agreement with other studies of the full-length apoA-I (Chetty et al., 2009). The remaining peptide, such as the region corresponding to residues 44-55, consists of predominantly β-sheet structures (Mei and Atkinson, 2011; Gursky et al., 2012). The C-terminus of apoA-I is involved in lipid binding and, as such, it possesses a large degree of flexibility. In the absence of lipids, this region is disordered. However, upon interaction with lipids or other apoA-I molecules, it reforms into an amphipathic helix, as shown in **Figure 5.1** (Chetty et al., 2009). This structural change was determined by site-directed, spin-label electron paramagnetic resonance spectroscopy (Oda et al., 2003)

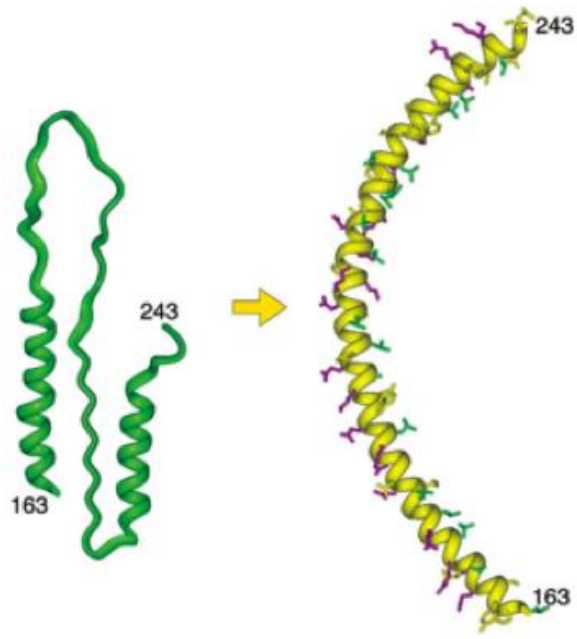

Figure 5.1 Structural conversion of the apoA-I C-terminus (residues 163-243), from a lipid-free conformation (green), to the extended helices, observed in the presence of lipids (yellow). Image taken from Oda *et al.* (Oda et al., 2003)

5.1.3. Techniques used to study the structure of apoA-I

Here, circular dichroism and, for the first time, SSNMR were used to determine the structural changes underlying apoA-I aggregation. Circular dichroism techniques can be used for solution and solid-states (thin film CD), with solution CD having been used to study many amyloidogenic proteins (Bieschke et al., 2010; Huang et al., 2000; Raimondi et al., 2011; McLaurin et al., 1998; Srinivasan et al., 2003; Jiménez et al., 2002; Chiti and Dobson, 2006).

5.1.3.1. Circular Dichroism

Circular dichroism (CD) is a powerful spectroscopic technique that can be used to rapidly determine the local secondary structure of proteins. Circular dichroism measures the difference in absorption of left and right handed circularly polarised light by molecules with chiral centres, as a function of wavelength (Li et al., 2009; Fasman, 1996). A beam of light contains electric and magnetic fields, and upon polarisation, the electric field (E) will oscillate in a single plane. This wave can be visualised as the combination of two vectors of equal length, but 90 ° out of phase (**Figure 5.2A**). These vectors trace out circles, one of which that rotates clockwise (E_R) and the other counter-clockwise (E_L), oscillating about the direction of propagation **(Z)**. The X and Y components of right-handed circular polarised light are shown in **Figure 5.2B**, and the vector sums in **Figure 5.2C**. The resulting right-handed electric wave (E_R) is depicted in **Figure 5.2D.**

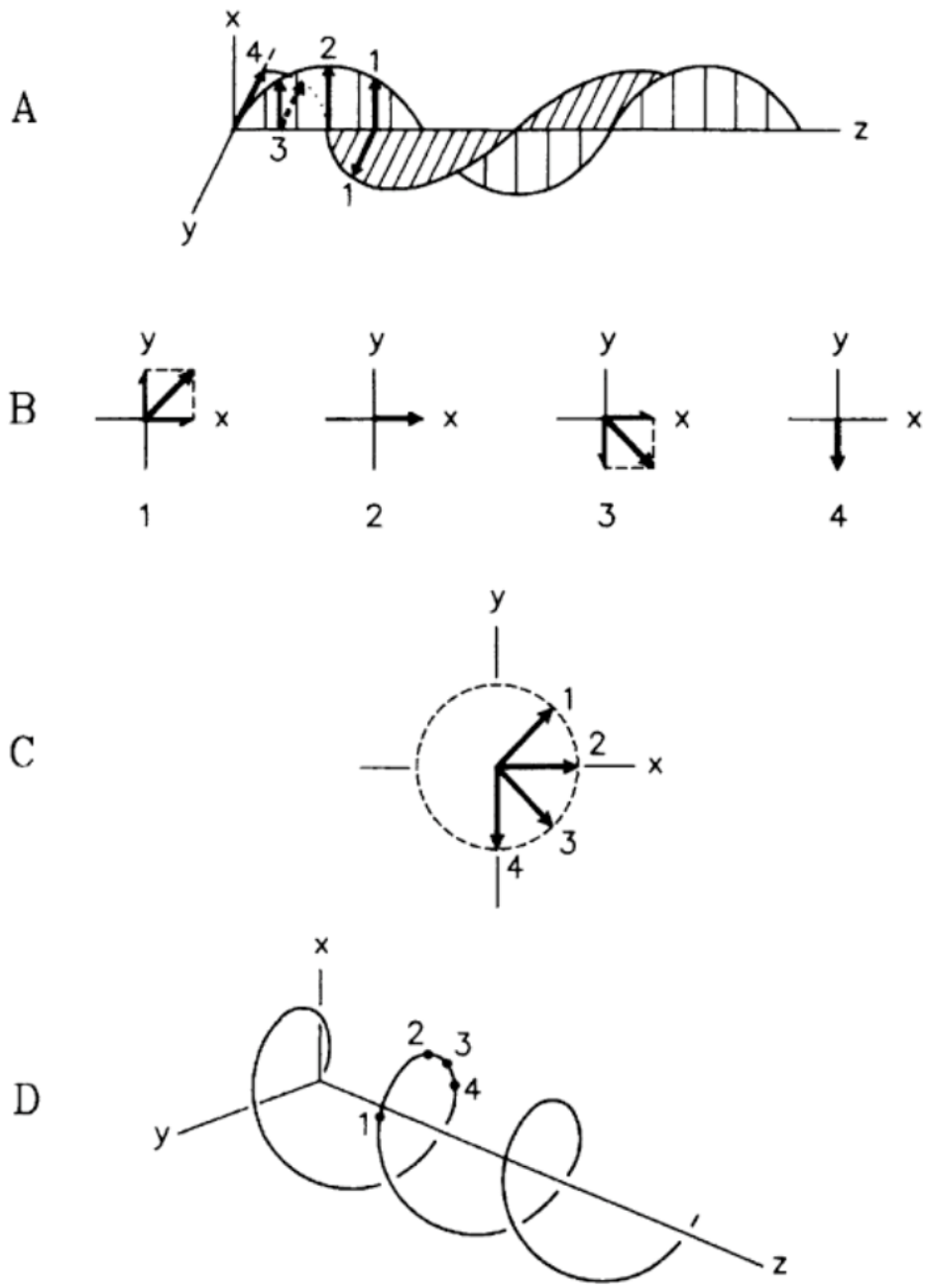

Figure 5.2 Description of right hand circularly polarised light. (**A**) The electric vectors, 90 ° out of phase, along the direction of light propagation (z), (**B**) the X and Y components of the electric vectors, (**C**) resulting sum of the vectors, highlighting a circular motion when viewed along the Z axis, and (**D**) right-handed circularly polarised light oscillating along the Z axis. Figure taken from Fasman (1996).

When asymmetric molecules with chiral centres interact with light, the chromophores in the molecule will absorb the left and right-handed circularly polarised light to different extents. In proteins, the CD active chromophores include the amide group in the peptide backbone, and the phenyl, phenolic and indole groups of the Phe, Tyr and Trp aromatic amino acid side chains, respectively (Fasman, 1996). The UV-CD spectra of proteins are dominated by contributions from the π to π* and n to π* electron transitions of the amide group in the peptide backbone (**Figure 5.3**). These transitions, and thus the spectra, are influenced by the geometry of the protein backbone, in particular the ϕ and ψ angles, which is highly sensitive to secondary structure (Whitmore and Wallace, 2008). Due to the well-defined $\phi 32$ and ψ angles in α-helical conformations, compared to the variability in β-sheet structures, structural analysis by circular dichroic is much more accurate at determining helical contributions (Whitmore and Wallace, 2008). However, CD spectra reflect the overall secondary structure of the protein.

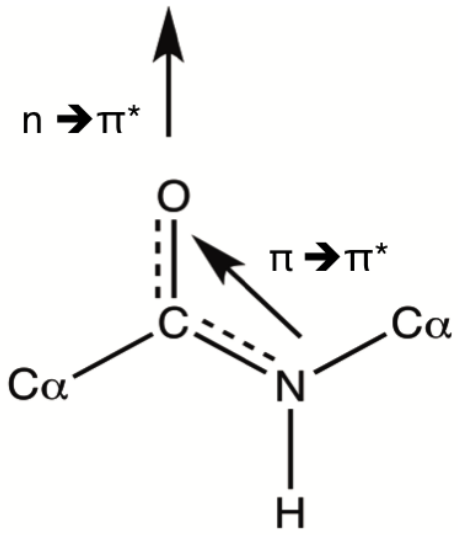

Figure 5.3 Structure of the peptide bonds with the orientation of the transition dipoles π to π* and n to π*.

For example, α-helical proteins produce a spectrum with negative bands at 222 nm, from the n➔π transition; 206 nm, from the parallel π➔π* transition; and a positive band at 190 nm from the perpendicular excitation π➔π* transition, as shown in **Figure 5.4** (Holzwarth and Doty, 1965). β-sheet structures produce negative bands at 218 nm and positive bands at 195 nm (Greenfield, 2007). CD values can be de-convoluted and fitted using algorithms based on libraries of proteins with known secondary structure to deduce the protein's secondary structural content (Whitmore and Wallace, 2008). However, the disadvantages to this technique include its inability to distinguish between a solution of homogenous proteins containing multiple secondary structure elements, and a heterogeneous sample consisting of some proteins containing just one secondary structural element, and other peptides containing another (Li et al., 2009).

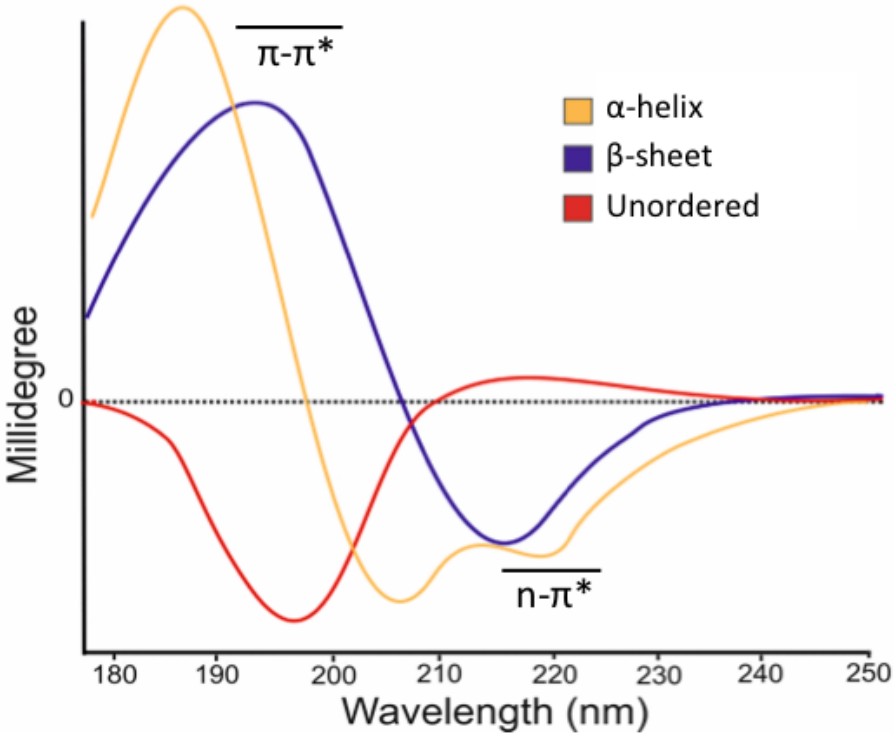

Figure 5.4 Far UV circular dichroism spectra of the main protein secondary structural elements.

5.1.4. Nuclear magnetic resonance

NMR is a powerful technique that can be utilised to study the structure and dynamics of proteins and has been since the late 1950's (Wuthrich, 2001; Kay, 2005), following its discovery in 1946 (Mlynarik, 2016). To date, 11,732 protein structures have been deposited in the Protein Data Bank determined by NMR, whilst only 99 have been produced through solid-state NMR techniques, with over 10 % of these structures based on the Aβ peptide (Berman et al., 2000).

5.1.4.1 Nuclear magnetic resonance theory

Nuclear magnetic resonance is a phenomenon in which the nuclei of atoms that contain a non-zero spin and a magnetic moment (μ_0), for example ^{1}H, ^{13}C and ^{15}N, interact with a static magnetic field (B_o). In the absence of a magnetic field, the nuclei's magnetic moments are randomly orientated, with equal energies and no net magnetisation. Upon its application, the B_0 magnetic field orientates the nuclear spins, which acts as a magnetic dipole moment, into either a low or high-energy state, with respect to the direction of B_0. This process is called the Zeeman effect (Mlynarik, 2016; Luca et al., 2003; Veeman, 1997; Hore, 1995).

For this introduction, the high-energy, antiparallel state will be referred to as β and the low-energy, parallel state as α. The difference between these 2 energy states (ΔE) is dependent on the strength of B_0 (as described in **Figure 5.5**), the gyromagnetic value of the nucleus of interest (γ) and Planck's constant ($h/2\pi$), which is outlined in **Equation 5.1** (Hore, 1995). At equilibrium, more nuclei align with B_0 in the low-energy state, than oppose B_0 in the high-energy state.

$$\boldsymbol{\Delta E = h\gamma B_0} \qquad \textbf{[5.1]}$$

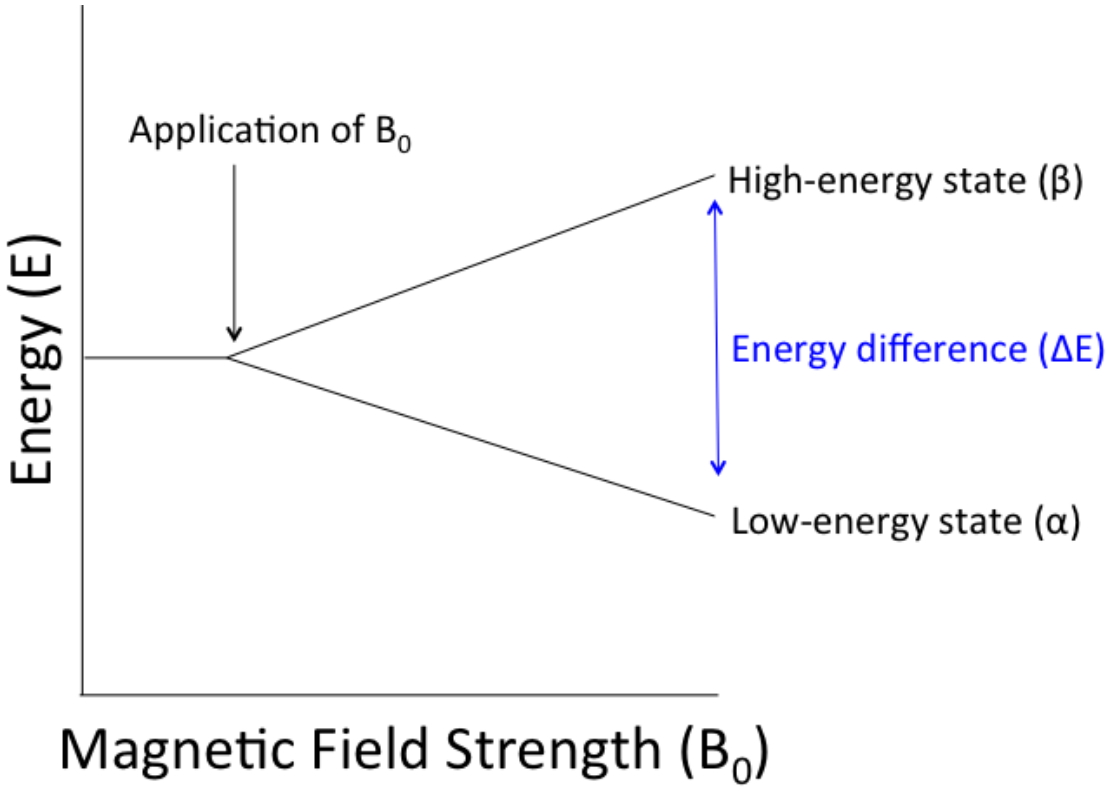

Figure 5.5 Schematic detailing the orientations of a nuclei's magnetic moment upon interaction with a magnetic field (B_0), in either the high (β) or low (α) energy state, giving rise to an energy difference (ΔE).

The population of nuclei in the high and low energy states is temperature-dependent, and thus, can be calculated by the Boltzmann distribution in **Equation 5.2**. In this equation, Nα and Nβ refer to the population of nuclei in the low and high-energy states, respectively; k_B is Boltzmann constant (1.3805 x10^{-23} m^2 kg s^{-2} K^{-1}), and T is temperature in Kelvin.

$$\frac{N\alpha}{N\beta} = \exp\left(\frac{\Delta E}{k_B T}\right) \qquad [5.2]$$

The net magnetisation difference observed between the high and low energy states is negligible, compared to the perpendicular B_0 strength, thus it cannot accurately be measured. Therefore, the orientation of the net magnetisation is transferred to a transverse plane by addition of a second, pulsed magnetic field B_1 at radiofrequency and perpendicular to the B_0 field, at 90 °. This results in the net magnetisation shifting away from the B_0 direction towards the B_1 (**Figure 5.6**), allowing detection (Mlynarik, 2016).

If the B_1 magnetic field is at a frequency that matches the ΔE of the target nuclei, referred to as the Larmor frequency, the nucleus absorbs the energy. This energy causes a perturbation in the orientation of the nuclear spin, causing re-alignment, with respect to the direction of B_0 (Rabi et al., 1938; Becker, 1993; Cavanagh et al., 1995; Becker, 1999; Bothwell and Griffin, 2011; Veeman, 1997).

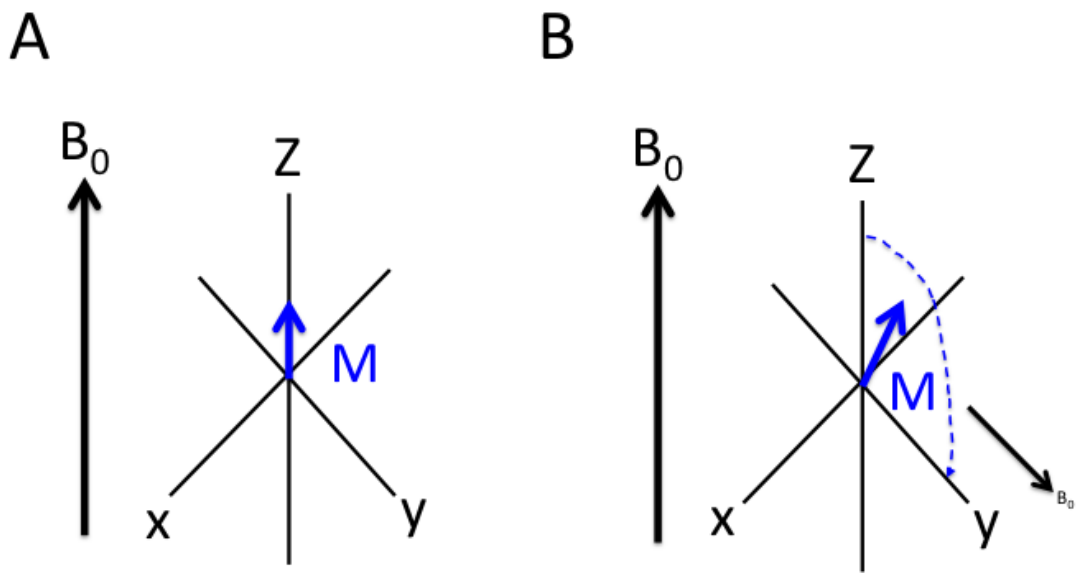

Figure 5.6 Net magnetisation of the nuclei's magnetic moments in (**A**) the B_0 magnetic field, along the Z axis, and (**B**) the B_0 and B_1 magnetic fields perpendicular to each other, resulting in a transfer of the net magnetisation away from the Z axis.

5.1.4.2 Relaxation times

The relaxation time of atoms in NMR experiments is described by two factors. The longitudinal relaxation (T_1), is the time required for the populations of the two nuclei spins to return to equilibrium, and has the rate constant $R_1=(1/T_1)$. The transverse relaxation (T_2), refers to the loss of phase coherence from the nuclei, and is the time taken for the net magnetisation to restore back to the original orientation, parallel to B_0, following the pulsed B_1. T_2 and has the rate constant $R_2=(1/T_2)$. T_2 is usually smaller than T_1 (Mlynarik, 2016). The rate at which repeated NMR scans can be obtained is dependent on the T_1 time (Wink, 1989; Cavanagh et al., 1995).

5.1.4.3 Chemical shift

The location of a nucleus with a molecule alters the magnetic field strength observed (B_0), and therefore, the size of the ΔE and Larmor frequency. These changes are referred to as the chemical shift (σ), a standardised unit described in parts per million (ppm), and calculated using **Equation 5.3**. This equation is based on the Larmor frequency of the nucleus of interest (ϖ) and the Larmor frequency of a standard nucleus (ϖ_{ref}), both measured in Hz. For ^{1}H NMR this standard is a proton in tetramethylsilane (TMS), which is given a chemical shift (σ) of 0 ppm (Mlynarik, 2016).

$$\sigma = \left(\frac{\varpi - \varpi_{ref}}{\varpi_{ref}}\right) \times 10^6 \qquad [5.3]$$

5.1.4.4 Chemical shielding

The biggest contributor to changes in chemical shift come from electron shielding. The observed nuclei are surrounded by electrons, each of which possesses their own small magnetic moment. These magnetic moments align in an orientation against the external magnetic field (B_0) direction. This leads to a net loss in magnetisation observed at the nucleus, resulting in a smaller Larmor frequency. **Equation 5.4** shows how B_{Local} (the effect of electron shielding) decreases the B_0, resulting in B_{ob}, the observed magnetic field.

$$\boldsymbol{B_{Observed} = B_{Applied} - B_{Local}} \qquad [\mathbf{5.4}]$$

The electron shielding of nuclei varies dramatically (Hz scale), depending on the specific environment of the nucleus (Cavanagh et al., 1995; Mlynarik, 2016). This is why TMS is used as the standard for both ^{1}H and ^{13}C NMR spectroscopy (**Figure 5.7**), the highly electron-donating silicon means that both the ^{1}H and ^{13}C nuclei are fully shielded (Hoffman, 2006; Mlynarik, 2016). Any reduction in electron shielding caused by the attachment of target nuclei to electron withdrawing groups results in a downfield shift of the chemical shift, to higher ppm values.

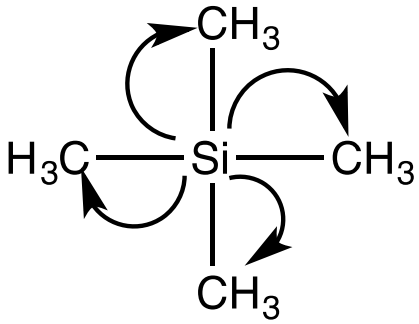

Figure 5.7 Chemical structure of TMS, highlighting the electron donating silicon that ensures full electron shielding of the adjoining carbon atoms.

5.1.4.5 Spin-spin (J) coupling

Nuclei of the same atom experiencing the same environment are referred to as equivalent, and will have the same chemical shift. Non-equivalent nuclei can interfere with the chemical shift of other nuclei by exerting an influence, both positive and negative, on the strength of the magnetic field observed (B_{ob}) by the nuclei of interest (Fukui, 1999; Becker, 1999; Bothwell and Griffin, 2011). This is called J coupling and effects nuclei within 3 bond lengths. J coupling leads to "splitting" of the NMR peaks by the n+1 rule, where n is the number of neighbouring nuclei (Cavanagh et al., 1995; Foster et al., 2007; Mlynarik, 2016), as demonstrated by the schematic in **Figure 5.8**. This coupling is independent of the orientation of the nucleus (Veeman, 1997). Splitting by spin-spin coupling can be used to assign NMR signals of similar nuclei, such as multiple CH_3 groups.

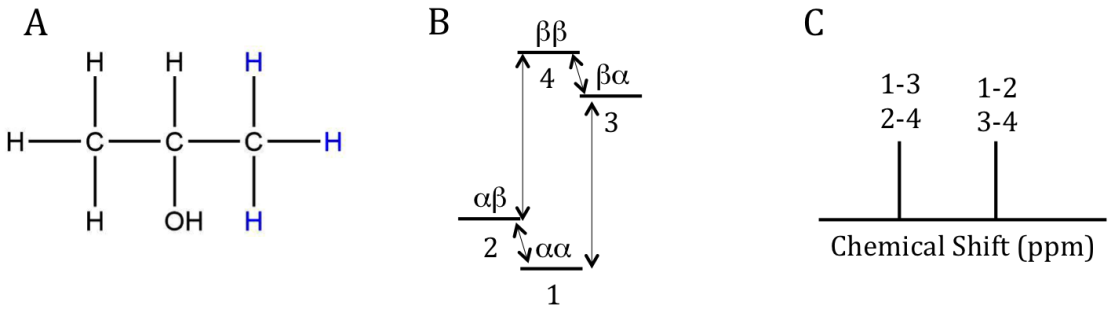

Figure 5.8 (**A**) Structure of propan-2-ol, highlighting the CH_3 protons of interest (blue) and (**B**) the energy states possible from splitting of the CH_3 environment by the hydrogen on the adjacent carbon. (**C**) The doublet peak in the CH_3 region of the ^1H NMR spectrum.

5.1.4.6 Dipolar coupling

J coupling requires the two interacting nuclei to be connected via chemical bonds. However, dipole-dipole interactions occur through space, and their strength is related to the distance (r) between 2 nuclei (I and S) cubed, and the angle of interaction (θ), as shown in **Figure 5.9**. The limit of dipole interactions is approximately 10 Å. The relationship between the strength of the dipole coupling, the distance and the angle are given in **Equation 5.5**. Here, μ_0 is the vacuum permeability constant and λ is the nuclear magnetogyric ratio.

$$H_D = \left(\frac{\mu_0}{4\pi}\right)\lambda^2\left(\frac{3cos^2\theta-1}{2r^3}\right) \qquad [5.5]$$

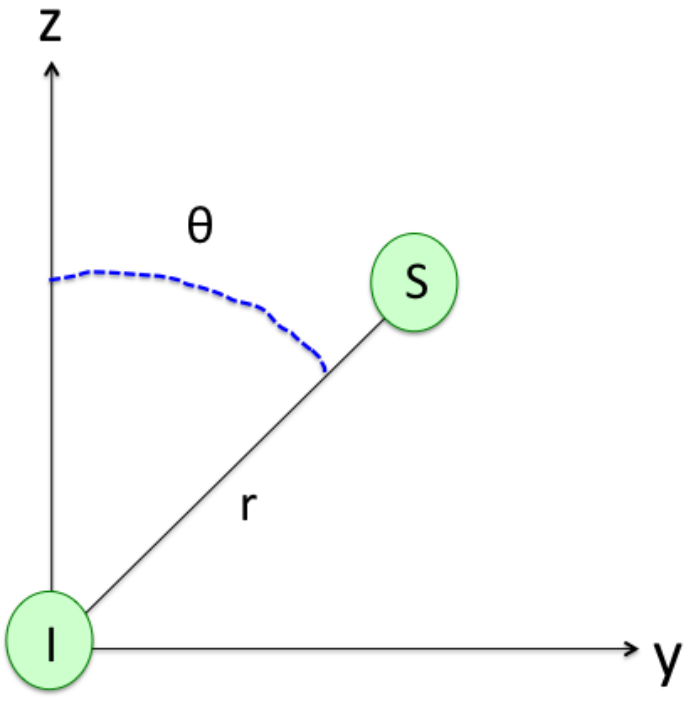

Figure 5.9 Dipolar coupling between two nuclei, I and S each with their own gyromagnetic value (γ) and a distance (r) of up to 10 Å.

Therefore, these couplings can be influenced by the tertiary or quaternary structure of a protein. Dipole-dipole interactions are caused by the magnetic effect of one nucleus influencing the observed magnetic field on a neighbouring nucleus; this can be the same nucleus (homonuclear) or a different nucleus (heteronuclear). These interactions are averaged out in solution-state NMR via Brownian tumbling. However, in solid-state NMR, these anisotropic dipolar interactions cause increased breath of peaks and lead to lower resolution spectra (Foster et al., 2007; Becker, 1999; Veeman, 1997).

5.1.4.7 Solution and solid-state NMR

In solution-state NMR, the natural Brownian tumbling of molecules within the solution averages out the anisotropy of dipole and chemical shielding interactions, leading to a well resolved spectrum with narrow peaks. In SSNMR, the fixed orientations of each molecule leads to orientationally distributed chemical structures, which produce broad peaks on the spectrum (Foster et al., 2007; Pines et al., 1973; Veeman, 1997), as shown in **Figure 5.10**. By utilising a combination of ultrahigh magnetic fields, magic angle spinning, proton decoupling and cross-polarisation techniques, high resolution solid-state spectra can be achieved that allow assignment of individual residues and determination of protein structure (Luca et al., 2003). The effect of each of these techniques will be discussed below.

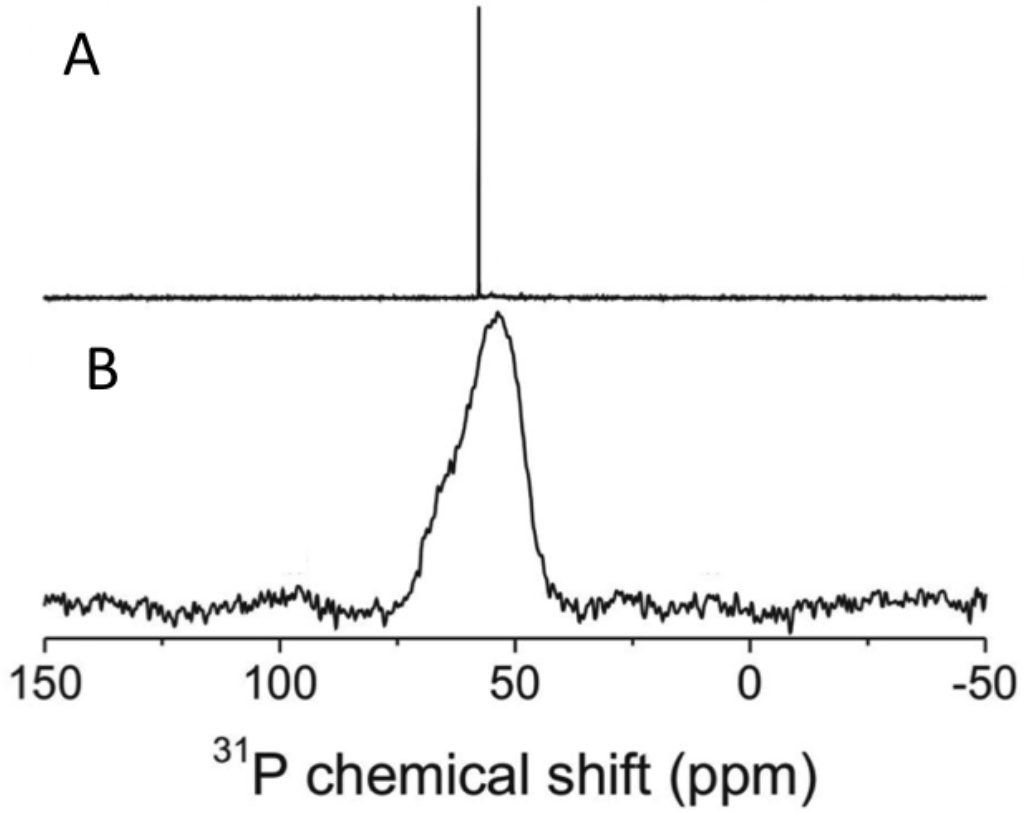

Figure 5.10 (**A**) Solution ^{31}P NMR and (**B**) solid-state ^{31}P CP MAS SSNMR spectra of DPPBA-truncated gold nanoparticles. Image taken from Marbella *et al.* (2016).

5.1.4.8 Magic angle spinning

Increased line width is a result of the inability of solid samples to tumble freely, leading to anisotropic dipole-dipole interactions and chemical shifts. Only the spin-spin interactions (J couplings) are consistent between solution and solid-state NMR, since these are not dependent on the nuclei's orientation. **Equation 5.5** indicates the angular dependence on the Hamiltonian equation, with the dipole-dipole interaction proportional to $(3\cos^2\theta-1)$. In solid-state experiments, the orientation of the nuclei, and thus the angle between two interacting dipoles (θ), is not consistent. However, when the sample is spun at an angle of 54.7 °, the angular term is removed (Bothwell and Griffin, 2011; Tycko, 2006).

Under these conditions, removal of the anisotropic chemical shifts and dipole-dipole interactions leads to a narrow spectrum, as shown in **Figure 5.11** (McDermott, 2009; Tycko, 2006).

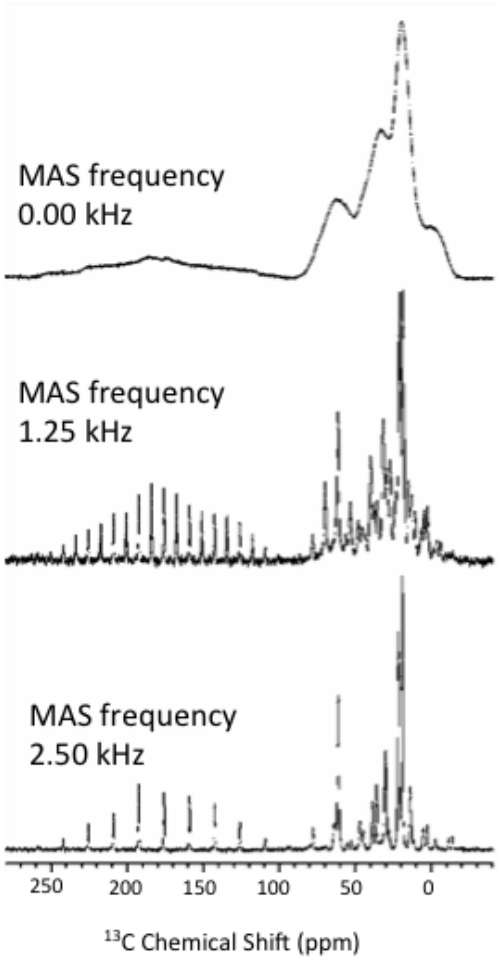

Figure 5.11 ^{13}C SSNMR spectrum of L-valine powder with increasing frequencies of MAS spinning. Image taken from Tycko (2006).

5.1.4.9 Cross-polarisation

Cross-polarisation (CP) involves transferring polarisation from nuclei with a high gyromagnetic ratio, such as hydrogen, to nuclei with a low ratio, such as ^{13}C and ^{15}N. This technique is often used to increase the relatively low sensitivity of ^{13}C and ^{15}N signals in proteins (Levitt et al., 1986; Kolodziejski and Klinowski, 2002;

Morris, 1980). In order for this to occur, the system has to adhere to the Hartmann-Hahn principle, outlined in **Equation 5.6**, where γ and B_1 are the gyromagnetic ratio and magnetic field strength of the abundant I nucleus, usually ^{1}H and the less sensitive S nucleus, such as ^{13}C, respectively.

$$\gamma I B_1 I = \gamma S B_1 S \qquad [5.6]$$

The ^{1}H magnetisation is orientated by an electromagnetic field at its Larmor frequency. The ^{13}C or ^{15}N resonance is obtained at the same time with a second electromagnetic field. As long as the 2 separate nuclei have the same Larmor frequency, a cross-relaxation and transfer of magnetisation will occur, from ^{1}H to ^{13}C or ^{15}N (Hartmann and Hahn, 1962). In the case of ^{13}C, the signal is enhanced up to 4 fold, as shown in **Figure 5.12**. The magnetisation grows, based on the CP rate (T_{HC}), which is dependent on the number of protons (Kolodziejski and Klinowski, 2002) and the distance between two nuclei. After reaching a maximum, the magnetisation decays, based on the I spin T_1 relaxation time (Fyfe et al., 2005). This allows increased acquisition of the spectra, since the T_1 relaxation time is dependent on the pulsed excitation of the proton, rather than the carbon nucleus. The pulse sequence for a basic Hartmann-Hahn cross-polarisation experiment is shown in **Figure 5.13.** The net magnetisation of the proton nucleus is shifted from the Z plane into the XY transverse plane by addition of a pulse at 90 °. Simultaneous spin locking pulses (B_1I and B_1S) are applied at, or close to, the resonance frequency of both the I and S nuclei, satisfying the Hartmann-Hahn condition. During this period (the contact time) the polarisation transfers from the I to the S nucleus. The B_1S field is switched off, allowing its free induction decay (Kolodziejski and Klinowski, 2002).

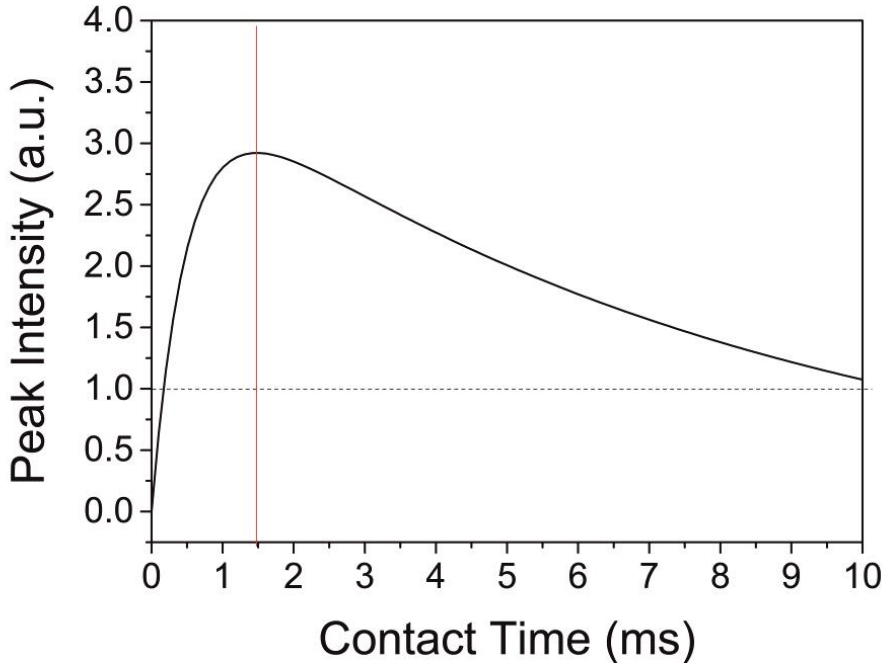

Figure 5.12 Magnetisation on the ^{13}C grows, based on the CP rate (T_{HC}), to a maximum contact time, before decaying, which is dependent on T^{I}_{1}, not the T^{S}_{1}.

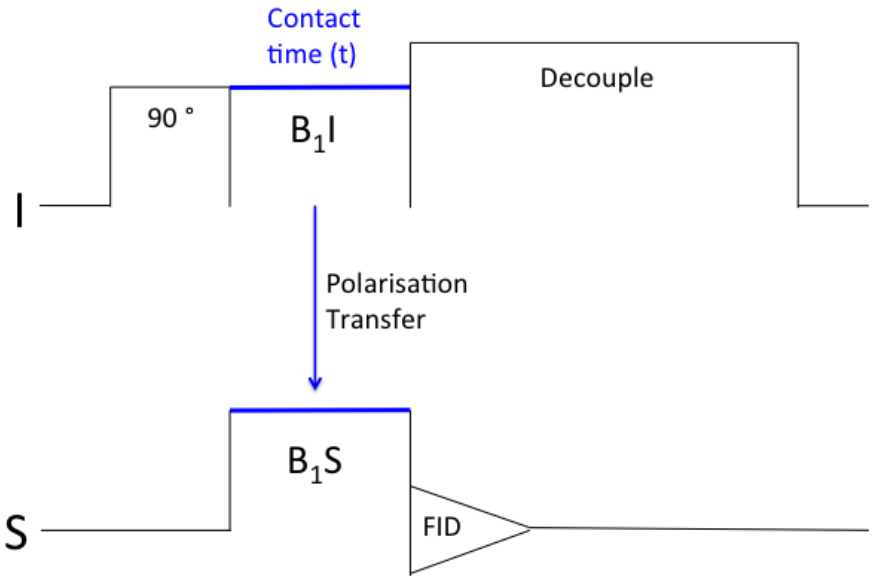

Figure 5.13 Cross-polarisation pulse sequence. The net magnetisation of the abundant nuclei (I) is shifted into the transverse plane by an initial magnetic field at 90 °. B_1I and B_1S, which satisfy the Hardmann-Hahn principle, are applied simultaneously, producing a contact time (t) where polarisation can cross from the I nucleus to the more sensitive S nucleus. (Kolodziejski and Klinowski, 2002).

5.1.4.10 INEPT polarisation transfer

Cross-polarisation, as mentioned above, is utilised in the majority of protein solid state MAS NMR experiments, in order to increase the signal detectable from the ^{13}C and ^{15}N nuclei. However, this technique requires heteronuclear dipolar couplings in order to transfer the cross-polarisation. These dipole interactions are averaged out by Brownian tumbling in soluble or dynamic protein regions, rendering this technique useful only in static systems (Zhang et al., 2016).

Insensitive nuclei enhanced by polarisation transfer (INEPT) uses a different pulse sequence in order to transfer the magnetisation through J couplings, rather than dipole interactions, thus allowing analysis of dynamic systems (Zhang et al., 2016; Nowacka et al., 2013). The J couplings rely on bound ^{1}H and ^{13}C nuclei, meaning only signals from protonated carbons are detected.

5.1.4.11 Combined CP and INEPT NMR analysis

Depending on the type of SSNMR experiment that is conducted, information can be gathered on the dynamics of a protein. Direct polarisation experiments allow observation of signals, regardless of whether the molecule is in a solid or mobile phase. Cross-polarisation is reliant on ^{1}H-X dipole interactions that become averaged out in a protein's dynamic regions (Zhang et al., 2016). As such, the CP spectra only gives rise to chemical shift intensities from regions of the protein that remain in a static state. Conversely, INEPT spectra record chemical shifts of nuclei from only mobile regions (Zhang et al., 2016; Sackewitz et al., 2008; Heise et al., 2005). By comparing all three of these spectra, the DP, CP and INEPT, it is possible to determine global changes in the secondary structure of proteins, and establish whether these structural changes cause a change in dynamics.

The combined use of CP and INEPT NMR spectra to establish amyloid mobility was utilised by Debelouchina *et al.* (2011) on the study of β_2-microglobulin. Comparison of amyloidogenic aggregates formed at two pH conditions determined different morphologies, not only in the β-sheet content but also in the aggregate's structural mobility. INEPT NMR experiments of β_2-microglobulin have also been utilised in the analysis of the SUP35 amyloid aggregates. INEPT spectra identified a rigid, amyloid core, referred to as the M domain, formed by 2 β-strands in the sequence. These regions were detected and assignable on the INEPT spectra, whereas the remaining regions of the protein did not, suggesting that these regions show increased mobility (Luckgei et al., 2014).

5.1.4.12 Multi-dimensional NMR

For small molecules, the chemical shift and splitting patterns of peaks should be sufficient to identify the chemical group to which they belong. However, due to overlapping signals and small differences in chemical shift values, identification of individual peaks is often difficult for larger systems, such as proteins. Instead, multi-dimensional NMR can be used to detect the nuclei from more than one element in an experiment. This allows deduction, for example, of ^{1}H nuclei connected to ^{13}C nuclei, via heteronuclear pulsed experiments. These experiments are essential for the structural analysis of proteins, where large number of resonances, all in close proximity, cause extensive overlap. Protein backbones contain amide bonds, meaning that a combination of carbon, nitrogen and hydrogen nuclei can all be probed, including simultaneously in 3D NMR experiments (Bothwell and Griffin, 2011; Wuthrick, 1990).

Mixing techniques such as dipole assisted rotational resonance (DARR)

allows the recoupling of long-range dipolar interactions. Magnetisation is transferred from the ^{1}H (I) to the ^{13}C (S1) nuclei. This ^{13}C (S1) can then transfer the magnetisation to other ^{13}C nuclei (S2), which are close in space and have overlapping spinning sidebands (Takegoshi et al., 2001). This mechanism of transfer requires S_1 and S_2 to be dipolar coupled.

5.1.5. Aims

This chapter describes the structural analysis of native-lyophilised, and aggregated apoA-I, formed under conditions determined in **Chapter 4**. A mechanism for apoA-I aggregation has already been proposed by Das et al. (2016), based on the crystal structure of apoA-I. However, there is currently no structure for apoA-I amyloid. Information on the structure of the aggregated material, deduced by NMR, could either confirm this theory, or suggest refinements. In **Chapter 4** it was shown that apoA-I is stable at pH 7, and that acidification to pH 4, or oxidation of the three-methionine residues, leads to its rapid conversion into insoluble material. The presence of heparin or oxidation of methionine residues on apoA-I enhances the aggregation, and leads to a more ordered amyloid morphology. This chapter of study will utilise a combination of circular dichroism and, for the first time, solid-state NMR in order to determine whether the native apoA-I structure undergoes a conformational change upon acidification or oxidation.

5.2 Methods

5.2.1 Circular Dichroism

5.2.1.1 Stability of apoA-I to UV radiation

UV stability tests of apoA-I were carried out on a Chirascan plus qCD spectrometer (Applied Photophysics) between 200 and 250 nm with a bandwidth of 1 nm and a path length of 2 mm. 50 scans of apoA-I and oxidised apoA-I (7.2 μM) in McIlvaine buffer at pH 7 were taken.

5.2.1.2 Thermal stability of apoA-I

The thermal stability of apoA-I and oxidised apoA-I (7.2 μM) in McIlvaine buffer at pH 7 was determined on a Chirascan plus qCD machine with a bandwidth of 1 nm and a 2 mm path length, between 200 and 250 nm, across a temperature range of 20 – 90 °C. The temperature was controlled with a Quantum Northwest temperature controller, with 1 °C increment. The temperature was maintained during the scan acquisition. The thermal denaturation data was analysed using the Global 3 Thermal Analysis Software.

5.2.1.3. ApoA-I secondary structure analysis

Secondary structure of apoA-I was determined by synchrotron radiation circular dichroism (CD) using a nitrogen flushed Module X end-station spectrometer at B23 Synchrotron Radiation CD Beam line at the Diamond Light Source, Oxfordshire UK. ApoA-I (72 μM) at pH 7 and pH 4, in the absence and presence of heparin (144 μM), was incubated at 37 °C with agitation. The concentration was increased to 72 μM to allow a narrow path length. This reduced the background noise resulting from the citrate in the buffer, which absorbs in the far UV region

(Miles and Wallace, 2006). Samples were taken at 0, 1, 2 and 5 hour intervals and centrifuged at 13,400 rpm, in a bench top centrifuge, to pellet any insoluble material. The concentration of the supernatant was measured before loading into quartz cuvettes with a path length of 0.2 mm. Circular dichroism experiments were performed between 185 and 260 nm, with an increment of 1 nm. The data was analysed using CDApps software (Siligardi et al., 2002) and fitting was performed using the CONTINLL algorithm with dataset SMP56 between 190 and 250 nm. The CONTINLL algorithm factors in the sample concentration, the protein molecular weight, path length and the mean mass of amino acids (113 Da), to produce spectra with a Δε scale, the per residue molar absorption unit ($M^{-1}cm^{-1}$).

5.2.1.4. Thin film circular dichroism

Samples of aggregated apoA-I, formed at pH 4 in the absence and presence of heparin, were deposited on Suprasil type quartz plates and dried under a stream of nitrogen at 23 °C to form a thin film. CD spectra were acquired between 180 and 260 nm using an integration time of 1 second and a bandwidth of 1.2 nm on a nitrogen flushed module B end-station spectrometer at the B23 Synchrotron radiation CD beam line at Diamond Light Source, Oxfordshire UK.

5.2.2. Preparation of samples for solid-state NMR

Uniformly ^{13}C and ^{15}N isotopically labeled apoA-I was incubated at 36 μM, alone and in the presence of 72 μM heparin, at pH 4 for 3 days at 37 °C, with agitation. Fibrils were harvested through centrifugation at 12,000 g and the supernatant removed. Samples were flash frozen in liquid nitrogen, prior to centrifugation

into a zirconium 3.2 mm rotor with a Kel-F cap (Brucker, U.K). ApoA-I at pH 7 was 189yophilized in order to produce a solid, apoA-I product. This was then centrifuged into a 3.2 mm zirconium NMR rotor.

5.2.2.1 One-dimensional solid-state NMR

One-dimensional proton-decoupled ^{15}N CP-MAS SSNMR experiments were carried out on a Brucker Avance 400 MHz spectrometer, operating at a magnetic field of 9.3 Tesla, equipped with a 3.2 mm HXY MAS probe at 25 °C. Hartmann-Hahn cross-polarisation was achieved at a proton nutation frequency of 78 kHz, a 2 ms contact time, 100 kHz proton decoupling with SPINAL-64 during the signal acquisition, and a recycle delay of 2 ms. Magic angle spinning was controlled at a frequency of 8 kHz ± 1 Hz. Each spectrum was the result of accumulating 20,000-100,000 transients.

5.2.2.2 Two–dimensional solid-state NMR

Two-dimensional ^{13}C-^{13}C spectra were recorded at a magnetic field of 9.3 Tesla with a 3.2 mm HXY probe operating in double resonance mode, with magic angle spinning at 14 kHz and the temperature maintained at 4 °C. Hartmann-Hahn cross-polarisation was achieved with a 2 ms contact time and 100 kHz proton decoupling with SPINAL-64 applied during signal acquisition. For broadband dipolar recoupling, spectra were recorded with a 10 ms mixing time, during which the proton nutation frequency was adjusted to the MAS frequency of 14 kHz to meet the dipolar assisted rotational resonance (DARR) condition. The time domain matrix was the result of 400 T_1 increments, each averaged over between 128 and 320 transients. Phase sensitivity was achieved using the States-

TPPI method. For selective dipolar recoupling, the proton nutation frequency was set to 100 kHz during a mixture time of 1-15 ms and the spinning frequency was adjusted to the frequency difference of the nuclei to be coupled.

5.2.2.3 Simulated spectra

Simulated spectra of the natively folded apoA-I (Δ185-243) were produced in order to establish whether the SSNMR spectra acquired here, were consistent with the crystal structure deduced by Mei and Atkinson (2011). SHIFTX2 online server was used to calculate the chemical shifts from the PDB 3R2P structure. This program combines sequence alignment and ensemble machine learning methods to calculate the backbone and side chain ^{1}H, ^{13}C and ^{15}N chemical shift from a library of 197 proteins, each with a resolution of at least 2.1 Å, deduced by X-ray crystallography (Han et al., 2011). These predicted chemical shift values were then used to generate a simulated DARR spectrum, using a C program developed by Professor D. Middleton. In order to simplify the spectra, only short-range couplings representing directly bonded atoms were used.

5.3. Results

5.3.1. Circular Dichroism

Solution circular dichroism was used to determine the secondary structural content of apoA-I. Scans were acquired during the early stages of aggregation, prior to removal of insoluble material by centrifugation. The time window available was dependent on the pH, heparin and oxidation state, as shown in **Chapter 4**. The insoluble material was measured separately, after being dried down into a thin film.

5.3.1.1. Stability of native apoA-I

ApoA-I was incubated at pH 7 and scanned 50 times with single scans of far UV synchrotron radiation, in order to monitor the stability of the peptide (**Figure 5.14A**). The data show no sign of protein degradation after 50 scans, suggesting that apoA-I is stable when exposed to UV radiation, and that changes observed following aggregation are caused by changes in structure, not radiation damage.

A fresh apoA-I solution at pH 7 was then monitored over 7 hours, under which conditions the protein was shown previously to be stable and not to aggregate (**Figure 4.4**), in order to monitor any structural changes during this time and to determine the secondary structural content of native apoA-I.

Prior to each measurement over the 7 hour period, apoA-I was incubated at 37 °C, with agitation. Insoluble material was removed through centrifugation, and the concentrations were measured using a nanodrop. CD scans were then acquired. **Figure 5.14B** shows the spectra remain similar over the 7-hour period, apart from a small change in intensity at the 2-hour point, confirming that no structural change occurs during incubation at pH 7.

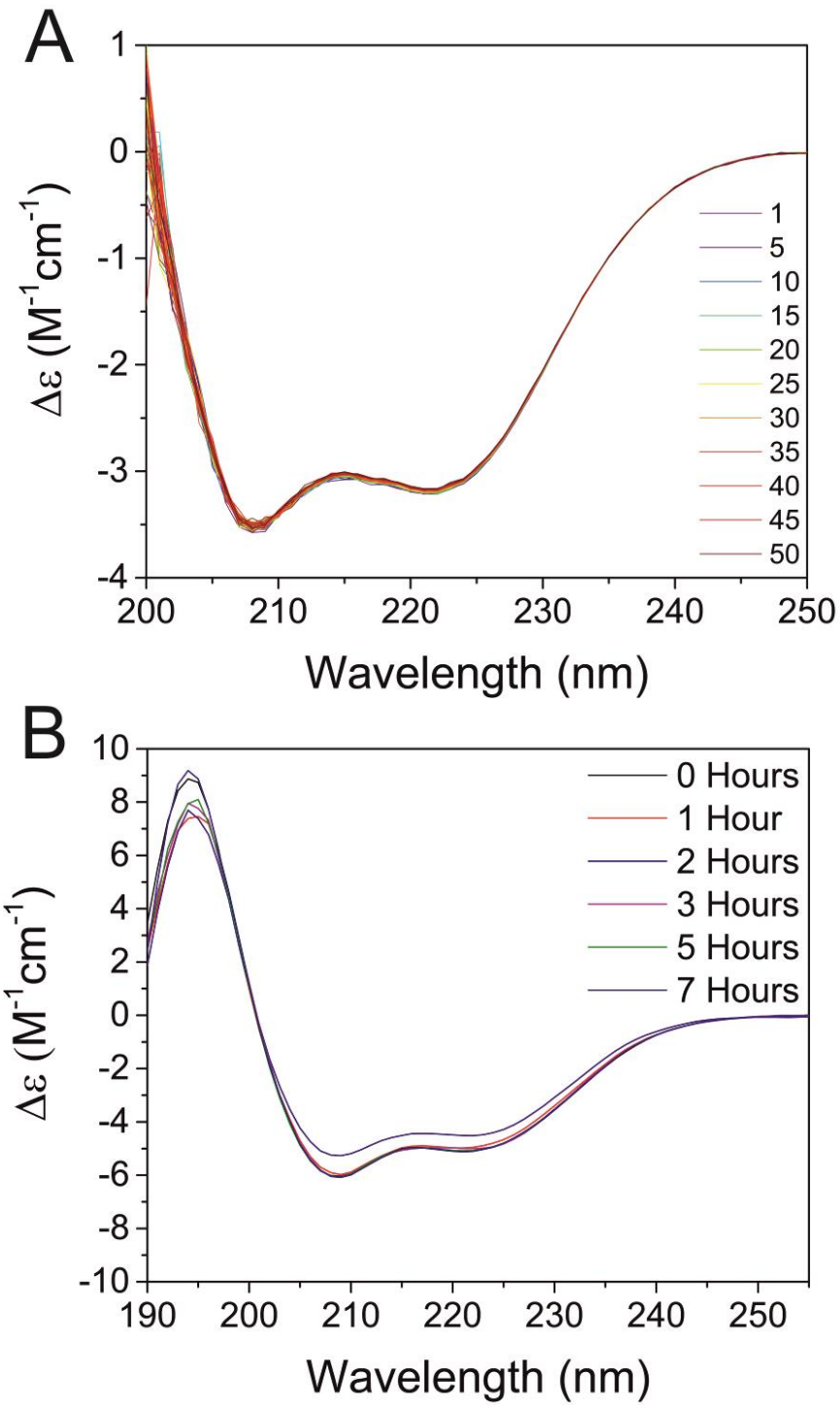

Figure 5.14. Far UV synchrotron radiation circular dichroism of apoA-I at pH 7. (**A**) 50 repeated scans of apoA-I (7.2μM) to determine the stability of the peptide under UV radiation. The numbers represent the number of repeated exposures to UV radiation. (**B**) ApoA-I (72 μM) monitored over 7 hours.

5.3.1.2 Secondary structure of native apoA-I

The spectrum of apoA-I (72 μM) at pH 7, after 0 and 5 hours incubation, are shown in **Figure 5.15A**, and are consistent with a high degree of α-helical structure, shown by the characteristic minima at 208 and 222 nm. Fits calculated from the CONTINLL algorithm are also shown, and were used to estimate the percentage secondary structure of apoA-I.

The CD spectra of proteins can be expressed as a combination of the individual secondary structural elements. The CONTINLL algorithm is based on the CONTIN method, which uses a ridge regression procedure, fitting the observed CD spectrum to a large database of reference proteins (Sreerama and Woody, 2000; Greenfield, 2007). This results in accurate estimates for proteins containing α-helical and β-sheet structures, which is of particular interest in amyloidogenic proteins, especially for those that contain a high proportion of native α-helices (Greenfield, 2007).

At pH 7, apoA-I is shown to consist of a majority of α-helical elements, which make up 60 % of the overall secondary structure. This value is consistent with previous studies (Nagao et al., 2014; Saito et al., 2003; Chetty et al., 2012; Chetty et al., 2009; Gursky et al., 2012; Das et al., 2014), which range between 60 and 80 % of α-helices, when measured with CD. The structure is also shown to remain stable, following incubation at 37 °C for 5 hours (**Table 5.1**).

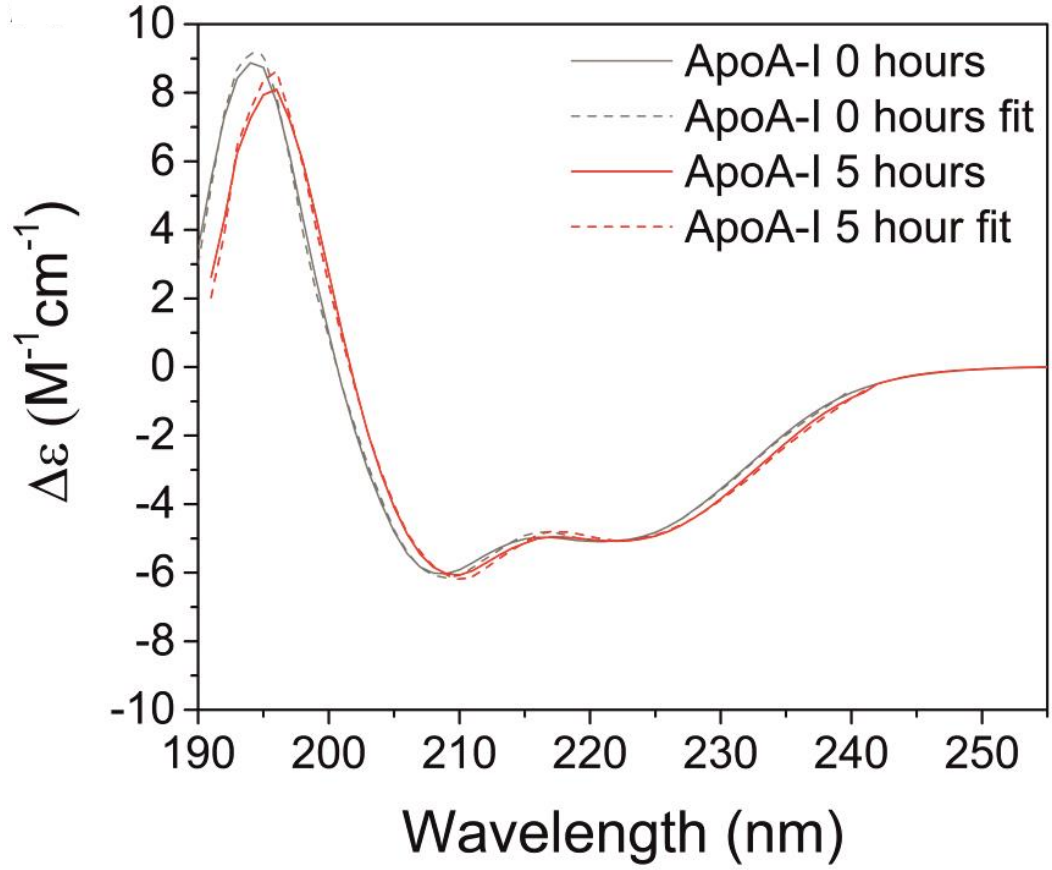

Figure 5.15 (**A**) CD spectra of apoA-I (72 μM) at pH 7 after 0 h and 5 h incubation, along with fits using the CONTINLL algorithm.

Table 5.1 Secondary structural content of apoA-I at pH 7 after 0, 2 and 5 hours incubation in the absence of heparin, calculated using CONTINLL algorithm fits, with the standard deviation (SD) shown.

	Percentage Secondary Structure				
Time	**α-helix**	**β-sheet**	**Turn**	**Unordered**	**S.D**
0 Hours	65	8	13	14	0.032
2 Hours	62	9	24	5	0.031
5 Hours	60	5	16	19	0.039

5.3.1.3. Structural rearrangement of apoA-I upon aggregation

In order to determine whether any structural rearrangement occurs upon aggregation, apoA-I was incubated under the conditions determined in **section 4.3**, at pH 4, in the absence and presence of heparin, at 37°C. After 2 hours incubation, samples of the aggregating apoA-I were removed and centrifuged to remove any insoluble material that could distort the CD signal, through light scattering and/or absorption flattening. The concentration was then re-measured and the sample loaded into quartz cuvettes. The supernatant was analysed by SRCD and the molar CD (Δε) calculated based on the new concentration.

The CD spectra for apoA-I alone, and in the presence of heparin at pH 4 (**Figure 5.16, A** and **B,** respectively) are shown after 0 and 2 hours of incubation. Fits of these spectra using the CONTINLL method were also performed to deduce the percentage secondary structure, and are also shown in **Figure 5.16**.

At pH 4, large quantities of apoA-I were precipitated, as described in **Chapter 4**, which after its removal, led to a reduced signal to noise ratio. In the absence of heparin, the remaining soluble protein retained a significant proportion of the native α-helical content, even after 2 hours (**Figure 5.16A**). However, in the presence of heparin, the intensities of the spectra are reduced, even at the initial time point, to the extent that the characteristic α-helical minima at 208 and 222 nm, are not distinguishable (**Figure 5.16B**).

Upon fitting of the apoA-I spectra, using the CONTINLL algorithm, the data was able to be accurately de-convoluted. This facilitated the calculation the secondary structural contributions, with a standard deviation of <0.1, apart from apoA-I in the presence of heparin, which was too close to the baseline. The fits for

the heparinated sample after 0 and 2 hours had a standard deviation of 0.52 and 0.68, respectively. This means the structural information deduced from this fitting must be treated with more caution. The protein concentration of the supernatant was so low that the data was not deemed to represent the aggregating material.

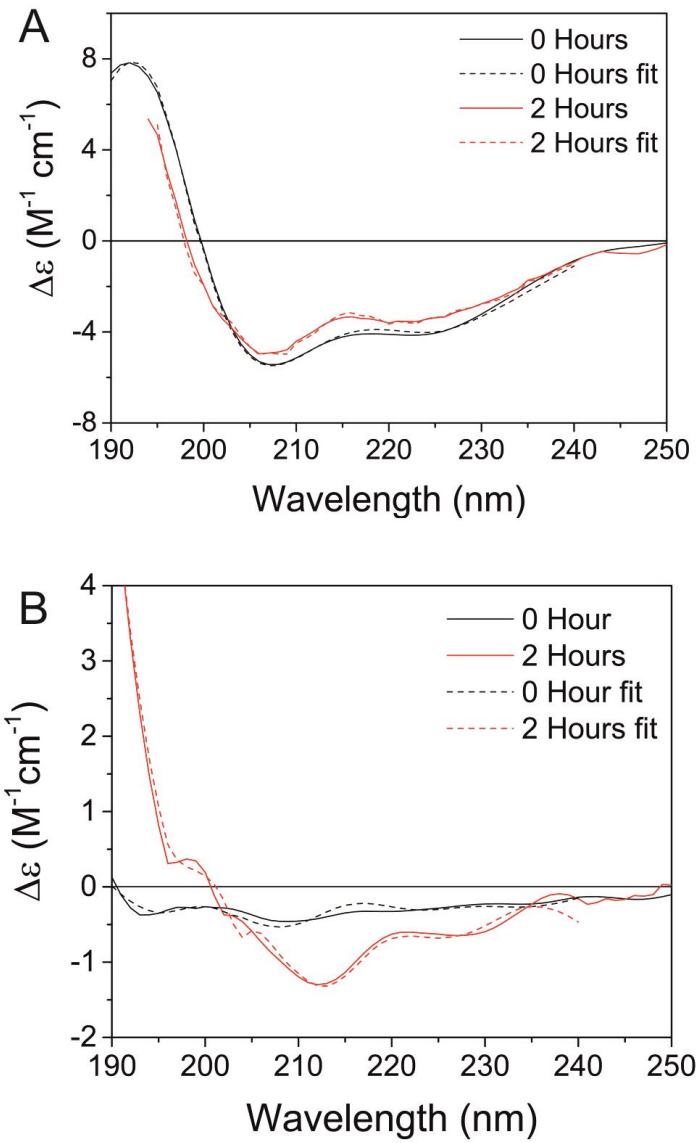

Figure 5.16. Far UV circular dichorism spectrum for apoA-I (72 μM) at pH 4 in the absence (**A**) and presence (**B**) of 144 μM heparin after 0 h and 2 h incubation, at 37 °C with agitation. Fits derived using the CONTINLL algorithm are also shown for each spectrum as dotted lines.

De-convolution of the apoA-I CD spectrum at pH 7, revealed a predominantly α-helical structure (65 % α-helical, 8% β-sheet, 13% turns and 14% unstructured), consistent with the crystal structure of C-terminally truncated apoA-I (Mei and Atkinson, 2011).

At pH 4, apoA-I alone has a slightly lower α-helical content, and an increase in unstructured regions (**Table 5.2**), but is still predominantly helical. After incubation for 2 hours, the helical contribution remains similar to the native structure, but an increase in β-sheet is observed (**Table 5.2**).

However, in the presence of heparin, at pH 4, a dramatic reduction in α-helical content, and an increase in β-sheet and unstructured regions are observed instantaneously. After 2 hours incubation, the reduction in protein concentration by precipitation means that the remaining soluble material does not accurately represent the aggregating material, as shown by the dramatic increase in the standard deviation. Therefore, the insoluble material was dried into thin films and analysed using thin film CD (**Section 5.3.1.4**).

Table 5.2. Secondary structural content of apoA-I at pH 7 and 4, in the absence and presence of heparin after 0 and 2 hours incubation, calculated using CONTINLL algorithm fits with standard deviation (SD) shown.

		Percentage secondary structure				
Condition	**Time (h)**	**α-helix**	**β-sheet**	**Turn**	**Unordered**	**S.D**
pH 7	0	65	8	13	14	0.032
	2	62	9	24	5	0.031
pH 7 + heparin	0	60	8	21	11	0.028
	2	65	9	14	12	0.033
pH 4	0	53	5	18	24	0.057
	2	61	16	21	2	0.095
pH 4 + heparin	0	4	41	22	32	0.521
	2	19	8	16	57	0.681

5.3.1.4. Thin film circular dichroism of apoA-I

The insoluble, aggregated material that was removed from solution, prior to obtaining the solution CD spectra, was analysed by thin film circular dichroism. This allowed determination of the secondary structure of the apoA-I aggregates, rather than the protein that was left in solution.

Thin film CD of the aggregated material formed in the absence of heparin produced a spectrum that appeared similar to apoA-I at pH 7, with spectral minima at 208 and 222 nm, suggestive of a high helical content remaining (**Figure 5.17**).

However, the material formed in the presence of heparin produced a spectrum that appeared to consist of both α-helical and β-sheet contributions. The spectrum maximum shifts from 193 nm to 195 nm, which is consistent with a conversion from α-helical to β-sheet. The spectra minimum at 222 nm, one of the identifying features of α-helices, becomes red shifted to 226 nm, and the intensity of the spectral minimum at 208 nm, is also reduced. These are all suggestive of an increase in β-sheet content (Chan et al., 2015).

Differential spectra, obtained by subtracting the heparinated sample from the sample of apoA-I alone, can be assigned to conformational changes occurring in the presence of heparin. This spectrum infers the presence of 40 % β-sheet content. However, this technique cannot determine whether the entire, heparinated aggregate contains 40 % β-sheets, or whether just the region that differs from the un-heparinated sample contains 40% β-sheets.

Therefore, thin film CD has to be used with caution. The random alignment of molecules in the film leads to anisotropic sampling, and it has been reported that thin film CD overestimates β-sheet content (Noguez, 2014).

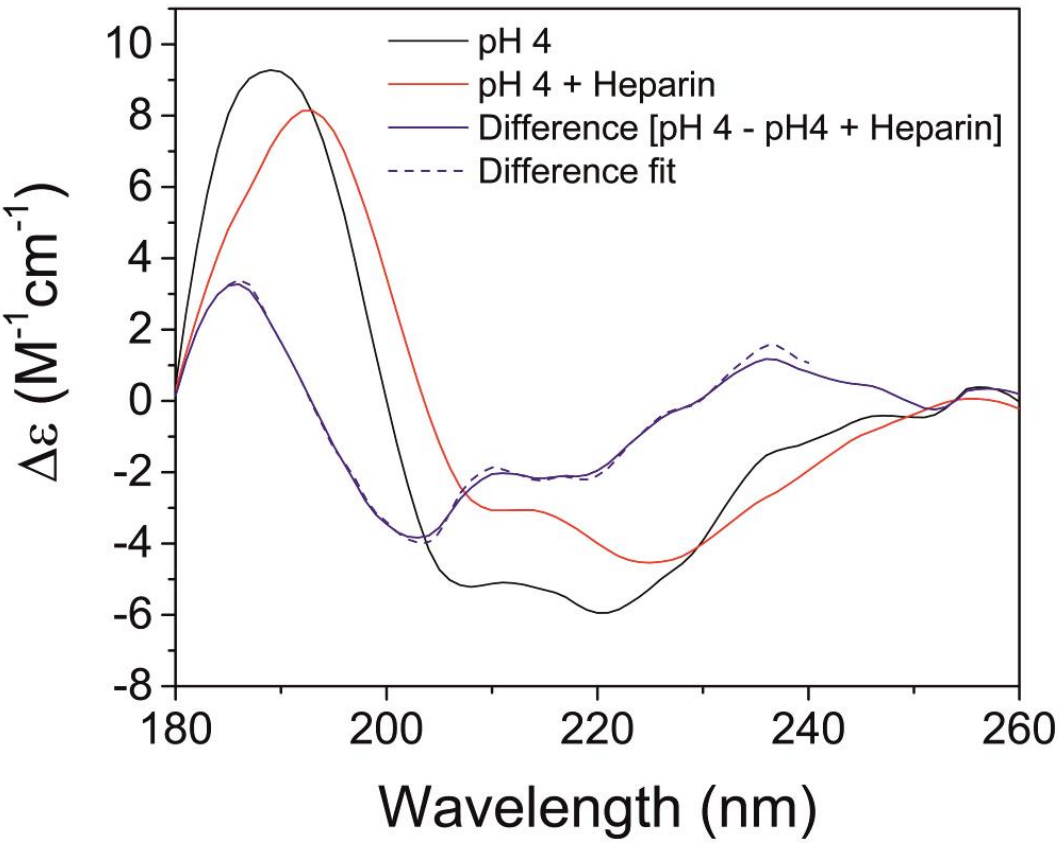

Figure 5.17. Thin-film far UV circular dichroism spectrum of apoA-I aggregates formed at pH 4, in the absence and presence of heparin.

5.3.1.5 Stability of oxidised apoA-I

Oxidation of apoA-I has been shown to induce its aggregation into amyloid-like aggregates, with typical fibril morphology, at a more physiologically relevant pH than the wild type apoA-I. As such, the structure of oxidised apoA-I was probed with CD.

Oxidised apoA-I was incubated in 10mM phosphate buffer, rather than McIlvaine buffer. This meant that CD scans could be acquired from 185-260 nm without excessive noise below 200 nm, caused by the citrate in the McIlvaine buffer.

In experiments mirroring those described in **section 5.3.1.1**, oxidised apoA-I underwent repeated scans of high intensity UV radiation, in order to determine whether the oxidised apoA-I was prone to UV degradation. **Figure 5.18** indicates that oxidised apoA-I at pH 7.5 remains stable to UV radiation, similar to wild type apoA-I.

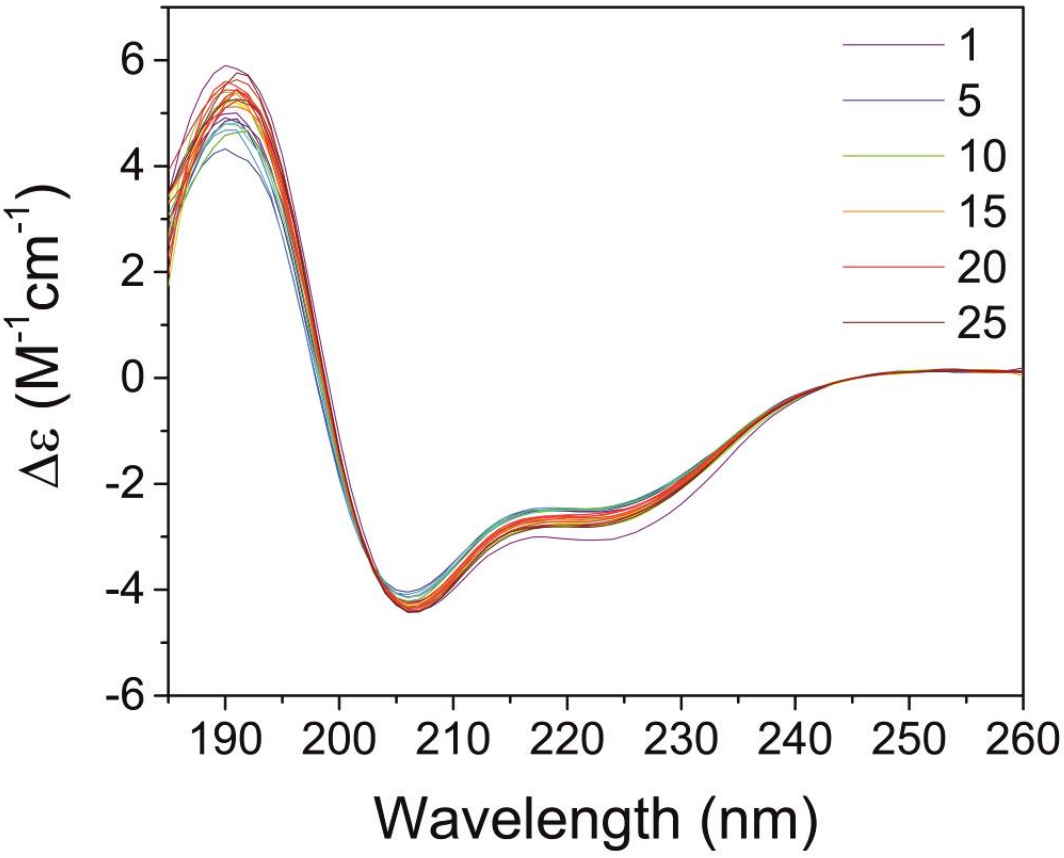

Figure 5.18 25 repeated scans of oxidised apoA-I (72 μM) at pH 7 with far UV synchrotron radiation to determine the stability of the peptide under UV radiation. Numbers represent the number of repeated exposures to UV radiation.

5.3.1.6. Secondary structure of oxidised apoA-I

Circular dichrosim spectra of oxidised apoA-I were obtained, in order to determine the secondary structural content. At pH 7.5, oxidised apoA-I has been shown to be stable and is not predisposed to aggregation (Chan et al., 2015). The spectrum of oxidised apoA-I, shown in **Figure 5.19A**, can be fitted with the CONTINLL algorithm, resulting in the secondary structural values shown in **Figure 5.19B**. These percentages confirm a predominantly helical conformation. However, the helical content of 46 % for the oxidised apoA-I is considerably lower than the 60 % α-helices in the un-oxidised apoA-I. This is concurrent with previous studies, which determined that the secondary structural content decreased by approximately 10 % upon oxidation of methionine residues (Chan et al., 2015). This 10 % reduction in helical content appears to have rearranged into unstructured regions, in agreement with Wong *et al*. (2010). It is thought that this decreased structural stability is what drives the aggregation of oxidised apoA-I into amyloid species.

Oxidised apoA-I at pH 6 was not studied by solution CD, due to the inaccuracy of the fitting observed at pH 4, in the presence of heparin. Instead thin film CD of oxidised apoA-I was attempted, in order to determine the secondary structural contributions of the aggregated material. However, upon drying down the insoluble aggregates, as done previously with native apoA-I at pH 4, the thin films were opaque, and lead to extensive light scattering when CD spectra were acquired.

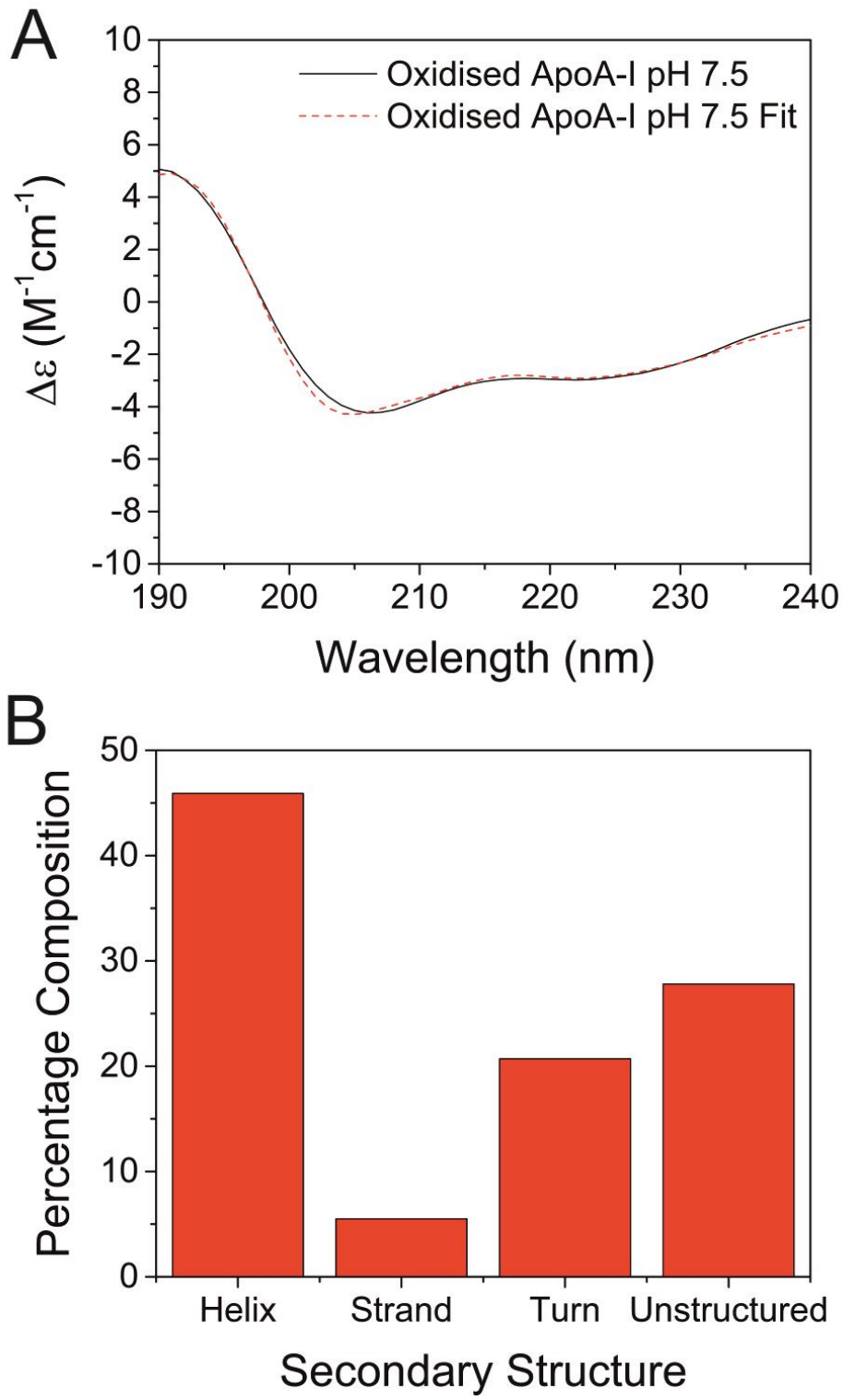

Figure 5.19 (**A**) CD spectra of oxidised apoA-I (72 μM) at pH 7.5, with the CONTINLL fitting, using dataset SMP56. (**B**) Secondary structural content of oxidised apoA-I at pH 7.5, estimated using the CONTINLL algorithm.

5.3.1.7 Circular dichroism of apoA-I (46-59)

ApoA-I (46-59) was shown in **Figure 4.17** to readily assemble into ThT-responsive aggregates, characteristic of amyloid. As such, the aggregation of apoA-I (46-59) was monitored for 4 hours with circular dichroism. At pH 7 (**Figure 5.20B**), apoA-I retains a predominantly random coil structure, with a spectra minimum around 195-200 nm and a maximum around 215 nm. Upon acidification to pH 4, the spectra in **Figure 5.20A** remains relatively unchanged, still suggestive of random coil structure. However, after incubation for 4 hours at pH 4, the spectra changes dramatically to one more associated with β-sheets.

However, upon fitting with CONTINLL algorithms, the secondary structure shows no difference, following aggregation (**Table 5.3**). This does not match the dramatic change in the shape of the spectra. As such, the fittings were not deemed to accurately represent the data and were rejected. Therefore, the structure of apoA-I (46-59) aggregates will be further studied by natural abundance SSNMR.

Table 5.3 Percentage secondary structure of apoA-I (46-59) at pH 7 and pH 4 after 0 and 4 hours incubation.

Condition	Time	Percentage secondary structure			
		α-helix	β-sheet	Turn	Unordered
pH 7	0 hours	5	40	22	33
	4 Hours	5	40	22	32
pH 4	0 Hours	5	40	22	34
	4 Hours	4	37	22	36

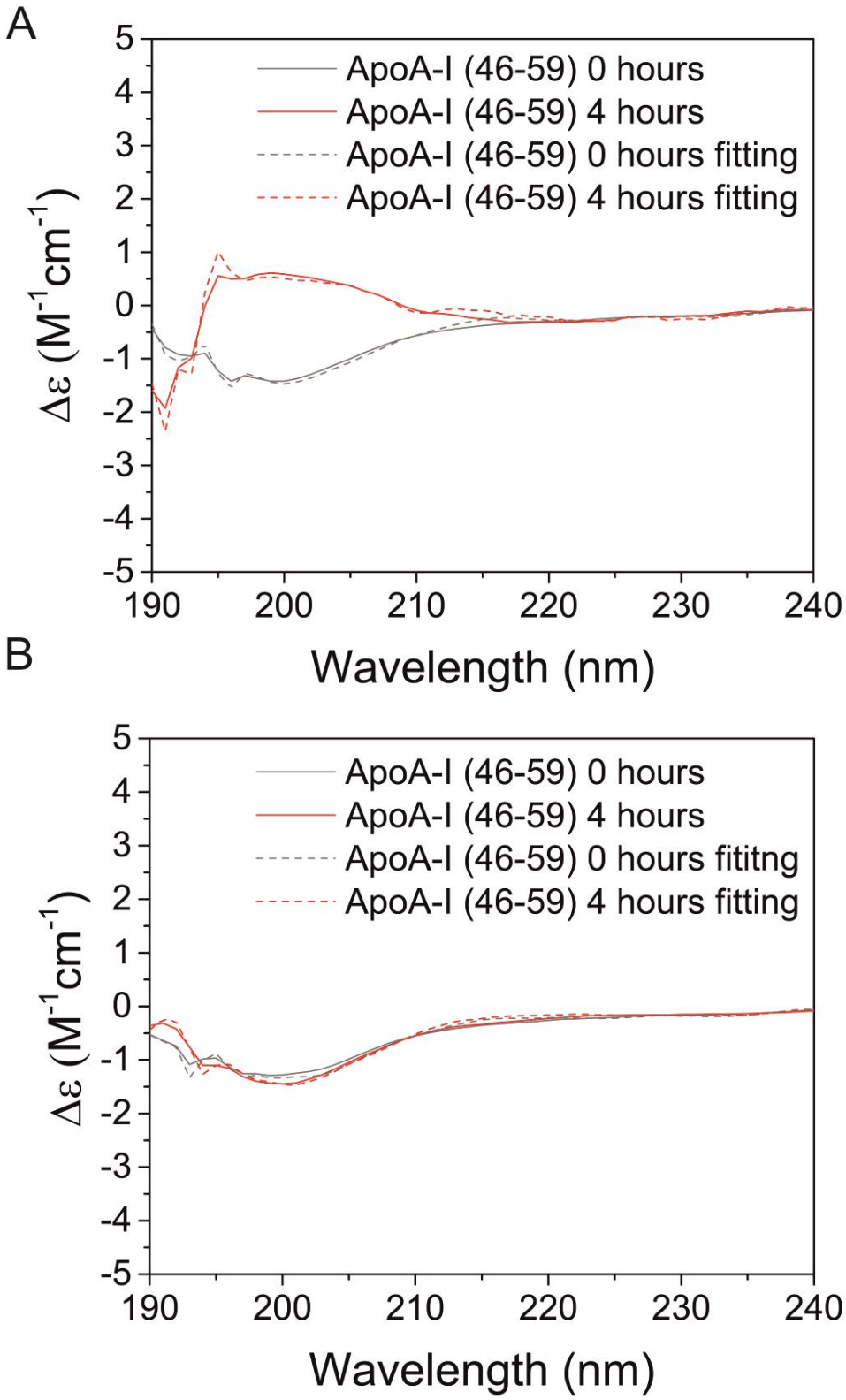

Figure 5.20 Circular dichroism of apoA-I (46-59) at the aggregation inducing pH 4 (**A**), and neutral pH 7 (**B**) where apoA-I (46-59) was shown to be stable and did not spontaneously aggregate.

5.3.2. Thermal stability studies of apoA-I

5.3.2.1 Thermal stability of native, soluble apoA-I

Thermal stability experiments were carried out on a bench top instrument, rather than at Diamond Light Source. At Diamond, high concentrations of apoA-I meant shorter path lengths could be used. Due to the lower radiation intensity of the bench top instrument, measurement required a longer path length, as such, the contribution from the citrate buffer at low wavelengths caused a high level of noise. Therefore, the spectra presented for thermal stability analysis of both apoA-I and oxidised apoA-I at 7.2 μM is shown from 200-250 nm.

Far UV circular dichroism measurements of apoA-I at pH 7, across a temperature range of 20-90 °C, were taken in order to determine whether the structure of apoA-I was dependent on temperature, and if so, what temperature induced a change in the native fold. At 20 °C, apoA-I produced a CD spectrum consistent with the scans of apoA-I in **Figure 5.21**, suggesting a high content of α-helical secondary structure. As the temperature increased, the intensity of the troughs at 208 nm and 224 nm, characteristic of α-helical contributions, reduced. As the temperatures exceeded 60 °C, the spectra appeared to take on a more random coil characteristic (**Figure 5.21A**), consistent with apoA-I undergoing thermal destabilisation. The isodichroic point around 203 nm is suggestive of a local 2 state population. This is confirmed by the spectra from these two separate species, shown in **Figure 5.21B**. The contribution of these two structural variants of apoA-I can be plotted against temperature, using the Global 3 Thermo Analysis software. The point where the 2 lines converge highlights a temperature of 57.5 °C, at which 50 % of the initial, mostly helical structure has converted into a random coiled structure (**Figure 5.21C**).

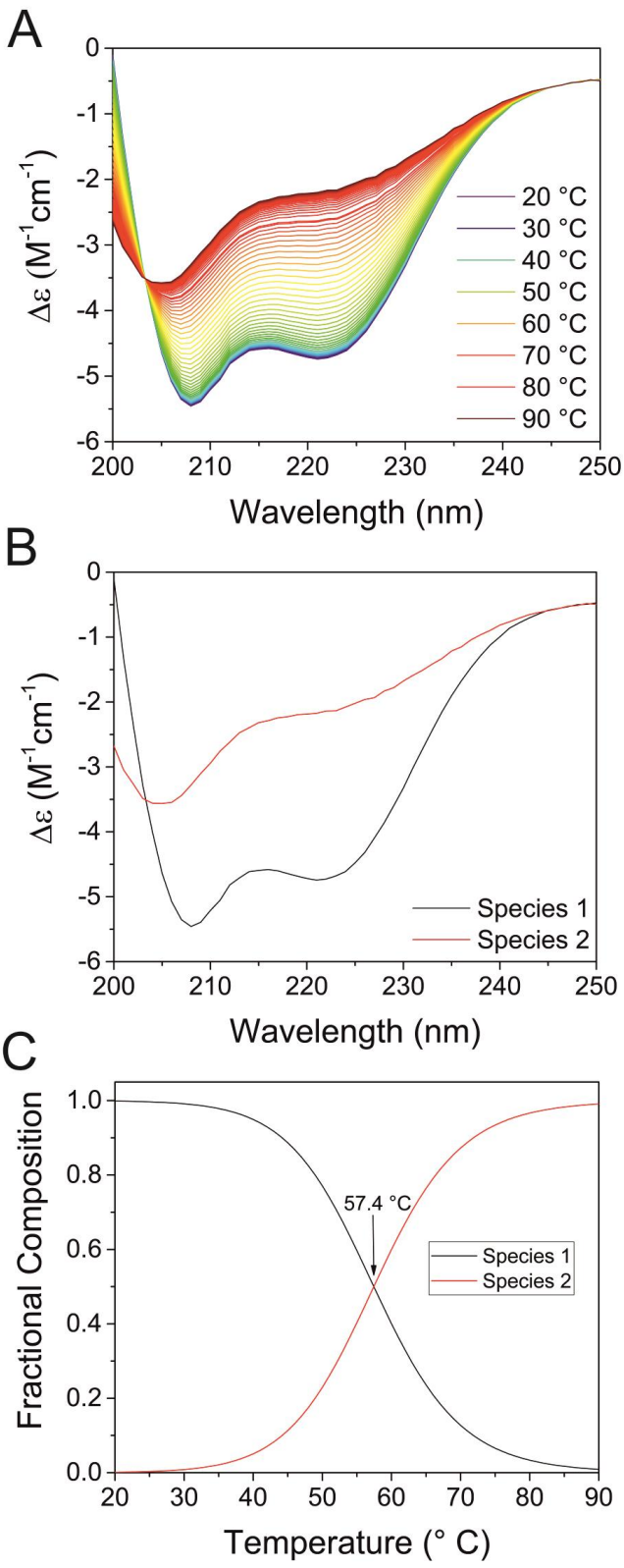

Figure 5.21 (**A**) Far UV circular dichroism spectrum of apoA-I at neutral pH incubated at increasing temperatures, (**B**) the 2 distinct species at the extremes of the temperature range and (**C**) the fractional composition of the 2 species at each temperature. Data was analysed by Global 3 thermo analysis software.

5.3.2.2. Thermal stability of oxidised apoA-I

Oxidation of methionine residues in apoA-I has been shown to reduce the secondary structural content of soluble apoA-I by approximately 10 % (Chan et al., 2015). However, one study has found that oxidation of methionine residues causes partial unfolding of the protein, and inhibition of dimerisation (Wong et al., 2010). Both of these studies deduced an increased susceptibility to thermal destabilisation, compared to the un-oxidised apoA-I.

Figure 5.22 shows that oxidised apoA-I undergoes two major transitions between 20 and 90 °C. At 20 °C oxidised apoA-I produces a CD spectra that appears similar to the native, soluble apoA-I (**Figure 5.22A** and **B**), thus, is qualitatively presumed to contain a high proportion of α-helices, due to the presence of spectral minima at 208 and 222 nm. Upon increasing the temperature above 30 °C, the spectra of oxidised apoA-I shows a decrease in intensity at 222 nm, and a blue shift of the 208 nm peak to approximately 205 nm, consistent with the formation of unordered structures. This is characteristic of protein unfolding. This is also similar to the transition of un-oxidised apoA-I at pH 7 from helical to random coil (**Figure 5.21B**), although oxidation decreases the temperature at which this conversion occurs by 25 °C. This effect has been reported elsewhere, but to a much lower extent (Wong et al., 2010). Upon further heating above 70 °C, CD spectra of oxidised apoA-I produces spectral minima at 208 and 222 nm, but at reduced intensities, consistent with refolding into α-helix structures, which has not been shown before. The lack of an isodichroic point at 203 nm confirms the 2-state transition observed in **Figure 5.21** no longer occurs. Therefore, this data confirms oxidation causes increased structural unfolding of apoA-I.

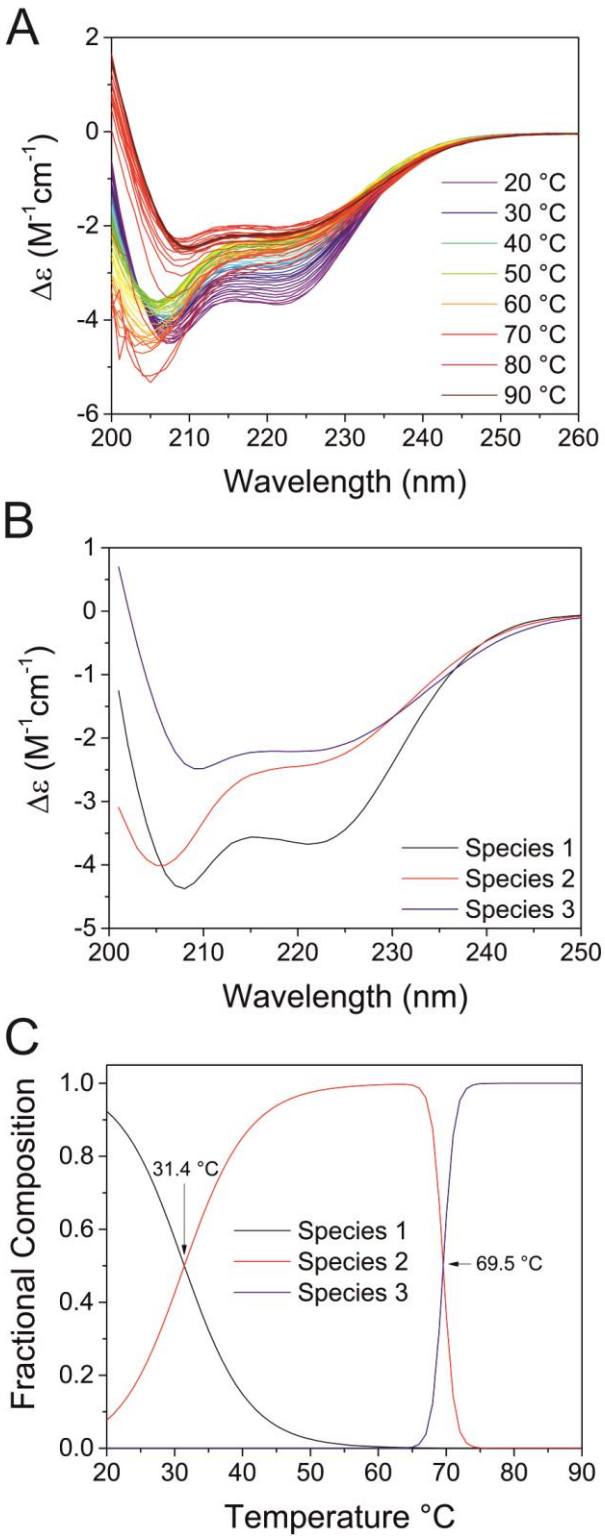

Figure 5.22 (**A**) Far UV circular dichroism spectrum of oxidised apoA-I at pH 7.5 incubated at increasing temperatures, (**B**) the 3 distinct species determined by the Global 3 Thermo Analysis software and (**C**) the fractional composition of the 3 species at each temperature.

5.3.3. Solid-state NMR

Since CD analysis of proteins can only give an estimation of the overall secondary structural content, SSNMR was utilised in order to determine local structural features at a higher resolution. **Chapter 3** describes the recombinant expression of uniformly ^{13}C and ^{15}N isotopically labeled apoA-I, allowing analysis by SSNMR. **Chapter 4** details the conditions that promoted the aggregation of apoA-I into insoluble material, characteristic of amyloid. This work allows a more in-depth study of the global structure of apoA-I, in particular the folding pattern of the native and aggregated forms of the protein, via a combination of one and two-dimensional SSNMR experiments.

5.3.3.1 Structure of native apoA-I

Initial SSNMR experiments were used to determine the structure of the native apoA-I protein at pH 7, where it has been shown to remain stable and avoid aggregation. Two-dimensional, ^{13}C-^{13}C CP-MAS SSNMR spectra were obtained for lyophilised apoA-I at pH 7. Cross-peaks identify nuclei in close proximity, such as those that are directly bonded, with the transfer of magnetisation from one nucleus to another during the mixing phase.

Figure 5.23 shows broad lines (±5 ppm) for the lyophilised sample (black), suggesting a degree of heterogeneity, which is common for SSNMR analysis of amyloid fibrils formed by full-length proteins (Morris et al., 2012). In addition to this heterogeneity, the overlap of individual amino acid peaks, caused by the large size of apoA-I, prevented a full residue assignment of the spectrum. However, the spectrum is suitably well resolved to observe cross-peaks from several amino acid species, in particular alanine, leucine, valine, threonine and

serine. The chemical shift patterns of these residues alone can be used to infer secondary structural content of the overall protein, given their uniform distribution throughout the apoA-I sequence (**Figure 2.3**). The spectrum of lyophilised apoA-I at pH 7 contains Cα-Cβ and Cα-carbonyl carbon cross-peaks for these amino acid residues with chemical shifts, which are characteristic of α-helices, as shown in **Table 5.4.**

Table 5.4 Average chemical shift (ppm) of amino acids, according to their secondary structural content (Wang and Jardetzky, 2002).

	Cα			Cβ			C-amide		
	α-helix	**β-sheet**	**Random Coil**	**α-helix**	**β-sheet**	**Random Coil**	**α-helix**	**β-sheet**	**Random Coil**
Ala	54.86	50.86	52.67	18.27	21.72	19.03	179.58	175.3	177.39
Gly	47.02	45.08	45.34				176.31	173.01	174.3
Leu	57.54	53.94	54.85	41.4	44.02	41.87	178.42	175.16	176.61
Pro	65.52	62.79	63.53	31.08	32.45	31.87	178.34	176.41	176.91
Ser	60.87	57.14	58.35	62.81	65.39	63.88	176.51	173.52	174.33
Thr	65.89	61.1	61.59	68.64	70.82	69.75	176.62	173.47	174.62
Val	65.69	60.72	61.8	31.41	33.81	31.68	177.75	174.66	175.76

The spectrum also shows a strong resemblance to a simulated spectrum of apoA-I (Δ185-243), which was produced from the predicted chemical shifts from the PDB 3R2P model determined by SHIFTX2 (Han et al., 2011). This provides strong evidence that the native protein at pH 7 is in a predominantly α-helical structure. It should be noted that the simulated spectrum corresponds to the apoA-I (Δ185-243) protein, whereas the lyophilised apoA-I spectrum contains signals from the full-length peptide (minus the first 2 residues). Therefore, the experimental spectrum contains signals from the remaining residues, 185-243, which are not present in the Mei and Atkinson model. These residues in apoA-I are believed to

be involved in lipid binding, and thus, have a highly variable secondary structure, consisting of either α-helical or random coil structures (Chetty et al., 2009). If this C-terminal region was in a random coil conformation, Cα-Cβ cross-peaks from threonine 197, 200, 237 and 242 and serine 201, 204, 224 and 228 residues would appear with chemical shifts of 61.6/69.8 ppm for the threonine residues (green circle), and 58.3/63.8 ppm for the serine residues (blue circle) (**Figure 5.23**). The Cα-Cβ cross-peaks for threonine and serine residues in α-helical conformations occur closer to the diagonal. Since no cross-peaks occur in the region associated with random coil, the spectra suggests that under the conditions studied here, the C-terminus of apoA-I is in an α-helical conformation.

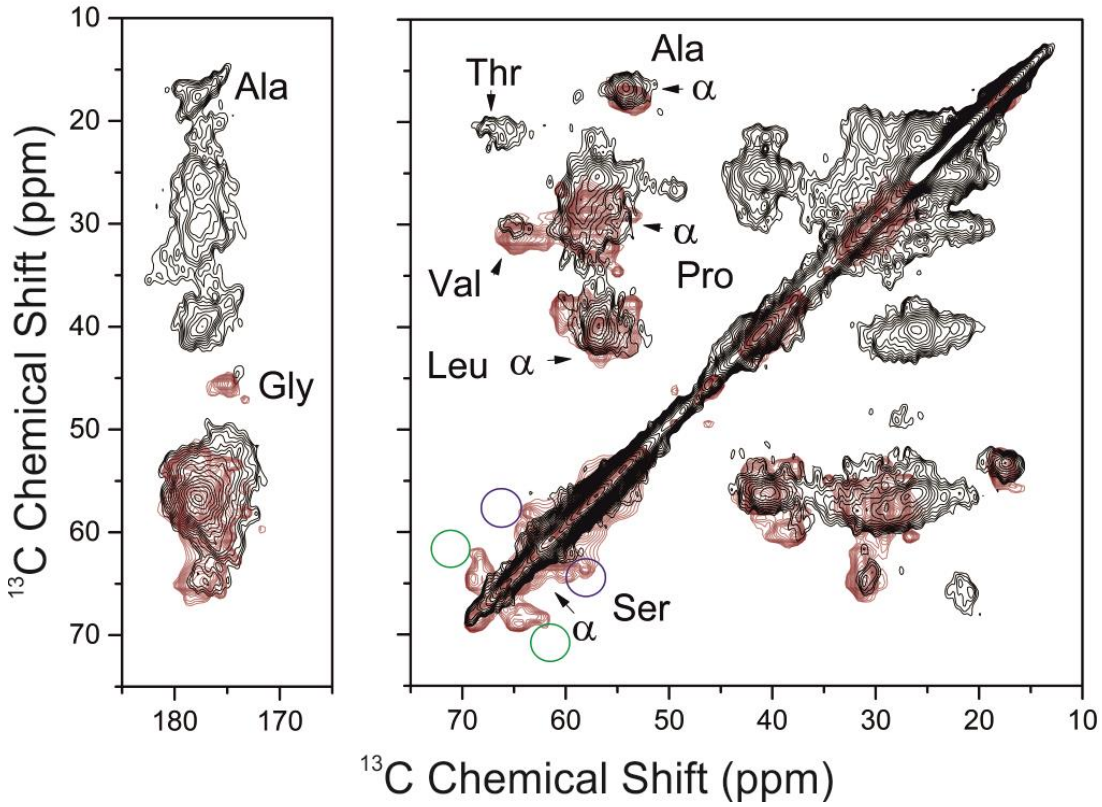

Figure 5.23 2D ^{13}C-^{13}C SSNMR spectra with DARR mixing of lyophilised apoA-I at pH 7 (black) and a simulated spectrum from the apoA-I (Δ185-243) model (Mei and Atkinson, 2011) in red. The blue and green circles highlight chemical shift regions associated with Thr and Ser residues in random coil conformations.

5.3.3.2 One-dimensional solid-state NMR of apoA-I aggregates

Proton-decoupled ^{15}N CP-MAS NMR spectra of apoA-I were acquired for lyophilised apoA-I at pH 7, and for the fibrillar material formed at pH 4 and pH 5 in the presence of heparin (**Figure 5.24**). Chemical shifts of the backbone amide nitrogen, in addition to the Cα, carbonyl and Cβ positions, are highly sensitive to protein secondary structure. **Figure 5.24** also includes the predicted ^{15}N chemical shift spectra for the apoA-I (Δ185-234) structure shown in red (Mei and Atkinson, 2011).

Figure 5.24A shows the amide ^{15}N chemical shifts for the native lyophilised apoA-I, centred around ≈119 ppm. This is consistent with the chemical shift of amide nitrogen atoms in α-helical conformation, which range from 114.8 ppm to 121.7 ppm, with an average of 118.3 ppm (Wang and Jardetzky, 2002). The experimental spectrum agrees with the simulated spectrum for apoA-I (Δ185-234), suggesting that at pH 7, lyophilised apoA-I shows a strong resemblance to the Mei and Atkinson (2011) model. The spectra in **Figures 5.23** and **5.24** also confirm that the lyophilisation of apoA-I does not affect the native structure.

Upon aggregation at pH 4, at both 36 and 18 μM (**Figure 5.24 B** and **C**), and at pH 5 at 36 μM (**Figure 5.24 D**) in the presence of heparin, apoA-I produces a ^{15}N spectrum peak centred around ≈121 ppm. Average chemical shifts for amino acid residues in β-sheet (122 ppm) and random coil (119.5 ppm) conformations are higher than those seen in corresponding α-helical (118.3 ppm) conformations (Wang and Jardetzky, 2002). In all three spectra of apoA-I at acidic pH, the experimental spectrum of the apoA-I aggregates show a deviation from the apoA-I (Δ185-234) simulated spectra.

In summary, although the spectra do not provide site-specific information, the 1D ^{15}N spectrum confirms the aggregation of apoA-I at acidic pH, in the presence of heparin, causes a structural rearrangement. This results in a shift from its natively α-helical structure, to an increased β-sheet and/or unordered structure.

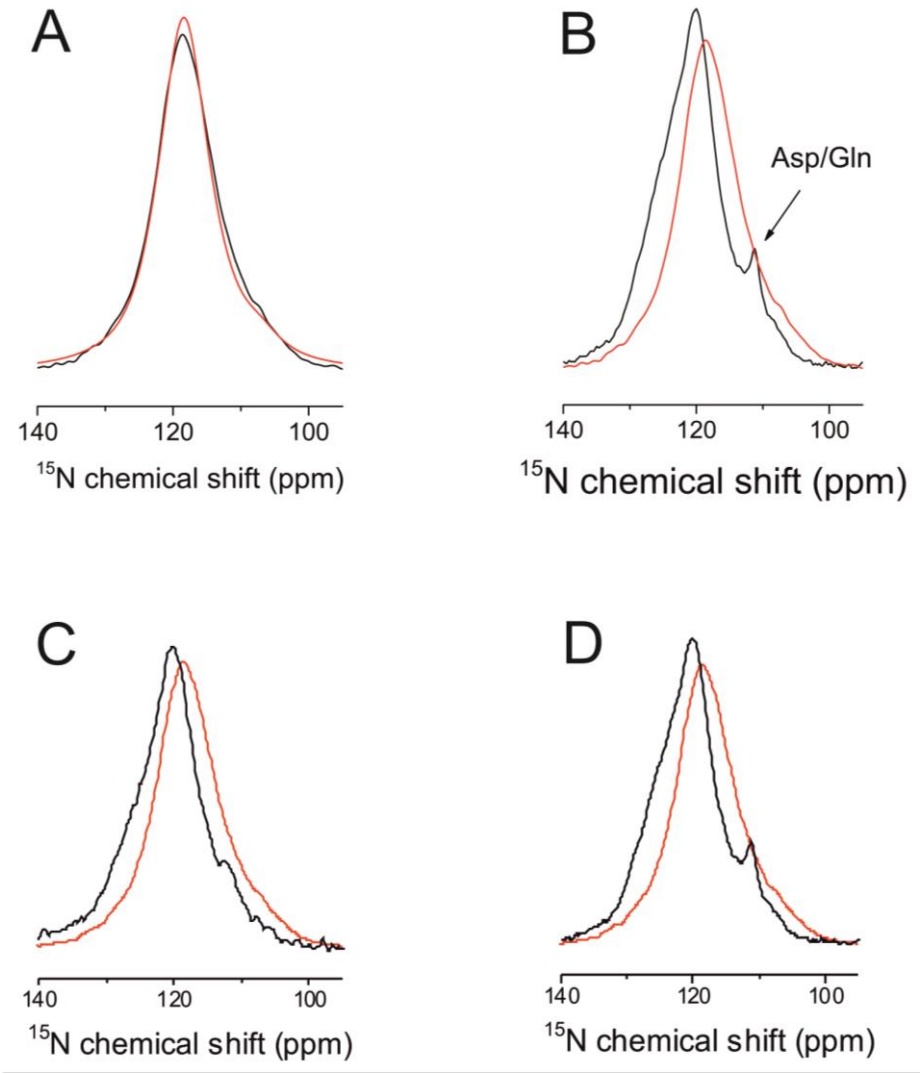

Figure 5.24 ^{15}N 1D SSNMR showing the backbone amide region of (**A**) lyophilised apoA-I at pH 7 and (**B-D**) aggregated apoA-I formed in the presence of heparin. Specific aggregation inducing conditions were (**B**) pH 4 with 36 μM apoA-I, (**C**) pH 4 with 18 μM apoA-I, and (**D**) pH 5 with 36 μM apoA-I. The simulated spectra for the apoA-I (Δ185-234) model, calculated using the SHIFTX2 online server, is shown in red.

5.3.3.3. Two-dimensional ssNMR of apoA-I aggregates

Two-dimensional ^{13}C-^{13}C CP-MAS SSNMR spectra for hydrated apoA-I aggregates, formed in the absence and presence of heparin (**Figure 5.25**), give more detail on the structural composition of the aggregates than was possible with one-dimensional studies (**Figure 5.24**). ApoA-I alone (red) shows a high similarity to apoA-I aggregates formed in the presence of heparin (black), despite the differences observed via XRD, TEM, CD and ThT, which suggested a different aggregation mechanism occurred in the presence of heparin. Both samples produce spectra with broad, overlapping peaks**.** The overlap is less than that observed for the lyophilised apoA-I at pH 7 in **Figure 5.23**, however, a sequential assignment is still not feasible.

The 2D spectrum of aggregated apoA-I (**Figure 5.25**) contains cross-peaks for Ala, Val, Leu, Ser and Thr residues that correspond to α-helical contributions, as observed with the lyophilised apoA-I at pH 7 in **Figure 5.23**. However, in addition to these α-helical cross-peaks, additional sets of cross-peaks for each of these residues are present, with chemical shifts associated with β-sheets. This suggests that upon aggregation, apoA-I undergoes a structural rearrangement, from a highly helical native structure, into a combination of α-helices and β-sheets. All 5 of the amino acids identified in **Figure 5.25** are uniformly distributed throughout the apoA-I sequence (**Figure 2.3**), meaning that it was not possible to locate the unique regions of the peptide that correspond to α-helices or β-sheets.

In summary, apoA-I aggregates, formed both in the absence and presence of heparin, contain both α-helical and β-sheet contributions, suggesting a partial conversion from its native α-helical content.

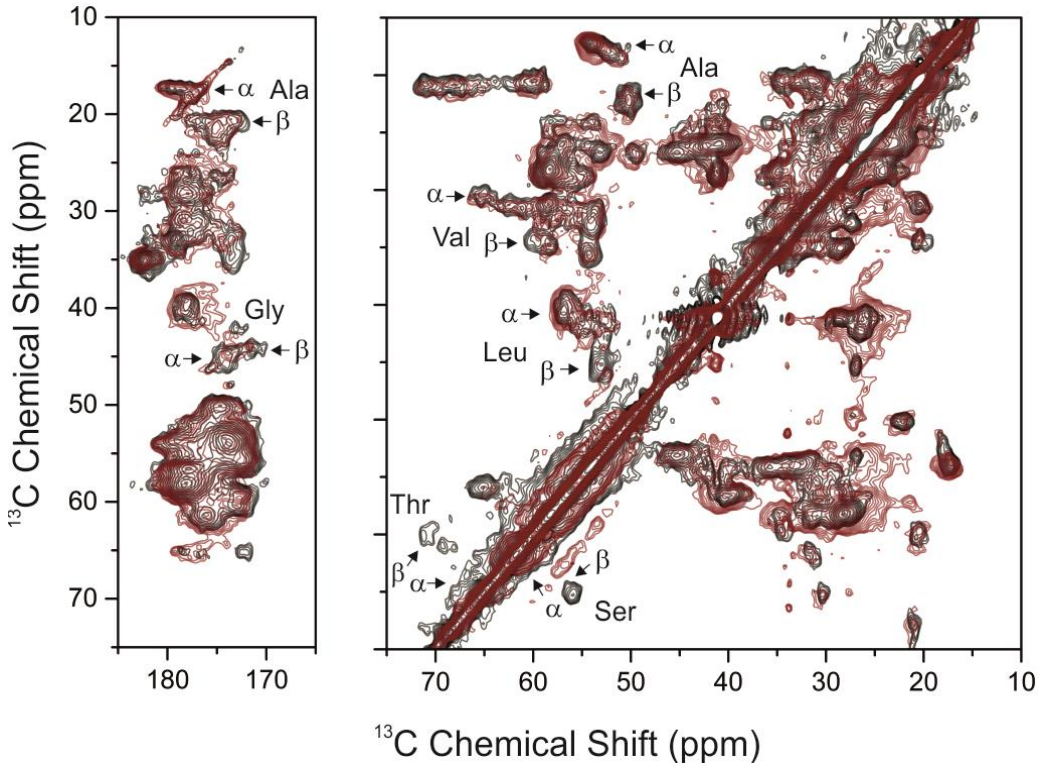

Figure 5.25 Two-dimensional ^{13}C-^{13}C CP-MAS SSNMR spectrum with DARR mixing of apoA-I aggregates formed in the absence (red) or presence (black) of heparin, showing the amide (left) and high field (right) carbon regions. Annotations of α and β refer to cross-peaks with chemical shifts consistent with the residues in an α-helical or β-sheet conformation.

5.3.3.4 Oxidised apoA-I

Chemical oxidation of apoA-I, with H_2O_2, was shown to induce aggregation into amyloid-like aggregates in **Chapter 4**, which are ThT-responsive and have an appearance of more typical amyloid morphology, compared to the aggregates formed by un-oxidised apoA-I (**Figure 4.22**). Here, the SSNMR spectra of oxidised apoA-I (blue) is very similar to the to the spectra of un-oxidised apoA-I aggregates formed at pH 4 in the presence of heparin (black), as shown in **Figure 5.26**. Both spectra contain cross-peaks corresponding to both α-helical and β-

sheet conformations, and are virtually superimposable. Therefore, it is reasonable to assume that the oxidised and heparinated aggregates have similar structures, and thus, are created as a result of the same changes to the core structure.

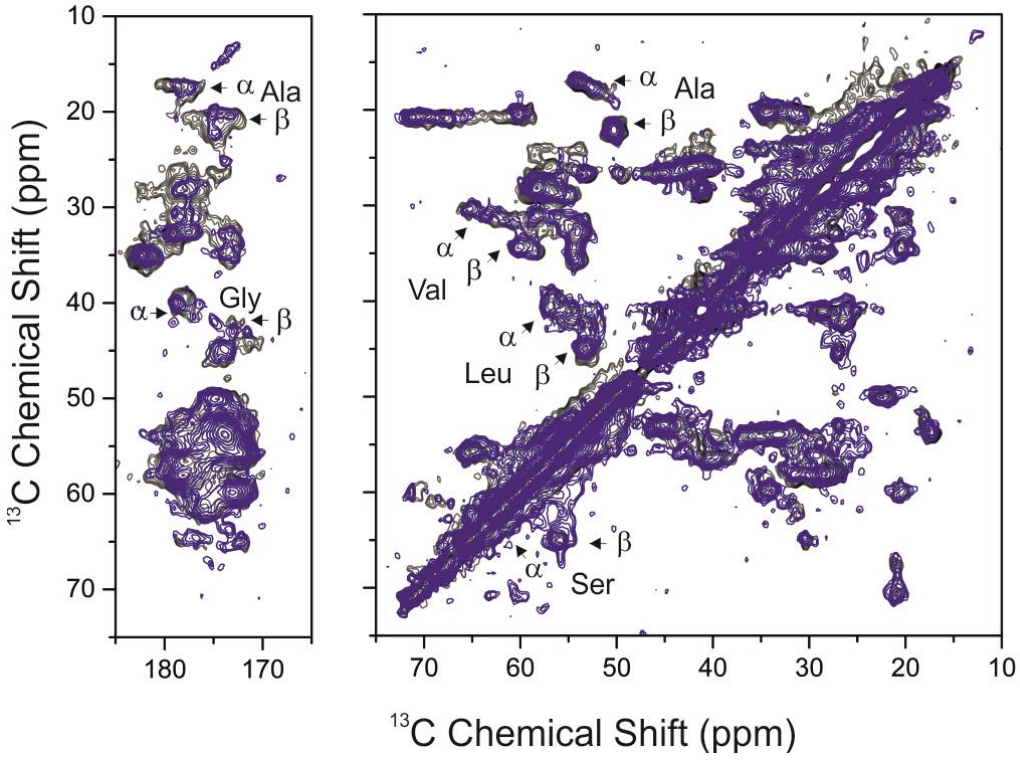

Figure 5.26 Two-dimensional ^{13}C-^{13}C CPMAS SSNMR spectra with DARR mixing of apoA-I aggregates formed at pH 4 in the presence of heparin (black) and oxidised apoA-I aggregates at pH 6 (blue).

5.3.3.5. β-sheet model of apoA-I

The N-terminal residues 1-80 and 1-100 of apoA-I are known to readily form into amyloid structures when cleaved from full-length apoA-I (Das et al., 2016; Das et al., 2014). A model for apoA-I (1-90) with a high percentage of β-sheet structure was produced by Professor David Middleton. This model consisted of residues 14-59 (incorporating the 2 hot spot regions 14-22 and 53-38) in an anti-parallel

β-strand conformation, with a turn encompassing Gly 33, Gly 37 and Gln 39, with disordered flanking regions. Back calculation of the ^{13}C chemical shifts of this structure allowed a simulated 2D ^{13}C-^{13}C SSNMR spectrum to be produced. The ^{13}C SSNMR spectrum of apoA-I aggregates formed in the presence of heparin (black), and the simulated spectrum for the simulated apoA-I (1-90) aggregated peptide (blue), are shown in **Figure 5.27.** The apoA-I (1-90) β-sheet simulation produces theoretical cross-peaks, which are concurrent with many of the cross-peaks for apoA-I in the presence of heparin. In particular, the simulated spectrum matches with the cross-peaks assigned to β-sheet conformations in the full-length apoA-I, but does not superimpose onto the α-helical cross-peaks. This suggests that the apoA-I aggregates contain the N-terminal 1-90 residues in majority β-sheet conformation.

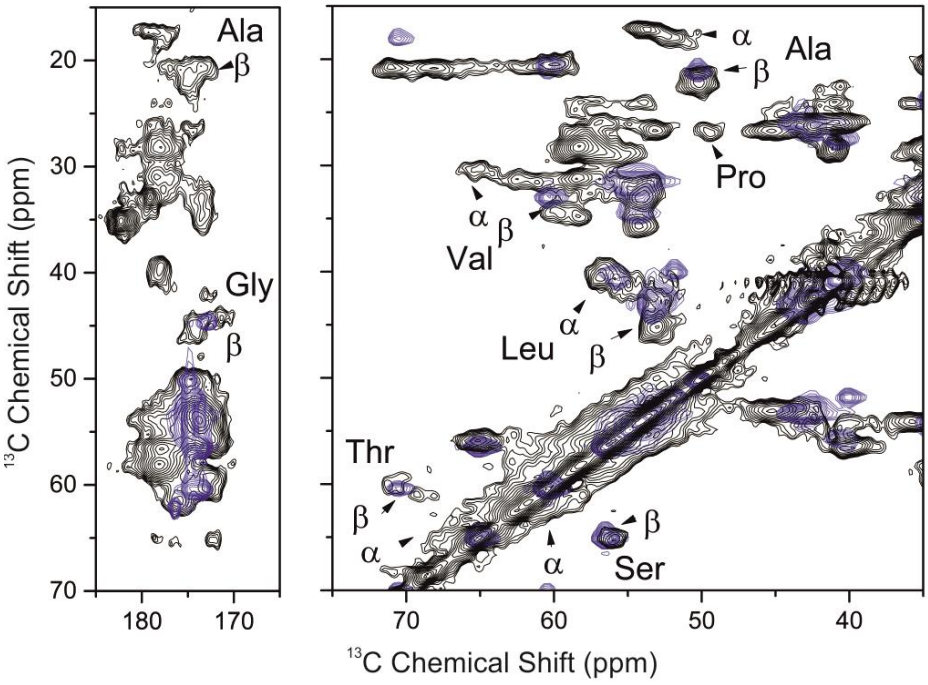

Figure 5.27 Two-dimensional ^{13}C-^{13}C CP-MAS SSNMR spectrum with DARR mixing of apoA-I aggregates formed in the presence of heparin (black) and a simulated spectrum for the model apoA-I (1-90) as entirely β-sheets (blue).

5.3.3.6 Structure of apoA-I 46-59

The structure of apoA-I (46-59) was probed through natural abundance ^{13}C 1D SSNMR. **Figure 4.17** indicates that apoA-I readily forms amyloid-like material at pH 4, which is consistent with a conversion from random coil to β-sheet structures, as shown by the circular dichroism spectra in **Figure 5.20**. A natural abundance ^{13}C SSNMR spectrum of apoA-I (46-59) aggregates for the α-carbon region is shown in **Figure 5.28**, alongside simulated spectra for the peptide sequence in entirely α-helical, random coil and β-sheet conformation, produced by Professor D. Middleton. The spectrum for the apoA-I (46-59) fibrils is in good agreement with the simulated β-sheet spectrum, and the small discrepancies could be explained by the disorder of the terminal residues.

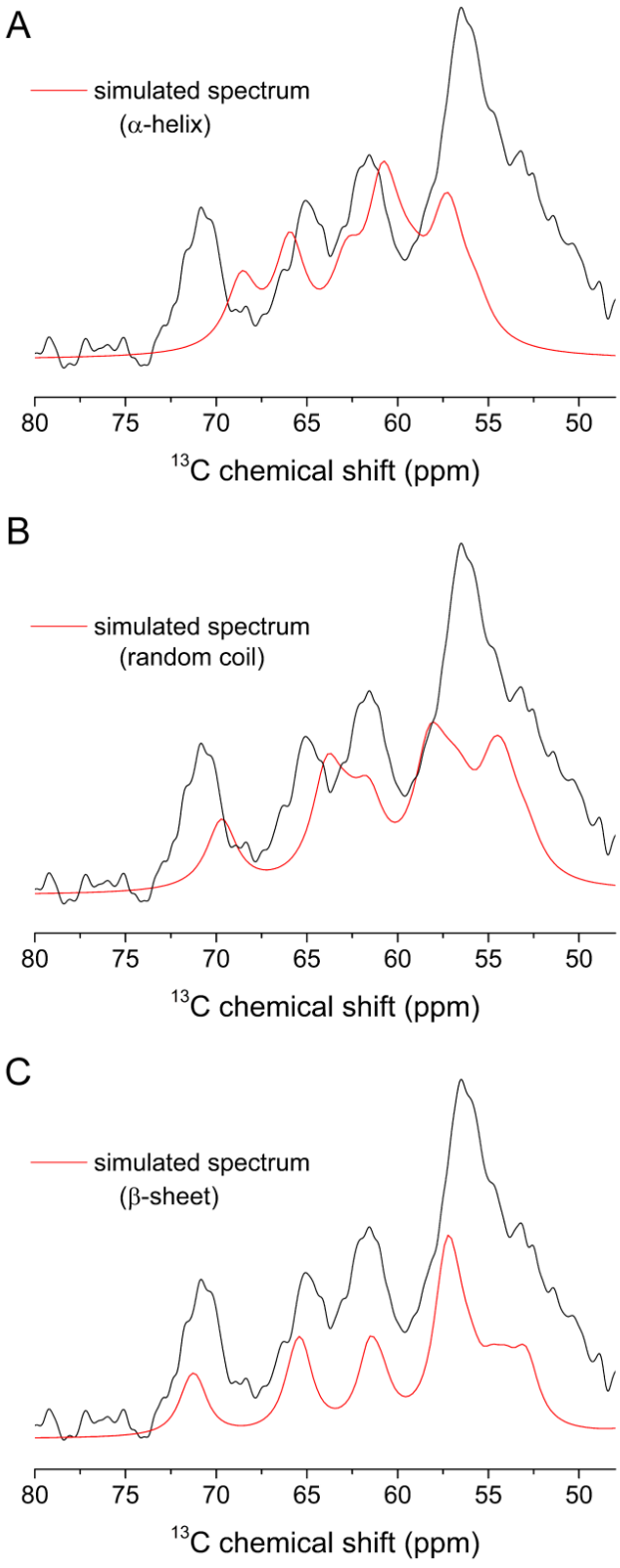

Figure 5.28 Cα region of the ^{13}C SSNMR spectrum of apoA-I (46-59) fibrils (black) with simulated spectra of the peptide in entirely α-helical (**A**) random coil (**B**) and β-sheet (**C**) conformations shown in red.

5.4 Discussion

ApoA-I solutions at pH 7 were analysed by CD and shown to be resistant to UV decay, and stable up to 57.4 °C. Upon deconvolution of the CD spectrum, the estimated secondary structure was consistent with the crystal structure deduced by Mei and Atkinson (Mei and Atkinson, 2011), with 60 % in α-helical and >10 % in β-sheet conformations. Upon acidification of apoA-I, a structural rearrangement occurred, resulting in a decrease in α-helical content and an increase in β-sheet. This conversion is enhanced in the presence of heparin. This is consistent with the formation of amyloid species, which convert into a highly ordered β-sheet conformation, prior to becoming insoluble fibrils that can no longer be measured by CD. In contrast to the solution CD, the thin-film CD appeared to remain helical in the absence of heparin, and produce a spectrum that contained signal contributions from both α-helices and β-sheets in the presence of heparin, with 40 % of the protein in a β-sheet conformation.

A combination of α-helices and β-sheets is something that is not commonly observed with amyloid formation. Usually, natively helical proteins refold into β-sheet structures, with minimal native content remaining (Ding et al., 2003). Therefore, the structure of the apoA-I aggregates was assessed by SSNMR.

Initial SSNMR studies were carried out on lyophilised apoA-I at pH 7, but due to broad and overlapping lines, sequential assignment of the spectrum was not possible. However, the spectrum was suitably resolved to identify 5 amino acids (Ala, Leu, Val, Ser and Thr) with cross-peaks correlating to their inclusion in α-helical structures. When the experimental spectrum was superimposed with a simulated spectrum for the apoA-I (Δ185-243) model deduced by Mei and Atkinson (2011), the two spectra were complementary.

NMR spectra of apoA-I aggregates, both those formed in the absence and presence of heparin, were acquired and compared to the native lyophilised apoA-I. Interestingly, the cross-peaks that correlated with α-helical elements in the lyophilised apoA-I occurred in the spectra of the aggregated material. However, novel cross-peaks for these amino acids within β-sheet structures were also present. Unfortunately, all 5 of these amino acids are uniformly distributed throughout the apoA-I sequence, so determining where the α-helical or β-sheet regions are within apoA-I was not possible. These findings confirmed the thin film CD spectra, which suggested the aggregates consisted of a combination of α-helical and β-sheet structures. Spectrum for oxidised apoA-I at pH 6 appeared similar to the wild type apoA-I aggregates, with both α-helical and β-sheet contributions.

5.4.1 Current model for apoA-I amyloidosis

A current theory detailing the mechanism of apoA-I amyloidosis is proposed by Das *et al.,* (2014; 2016). Three N-terminal "hot spot" regions, consisting of residues 14-22, 53-58 and 69-72, are protected from spontaneous aggregation by their incorporation in the 4-helical bundle, which makes up the majority of the native N-terminus. Destabilisation of this 4-helical bundle, by mutation or oxidation, leads to the spontaneous aggregation of the hot spots into β-sheet structures, which extend up to residues 76-81. This short sequence, EKETEG acts as a natural β-sheet breaker at neutral pH, resulting in apoA-I (1-76) consisting of β-sheets, and the remaining C-terminus retaining its native fold. This opens apoA-I up to cleavage, in particular at residue 83, forming N-terminal fragments that deposit as amyloid in familial apoA-I amyloidosis.

However, upon protonation of the glutamic acid at acidic pH, the EKETEG sequence loses its β-sheet breaking ability, allowing the β-sheet to propagate into the C-terminus, forming full-length apoA-I amyloid.

ApoA-I (1-90) in a β-sheet conformation was modeled and back calculation of the ^{13}C chemical shifts produced a simulated NMR spectrum. The simulated spectrum superimposes well onto the apoA-I aggregates, with the simulated correlating with the β-sheet cross-peaks for the experimental spectrum. This suggests that the full-length apoA-I aggregates contain the first 1-90 residues in a β-sheet conformation. However, this spectrum does not rule out other structural possibilities, including β-sheet formation in other areas.

5.4.2 Refinement of the model for apoA-I amyloidosis

Based on the SSNMR data presented here, a modification of the current model for apoA-I amyloidosis is proposed. Following acidification or oxidation, the apoA-I N-terminus becomes less stable, leading to the exposure of the hot spot regions at residues 14-22, 53-58 and 69-72. This allows their spontaneous aggregation into β-sheet structures in the N-terminus, which extend up to the β-sheet breaking sequence at residues 76-81, in keeping with the current theory. However, it is proposed here that the remaining apoA-I sequence, incorporating approximately residues 76-243, retains its native α-helical structure, even at acidic pH, as modeled in **Figure 5.29**. This explains the splitting of the alanine, valine, leucine, threonine and serine cross-peaks into chemical shifts associated with both α-helical and β-sheet structures. This model is also supported by the CD data presented here, which suggests a decrease in the native helical content, resulting a mixture of α-helices and β-sheets in the aggregated material.

It is likely that the pro-amyloidogenic effects of heparin are caused by its interaction with apoA-I aiding in the destabilisation of the N-terminus. This explains why the ThT response is concentration-dependent, but only affects the initial stage of aggregation, rather than the secondary elongation.

What these data cannot deduce, for certain, is whether the α-helical and β-sheet contributions in the CD and SSNMR spectra are present in each molecule of apoA-I, or whether the conditions studied here promote the formation of 2 distinct apoA-I species. One species may consist of the native helical structure, whilst the other is converted to predominantly β-sheets following amyloidosis. The intensities of the SSNMR, and the CD spectra both consistently estimate the β-sheet content to be roughly 40 %. Although this figure must be treated with caution, the consistency and the high percentage of β-sheet is suggestive that each monomer contains a combination of α-helix and β-sheet.

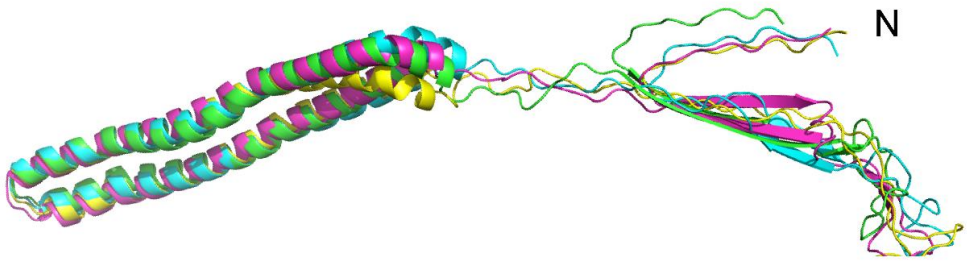

Figure 5.29 Five models for aggregated apoA-I (Δ185-243) (PDB 3R2P) with the N-terminal 1-75 region in a non-helical conformation, whilst residues 76-180 retain their natively helical structure. Residues 14-59, incorporating the hot spot regions 14-22 and 53-58 are modeled as antiparallel β-sheets, separated by a turn including Gly 33, Gly 37 and Gln 39. The remaining N-terminal residues are disordered. Figure produced by D. Middleton.

6. Inhibition of apoA-I aggregation

6.1. Introduction

6.1.1. Amyloid inhibition

The misfolding of proteins into amyloid species is linked to a whole range of disease states, as outlined in **section 1.1.2**. ISA currently recognises 30 human proteins capable of forming amyloid, many of which are involved in pathological links to amyloid-related diseases (Sipe et al., 2014). These include Aβ and tau in Alzheimer's disease, α-synuclein and tau in Parkinson's disease, IAPP in type II diabetes, immunoglobulin light chain in AL amyloidosis, medin in aortic medial amyloidosis, and apoA-I in apoA-I amyloidosis, associated with atherosclerosis (Chiti and Dobson, 2006). From this list, it is clear that the proteins involved in amyloidosis are not all structurally or sequentially linked, and can include: full-length proteins, peptide fragments or products of general protein decay (Stefani, 2007). As such, large variety in amyloidogenic proteins makes developing therapeutic compounds for inhibiting their aggregation difficult, and various methods will be discussed in detail later in this introduction. Deposition of amyloid fibrils is detrimental to health, and leads to many of the diseases listed in **Table 1.1** (Chiti and Dobson, 2006). However, in many amyloid associated diseases, it is the cytotoxic oligomeric intermediates that mediate the disease pathology (Meier et al., 2006; Kayed, 2003). Therefore, there is increased motivation for research into devising techniques for inhibiting the aggregation of native amyloidogenic proteins into both the oligomeric species, known to be cytotoxic; and full-length fibrils, the deposition of which causes further disease progression (Hard and Lendel, 2012).

Despite the lack of understanding of the specific mechanism behind the aggregation of most amyloid proteins, a general mechanism of protein unfolding, prior to aggregation has been found to be common to most, including apoA-I. This suggests that a particular method of inhibition for one species of amyloidogenic protein, may be suitable for other, non-related species (Hard and Lendel, 2012; Wang and Raleigh, 2014). The potential for this general amyloid inhibition strategy is highlighted by the ability of some amyloidogenic proteins to be seeded by amyloid fibrils from other, non-related amyloid proteins (Larsson et al., 2011), suggesting a common aggregation mechanism. Common methods for amyloid inhibition are outlined below and summarised in **Figure 1.14**.

6.1.1.1. Targeting the protein source

Amyloid formation is dependent on the presence of the amyloidogenic peptide, be it the wild type protein, a mutant protein, or a cleaved peptide. Reduction of the concentration of the amyloidogenic peptide, at an expression or post-translational modification level, can be a highly effective treatment against systemic amyloidosis (Gillmore and Hawkins, 2006). Examples of this technique include anti-inflammatory drugs targeting the production of SAP in AA amyloidosis, chemotherapy against B-cells to reduce immunoglobulin light chains, such as Melphalan (Kyle et al., 1997); liver transplantation to remove the abnormal TTR mutant, and targeting the β and γ secretase enzymes to inhibit the cleavage of the amyloidogenic Aβ(1-40) and (1-42) fragments (Gillmore and Hawkins, 2006). Alternatively, inhibiting the interaction of amyloidogenic proteins with GAG's, known to promote amyloidosis, is another promising general amyloid inhibitor. Fibrillex™, an N-acetylglucosamine analogue of

heparin, binds to amyloid precursor proteins and stops the interaction of heparin with amyloidogenic proteins (Gillmore and Hawkins, 2006).

6.1.1.2. Promoting alternative folding pathways

It is widely accepted that protein oligomers or aggregation intermediates, rather than fibrillar species, in many cases, lead to the cytotoxic entity of amyloidogenic proteins, manifesting in cell death and amyloid-associated disease progression (Kayed, 2003). In some cases, the native protein readily forms oligomeric species, which remain cytotoxic for a prolonged period of time. Agents that promote the aggregation of these proteins into the benign fibril or amyloid-like structures, which do not result in cytotoxicity, could reduce the disease pathology (Bodner et al., 2006; Madine and Middleton, 2010). GAG's have the potential to promote aggregation of a protein into a non-toxic fibrillar structure, avoiding potential cytotoxic oligomeric species (Iannuzzi et al., 2015). Promoting the formation of amyloid-like structures can both avoid the cytotoxic oligomer species, and inhibit fibril elongation. The ZAβ3 inhibitor forms a dimer around the β-hairpin structure of Aβ, creating a four-stranded β-sheet, in effect stabilising the monomeric amyloid (W. Hoyer et al., 2008).

6.1.1.3 Peptide based β-sheet breakers

The amyloidogenic propensity of Aβ arises from a central hydrophobic hot spot region comprising residues 17-21, in addition to contributions from residues 32-37 and 37-42 (Doig and Derreumaux, 2015). Such hot spot regions, which initiate amyloid formation, are found in all amyloidogenic proteins (Amijee et al., 2009). Targeting these sequences with short complementary peptides to block

aggregation or inhibit elongation of the extending fibril are attractive therapeutic techniques. Designing these inhibitors against the amyloidogenic protein sequence can increase specificity (Tjernberg et al., 1996; Soto et al., 1998). The iAβ5 β-sheet breaker peptide was shown to not only inhibit *in vitro* amyloidosis of Aβ, but also completely inhibit fibril formation *in vivo* in the brains of rats (Soto, et al., 1998). However, one problem with these short peptides is their potential to increase amyloidosis through elongation of the fibril (Hard and Lendel, 2012). As such, these short peptide sequences have since been modified to include proline residues, a natural β-sheet breaker (Wood et al., 1995); charged amino acid ends, to increase solubility; and the use of D-amino acids rather than L isomers, in order to avoid proteolytic cleavage (Soto *et al.*, 1998; Doig and Derreumaux, 2015; Jagota and Rajadas, 2013). N-methylation of the backbone residues of these short peptide β-sheet breakers not only increases solubility of the peptide, but interferes with hydrogen bonding on the outer edge of the extending amyloid fibril, inhibiting further elongation (Hughes et al., 2000; Kokkoni et al., 2006).

6.1.1.4. Small molecule inhibition of amyloidosis

Designing small molecules against the aggregation of amyloidogenic proteins has proven to be much more difficult than normal drug design, partially due to the lack of understanding about the aggregation mechanism of most proteins. Therefore, the majority of the successful small molecules act as general anti-amyloid agents, having inhibitory effects on several amyloidogenic proteins (Hard and Lendel, 2012), and are often found from screening of extensive compound libraries. One of the issues with researching these compounds is their

potential interaction with fluorescent amyloid binding molecules used to quantify amyloid formation. For example, interactions occur between the small molecule rifampicin and ThT in the study of IAPP amyloidosis (Meng et al., 2008) and between Congo red, which can inhibit amyloidosis, and ThT (Buell et al., 2010). Studies into the inhibition of tau aggregation screened a library of 200,000 compounds, which identified 77 successful inhibitor compounds, based on 4 groups: the N-phenylamines, anthraquinones, phenylthiazolylhydrazides and thioxothiazolidinones (Bulic et al., 2009). This work highlighted the requirement for ring structures and hydrophobic patches (**Figure 6.1**), which promote hydrogen bonding to the protein (Bulic et al., 2009).

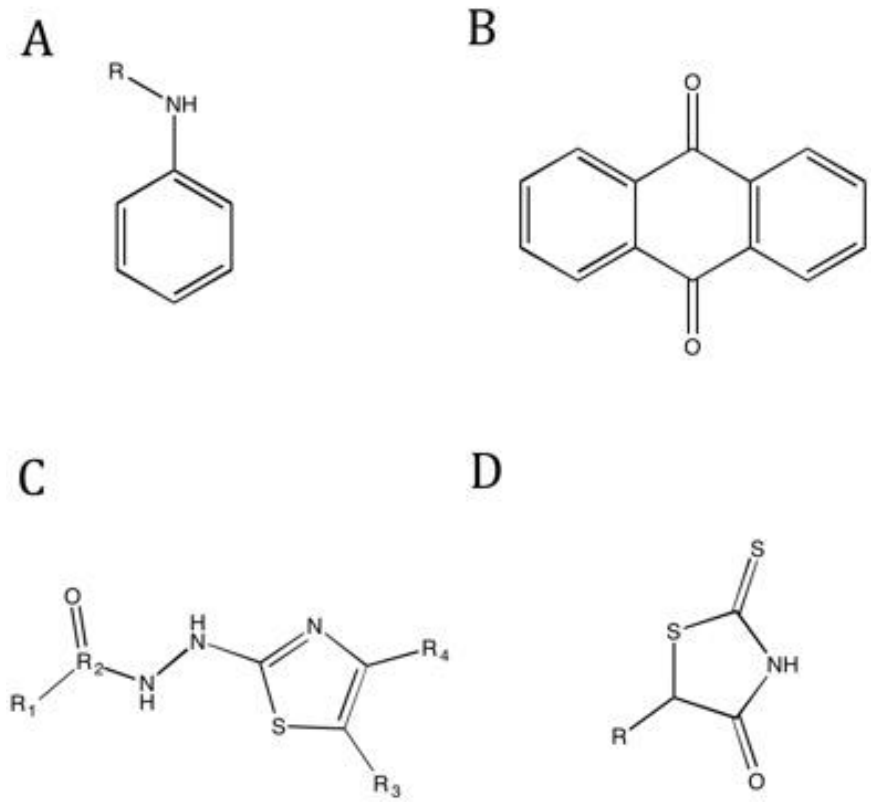

Figure 6.1 Structure of (**A**) N-phenylamines, (**B**) 9,10-anthraquinone, (**C**) phenylthiazolylhydrazides (Pickhardt et al., 2007), and (**D**) thioxothiazolidinines (Bursavich et al., 2007), all successful inhibitors of tau aggregation.

Some small molecule compounds can be easily modified in order to exhibit different effects on amyloid aggregation. For example, inositol compounds have the ability to both inhibit and promote the aggregation of Aβ into β-sheet structures, depending on the specific orientation of the hydroxyl groups.

Scyllo-inositol (**Figure 6.2 A**) has been shown to inhibit the aggregation of Aβ by stabilising small, soluble Aβ complexes, with no fibrils visible by TEM. As with the tau compounds, hydrophilic patches were key in forming hydrogen bonds between the inhibitor and the soluble Aβ monomer. Removal of the hydroxyl groups from scyllo-inositol, to form 1-4-dideoxy-scyllo-inositol (**Figure 6.2 B**), decreased the inhibitory effect, with intermediate length fibrils and amorphous aggregates visualised by TEM. This highlights an essential structure-activity relationship with the hydroxyl groups. However, increasing the hydrophobicity of the compound with two methyl groups (**Figure 6.2 C**) also prevented the elongation of full-length fibrils, by stabilising the proto-filament intermediate, which often can be a cytotoxic oligomeric species (Hawkes et al., 2010).

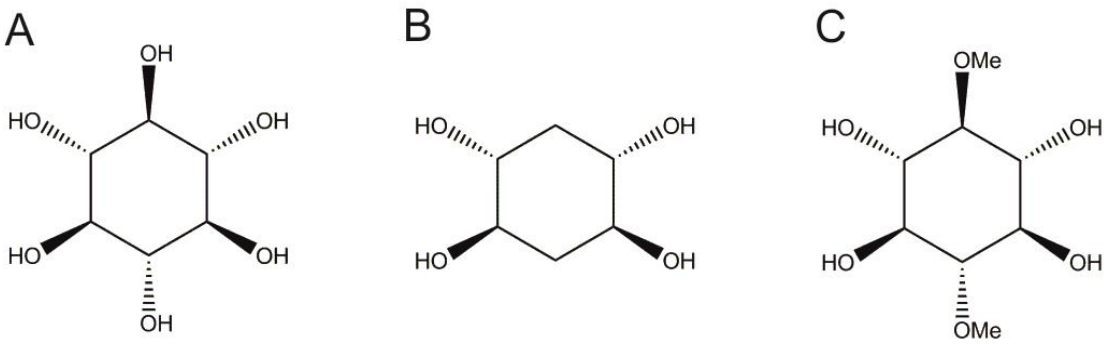

Figure 6.2 Structure of (**A**) Scyllo-inositol, (**B**) 1-4-dideoxy-scyllo-inositol, and (**C**) 1,4,di-O-methyl-scyllo-inositol.

From a screening of 169 compounds, 15 were shown to inhibit the aggregation of α-synuclein in vitro, including dopamine. However, the inhibition of α-synuclein by dopamine and L-dopa lead to a build up in the levels of cytotoxic protofibrils (Conway et al., 2001). This highlights the complexity of designing amyloid inhibitors that are suitable for pharmacological use.

6.1.2. Polyphenol compounds

Polyphenols are natural, secondary metabolites of plants found in fruits, vegetables and cereals. Over 8000 natural polyphenol compounds have been identified and can be split into 4 main characteristic groups: phenolic acids, stilbenes, lignans and flavonoids (**Figure 6.3**).

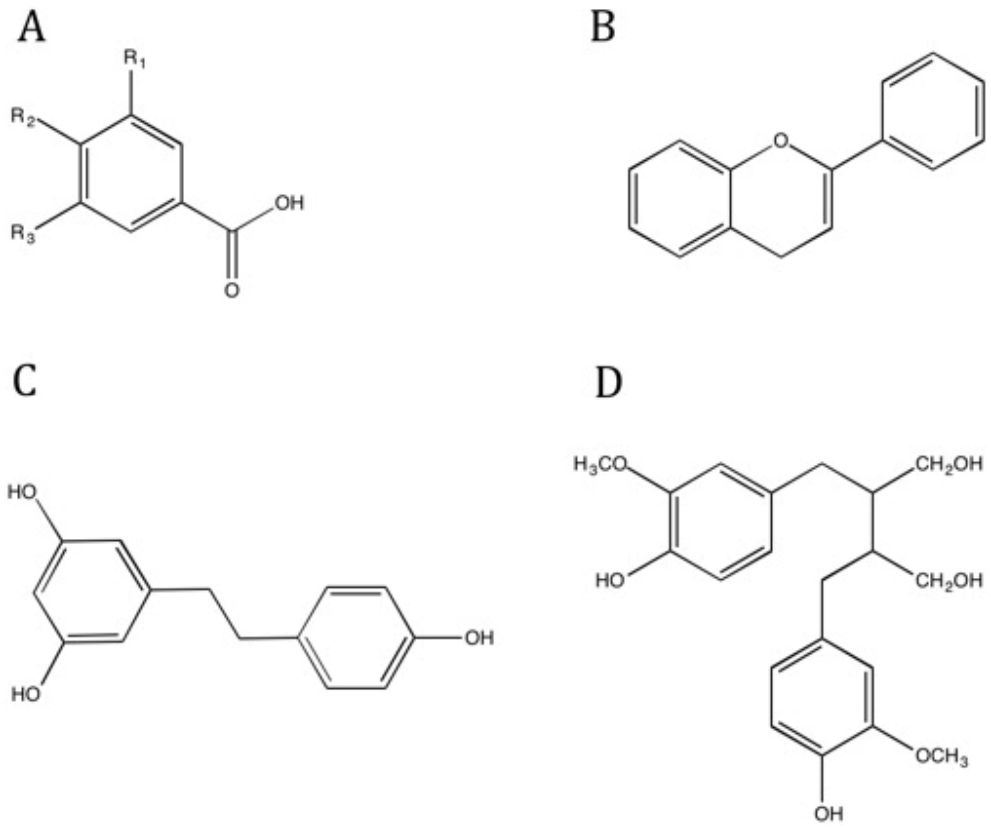

Figure 6.3 Four main groups of natural polyphenol compounds: (**A**) phenolic acid (hydroxyl-benzioc), (**B**) flavonoids, (**C**) stilbenes and (**D**) lignans.

The most studied of the 4 polyphenol groups are the flavonoids, which are comprised of 2 aromatic rings connected by three carbons in an oxygenated heterocycle (**Figure 6.3 B**) (Pandey and Rizvi, 2009). The health benefits of polyphenol compounds are extensive, including: cardio-protective, anti-cancer, anti-diabetic, anti-aging, UV protection, improved metabolism, and neuro-protective effects (Pandey and Rizvi, 2009). From a screening of over 184,000 compounds, 25 benzothiazole compounds were found to inhibit the aggregation of huntingtin. This included the discovery of the green tea polyphenol epigallocatechin gallate (EGCG) (Ehrnhoefer et al., 2006). Later work discovered the inhibitory effects of EGCG on the aggregation of Aβ, α-synuclein (Ehrnhoefer et al., 2008; Bieschke et al., 2010) and the amyloid model κ-casein (Hudson et al., 2009).

6.1.2.1 Epigallocatechin gallate

Green tea has long been associated with increased cardiovascular function and metabolic health (Wolfram, 2007). The polyphenol compounds, in particular the flavonoids, appear to be responsible for this. The major flavonoid in green tea is epigallocatechin gallate (EGCG) (Doig and Derreumaux, 2015), the structure of which is shown in **Figure 6.4.** EGCG in isolation has been shown to: reduce the oxidative damage to DNA, reduce the postprandial lipid response in patients with hypertriglyceridemia, decrease glucose plasma levels in patients suffering from type II diabetes mellitus, reduce the progression of atherosclerosis, inhibit smooth muscle cell proliferation, and increase weight loss and energy expenditure (Wolfram, 2007; Nagao et al., 2005; Rudelle et al., 2007; Wolfram et al., 2006; Chyu, 2004; Won et al., 2006; Kavantzas et al., 2006).

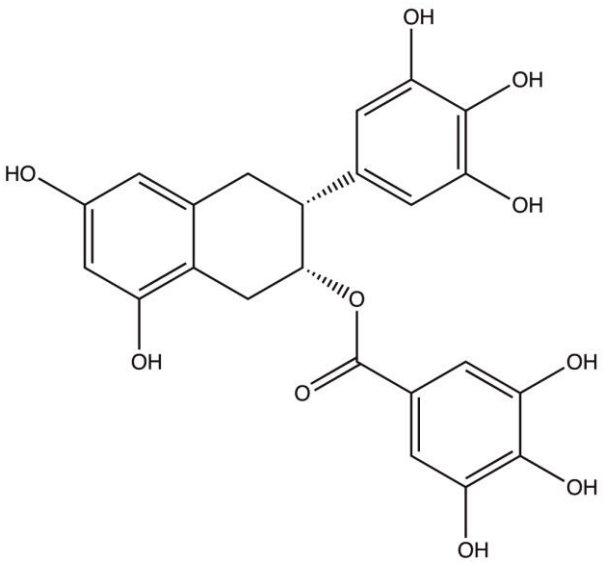

Figure 6.4 Chemical structure of epigallocatechin gallate, an amyloid inhibitor.

EGCG has been shown to have amyloidosis-inhibiting effects on Aβ, α-synuclein and huntingtin (Ehrnhoefer et al., 2006; Bieschke et al., 2010; Ehrnhoefer et al., 2008; Masuda et al., 2006; Doig and Derreumaux, 2015), as well as causing a structural remodelling of mature α-synuclein (Bieschke et al., 2010), Aβ1-40 and IAPP fibrils (Palhano et al., 2013).

EGCG is thought to promote an off-pathway aggregation mechanism of amyloidogenic proteins into unstructured, non-toxic oligomers, which lack the ability to progress into amyloid fibrils (Ehrnhoefer et al., 2008). However, the precise mechanism of how this occurs is currently unknown (Wang and Raleigh, 2014). EGCG has been shown to interact with Aβ, via hydrogen bonds at residues 1-16 and via hydrophobic interactions at residues 17-42 (Wang et al., 2010). EGCG is reported to inhibit the aggregation of apoA-I (1-83) and the apoA-I (1-83/G26R) Iowa mutant, but produced mixed results on its ability to disaggregate preformed fibrils (Nakajima et al., 2016). As yet, no interaction has been reported

for full-length, wild type apoA-I with EGCG, which could be a potential therapy for atherosclerosis.

6.1.3. Aims

This chapter aims to determine whether green tea polyphenols, including EGCG, affect the aggregation propensity of apoA-I and/or the properties of the aggregates. The binding of EGCG to apoA-I aggregates will be determined using a co-sedimentation experiment, and the effects of EGCG on apoA-I aggregation will then be studied using ThT fluorescence. Finally, the structure of apoA-I aggregates formed in the presence of EGCG, and with EGCG added after aggregation has ceased will be determined via SSNMR and compared to apoA-I aggregates alone.

6.2. Methods

6.2.1 Isolation of polyphenol compounds from green tea

2 g of green tea (Twining's™ pure) was added to 40 mL of water. The solution was microwaved at 900 W of power for 2 cycles of 30 seconds, followed by 4 cycles of 15 seconds with a minute between each heating. The solution was filtered through a 1μm filter paper (Whatman) and filtered with a 0.2 μm corning syringe filter. The solution was then freeze-dried at -70 °C and 0.0026mbar pressure for 24 hours, using a Christ-Alpha 2 system.

6.2.2 Characterisation of compounds isolated from green tea

A catechin mixture (Sigma) was purchased as a reference set for the polyphenol compounds present in green tea, to assist in the assignment of high performance

liquid chromatography (HPLC) spectral peaks. Analysis certificates confirming the mass and purity of the compounds can be found in **Appendix 5**. The reference material and mixture of compounds isolated from green tea were separated using HPLC, in order to characterise the unknown compounds. Separation was performed on a Nexera UHPLC (Shimadzu) system, with a mobile phase of 0.1 % orthophosphate in ultrapure water (A) or in acetonitrile (B), whilst the static phase consisted of a shim-pack XR-ODS 2.2 μm reverse phase column. The gradient elution, at a flow rate of 1 mL/min consisted of 0-3 minutes (5% of B), 3-10 minutes (5-20 % B), 10-13 minutes (20-50 %) and 13-13.1 minutes (50-5 % B). Green tea extracts were diluted to 7.2 mg/ml of lyophilised material in water, prior to HPLC analysis.

6.2.3. Effect of green tea compounds on the aggregation of apoA-I

The ThT fluorescence experiments carried out in this section of work, mirrored those for the continual read experiments in **Section 4.3.2**. ApoA-I (7.2 μM) was incubated with ThT alone and in the presence of 14.4 μM heparin. Samples were also incubated with, or without, either pure EGCG or green tea extract at 2-fold molar excess to the apoA-I. After measuring the fluorescence for 10 minutes, concentrated HCl was added to reduce the sample to pH 4 and induce aggregation. ThT fluorescence measurements were taken for 300 minutes, with the initial increase in fluorescence (ΔF_I) and total increase in ThT fluorescence (ΔF_T) recorded.

6.2.4 Determination of compounds binding to EGCG by HPLC

200 µL of apoA-I fibrils (formed at 36 µM) and Aβ fibrils (formed at 44 µM) were centrifuged for 10 minutes at 12,000 g. 200 µL of a 1/10 dilution of the compounds isolated from green tea was added to the fibrillar pellets, and incubated at 37 °C for 24 hours, with agitation. The fibrils were pelleted through centrifugation and the supernatant removed, prior to analysis by HPLC.

6.2.5. Absorbance of EGCG

In order to deduce whether the EGCG concentration could be measured by absorbance and utilised to measuring the binding of EGCG to apoA-I, EGCG at a range of concentrations from 0.01 mM to 1 mM was scanned across a UV range of 190 to 360 nm. The maximum absorbance intensity at 274 nm was recorded.

6.2.6. Binding of EGCG to apoA-I

ApoA-I (36 µM) was incubated in the presence and absence of increasing concentrations of EGCG at pH 4, at 37 °C with agitation for 3 days. Following the production of insoluble material, EGCG was added to the apoA-I samples that did not contain any EGCG during fibril formation and left for 24 hours. The insoluble material was removed through centrifugation at 13,400 rpm in a bench-top centrifuge. The absorbance of the supernatant at 274 nm was then measured and used to determine how much EGCG remained in solution.

6.2.7. Solid-state NMR

ApoA-I (36 µM) was incubated in the presence and absence of a 2-fold molar excess of EGCG at pH 4, at 37°C with agitation for 3 days, in order to form

insoluble aggregates. Following the production of insoluble material, EGCG was added to the apoA-I samples that did not contain any EGCG during fibril formation, and left for 24 hours. Fibrils were harvested through centrifugation at 12,000 g for 10 minutes. The aggregates were frozen in liquid nitrogen, prior to centrifugation into a zirconium 3.2 mm rotor with a Kel-F cap (Bruker, U.K).

6.2.7.1 One-dimensional solid-state NMR

One dimensional proton-decoupled ^{15}N CP-MAS SSNMR experiments were carried out on a Bruker Avance 400 MHz spectrometer, operating at a magnetic field of 9.3 Tesla, equipped with a 3.2 mm HXY MAS probe at 25 °C. Hartmann-Hahn cross-polarisation was achieved at a proton nutation frequency of 78 kHz, a 2 ms contact time, 100 kHz proton decoupling with SPINAL-64 applied during the signal acquisition, and a recycle delay of 2 ms. MAS was controlled at a frequency of 8 kHz ± 1 Hz. Each spectrum was the result of accumulating 20,000-100,000 transients. Direct polarisation (DP) experiments were the same except the CP step was replaced with a 3.5 ms 90 ° pulse at the ^{13}C frequency.

6.2.7.2 Two–dimensional solid-state NMR

Two-dimensional ^{13}C-^{13}C spectra were recorded at a magnetic field of 16.3 Tesla on a Bruker Avance III 700 MHz spectrometer, with a 3.2 mm HXY probe operating in double resonance mode, with magic angle spinning at 14 kHz and the temperature maintained at 4 °C. Hartmann-Hahn cross-polarisation was achieved with a 2 ms contact time, and 100 kHz proton decoupling with SPINAL-64 applied during signal acquisition. During the mixing time of 10 ms, the ^{1}H nutation frequency was lowered to 14 kHz, to achieve DARR mixing.

6.3 Results

6.3.1 Isolation of compounds from green tea

Green tea compounds were extracted, following methods described in **section 6.2.1**. The compounds in the tea extract were then separated using HPLC, producing the chromatograph shown in **Figure 6.5**. Nine separate peaks corresponding to individual compounds were identified by HPLC and labelled a-i, according to increased retention times.

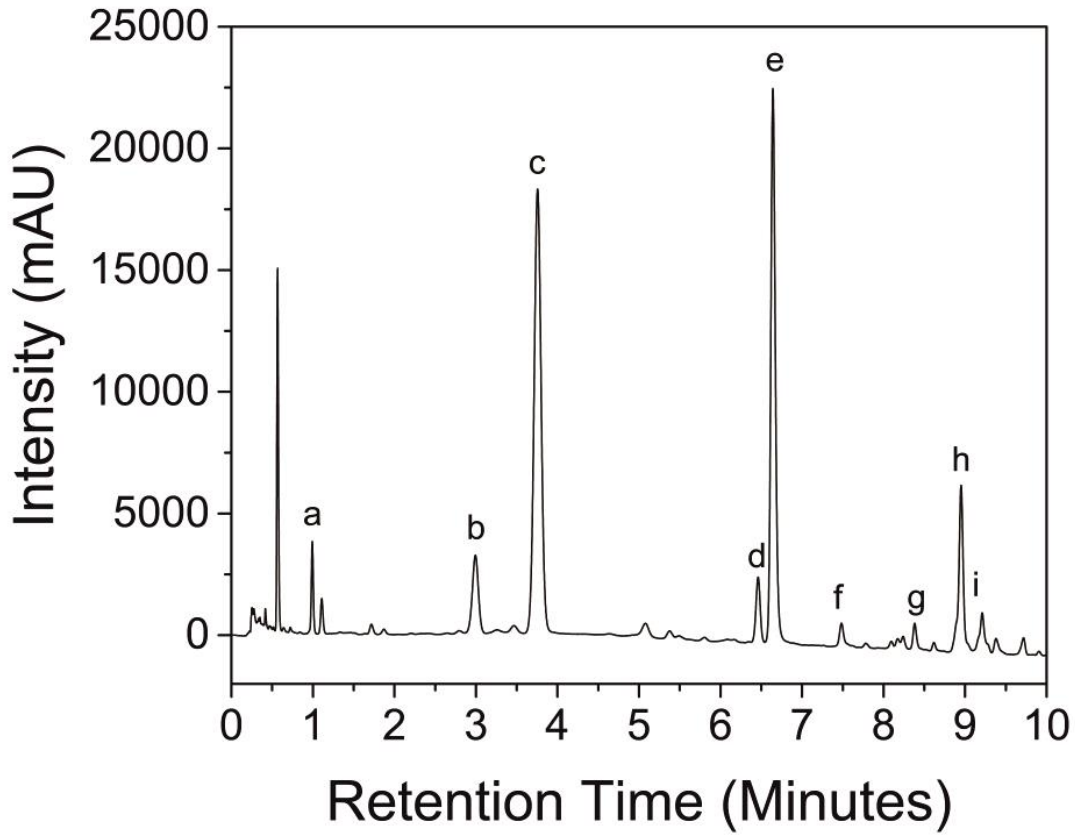

Figure 6.5 HPLC chromatograph for the separation of compounds extracted from green tea. The compounds were labelled a-i, according to their retention time.

In order to determine what each of the uncharacterised compounds labelled a-i in **Figure 6.5** were, a reference catechin mixture was purchased from Sigma and separated using the same HPLC system. This reference set mixture contains 8 common catechins present in green tea. Separation by HPLC matched the reference material provided in **Appendix 5**, identifying the compounds in **Figure 6.6** as (1) gallocatechin, (2) caffeine, (3) catechin, (4) epicatechin, (5) epogallocatechin-3-gallate (EGCG), (6) gallocathin-3-gallate, (7) epicathechin-3-gallate, and (8) catechin-3-gallate. The structures for each of these compounds are shown in **Figure 6.7**.

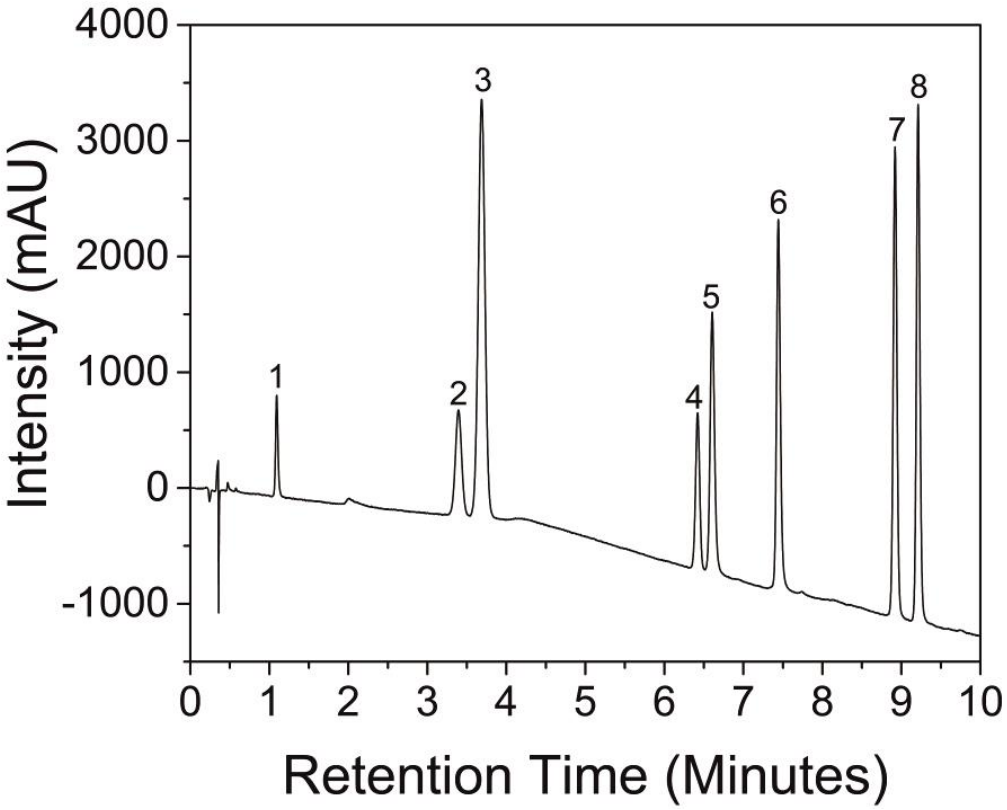

Figure 6.6 HPLC chromatograph of the separation of compounds present in the Sigma catechin reference set. Numbers refer to (1) gallocatechin, (2) caffeine, (3) catechin, (4) epicatechin, (5) epogallocatechin-3-gallate (EGCG), (6) gallocathin-3-gallate, (7) epicathechin-3-gallate, and (8) catechin-3-gallate.

1. Gallocatechin

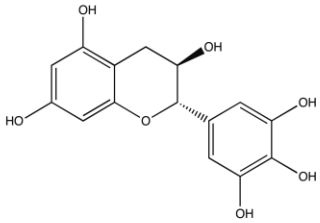

2. Caffeine

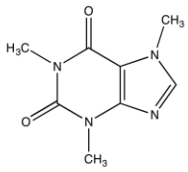

3. Catechin

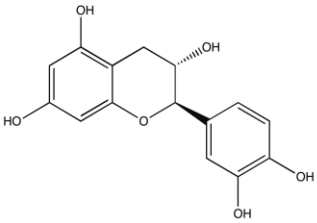

4. Epicathechin

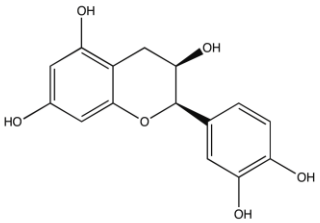

5. Epigallocatechin-3-gallate

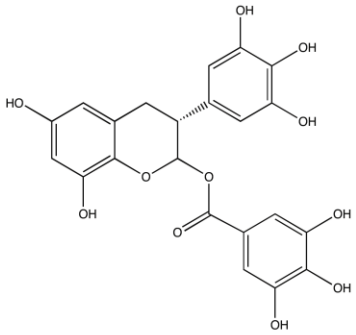

6. gallcathechin-3-gallate

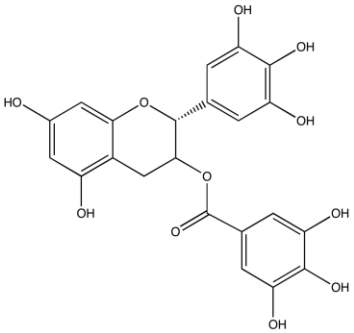

7. Epicatechin-3-gallate

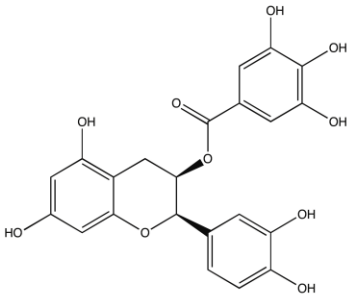

8. Catechin-3-gallate

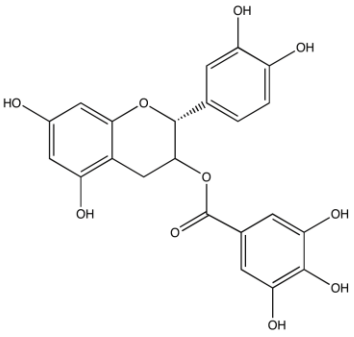

Figure 6.7 Chemical structures for the 8 compounds in the catechin mix purchased from Sigma.

The chromatograms in **Figure 6.5** and **6.6** exhibit peaks with almost identical retention times, apart from peak (g) in **Figure 6.5**, which does not match up with any compounds in the catechin mixture. Therefore, it is reasonable to assume that the compounds isolated from green tea extracts in **Figure 6.5** are (a) gallocatechin, (b) caffeine, (c) catechin, (d) epicatechin, (e) epogallocatechin-3-gallate (EGCG), (f) gallocathin-3-gallate, (h) epicathechin-3-gallate, and (i) catechin-3-gallate. Now that the compounds from the tea extract have been identified, they will be referred to by the numbers 1-8.

6.3.2 Concentration of catechins in green tea extracts

HPLC analysis of the reference material, which contained each of the 8 compounds at 100 µg/ml, allows estimation of the catechin concentration in the green tea extract, based on the peak area. The concentration of each catechin is shown in **Table 6.1,** confirming that epigallocatechin-3-gallate (EGCG), highlighted in bold, is the most abundant compound in green tea.

Table 6.1 HPLC retention time, peak intensity, area under the peak, reference concentration scaling factor, and the concentration of each of the 8 catechins in the green tea extract.

Compound	Retention Time (min)	Peak Height	Peak Area	Scaling Factor	Concentration (µg/ml)
Gallo-catechin	1.1	1364.3	42.8	0.31	139.3
Caffeine	3.0	3202.6	286.9	0.86	335.0
Catechin	3.8	18240.7	1822.8	3.61	504.4
Epi-catechin	6.5	2481	136.5	0.82	165.8
EGCG	**6.6**	**22504.1**	**1419.0**	**1.50**	**947.2**
Gallocathin-gallate	7.5	951.1	62.3	1.84	33.9
Epicatechin-gallate	9.0	6840.1	453.8	2.22	204.0
Catechin-gallate	9.2	1635.5	128.3	2.33	54.9

6.3.3. Effect of green tea extracts on Aβ and apoA-I amyloidosis.

EGCG has been shown previously to inhibit the aggregation of Aβ *in vitro* (Ehrnhoefer et al., 2008). Therefore, the effects of green tea extracts on the aggregation of Aβ were assessed by ThT fluorescence. Aβ was prepared as detailed in Stewart *et al*. (2016). **Figure 6.8** confirms that incubation of Aβ (35 μM) in conditions that promote the aggregation of apoA-I, leads to its aggregation into ThT responsive material after approximately 10 minutes. Inclusion of green tea extract at a concentration of 1.5 mM, calculated using the molecular weight of EGCG, inhibits the formation of ThT responsive material, confirming that the green tea extract inhibits Aβ amyloidosis.

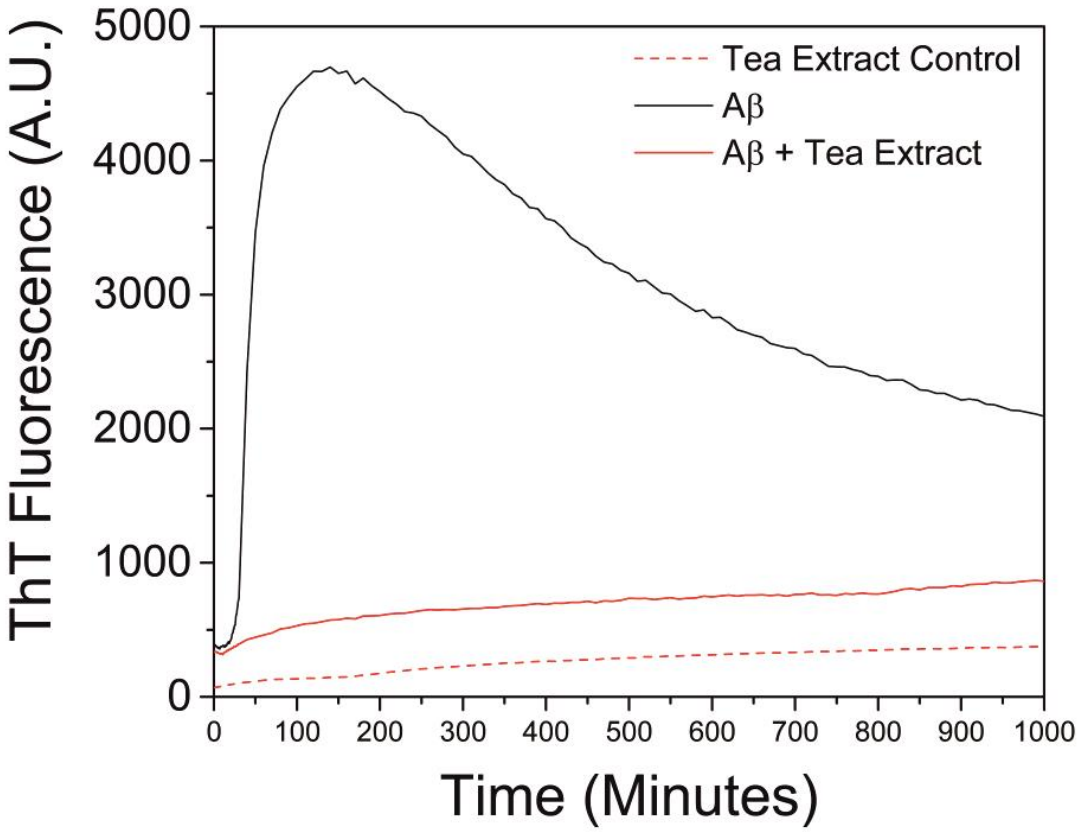

Figure 6.8 ThT fluorescence in the presence of Aβ (35 μM) alone, and with 1.5 mM green tea extract.

Given that the data here suggests green tea extracts inhibits Aβ aggregation, in addition to pure EGCG, as shown by Ehrnhoefer *et al*., (2008), ThT experiments were carried out to assess the ability of both the green tea extract and pure EGCG to inhibit apoA-I aggregation.

The experiment followed previous ThT procedures, and apoA-I (7.2 μM) was incubated, alone or in the presence of a 2-fold molar excess of heparin, and/or EGCG or green tea extract at pH 7, prior to addition of concentrated HCl, to reduce the sample to pH 4 and induce aggregation.

Figure 6.9A shows that in all 6 conditions (± heparin and ± EGCG/ tea extract), apoA-I at pH 7 showed a low ThT fluorescence, consistent with control samples and no amyloid formation during the entire experiment. This is consistent with previous findings, such as those in **Figure 4.5** and **4.7**, and confirms that EGCG does not induce a ThT response at pH 7.

Following acidification to pH 4, apoA-I aggregates into insoluble material, with an increase in ThT fluorescence. This ThT response is dramatically enhanced in the presence of heparin (**Figure 4.5** and **4.7**). In samples containing either a 2-fold excess of EGCG, or green tea extract, the ThT fluorescence response shows virtually no difference, neither in the initial increase (F_I), nor the total ThT fluorescence after 300 minutes (F_T) (**Figure 6.9B**). This suggests that these catechins do not exhibit any inhibitory effects on the aggregation of apoA-I, as they do with Aβ.

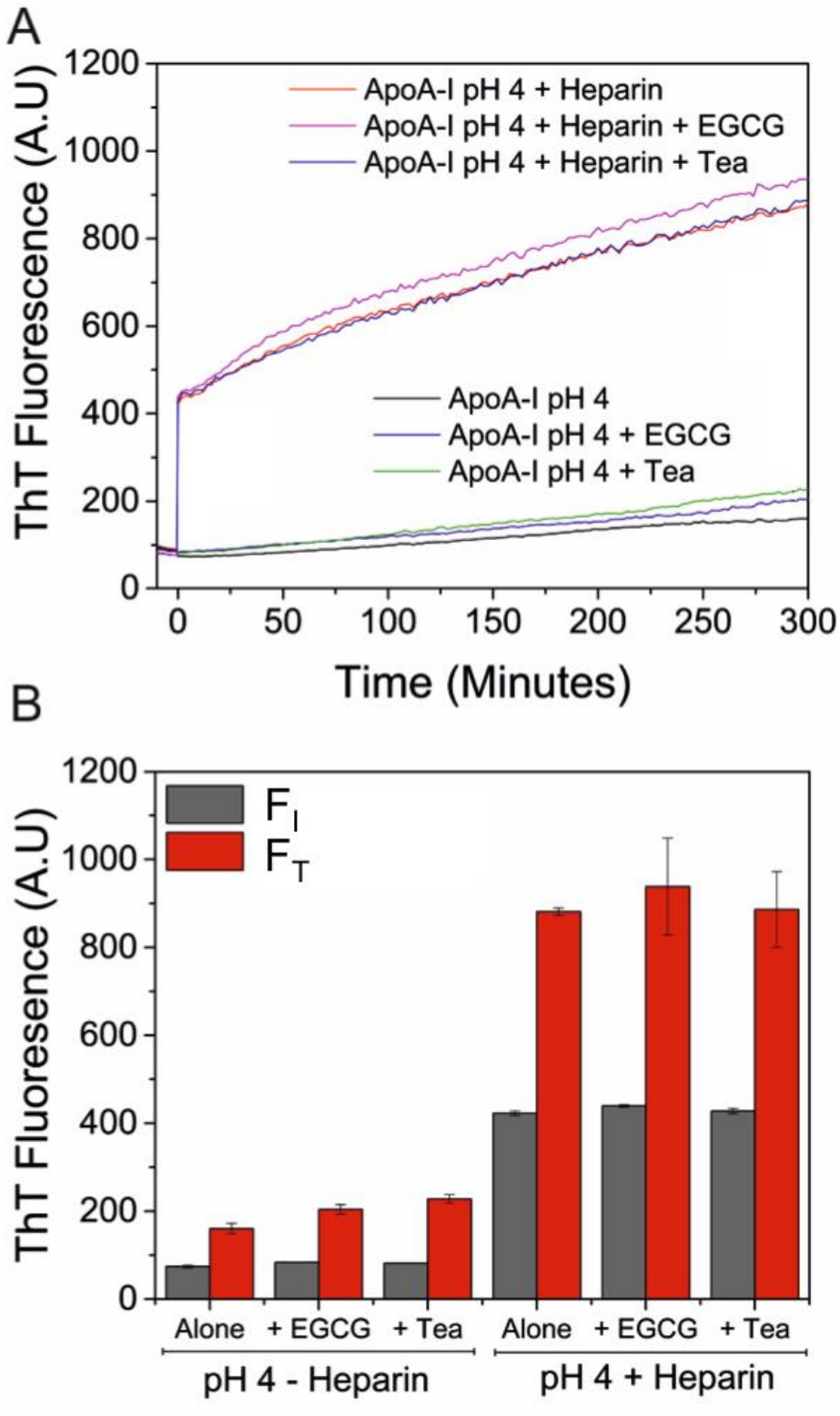

Figure 6.9 ThT fluorescence of apoA-I incubated at pH 4 in the presence or absence of heparin, and with the addition of EGCG or green tea extract, prior to acidification. Measurements are the mean of 3 samples ± standard error.

6.3.4 Binding of green tea extracts to apoA-I.

The binding of catechins extracted from green tea to both Aβ and apoA-I was assessed using co-sedimentation experiments. Green tea extract was added to preformed Aβ and apoA-I fibrils, and incubated with agitation for 24 hours. The insoluble aggregates were then removed through centrifugation, co-pelleting any bound catechin compounds. The remaining concentration of each compound was estimated using HPLC analysis. Pure EGCG was then added to apoA-I fibrils, incubated for 24 hours, then the fibrils and any bound EGCG were removed through centrifugation. The remaining concentration of EGCG left in the supernatant was calculated, using the absorbance of EGCG at 274 nm (**Section 6.3.4.2**).

6.3.4.1 Calculation of catechin binding by HPLC analysis

EGCG has previously been shown to inhibit amyloidosis of Aβ, by binding to the natively unfolded protein and inhibiting its conversion into β-sheet structures (Ehrnhoefer et al., 2008; Bieschke et al., 2010). Therefore, we would expect to see a reduction in the HPLC spectrum peak for the EGCG compound (peak 5) in the supernatant, following incubation with Aβ.

Figure 6.10A confirms a considerable selective reduction in peak intensity for compounds 2, 4, 5 and 7 corresponding to caffeine, epicatechin, epogallocatechin-3-gallate (EGCG), and epicathechin-3-gallate. **Table 6.2** confirms the reduction in the concentration for these 4 compounds, suggesting 89, 100, 100 and 92 % of the caffeine, epicatechin, epogallocatechin-3-gallate (EGCG), and epicathechin-3-gallate, respectively, was bound to Aβ and removed

from the solution by co-precipitation with the Aβ. EGCG is shown to bind to Aβ at a higher concentration than any of the other catechin compounds.

Upon incubation of the tea extract with apoA-I, the HPLC analysis of the supernatant shows a considerable reduction in the peak intensity for epigallocatechin-3-gallate (5), gallocathin-3-gallate (6) and epicathechin-3-gallate (7). (**Figure 6.10 B**) However, from the 9 identified compounds, EGCG shows the greatest reduction in concentration (**Table 6.2**), with 232 μmoles binding to apoA-I.

This data confirms that Aβ binds to EGCG, as expected, since EGCG inhibits the aggregation of Aβ. However, interestingly, even though EGCG does not induce a reduction in the aggregation of apoA-I, it appears to bind with high affinity.

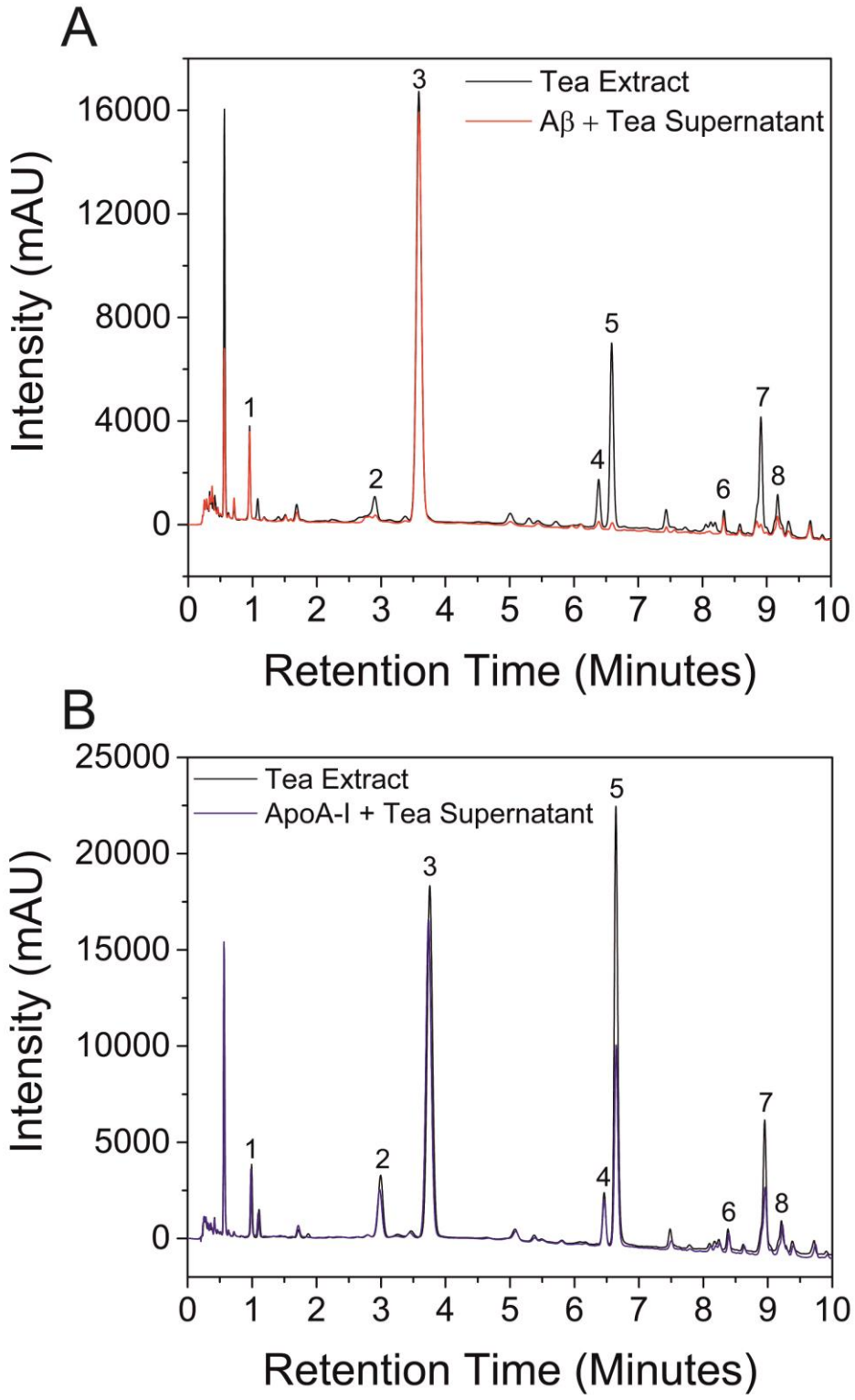

Figure 6.10 HPLC spectrum of the supernatant, following incubation of the green tea extract with (**A**) Aβ and (**B**) apoA-I fibrils, and removal of the insoluble aggregates and associated compounds by centrifugation. HPLC spectra of the green tea extract control are also included for intensity comparison.

Table 6.2 Analysis of the green tea supernatant following incubation with preformed Aβ and apoA-I fibrils. The * indicates compounds that did not produce a measureable peak at the expected retention time.

	Aβ (8 nmoles)				
	Control (µg/ml)	**Supernatant (µg/ml)**	**Bound (µg/ml)**	**Bound (%)**	**Bound (µmoles)**
Gallo-catechin	343.5	301.8	41.6	12.1	27.2
Caffeine	124.7	14.2	110.5	88.6	113.8
Catechin	449.1	434.0	15.1	3.4	10.4
Epi-catechin	127.3	*	127.3	100	87.7
Epigallocathechin-3-gallate	297.7	*	297.7	100	129.9
Gallocathin-gallate	19.1	3.8	15.4	80.2	6.7
Epicatechin-gallate	140.0	10.9	129.1	92.2	58.4
Catechin-gallate	65.5	20.3	45.2	69.0	20.4

	ApoA-I (7.2 nmoles)				
	Control (µg/ml)	**Supernatant (µg/ml)**	**Bound (µg/ml)**	**Bound (%)**	**Bound (µmoles)**
Gallo-catechin	337.1	329.9	7.3	2.2	4.7
Caffeine	302.9	240.3	62.6	20.7	64.4
Catechin	506.4	460.3	46.0	9.1	31.7
Epi-catechin	154.9	156.9	0	0	0
Epigallocathechin-3-gallate	958.7	425.5	533.2	55.6	232.7
Gallocathin-gallate	35.2	10.3	24.8	70.6	10.8
Epicatechin-gallate	200.3	102.3	98.0	48.9	44.3
Catechin-gallate	52.7	43.0	9.7	18.5	4.4

6.3.4.2 Calculation of EGCG binding to apoA-I by absorbance

EGCG, at a range of concentrations from 0.1 mM to 1 mM, was scanned with UV radiation in order to determine whether UV absorbance was a viable quantitative method for determining the concentration of EGCG.

Figure 6.11A shows that the absorbance of EGCG, between 250 and 320 nm, was dependent on the concentration of EGCG added, with the intensity of the peak absorbance at 274 nm increasing with higher concentrations of EGCG, and an average extinction co-efficient of 16,816 $M^{-1}cm^{-1}$. When EGCG concentration was plotted against the absorbance intensity at 274 nm, a linear relationship was shown (**Figure 6.11B**), which confirms that the intensity at 274 nm can be used to estimate EGCG concentration, over a range of 0 to 500 μM.

Analysis of the supernatant remaining after the removal of aggregated apoA-I, and any bound catechins from the green tea extract by HPLC, indicated that EGCG bound to apoA-I. The next stage involved assessing whether EGCG bound to apoA-I during the aggregation process, or just to preformed fibrils. A simple method of confirming which of these interactions occur involved incubating apoA-I in aggregation-inducing conditions, with increasing concentrations of EGCG added before or after promoting fibril formation. Removal of the aggregated material and tightly bound EGCG by centrifugation, as previously, will allow the absorbance of the supernatant at 274 nm to be taken, and the remaining concentration calculated from the concentration plot in **Figure 6.11B**.

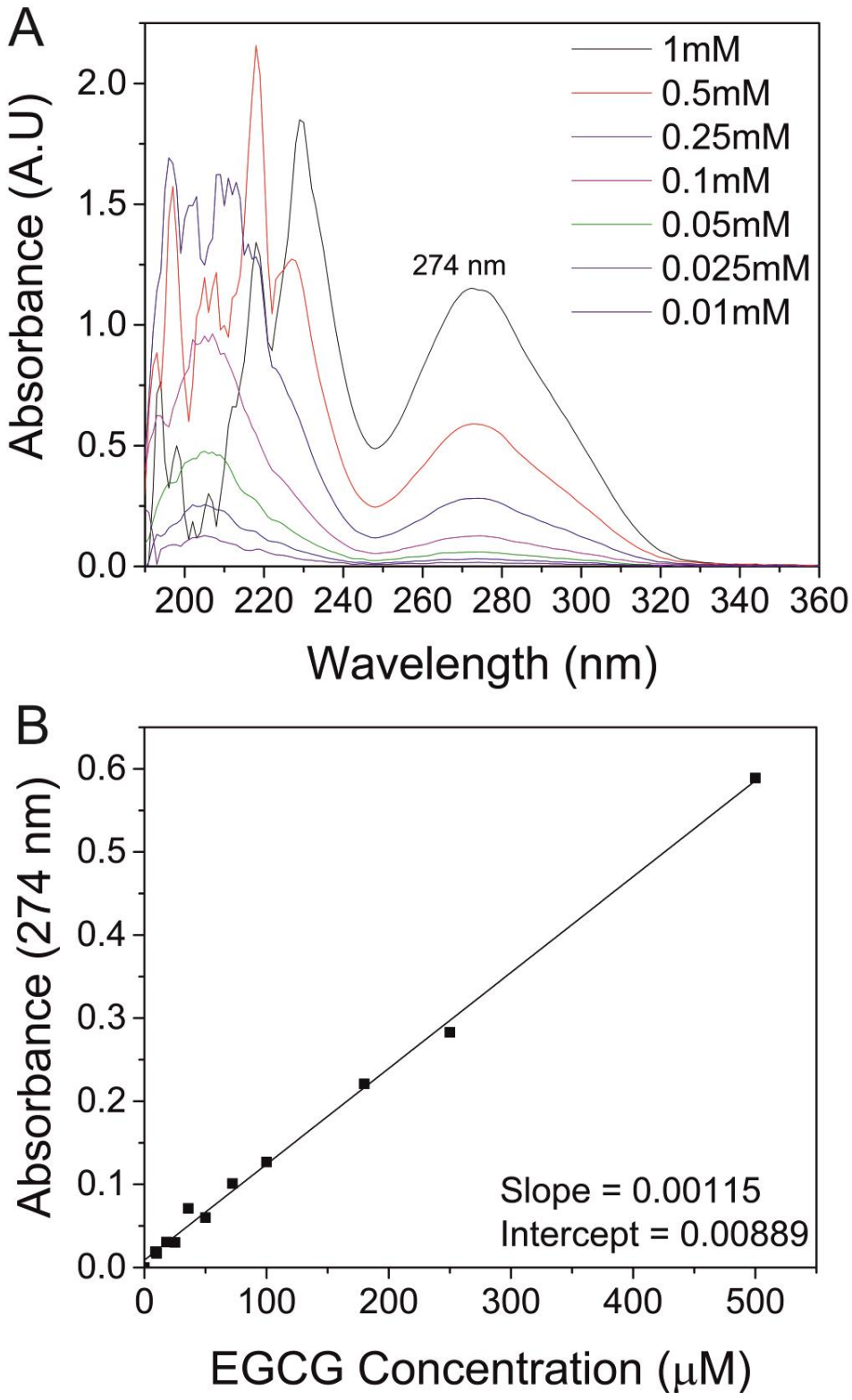

Figure 6.11 (**A**) Concentration dependence of EGCG on absorbance intensity between 190 and 360nm, with a peak absorbance at 274 nm. (**B**) Plot of absorbance intensity at 274 nm against EGCG concentration, showing a linear relationship.

In order to quantify the binding potential of EGCG to apoA-I, EGCG was added at a range of concentrations, from 9 to 180 µM, representing ¼ to 5-fold molar excess, compared to apoA-I at 36 µM. Binding of EGCG to apoA-I was monitored under 2 conditions: (i) EGCG was added to apoA-I (36 µM) at pH 7, prior to acidification with concentrated HCL, which was shown in **Section 4.3.2**, to induce aggregation of apoA-I, and (ii) with EGCG added to pre-formed apoA-I aggregates at pH 4. The experiment scheme is shown in **Figure 6.12.**

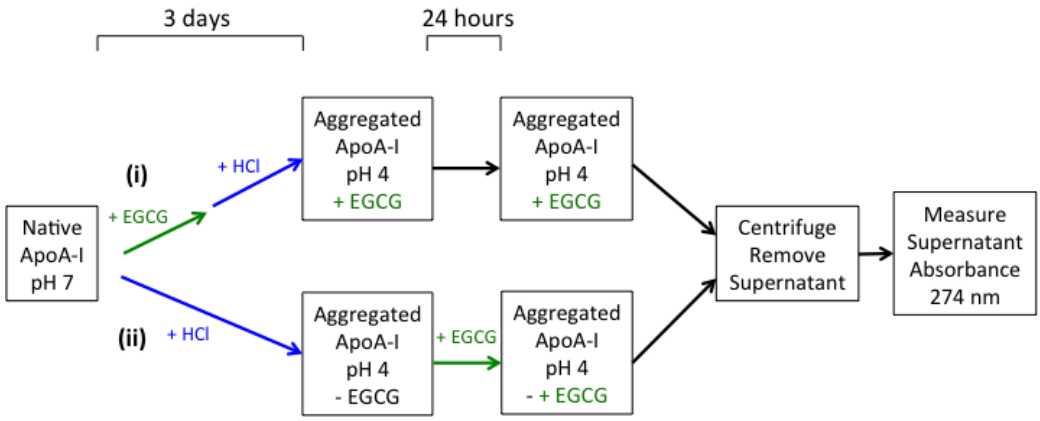

Figure 6.12 Experiment schematic showing the aggregation of apo-I (i) with EGCG added, prior to induction of aggregation (+), and (ii) with EGCG added to preformed fibrils (- +).

Figure 6.13A shows a reduction in the concentration of EGCG remaining in the supernatant, after removal of the apoA-I aggregates. This is consistent with EGCG binding to apoA-I. It also shows no difference between the amount of EGCG that binds to apoA-I when added before or after the induction of aggregation.

At apoA-I: EGCG molar concentrations of 36:9 µM and 36:18 µM, no EGCG remains in solution following sedimentation of the insoluble apoA-I material. This suggests that all of EGCG has bound to the apoA-I and co-sedimented with the protein aggregates. At equimolar concentrations, approximately 60 % of the

EGCG added had bound to apoA-I and was removed through sedimentation. When EGCG was in a 2 and 5 fold molar excess to apoA-I 36:72 μM and 36:180 μM, respectively, approximately 55% and 25 % of the EGCG added had bound and co-pelleted with apoA-I, respectively. Interestingly, this corresponds to approximately 34 μM at both concentrations. Therefore, saturation of apoA-I with EGCG appears to occur at approximately 34 μM when the stoichiometry of apoA-I and EGCG is equal. Conversely, estimation of the catechin concentrations remaining by HPLC showed that an excess of EGCG binds to apoA-I, at a molar ratio of 1:32 for apoA-I to EGCG. However, this data should be treated with caution, since it is based on integration of the HPLC peak areas.

The binding of EGCG to apoA-I could be modelled using the Hill equation (**Equation 6.1**) and Origin Pro software, where the bound EGGC (B) is related to the maximum binding (B_{max}), the concentration of EGCG added (A), the hill co-efficient (n) and the dissociation constant (k_D). This produces an apparent dissociation constant of 29.5 μM and 40.5 μM, for EGCG binding during the aggregation process and to pre-formed aggregates, respectively (**Figure 6.13B**).

$$B = B_{max}[A]^n / k_D + [A]^n \qquad \textbf{[6.1]}$$

The apparent dissociation constant for EGCG added to pre-formed fibrils has to be considered with caution, since only 5 data points are plotted, and because of the increased error in the sample containing a 5-fold molar excess. This binding data is calculated based on the assumption that, as shown via ThT, EGCG does not inhibit the aggregation of apoA-I. However, EGCG may be affecting the aggregation of apoA-I, or disturbing the pre-formed fibril, in a manner that is unfeasible to detect via ThT, which could affect the binding of EGCG to apoA-I.

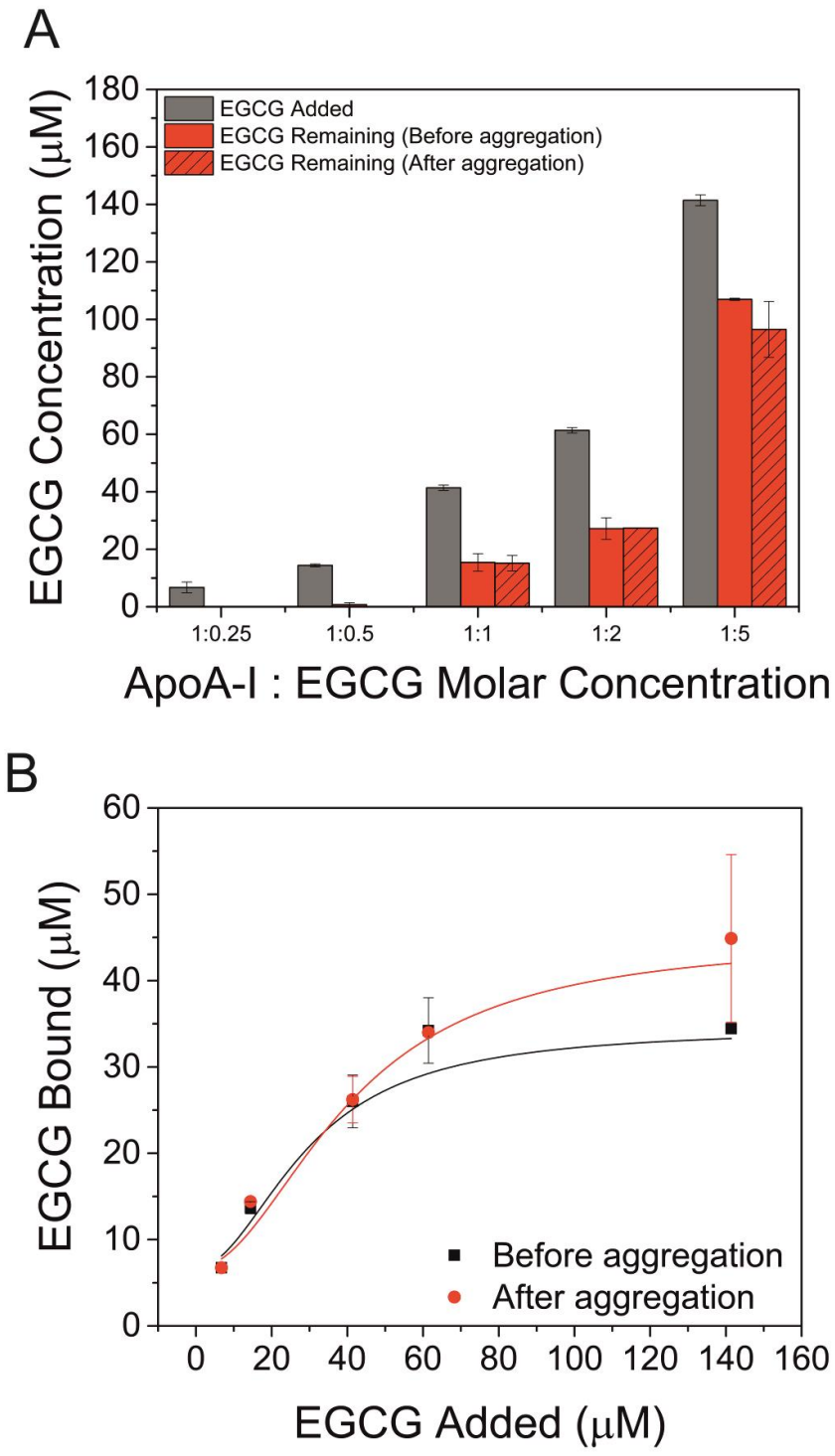

Figure 6.13 (**A**) Concentration of EGCG remaining in solution, after pelleting the insoluble apoA-I material, compared to the concentration of EGCG added. EGCG was added either before or after aggregation. Concentrations are representative of triplicate samples, with standard error shown. (**B**) EGCG binding to apoA-I modelled by the hill equation.

6.3.5 Secondary structure of EGCG treated apoA-I aggregates

EGCG has been shown to remodel mature amyloid fibrils (Bieschke et al., 2010; Palhano et al., 2013), which has therapeutic implications as a method of reversing amyloid deposition in amyloid-associated disease pathology.

6.3.5.1 EGCG added to preformed aggregates

Figure 6.14A shows the two-dimensional cross-polarisation ^{13}C-^{13}C MAS spectrum for apoA-I aggregates formed at pH 4 in the absence of heparin (black), and following treatment of the preformed aggregates with EGCG (red)**.** The spectrum of the EGCG treated aggregates contain cross-peaks for several easily assigned residues, with chemical shifts that correspond to both α-helical and β-sheet content within the aggregates. This is consistent with the untreated apoA-I aggregates formed in the absence of heparin (black).

However, when apoA-I aggregates are treated with EGCG, the intensities of the cross-peaks with chemical shifts that correspond to α-helical contributions are profoundly reduced, compared to those for the untreated aggregates. Caution should be taken when estimating the percentage contribution of secondary structural components, based on the intensities of chemical shifts. However, the dramatic decrease in the intensity of the α-helical cross-peaks, in particular for alanine (54.9/18.3 ppm for the Cα/Cβ), and valine (66.0/31.4 ppm for the Cα/Cβ) as shown in **Figure 6.14 B** and **C,** respectively, and the complete disappearance of the alanine α-helical cross-peak (179.6/18.3 ppm for the C-amide/Cβ) in the carbonyl region, is sufficient to confirm that EGCG causes a decrease in helical structures.

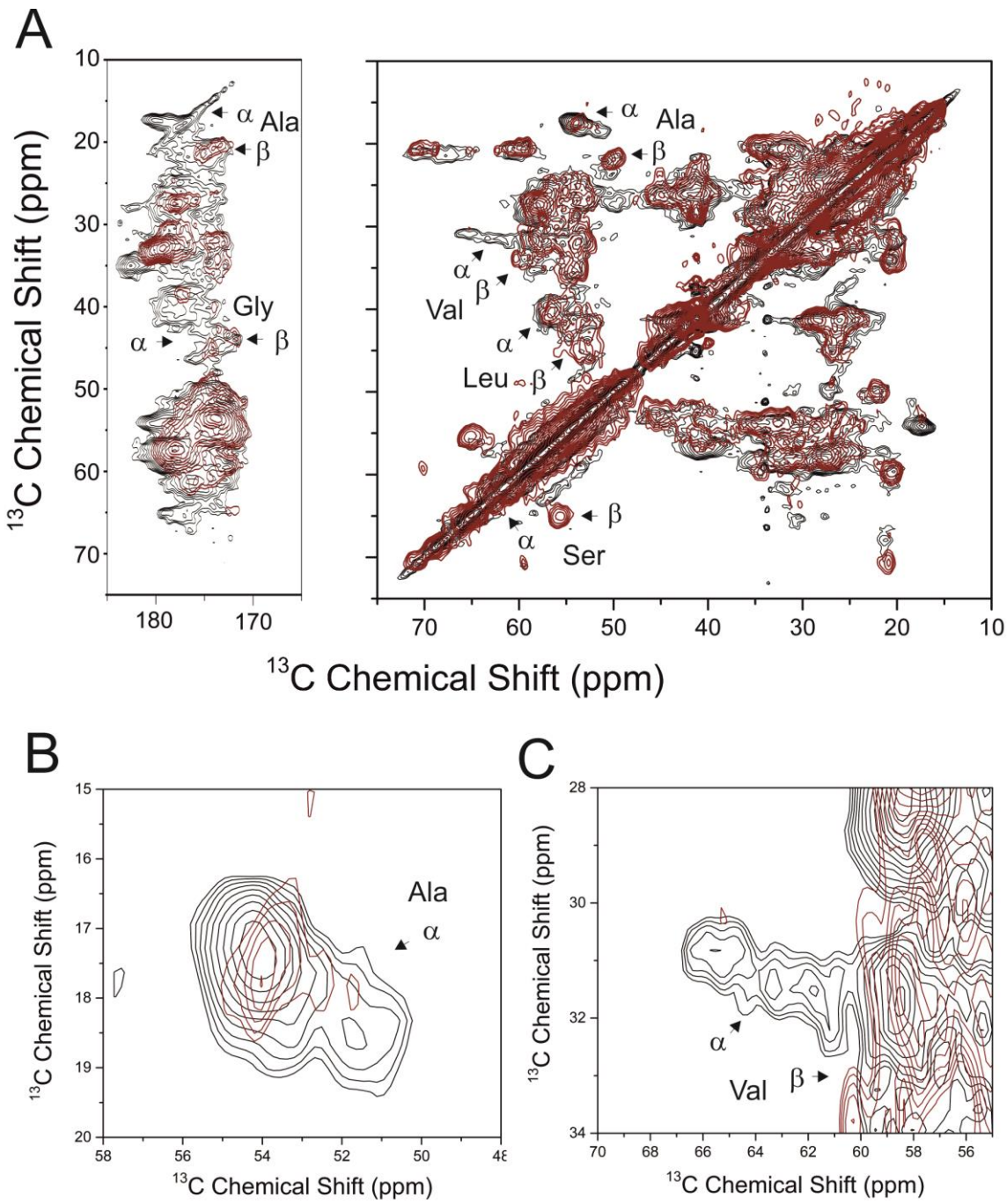

Figure 6.14 2D ^{13}C-^{13}C SSNMR spectra with DARR mixing of (**A**) apoA-I aggregates formed in the absence of heparin that are untreated (black) or with EGCG added to preformed aggregates (red). Figures (**B**) and (**C**) show the alanine and valine regions in more detail, highlighting the decrease in cross-peak intensity at chemical shifts associated with α-helices, upon treatment with EGCG.

6.3.5.2 EGCG added during aggregation of apoA-I

After determining that the addition of EGCG to pre-formed apoA-I aggregates resulted in a reduction of α-helical structures, a spectrum was acquired for apoA-I aggregates formed in the presence of EGCG.

The spectrum of apoA-I aggregates formed in the presence of EGCG (**Figure 6.15A** blue) contains cross-peaks for several easily assignable amino acids, with cross-peaks associated with both α-helical and β-sheet structures. However, when compared to the NMR spectrum of untreated apoA-I aggregates (**Figure 6.15A** black), the inclusion of EGCG during aggregation is shown to result in a decrease in the intensity of the α-helical contributions. The extent of intensity decrease in the α-helical cross-peaks is shown for alanine (**Figure 6.15B**) and valine (**Figure 6.15C**) residues.

This data suggests that treatment of apoA-I with EGCG, both during and after aggregation into amyloid-like fibrils, causes a change in the aggregates structure, resulting in a reduced α-helical content.

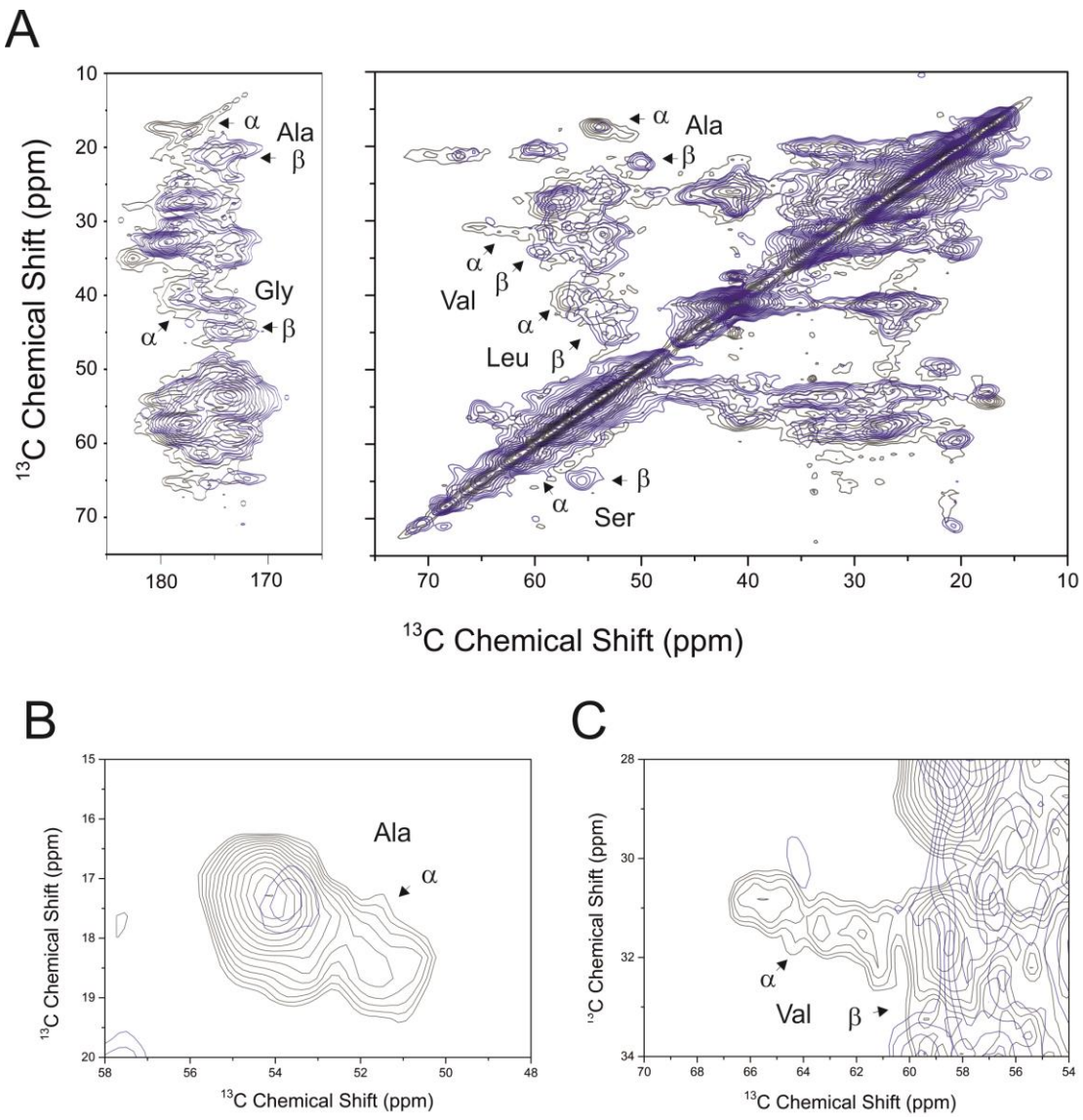

Figure 6.15 2D ^{13}C-^{13}C SSNMR spectra with DARR mixing of (**A**) apoA-I aggregates formed in the absence of heparin that are untreated (black) or formed in the presence of EGCG (blue). Figures (**B**) and (**C**) show the alanine and valine regions in more detail, highlighting the decrease in cross-peak intensity at chemical shifts associated with α-helices, upon treatment with EGCG.

6.3.6 Effects of EGCG on the dynamics of apoA-I aggregates.

6.3.6.1 Dynamics of apoA-I aggregates

Determination of the overall protein secondary structure from one-dimensional ^{13}C SSNMR experiments relies on the characteristic chemical shift patterns of the amide carbonyl, α-carbon, and β-carbons as markers for protein secondary structure. By utilising a range of 1D ^{13}C SSNMR techniques, it is possible to deduce whether the secondary structural contribution in the NMR spectrum originates from either a static or dynamic region of the peptide. **Section 5.1.4.9,** and **5.1.4.10** describe the theory behind the CP and INEPT NMR experiments in detail, and the benefits of each. **Section 5.1.4.11** describes how a combination of DP, CP and INEPT experiments can be used to determine the dynamics of a protein region. In summary, DP spectra show signals from the full protein, whereas, due to the requirement for dipolar interactions in CP experiments, this technique only collects signals from static regions of the peptide. INEPT experiments on the other hand, rely on J couplings. Therefore, they are able to detect interactions within dynamic regions of proteins.

Figure 6.16 contains DP, CP and INEPT spectra of apoA-I aggregates formed at pH 4 in the absence of heparin. The DP spectrum in red produces broad peaks in the carbonyl and alpha carbon regions with chemical shifts of 172.5-175.9 ppm and 51.9-54.6 ppm respectively, which are concurrent with the average chemical shift of amino acids in a β-sheet conformation (174.5 ppm and 55.1 ppm for the amide and α-carbon, respectively). Shoulder peaks in the amide carbon region of the spectrum at approximately 180 ppm, and in the α-carbon region at approximately 60 ppm, is suggestive of α-helical contributions (177.5 ppm and 59.6 ppm for the amide and α-carbons, respectively).

The CP spectrum in black shows a high degree of similarity to the DP spectrum, although individual peaks within the broad 172.5-175.9 ppm amide carbon peak are more resolved. The high intensity, and similarity to the DP spectrum suggests the apoA-I aggregates are dynamically constrained.

Conversely, the INEPT spectrum contains no distinguishable peaks above the background noise. This suggests the protein contains no mobile or dynamic regions, in concurrence with the CP data.

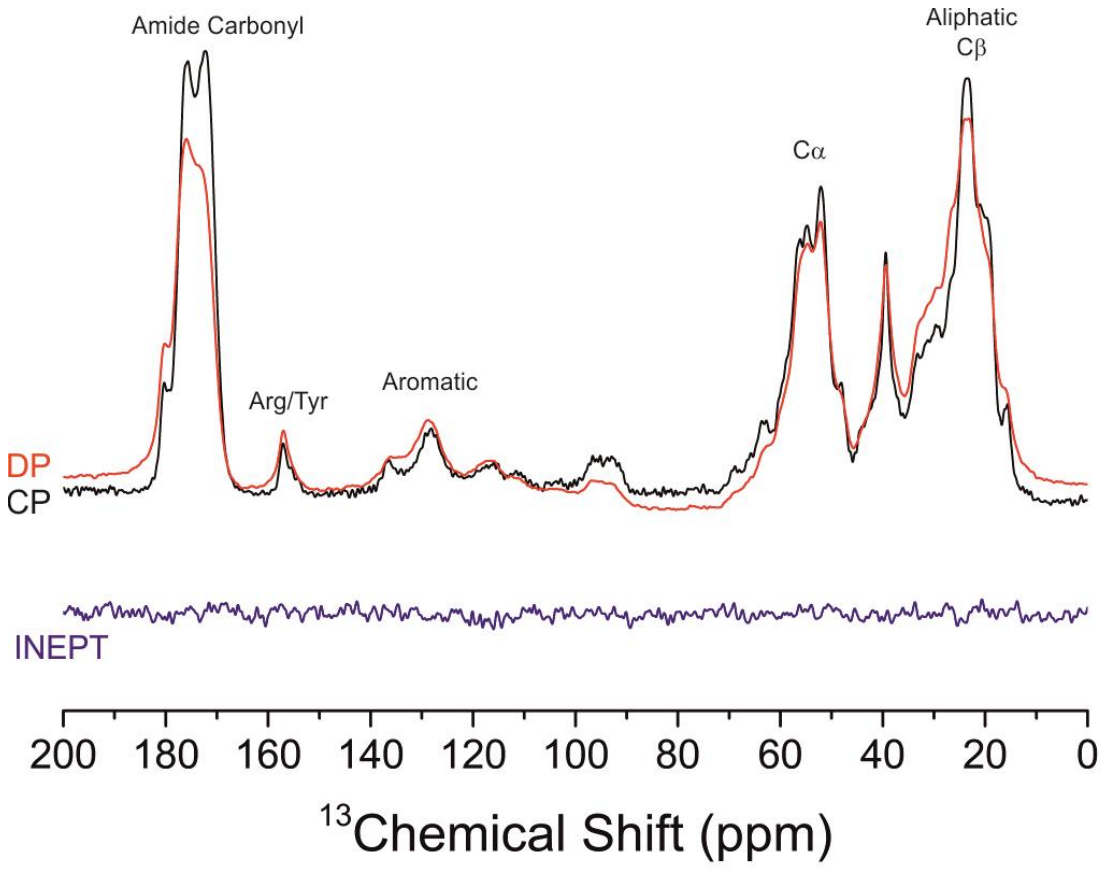

Figure 6.16 DP (red) CP (black) and INEPT (blue) MAS SSNMR of apoA-I aggregates formed at pH 4 in the absence of heparin.

6.3.6.2 Dynamics of EGCG treated apoA-I aggregates

DP and CP spectra were acquired for apoA-I, with EGCG added to preformed fibrils (**Figure 6.17A**), and apoA-I fibrils formed in the presence of EGCG (**Figure 6.17B**) in order to determine whether treatment with EGCG caused a change in the dynamics of the apoA-I aggregates.

When EGCG was added to preformed fibrils, the DP SSNMR spectrum acquired (**Figure 6.17A black**) contains a broad peak, spanning both chemical shift values associated with the presence of both β-sheet and α-helices. The main amide carbon peak at 174 ppm matches the predicted β-sheet value of 174.5 ppm calculated by Wang and Jardetzky (2002), whilst the shoulder at 177 ppm corresponds with the predicted value of 177.5 ppm for α-helical contributions. The α-carbon region of the spectrum contains a main peak at 53.7 ppm, consistent with the average chemical shift for the α-carbons in a β-sheet conformation (55.14 ppm). However, a the peak shoulder at 59.8 ppm is suggestive of α-helical contributions (Wang and Jardetzky, 2002). The line widths of the DP spectrum also appear narrower than the untreated apoA-I spectrum in **Figure 6.16**, suggestive of increased ordering. In summary, the DP spectrum for apoA-I aggregates with EGCG added after their formation, suggest the presence of both α-helical and β-sheet structures, as shown previously in the 2D ^{13}C NMR spectra, similar to the untreated aggregates.

CP experiments of apoA-I with EGCG added to preformed fibrils (**Figure 6.17A red**) produce a spectrum with a much lower intensity than the DP spectrum (**Figure 6.17A black**). This is suggestive that not all of the protein is in a dynamically constrained conformation, as was seen for the untreated apoA-I

aggregates (**Figure 6.16**). The peaks in the CP spectrum coincide with the chemical shifts for the peaks in the DP spectrum, suggesting both α-helical and β-sheet structures remain in the static regions of the protein.

The DP spectrum for apoA-I aggregates formed in the presence of EGCG (**Figure 6.17B black**) is consistent with the DP spectrum of aggregated apoA-I alone (**Figure 6.16**) and apoA-I with EGCG added to preformed fibrils (**Figure 6.17A**). However, it is not as well resolved as either of these spectra. A broad peak in the carbonyl region, with a chemical shift of 174 ppm (**Figure 6.17B black**), is easily identifiable as β-sheet by Wang and Jardetzky (2002) who predict chemical shifts of 174.5 ppm for β-sheet structures. Unfortunately, the broad width of the peak makes any contribution from α-helices at the predicted chemical shift of 177.5 ppm, which were observed in the DP spectrum for aggregated apoA-I alone and apoA-I with EGCG added after aggregation as shoulder peaks, difficult to distinguish.

CP experiments produce a spectrum with much lower intensity peaks, compared to the DP spectrum, instantly suggestive of a less constrained conformation. The chemical shift pattern in the carbonyl region, in particular a broad line spanning both 174 ppm and 177 ppm, implies both α-helical and β-sheet contributions are present in the static phase of the apoA-I aggregates (Wang and Jardetzky, 2002).

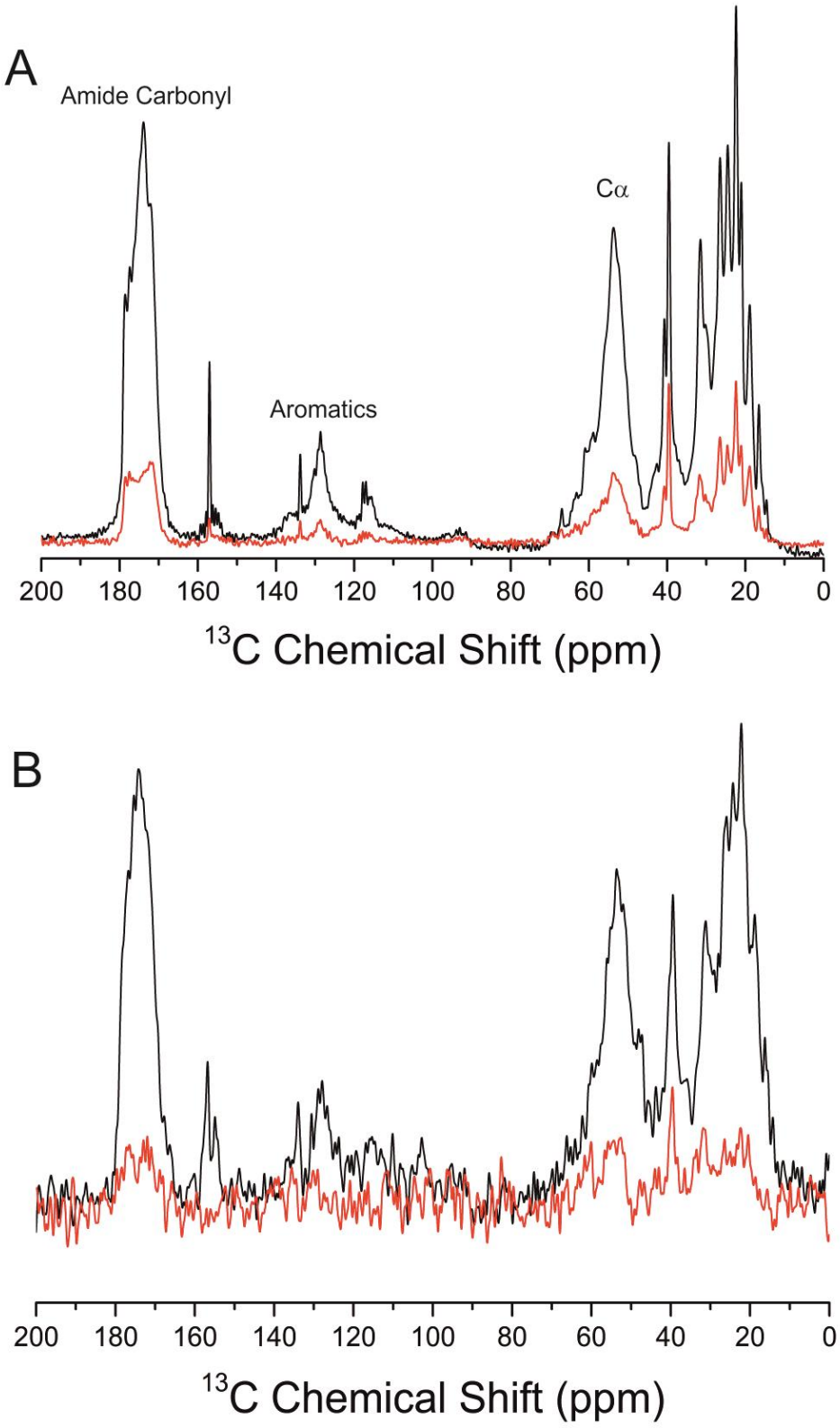

Figure 6.17 1D ^{13}C DP (black) and CP (red) SSNMR spectra of (**A**) apoA-I with EGCG added to preformed apoA-I aggregates, and (**B**) apoA-I aggregates formed in the presence of EGCG.

The data presented in **Figure 6.16** suggests that untreated apoA-I aggregates are dynamically constricted. However, the inclusion of EGCG, both during aggregation and added pre-formed aggregates, results in a reduced CP spectra intensity (**Figure 6.17**), suggestive of increased protein dynamics.

INEPT spectra were acquired for EGCG added to preformed apoA-I aggregates (**Figure 6.18A**), and for apoA-I aggregates formed in the presence of EGCG (**Figure 6.18B**). Both spectra contain intense peaks that were not observed in the untreated apoA-I INEPT spectrum (**Figure 6.16**). This suggests that treatment of apoA-I with EGCG leads to increased structural dynamics in the aggregated material.

The 1D INEPT spectrum observed when EGCG was added to preformed fibrils is not well resolved in the aromatic or α-carbon regions, making overall secondary structure estimations difficult. However, the presence of a peak consistent with the β-carbon of threonine residues at 68.9 ppm is suggestive of their involvement in α-helical structures (Wang and Jardetzky, 2002).

The two-dimensional INEPT spectrum of apoA-I aggregates formed in the presence of EGCG, shown in **Figure 6.18B** gives further insights into the structural arrangement of apoA-I treated with EGCG. Cross-peaks for aromatic ^{13}C and $^{1}H\alpha$ are detected at chemical shifts of approximately 110-130 ppm and 3.5-4.5 ppm, respectively. Cross-peaks also occur in the Cα and Cβ regions with chemical shifts of 0-40 and 40-60 ppm, respectively. Both of these ^{13}C chemical shift patterns are consistent with the 1D ^{13}C peaks in **Figure 6.18A**.

In summary, the INEPT spectra suggest that the inclusion of EGCG, either during aggregation, or to preformed fibrils results in an increased dynamic structure of the apoA-I aggregates.

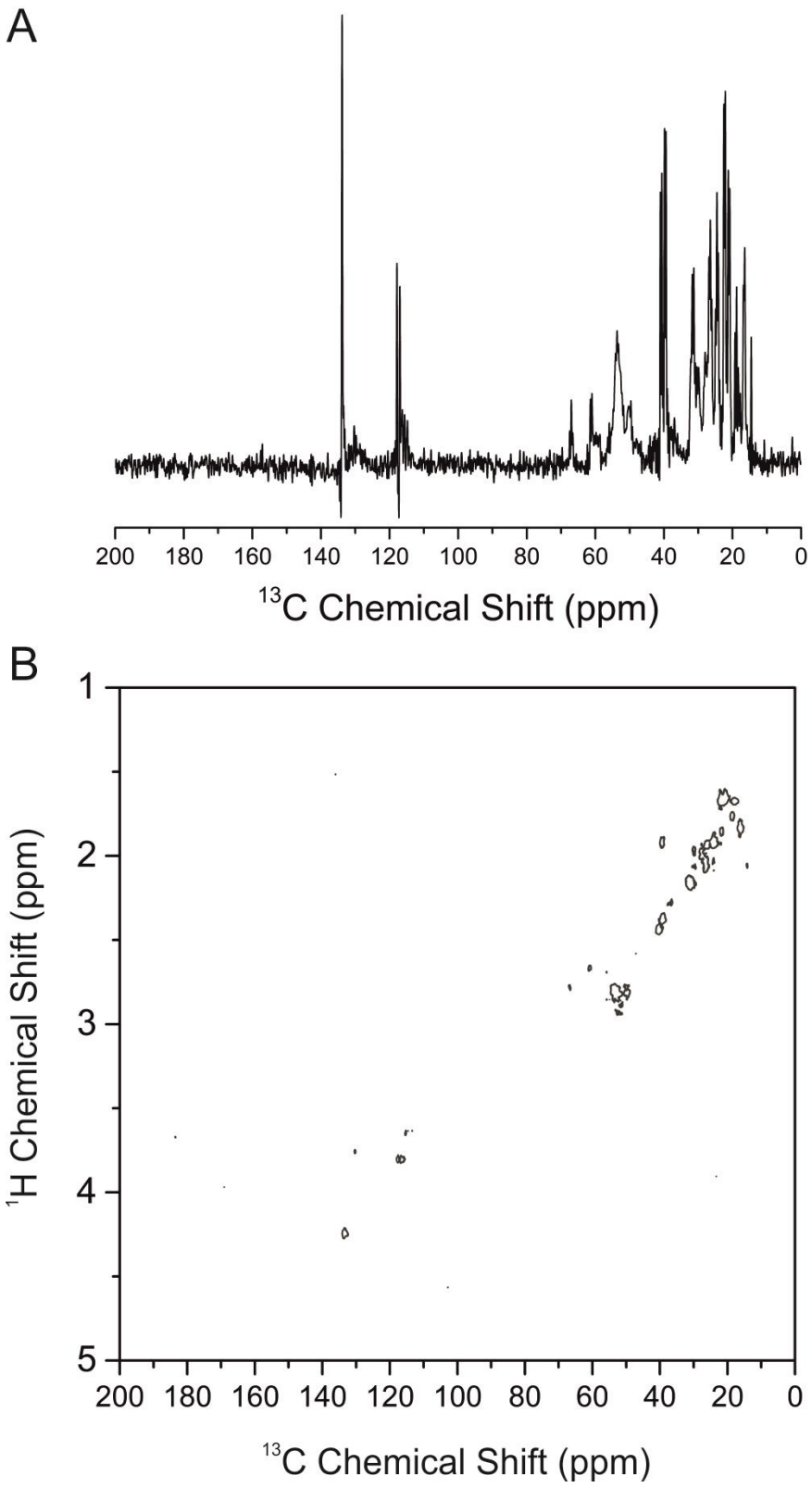

Figure 6.18 (**A**) INEPT SSNMR spectra of apoA-I with EGCG added to preformed fibrils, and (**B**) 2D ^{13}C-^{1}H INEPT SSNMR spectra of apoA-I fibrils formed in the presence of EGCG.

6.4 Discussion

The ability of polyphenols and catechins, in particular epigallocathin gallate (EGCG), to inhibit aggregation of amyloidogenic proteins has been well documented (Ehrnhoefer et al., 2006; Ehrnhoefer et al., 2008; Hudson et al., 2009; Bieschke et al., 2010). The EGCG compound has been shown to inhibit the aggregation of Aβ, huntingtin, α-synuclein, IAPP and amyloid models (Doig and Derreumaux, 2015; Ehrnhoefer et al., 2008; Bieschke et al., 2010; Masuda et al., 2006), as well as cause a structural rearrangement in preformed fibrils (Palhano et al., 2013; Bieschke et al., 2010). However the precise mechanism behind this inhibition is still unknown. The current leading theory involves EGCG driving the aggregation of the amyloidogenic protein into an alternative conformation, possibly an oligomeric state, which is unable to undergo further aggregation into amyloid species (Ehrnhoefer et al., 2008). EGCG has been shown to inhibit the aggregation of apoA-I (1-83/G26R) (Nakajima et al., 2016), but no other inhibitory studies of full-length, wild type apoA-I exist. Due to the aggregation inhibiting effects of EGCG on other amyloidogenic proteins, including the mutated apoA-I (1-83/G26R) species, it was questioned whether the non-specificity of this amyloid inhibition extended to full-length apoA-I.

Initially, experiments were carried out in order to determine the identity of catechins present in a green tea extract. Analysis by HPLC and comparison to a catechin reference set determined 8 catechin compounds were present, the most abundant of which were catechin, and epigallocatechin gallate (EGCG). As such, the effects of the green tea extract on the aggregation of Aβ and apoA-I were assessed. The green tea extract was shown to inhibit the aggregation of Aβ, as expected, given the previously published literature on purified EGCG inhibiting

the amyloidosis of Aβ. However, neither the green tea extract, nor pure EGCG were shown to inhibit the aggregation of apoA-I.

Despite not showing an inhibitory effect on the aggregation of apoA-I, experiments were carried out to determine which, if any, of the catechins present in green tea bound to Aβ and apoA-I. Co-sedimentation of EGCG with Aβ and apoA-I aggregates, and analysis of the resulting supernatant by HPLC identified 4 compounds bound to Aβ aggregates (caffeine, epicatechin, EGCG and epicathingallate), whilst only EGCG bound to apoA-I aggregates with high affinity. Therefore, the binding of pure EGCG to apoA-I aggregates was calculated, using the absorbance of EGCG, which was found to bind at roughly equimolar concentrations. The discovery that EGCG interacts with apoA-I, despite not inhibiting its aggregation, is interesting and could potentially direct further research into apoA-I amyloid inhibitors.

Given that EGCG was shown to bind to apoA-I, the structure of the apoA-I aggregates treated with EGCG was assessed through SSNMR. EGCG was either added to preformed fibrils, or included during the aggregation process. SSNMR determined that treatment with EGCG, in both conditions, lead to a structural rearrangement in the apoA-I aggregates. 2D SSNMR identified a reduction in α-helical content, upon treatment with EGCG, whilst the β-sheet content appears to remain unchanged. This structural rearrangement coincided with an increase in the protein dynamics, as determined through a combination of CP and INEPT SSNMR experiments. However, this data cannot determine whether EGCG induces a structural change in apoA-I aggregates that gives rise to a more dynamic structure, or whether EGCG solubilises apoA-I aggregates, leading to increased protein dynamics.

In the model proposed in Chapter 5 of this thesis, the β-sheet structures are restricted to the N-terminal 90/100, whilst the C-terminus retains its native helical content. Therefore, given the data presented here, it is further proposed that EGCG interacts with the C-terminus of the apoA-I aggregates, both during and after the formation of fibrils. This interaction interferes with the α-helical structures, converting the C-terminus into a more dynamic structure, whilst the N-terminal β-sheet structures remain unaffected. The increase in dynamics of the helical C-terminus is confirmed by the presence of a peak in the 1D ^{13}C INEPT spectrum, corresponding to threonine residues in an α-helical conformation. 5 threonine residues are present in the C-terminus (90-243) region of apoA-I that is thought to be in an α-helical conformation.

Binding of EGCG to the C-terminus would also explain why EGCG appears to have no effect on the aggregation of apoA-I into amyloid-like aggregates, as determined by both ThT and SSNMR, since the β-sheet structures characteristic of amyloid are confined to the N-terminus. Neither an increase in the intensity of the β-sheet cross-peaks is observed upon treatment with EGCG, nor is an enhanced ThT response. Therefore, it can be assumed that the interaction of EGCG with the C-terminus of apoA-I does not induce β-sheet formation in the C-terminus, nor propagation of the N-terminal β-sheet into the remaining protein, as originally proposed by Das *et al.* (2014).

Further work on studying the interaction of apoA-I with EGCG, in order to determine how the compound causes a structural reformation, and the potential effects it could have on the apoA-I aggregates morphology, is discussed in **Chapter 7.**

7. General discussion and future work

The overall aims of the research presented in this thesis have been to study the conditions that induce the misfolding of apoA-I into amyloid-like structures and investigate the structure of these aggregates.

7.1 ApoA-I aggregation

Current literature on apoA-I aggregation identifies 2 separate mechanisms that result in the deposition of amyloid-like material. In acquired amyloidosis, full-length apoA-I becomes deposited as amyloid fibrils in arteries and associates with atherosclerotic plaques (Das et al., 2016; Ramella et al., 2011; Ramella et al., 2012; Mucchiano, Häggqvist, et al., 2001; Wong et al., 2010; Chan et al., 2015). In familial apoA-I amyloidosis, N-terminal fragments of apoA-I, incorporating peptides 80-100 amino acids in length, become deposited within major organs (Raimondi et al., 2011; Das et al., 2016; Andreola et al., 2003; Adachi et al., 2014; Vigushin D.M et al., 1994). In both cases, aggregation of apoA-I leads to the misfolding of the native apoA-I. This manifests into poor cardiac health, via 3 processes: a reduction in the HDL driven RCT, deposition of insoluble amyloid increases the plaque loading in atherosclerotic lesions, and an increased inflammatory response at atherosclerotic sites, due to possible cytotoxic amyloid intermediates.

7.2 Current mechanism for apoA-I aggregation

Native apoA-I, in its lipid-free state, possesses a high helical content, between 60-80 %, depending on the conformation of the flexible C-terminus. The current model describing the mechanism of apoA-I aggregation has been proposed by

Das *et al.* (2016; 2014) and details how the N-terminal 4 helical bundle inhibits the SRE regions, residues 14-22, 53-58, and 69-72, from spontaneously aggregating into β-sheet structures. Mutations in this region or oxidation of methionine residues lead to destabilisation of the N-terminus. This allows the SRE regions to rearrange into β-sheet structures. The EKETEG region, spanning residues 76-81, acts as a natural β-sheet breaker at neutral pH, limiting the β-sheet propagation to the N-terminal 1-76 residues (Das et al., 2014). This exposed region is now more accessible to proteases that cleave the N-terminal 1-83 peptide, resulting in its deposition as amyloid. Alternatively, upon protonation of the glutamic acid residues in the β-sheet breaking sequence, this protective property is lost. Therefore, the β-sheets formed from the SRE elements can propagate into the C-terminus, extending into a β-zipper, which then forms full-length amyloid (Das et al., 2014).

This mechanism is supported by the high number of mutations in the N-terminal 1-80 peptide that result in destabilisation of the 4-helical bundle. This opens the structure up to proteolytic cleavage, explaining why N-terminal fragments of mutated apoA-I appear as amyloid in familial apoA-I amyloidosis.

7.3 Expression of apoA-I

Recombinant apoA-I was expressed following previously published methods (Oda et al., 2001; Ryan et al., 2003) with suitable yields to facilitate biophysical analysis described in Chapter 4. Expression in minimal media enriched with ^{13}C glucose and ^{15}N ammonium chloride allowed the first SSNMR spectrum of apoA-I to be collected, aiding structural analysis. SLIM based PCR methods were utilised to produce plasmid DNA for several apoA-I mutants, including G26R, L44Stop,

L90P, K96C and R173C. Agarose gel electrophoresis confirmed the PCR reaction, used to incorporate mutated primers, had produced large quantities of DNA, whilst gene-sequencing data showed the intended mutations were successfully incorporated. The L44Stop mutation was unable to be expressed, and, of the remaining 4 mutants that were expressed, none produced a protein product that matched the predicted mass, when measured by electrospray ionisation mass spectrometry. The L90P mutant, which is of particular interest in this work, causes an increased rate in the aggregation of the apoA-I 1-93 peptide. DNA sequencing confirmed the introduction of the proline in the correct position and expression of the protein produced a band that appeared in the correct region on an SDS gel. However, upon treatment with 45 % formic acid, in order to cleave the his-tag between the formic acid labile Asp-Pro sequence, 2 smaller peptides were detected on an SDS gel and via mass spectrometry. After studying the sequence, the mutated proline in position 90 was found to produce a second acid labile Asp-Pro sequence, leading to the production of peptides corresponding to residues 3-89 and 90-243.

7.3.1 Further work with apoA-I (3-89) and (90-243)

Unfortunately, isolation of these two peptides from the his-tag was not attempted, due to time restrictions in the project and the focus on full-length apoA-I. However, a simple HPLC process should be able to separate out the 2,533 Da his-tag and linker region, the 10,005 Da apoA-I (3-89) peptide, and the 17,881 Da apoA-I (90-243) peptide.

N-terminal fragments of apoA-I are commonly found deposited as amyloid in familial associated amyloidosis. Although structural analysis has already been

attempted on N-terminal peptides of apoA-I, the expression methods used here, in particular the ability to produce labelled apoA-I, would allow SSNMR analysis of both the soluble and aggregated peptide. Structural analysis of the aggregated apoA-I (3-89) peptide would confirm whether this region contains entirely β-sheet structures. If this is the case, then it is justified to assume that the α-helical contributions detected by CD and SSNMR arise from the C-terminus, as proposed in the refined amyloidosis model in **Chapter 5**.

Currently, the structure of soluble, lipid-free apoA-I is incomplete, with the C-terminal 185-243 residues not shown in the model proposed by Mei and Atkinson (2011). Isolation of the apoA-I (90-243) peptide would allow structural analysis of the full C-terminus region of apoA-I, and refinement of the full-length structure. This peptide could also be used to determine whether the C-terminus of apoA-I has a natural propensity to aggregate, by repeating the biophysical experiments carried out in **Chapter 4**. The current model for full-length apoA-I amyloidosis assumes that the C-terminus has no natural propensity to aggregate. It proposes that the presence of β-sheets in the C-terminus only occurs, due to extension of the N-terminal β-sheets. If it is found that apoA-I (90-243) can form amyloid in isolation, it would dispute the Das *et al.* (2016) model. If apoA-I (90-243) only forms amyloid when seeded with apoA-I (3-89) amyloid, it could confirm the Das *et al.* model. However, if apoA-I (90-243) does not aggregate under any physiologically relevant conditions, it will support the refinement proposed in **Chapter 5**.

7.4 Conditions that promote aggregation of apoA-I

In this study, apoA-I was incubated at a range of pH conditions, alone, and in the presence of a 2-fold molar excess of heparin. Acidic pH induced a conversion from soluble apoA-I into insoluble aggregates both in the absence and presence of heparin, with an excess of 90 % of protein precipitating out of solution.

In the absence of heparin, the insoluble aggregates were ThT responsive, bound to Congo red dye and exhibited a green birefringence. However, they did not have the typical amyloid morphology when viewed by TEM, or produce XRD patterns consistent with the presence of β-sheet structures. CD experiments showed that after 2 hours incubation, both the remaining soluble material and the insoluble aggregates retained a high proportion of the native helical content.

Conversely, when incubated with an excess of heparin, the insoluble material gave rise to a ThT response, a green birefringence when stained with Congo red, exhibited a more common amyloid morphology, and produced intense XRD reflections, consistent with the presence of β-sheets. ThT data confirmed the ThT response was heparin concentration-dependent. CD analysis of the aggregates determined a dramatic reduction in α-helical content, with an increase in β-sheet structures, which is characteristic of amyloid. The thin film CD spectra contained both α-helical and β-sheet contributions and, upon comparison to the aggregates formed in the absence of apoA-I, the β-sheet contribution was calculated to be approximately 40 %.

Oxidation of apoA-I was confirmed through MS, and CD analysis determined a slight reduction in the α-helical content at neutral pH, suggesting unfolding of the native structure. This is consistent with previous analysis of chemical oxidation of apoA-I (Chan et al., 2015). Intrinsic fluorescence studies

implied that the oxidised apoA-I has a more relaxed structure, with increased exposure of the 4-tryptophan residues to hydrophobic environments. Upon incubation at pH 6, the oxidised apoA-I readily formed ThT reactive aggregates, with a morphology similar to the apoA-I aggregates, formed in the presence of heparin.

The conditions determined here that promote aggregation of apoA-I are physiologically relevant. At sites of atherosclerotic lesions, where apoA-I is deposited, the local pH can be reduced dramatically, given the immune response against the oxidised LDL (Thijssen and Mensink, 2005). GAG's, such as heparin, are commonly associated with amyloid deposits (Cohlberg et al., 2002). Oxidation of methionine residues on apoA-I by myeloperoxidsase has been shown to induce aggregation into amyloid species (Chan et al., 2015).

7.5 SSNMR analysis of apoA-I amyloid

The PDB contains a distinct lack of apoA-I structures determined by NMR. To date, only 4 structures have been deduced, corresponding to residues 142-187 (Wang et al., 1997) 166-185 (Wang et al., 1996) and 1-93 (Mangione et al., 2001). This is due to the high flexibility of the apoA-I structure, which gives rise to broad line widths, which was observed in the SSNMR spectra obtained for this thesis. However, new structural information could be deduced from the ^{13}C spectra, in regards to the local secondary structural content, which has previously been unavailable.

Thin film CD of apoA-I aggregates, formed in the presence of heparin, suggested the presence of both α-helical and β-sheet content, something uncommon in amyloid species. SSNMR confirmed that the aggregated material

formed at pH 4 alone, in the presence of heparin, and upon oxidation at pH 6, all retained a high proportion of their native α-helical elements, whist also possessing cross-peaks that are consistent with the presence of β-sheet elements. This conflicts with the mechanism of apoA-I amyloidosis, proposed by Das *et al.* (2016), which claims that the entire aggregate consists of β-sheet in acidic conditions.

Therefore, a refinement of the amyloidosis mechanism is suggested in **Chapter 5**. Destabilisation of the 4-helical bundle in native apoA-I, either by acidification or oxidation of the 3-methionine residues, results in the conversion of residues 1-90 into a non-helical conformation, with the conversion of the hot-spot regions into β-sheets. However, the β-sheet structures are restricted to the N-terminus, and the C-terminus of apoA-I retains its majority α-helical content, as shown in **Figure 5.29**, unlike the mechanism proposed by Das *et al.* (2016).

7.5.1 Future SSNMR experiments

In order to confirm this theory, more detailed structural analysis of apoA-I via SSNMR is required. In addition to the experiments outlined above for the apoA-I (3-89) and apoA-I (90-243) peptides, spectra for amino acids located in solely the N or C-terminus of apoA-I would confirm the local secondary structure. Unfortunately, all 18 amino acids in apoA-I (excluding cysteine and isoleucine) are uniformly distributed among residues 1-89 and 90-243. Isoleucine could be mutated into either region, and its conformation probed by ^{13}C-^{13}C CP SSNMR, since the Cα -Cβ cross-peaks produced by isoleucine are easily assignable on the 2D ^{13}C spectrum.

Alanine is an attractive alternative amino acid, since their cross-peaks are one of the most identifiable in the complex spectrum produced by full-length apoA-I, and their chemical shift patterns make it easy to distinguish between their α-helical and β-sheet signals. Only 2 alanine residues are present in the N-terminal (1-90) region, compared to 17 in the C-terminus, which are distributed throughout residues 95-229. Production of a double mutant to remove the alanine residues at positions 15 and 37 would result in an alanine Cα-Cβ cross-peak, solely from the C-terminus of apoA-I. Mutation from alanine to leucine would have a minimal effect on the structure of apoA-I. If the cross-peak occurs only at chemical shifts associated with α-helical contributions, then it supports the refined theory. Any β-sheet signals would mean the model needs further revision.

Similarly, the lone tryptophan residue in the C-terminus at position 108 could be mutated out of the sequence, leaving the ^{13}C cross-peaks corresponding to the 3 tryptophan residues in the N-terminus.

All three of these methods could make use of the uniformly labelling techniques used in this chapter. Alternatively, a combination of mutagenesis and sporadic labelling, or addition of excess labelled amino acid to a minimal media expression, would produce an NMR spectra containing cross peaks from just the amino acid of interest, such as alanine residues only in the C-terminus.

7.6 ApoA-I inhibition

The overall aim of studying the structure of amyloidogenic proteins is to improve the understanding of how the soluble, native protein misfolds into amyloid, and thus, manifests itself in disease pathology. This can then direct the design of

therapeutic techniques in order to control or inhibit the disease progression. Currently, there are no known compounds that inhibit the aggregation of apoA-I.

EGCG, a catechin found in green tea, has been shown to inhibit the aggregation of several amyloidogenic proteins, including Aβ, α-synuclein and huntingtin. Data presented here confirms that EGCG binds to apoA-I with micromolar affinity, but does not cause a reduction in the production of ThT responsive material. However, binding of EGCG to apoA-I does induce a structural change in the aggregates formed at acidic pH. EGCG leads to a reduction in the helical content of apoA-I aggregates and an increase in the protein dynamics. If EGCG can inhibit the amyloidosis of apoA-I, or cause an alternative aggregation mechanism, this could have potential health benefits. A reduction in fibril formation may allow apoA-I to retain its native function in the atheroprotective reverse cholesterol transport, or reduce the atherosclerotic plaque load. Alternatively, since EGCG is known to bind to apoA-I, structural analogues could be designed, based on the apoA-I-EGCG interaction, as potential drug compounds with higher efficacy.

Future work on the interaction of apoA-I with EGCG should focus on determining whether EGCG effects the aggregation of apoA-I. This will involve extensive biophysical analysis, similar to that carried out in **Chapter 4**. EGCG has been shown to compete with ThT for binding sites on amyloid (Palhano et al., 2013), so alternative methods of measuring aggregation kinetics might be required. Determination of whether the EGCG modified apoA-I structure induces cytotoxicity of the fibrils will also be important in taking this compound forward as a treatment model. If EGCG inhibits fibril formation, but induces the formation of off-pathway aggregates that are cytotoxic to endothelial or other cardiac cells,

the treatment mechanism fails. Alternatively, if EGCG is solubilising the fibrils, which is a possibility, given the increased dynamics upon treatment with EGCG, this could also lead to the production of cytotoxic oligomers. Therefore, cell viability studies are essential future work, both in the study of the inhibition of aggregation and treatment of preformed fibrils.

In addition to the NMR data presented in **Chapter 6**, CD analysis of apoA-I aggregates, in particular the use of orientated thin film SRCD, could give further insight into the structural changes observed during the aggregation in the presence of EGCG, and whether EGCG added to preformed fibrils alters their conformation. Computer modelling of the interaction between EGCG and apoA-I could allow comparison to how EGCG interacts with Aβ, huntingtin and α-synuclein, for which it is known to inhibit amyloidosis. Since EGCG appears to induce an alteration in the helical region of the apoA-I aggregates, the refined amyloidosis model would suggest an interaction involving the C-terminus of apoA-I. This would also explain why EGCG does not cause a reduction in the ThT response, caused by the β-sheet structures, located in the N-terminus. This could be confirmed through determining whether EGCG will bind to the apoA-I (3-89) and apoA-I (90-243) peptides separately.

In conclusion, the research carried out in this thesis has furthered the understanding of apoA-I aggregation, and has begun assessing a known amyloid inhibitor for its effects on apoA-I.

References

Acton, S., Rigotti, A., Landschulz, K.T., Xu, S., Hobbs, H.H. and Krieger, M. 1996. Identification of Scavenger Receptor SR-BI as a High Density Lipoprotein Receptor. *Science*. **271**(5248),pp.518–520.

Adachi, E., Kosaka, A., Tsuji, K., Mizuguchi, C., Kawashima, H., Shigenaga, A., Nagao, K., Akaji, K., Otaka, A. and Saito, H. 2014. The extreme N-terminal region of human apolipoprotein A-I has a strong propensity to form amyloid fibrils. *FEBS letters*. **588**(3),pp.389–394.

Adachi, E., Nakajima, H., Mizuguchi, C., Dhanasekaran, P., Kawashima, H., Nagao, K., Akaji, K., Lund-Katz, S., Phillips, M.C. and Saito, H. 2012. Dual Role of an N-terminal Amyloidogenic Mutation in Apolipoprotein A-I: Destabilization of helix bundle and enhancement of fibril formatio. *Journal of Biological Chemistry*. **288**(4),pp.2848–2856.

Aguilar-Espinosa, S.L., Mendoza-Espinosa, P., Delgado-Coello, B. and Mas-Oliva, J. 2013. Lecithin cholesterol acyltransferase (LCAT) activity in the presence of Apo-AI-derived peptides exposed to disorder-order conformational transitions. *Biochemical and biophysical research communications*. **441**(2),pp.469–475.

Ahmed, M., Davis, J., Aucoin, D., Sato, T., Ahuja, S., Aimoto, S., Elliott, J.I., Van Nostrand, W.E. and Smith, S.O. 2010. Structural conversion of neurotoxic amyloid-β1–42 oligomers to fibrils. *Nature Structural & Molecular Biology*. **17**(5),pp.561–567.

Ajees, A.A., Anantharamaiah, G.M., Mishra, V.K., Hussain, M.M., Murthy, H.M.K., Ericson, K., Gan, C., Cheong, I., Rago, C., Samuels, Y., Velculescu, V.E., Kenneth, W., Huso, D.L., Vogelstein, B., Papado-, N., Kotwal, J. and Murthy, K.H.M. 2006. Crystal structure of human apolipoprotein A-I: insights into its protective effect against cardiovascular diseases. *Proc Natl Acad Sci U S A*. **103**(7),pp.2126–2131.

Alexander, E.T., Tanaka, M., Kono, M., Saito, H., Rader, D.J. and Phillips, M.C. 2009. Structural and functional consequences of the Milano mutation (R173C) in human apolipoprotein A-I. *The Journal of Lipid Research*. **50**(7),pp.1409–1419.

Alies, B., Hureau, C. and Faller, P. 2013. The role of metal ions in amyloid formation: general principles from model peptides. *Metallomics : integrated biometal science*. **5**(3),pp.183–92.

Amijee, H., Bate, C., Williams, A., Virdee, J., Jeggo, R., Spanswick, D., David, I.C., Treherne, J.M., Mazzitelli, S., Chawner, R., Eyers, C.E. and Doig, A.J. 2012. The N-Methylated Peptide SEN304 Powerfully Inhibits Aβ (1-42) Toxicity by Perturbing Oligomer Formation. *Biochemistry*. **51**(42),pp.8338–8352.

Amijee, H., Madine, J., Middleton, D. a and Doig, A.J. 2009. Inhibitors of protein aggregation and toxicity. *Biochemical Society transactions*. **37**(Pt 4),pp.692–6.

Andreola, A., Bellotti, V., Giorgetti, S., Mangione, P., Obici, L., Stoppini, M., Torres, J., Monzani, E., Merlini, G. and Sunde, M. 2003. Conformational switching and fibrillogenesis in the amyloidogenic fragment of apolipoprotein A-I. *Journal of Biological Chemistry*. **278**(4),pp.2444–2451.

Andrews, L.J. and Forster, L.S. 1972. Protein difference spectra. Effect of solvent and charge on tryptophan. *Biochemistry*. **11**,pp.1875–1879.

Annema, W. and von Eckardstein, A. 2013. High-Density Lipoproteins. *Circulation Journal*. **77**(10),pp.2432–2448.

Aterman, K. 1976. A historical note on the iodine-sulphuric acid reaction of amyloid. *Histochemistry*. **49**,pp.131–143.

Baglioni, S., Casamenti, F., Bucciantini, M., Luheshi, L.M., Taddei, N., Chiti, F., Dobson, C.M. and Stefani, M. 2006. Prefibrillar Amyloid Aggregates Could Be Generic Toxins in Higher Organisms. *Journal of Neuroscience*. **26**(31),pp.8160–8167.

Barnhart, M.M. and Chapman, M.R. 2006. Curli Biogenesis and Function. *Annual Review of Microbiology*. **60**(1),pp.131–147.

Becker, E.D. 1993. A brief history of nuclear magnetic resonance. *Analytical Chemistry*. **65**(6),p.295A–302A.

Becker, E.D. 1999. *High resolution NMR: Theory and chemical applications* 3rd ed. ACADEMIC PRESS INC JNL-COMP SUBSCRIPTIONS, 525 B ST, STE 1900, SAN DIEGO, CA 92101-4495.

Berman, H., Westbrook, J., Feng, Z., Gilliland, G., Bhat, T., Weissig, H., Shindyalov, I. and Bourne, P. 2000. The Protein Databank. *Nucleic Acids Research*.

[Online],pp.235–242. [Accessed 30 January 2017]. Available from: www.rcsb.org.

Berthelot, K., Cullin, C. and Lecomte, S. 2013. What does make an amyloid toxic: Morphology, structure or interaction with membrane? *Biochimie*. **95**(1),pp.12–19.

Biancalana, M. and Koide, S. 2010. Molecular mechanism of thioflavin T binding to amyloid fibrils. *Biochemical and biophysical proteins and proteomics*. **1804**(7),pp.1405–1412.

Bieschke, J., Russ, J., Friedrich, R.P., Ehrnhoefer, D.E., Wobst, H., Neugebauer, K. and Wanker, E.E. 2010. EGCG remodels mature alpha-synuclein and amyloid-beta fibrils and reduces cellular toxicity. *Proceedings of the National Academy of Sciences of the United States of America*. **107**(17),pp.7710–5.

Bodin, K., Ellmerich, S., Kahan, M.C., Tennent, G.A., Loesch, A., Gilbertson, J. a, Hutchinson, W.L., Mangione, P.P., Gallimore, J.R., Millar, D.J., Minogue, S., Dhillon, A.P., Taylor, G.W., Bradwell, A.R., Petrie, A., Gillmore, J.D., Bellotti, V., Botto, M., Hawkins, P.N. and Pepys, M.B. 2010. Antibodies to human serum amyloid P component eliminate visceral amyloid deposits. *Nature*. **468**(7320),pp.93–7.

Bodner, R.A., Housman, D.E. and Kazantsev, A.G. 2006. New directions for neurodegenerative disease therapy: Using chemical compounds to boost the formation of mutant protein inclusions. *Cell Cycle*. **5**(14),pp.1477–1480.

Borhani, D.W., Rogers, D.P., Engler, J. a and Brouillette, C.G. 1997. Crystal structure of truncated human apolipoprotein A-I suggests a lipid-bound conformation. *Proceedings of the National Academy of Sciences of the United States of America*. **94**(23),pp.12291–12296.

Bothwell, J.H.F. and Griffin, J.L. 2011. An introduction to biological nuclear magnetic resonance spectroscopy. *Biological Reviews*. **86**(2),pp.493–510.

Brumshtein, B., Esswein, S.R., Landau, M., Ryan, C.M., Whitelegge, J.P., Phillips, M.L., Cascio, D., Sawaya, M.R. and Eisenberg, D.S. 2014. Formation of amyloid fibers by monomeric light chain variable domains. *Journal of Biological Chemistry*. **289**(40),pp.27513–27525.

Brumshtein, B., Esswein, S.R., Salwinski, L., Phillips, M.L., Ly, A.T., Cascio, D., Sawaya, M.R. and Eisenberg, D.S. 2015. Inhibition by small-molecule ligands

of formation of amyloid fibrils of an immunoglobulin light chain variable domain. *eLife*. **4**(NOVEMBER2015),pp.1–15.

Buell, A.K., Dobson, C.M., Knowles, T.P.J. and Welland, M.E. 2010. Interactions between Amyloidophilic dyes and their relevance to studies of amyloid inhibitors. *Biophysical Journal*. **99**(10),pp.3492–3497.

Bulawa, C.E., Connelly, S., DeVit, M., Wang, L., Weigel, C., Fleming, J. a., Packman, J., Powers, E.T., Wiseman, R.L., Foss, T.R., Wilson, I. a., Kelly, J.W. and Labaudiniere, R. 2012. Tafamidis, a potent and selective transthyretin kinetic stabilizer that inhibits the amyloid cascade. *Proceedings of the National Academy of Sciences*. **109**(24),pp.9629–9634.

Bulic, B., Pickhardt, M., Schmidt, B., Mandelkow, E.M., Waldmann, H. and Mandelkow, E. 2009. Development of tau aggregation inhibitors for alzheimer's disease. *Angewandte Chemie - International Edition*. **48**(10),pp.1740–1752.

Bursavich, M.G., Gilbert, A.M., Lombardi, S., Georgiadis, K.E., Reifenberg, E., Flannery, C.R. and Morris, E.A. 2007. Synthesis and evaluation of aryl thioxothiazolidinone inhibitors of ADAMTS-5 (Aggrecanase-2). *Bioorganic and Medicinal Chemistry Letters*. **17**(5),pp.1185–1188.

Cabriolu, R., Kashchiev, D. and Auer, S. 2010. Atomistic theory of amyloid fibril nucleation. *Journal of Chemical Physics*. **133**(22).

Casu, B., Naggi, A. and Torri, G. 2015. Re-visiting the structure of heparin. *Carbohydrate Research*. **403**,pp.60–68.

Cavanagh, J., Fairbrother, W., Palmer, A. and Skelton, N. 1995. *Protein NMR spectroscopy* 2nd ed. ACADEMIC PRESS INC JNL-COMP SUBSCRIPTIONS, 525 B ST, STE 1900, SAN DIEGO, CA 92101-4495.

Cecilia Noguez, F.H. 2014. Ab Initio Electronic Circular Dichroism of Fullerenes, Single-Walled Carbon Nanotubes, and Ligand-Protected Metal Nanoparticles. *Chirality*. **26**(April),pp.553–562.

Chan, G.K.L., Witkowski, A., Gantz, D.L., Zhang, T.O., Zanni, M.T., Jayaraman, S. and Cavigiolio, G. 2015. Myeloperoxidase-mediated methionine oxidation promotes an amyloidogenic outcome for apolipoprotein A-I. *Journal of Biological Chemistry*. **290**(17),pp.10958–10971.

Chapman, M.R., Robinson, L.S., Pinkner, J.S., Roth, R., Heuser, J., Hammar, M.,

Normark, S. and Hultgren, S.J. 2002. Role of Escherichia coli curli operons in directing amyloid fiber formation. *Science*. **295**(5556),pp.851–855.

Cherny, I., Rockah, L., Levy-Nissenbaum, O., Gophna, U., Ron, E.Z. and Gazit, E. 2005. The formation of Escherichia coli curli amyloid fibrils is mediated by prion-like peptide repeats. *Journal of Molecular Biology*. **352**(2),pp.245–252.

Chetty, P., Mayne, L., Kan, Z.-Y., Lund-Katz, S., Englander, S.W. and Phillips, M.C. 2012. Apolipoprotein A-I helical structure and stability in discoidal high-density lipoprotein (HDL) particles by hydrogen exchange and mass spectrometry. *Proceedings of the National Academy of Sciences of the United States of America*. **109**(29),pp.11687–92.

Chetty, P.S., Mayne, L., Lund-Katz, S., Stranz, D., Englander, S.W. and Phillips, M.C. 2009. Helical structure and stability in human apolipoprotein A-I by hydrogen exchange and mass spectrometry. *Proceedings of the National Academy of Sciences of the United States of America*. **106**(45),pp.19005–19010.

Chiti, F. and Dobson, C.M. 2006. Protein Misfolding, Functional Amyloid, and Human Disease. *Annual Review of Biochemistry*. **75**(1),pp.333–366.

Chiu, J. 2004. Site-directed, Ligase-Independent Mutagenesis (SLIM): a single-tube methodology approaching 100% efficiency in 4 h. *Nucleic Acids Research*. **32**(21),pp.e174–e174.

Chyu, K.Y. 2004. Differential Effects of Green Tea-Derived Catechin on Developing Versus Established Atherosclerosis in Apolipoprotein E-Null Mice. *Circulation*. **109**(20),pp.2448–2453.

Coelho-Cerqueira, E., Pinheiro, A.S. and Follmer, C. 2014. Pitfalls associated with the use of Thioflavin-T to monitor anti-fibrillogenic activity. *Bioorganic and Medicinal Chemistry Letters*. **24**(14),pp.3194–3198.

Cohen, S.I.A., Linse, S., Luheshi, L.M., Hellstrand, E., White, D.A., Rajah, L., Otzen, D.E., Vendruscolo, M., Dobson, C.M. and Knowles, T.P.J. 2013. Proliferation of amyloid-β42 aggregates occurs through a secondary nucleation mechanism. *Proceedings of the National Academy of Sciences of the United States of America*. **110**(24),pp.9758–63.

Cohlberg, J. a., Li, J., Uversky, V.N. and Fink, A.L. 2002. Heparin and other glycosaminoglycans stimulate the formation of amyloid fibrils from Alpha-

synuclein in vitro. *Biochemistry*. **41**(5),pp.1502–1511.

Conway, K.A., Rochet, J.C., Bieganski, R.M. and Lansbury, P.T. 2001. Kinetic stabilization of the α-synuclein protofibril by a dopamine-α-synuclein adduct. *Science*. **294**(5545),pp.1346–1349.

Das, M., Mei, X., Jayaraman, S., Atkinson, D. and Gursky, O. 2014. Amyloidogenic Mutations in Human Apolipoprotein A-I are not Necessarily Destabilizing: A Common Mechanism of ApoA-I Misfolding in Familial Amyloidosis and Atherosclerosis. *FEBS Journal*. **281**(11),pp.2525–2542.

Das, M., Wilson, C.J., Mei, X., Wales, T.E., Engen, J.R. and Gursky, O. 2016. Structural Stability and Local Dynamics in Disease-Causing Mutants of Human Apolipoprotein A-I: What Makes the Protein Amyloidogenic? *Journal of Molecular Biology*. **428**(2),pp.449–462.

Davidson, W.S. and Thompson, T.B. 2007. The structure of apolipoprotein A-I in high density lipoproteins. *The Journal of biological chemistry*. **282**(31),pp.22249–22253.

Debelouchina, G.T., Platt, G.W., Bayro, M.J., Radford, S.E. and Griffin, R.G. 2011. NIH Public Access. . **132**(30),pp.10414–10423.

Demuro, A., Smith, M. and Parker, I. 2011. Single-channel Ca2+ imaging implicates Aβ1-42 amyloid pores in Alzheimer's disease pathology. *Journal of Cell Biology*. **195**(3),pp.515–524.

Desai, H. V., Aronow, W.S., Peterson, S.J. and Frishman, W.H. 2010. Cardiac Amyloidosis. *Cardiology in Review*. **18**(1),pp.1–11.

Ding, F., Borreguero, J.M., Buldyrey, S. V., Stanley, H.E. and Dokholyan, N. V. 2003. Mechanism for the α-helix to β-hairpin transition. *Proteins: Structure, Function and Genetics*. **53**(2),pp.220–228.

Dobson, C.M. 2003. Protein Folding and Misfolding. *Nature*. **426**(December).

Doig, A.J. and Derreumaux, P. 2015. Inhibition of protein aggregation and amyloid formation by small molecules. *Current Opinion in Structural Biology*. **30**,pp.50–56.

Dubrey, S.W., Hawkins, P.N. and Falk, R.H. 2011. Amyloid diseases of the heart: assessment, diagnosis, and referral. *Heart (British Cardiac Society)*. **97**(1),pp.75–84.

von Eckardstein, a, Nofer, J.R. and Assmann, G. 2001. High density lipoproteins

and arteriosclerosis. Role of cholesterol efflux and reverse cholesterol transport. *Arteriosclerosis, thrombosis, and vascular biology*. **21**(1),pp.13–27.

Ehrnhoefer, D.E., Bieschke, J., Boeddrich, A., Herbst, M., Masino, L., Lurz, R., Engemann, S., Pastore, A. and Wanker, E.E. 2008. EGCG redirects amyloidogenic polypeptides into unstructured, off-pathway oligomers. *Nature structural & molecular biology*. **15**(6),pp.558–66.

Ehrnhoefer, D.E., Duennwald, M., Markovic, P., Wacker, J.L., Engemann, S., Roark, M., Legleiter, J., Marsh, J.L., Thompson, L.M., Lindquist, S., Muchowski, P.J. and Wanker, E.E. 2006. Green tea (-)-epigallocatechin-gallate modulates early events in huntingtin misfolding and reduces toxicity in Huntington's disease models. *Human Molecular Genetics*. **15**(18),pp.2743–2751.

Fasman, G.. 1996. *Circular Dichrosim and the conformational analysis of biomolecules*. Springer Science.

Finder, V.H., Vodopivec, I., Nitsch, R.M. and Glockshuber, R. 2010. The Recombinant Amyloid-β Peptide Aβ1-42 Aggregates Faster and Is More Neurotoxic than Synthetic Aβ1-42. *Journal of Molecular Biology*. **396**(1),pp.9–18.

Fisher, E.A., Feig, J.E., Hewing, B., Hazen, S.L. and Smith, J.D. 2012. High-Density Lipoprotein Function, Dysfunction, and Reverse Cholesterol Transport. *Arteriosclerosis, Thrombosis, and Vascular Biology*. **32**(12),pp.2813–2820.

Foster, M.P., Mcelroy, C. a and Amero, C.D. 2007. Current Topics Solution NMR of Large Molecules and Assemblies. *Biochemistry*. **46**(2),pp.331–40.

Fowler, D.M., Koulov, A. V., Balch, W.E. and Kelly, J.W. 2007. Functional amyloid – from bacteria to humans. *Trends in Biochemical Sciences*. **32**(5),pp.217–224.

Fukui, H. 1999. Theory and calculation of nuclear spin–spin coupling constants. *Progress in Nuclear Magnetic Resonance Spectroscopy*. **35**(3),pp.267–294.

Fyfe, C.A., Brouwer, D.H. and Tekely, P. 2005. Measurement of NMR Cross-Polarization (CP) rate constants in the slow CP regime: Relevance to structure determinations of zeolite-sorbate and other complexes by CP magic-angle spinning NMR. *Journal of Physical Chemistry A*. **109**(28),pp.6187–6192.

Gasteiger, E., Gattiker, A., Hoogland, C., Ivanyi, I., Appel, R.. and Bairoch, A. 2003. ExPASy: The proteomics server for in-depth protein knowledge and

analysis. *Nucleic Acids Research*. [Online],pp.3784–3788. [Accessed 30 January 2017]. Available from: http://web.expasy.org/compute_pi/.

Gatti, G., Casu, B., Hamer, G. and Perlin, A. 1979. Studies on the Conformation of heparin by 1H and 13C NMR spectroscopy. *Macromolecules*. **12**(5),pp.1001–1007.

Gillam, J.E. and MacPhee, C.E. 2013. Modelling amyloid fibril formation kinetics: mechanisms of nucleation and growth. *Journal of Physics: Condensed Matter*. **25**(37),p.373101.

Gillmore, J.D. and Hawkins, P.N. 2006. Drug Insight: emerging therapies for amyloidosis. *Nature clinical practice. Nephrology*. **2**(5),pp.263–270.

Girych, M., Gorbenko, G., Trusova, V., Adachi, E., Mizuguchi, C., Nagao, K., Kawashima, H., Akaji, K., Lund-Katz, S., Phillips, M.C. and Saito, H. 2014. Interaction of Thioflavin T with amyloid fibrils of apolipoprotein A-I N-terminal fragment: Resonance energy transfer study. *Journal of Structural Biology*. **185**(1),pp.116–124.

Greenfield, N. 2007. Using circular dichroism spectra to estimate protein secondary structure. *Nat Protoc.* **1**(6),pp.2876–2890.

Guijarro, J., Sunde, M., Jones, J.A., Campbell, I.D. and Dobson, C.M. 1998. Amyloid fibril formation by an SH3 domain. *Proceedings of the National Academy of Sciences of the United States of America*. **95**(8),pp.4224–4228.

Gursky, O., Mei, X. and Atkinson, D. 2012. The crystal structure of the C-terminal truncated apolipoprotein A-I sheds new light on amyloid formation by the N-terminal fragment. *Biochemistry*. **51**(1),pp.10–18.

Haass, C. and Selkoe, D.J. 2007. Soluble protein oligomers in neurodegeneration: lessons from the Alzheimer's amyloid β-peptide. *Nature Reviews Molecular Cell Biology*. **8**(2),pp.101–112.

Hackl, E. V., Darkwah, J., Smith, G. and Ermolina, I. 2015. Effect of acidic and basic pH on Thioflavin T absorbance and fluorescence. *European Biophysics Journal*. **44**(4),pp.249–261.

Han, B., Liu, Y., Ginzinger, S.W. and Wishart, D.S. 2011. SHIFTX2: Significantly improved protein chemical shift prediction. *Journal of Biomolecular NMR*. **50**(1),pp.43–57.

Hard, T. and Lendel, C. 2012. Inhibition of amyloid formation. *Journal of*

Molecular Biology. **421**(4–5),pp.441–465.

Harper, J.D., Lieber, C.M. and Lansbury Jr., P.T. 1997. Atomic force microscopic imaging of seeded fibril formation and fibril branching by the Alzheimer's disease amyloid-beta protein. *Chemistry & Biology*. **4**(12),pp.951–959.

Harper, J.D., Wong, S.S., Lieber, C.M. and Lansbury, P.T. 1997. Observation of metastable Abeta amyloid protofibrils by atomic force microscopy. *Chemistry & Biology*. **4**(2),pp.119–125.

Hartmann, S.R. and Hahn, E.L. 1962. Nuclear Double Resonanace in the Rotating Frame. *Phys Rev*. **128**(5),pp.2042–2053.

Hawkes, C.A., Deng, L.H., Shaw, J.E., Nitz, M. and McLaurin, J. 2010. Small molecule β-amyloid inhibitors that stabilize protofibrillar structures in vitro improve cognition and pathology in a mouse model of Alzheimer's disease. *European Journal of Neuroscience*. **31**(2),pp.203–213.

Hazenberg, A., Dikkers, F., Hawkins, P., Bijzet, J., Rowczenio, D., Gilbertson, J., Posthumus, M., Leijsma, M. and Hazenberg, B. 2009. Laryngeal presentation of systemic apolipoprotein A-I-derived amyloidosis. *Laryngoscope*. **119**(3),pp.608–615.

Heise, H., Hoyer, W., Becker, S., Andronesi, O.C., Riedel, D. and Baldus, M. 2005. Molecular-level secondary structure, polymorphism, and dynamics of full-length alpha-synuclein fibrils studied by solid-state NMR. *Proceedings of the National Academy of Sciences of the United States of America*. **102**(44),pp.15871–15876.

Hoffman, R.E. 2006. Standardization of chemical shifts of TMS and solvent signals in NMR solvents. *Magnetic Resonance in Chemistry*. **44**(6),pp.606–616.

Holzwarth, G. and Doty, P. 1965. the Ultraviolet Circular Dichroism of Polypeptides. *Journal of the American Chemical Society*. **87**(4),pp.218–228.

Hore, P. 1995. *Nucelar Magnetic Resonance*. Oxford University Press, Oxford.

Hoshino, T., Mahmood, M.I., Mori, K. and Matsuzaki, K. 2013. Binding and aggregation mechanism of amyloid β-peptides onto the GM1 ganglioside-containing lipid membrane. *Journal of Physical Chemistry B*. **117**(27),pp.8085–8094.

Howie, A.J. and Brewer, D.B. 2009. Optical properties of amyloid stained by Congo red: History and mechanisms. *Micron*. **40**(3),pp.285–301.

Hoyer, W., Gronwall, C., Jonsson, A., Stahl, S. and Hard, T. 2008. Stabilization of a β-hairpin in monomeric Alzheimer's amyloid-β peptide inhibits amyloid formation. *Proc Natl Acad Sci U S A*. **105**(13),pp.5099–5104.

Hoyer, W., Gronwall, C., Jonsson, A., Stahl, S. and Hard, T. 2008. Stabilization of a β-hairpin in monomeric Alzheimer's amyloid-β peptide inhibits amyloid formation. *Proceedings of the National Academy of Sciences*. **105**(13),pp.5099–5104.

Huang, T.H., Yang, D.S., Plaskos, N.P., Go, S., Yip, C.M., Fraser, P.E. and Chakrabartty, A. 2000. Structural studies of soluble oligomers of the Alzheimer β-amyloid peptide. *Journal of molecular biology*. **297**(1),pp.73–87.

Huang, Y., DiDonato, J.A., Levison, B.S., Schmitt, D., Li, L., Wu, Y., Buffa, J., Kim, T., Gerstenecker, G.S., Gu, X., Kadiyala, C.S., Wang, Z., Culley, M.K., Hazen, J.E., Didonato, A.J., Fu, X., Berisha, S.Z., Peng, D., Nguyen, T.T., Liang, S., Chuang, C.-C., Cho, L., Plow, E.F., Fox, P.L., Gogonea, V., Tang, W.H.W., Parks, J.S., Fisher, E.A., Smith, J.D. and Hazen, S.L. 2014. An abundant dysfunctional apolipoprotein A1 in human atheroma. *Nature medicine*. **20**(2),pp.193–203.

Hudson, S.A., Ecroyd, H., Dehle, F.C., Musgrave, I.F. and Carver, J.A. 2009. (-)-Epigallocatechin-3-Gallate (EGCG) Maintains κ-Casein in Its Pre-Fibrillar State without Redirecting Its Aggregation Pathway. *Journal of Molecular Biology*. **392**(3),pp.689–700.

Hughes, E., Burke, R.M. and Doig, A.J. 2000. Inhibition of toxicity in the β-amyloid peptide fragment β-(25-35) using N-methylated derivatives. A general strategy to prevent amyloid formation. *Journal of Biological Chemistry*. **275**(33),pp.25109–25115.

Iannuzzi, C., Irace, G. and Sirangelo, I. 2015. The effect of glycosaminoglycans (GAGs) on amyloid aggregation and toxicity. *Molecules*. **20**(2),pp.2510–2528.

Ioannou, Y. a 2001. Multidrug permeases and subcellular cholesterol transport. *Nature reviews. Molecular cell biology*. **2**(September),pp.657–668.

Jagota, S. and Rajadas, J. 2013. Synthesis of d-amino acid peptides and their effect on beta-amyloid aggregation and toxicity in transgenic Caenorhabditis elegans. *Medicinal Chemistry Research*. **22**(8),pp.3991–4000.

Jahn, T.R., Makin, O.S., Morris, K.L., Marshall, K.E., Tian, P., Sikorski, P. and Serpell, L.C. 2010. The Common Architecture of Cross-β Amyloid. *Journal of*

Molecular Biology. **395**(4),pp.717–727.

Janson, J., Ashley, R.H., Harrison, D., McIntyre, S. and Butler, P.C. 1999. The mechanism of islet amyloid polypeptide toxicity is membrane disruption by intermediate-sized toxic amyloid particles. *Diabetes*. **48**(17),pp.491–498.

Jiménez, J.L., Nettleton, E.J., Bouchard, M., Robinson, C. V, Dobson, C.M. and Saibil, H.R. 2002. The protofilament structure of insulin amyloid fibrils. *Proceedings of the National Academy of Sciences of the United States of America*. **99**(14),pp.9196–9201.

Kavantzas, N., Chatziioannou, A., Yanni, A.E., Tsakayannis, D., Balafoutas, D., Agrogiannis, G. and Perrea, D. 2006. Effect of green tea on angiogenesis and severity of atherosclerosis in cholesterol-fed rabbit. *Vascular Pharmacology*. **44**(6),pp.461–463.

Kay, L.E. 2005. NMR studies of protein structure and dynamics. *Journal of Magnetic Resonance*. **173**(2),pp.193–207.

Kayed, R. 2003. Common Structure of Soluble Amyloid Oligomers Implies Common Mechanism of Pathogenesis. *Science*. **300**(5618),pp.486–489.

Khan, S., Gor, J., Mulloy, B. and Perkins, S.J. 2010. Semi-Rigid Solution Structures of Heparin by Constrained X-ray Scattering Modelling: New Insight into Heparin-Protein Complexes. *Journal of Molecular Biology*. **395**(3),pp.504–521.

Klunk, W.E., Jacob, R.F. and Mason, R.P. 1999a. Quantifying amyloid b-peptide (Aβ) aggregation using the Congo red-Aβ (CR-Aβ) spectrophotometric assay. *Analytical Biochemistry*. **266**(1),pp.66–76.

Klunk, W.E., Jacob, R.F. and Mason, R.P. 1999b. Quantifying amyloid β-peptide (Aβ) aggregation using the Congo red-Aβ (CR-aβ) spectrophotometric assay. *Analytical biochemistry*. **266**(1),pp.66–76.

Knight, J.D. and Miranker, A.D. 2004. Phospholipid catalysis of diabetic amyloid assembly. *Journal of molecular biology*. **341**(5),pp.1175–1187.

Kokkoni, N., Stott, K., Amijee, H., Mason, J.M. and Doig, A.J. 2006. N-methylated peptide inhibitors of β-amyloid aggregation and toxicity. Optimization of the inhibitor structure. *Biochemistry*. **45**(32),pp.9906–9918.

Kolodziejski, W. and Klinowski, J. 2002. Kinetics of cross-polarization in solid-state NMR: A guide for chemists. *Chemical Reviews*. **102**(3),pp.613–628.

Kumar, A., Nisha, C.M., Silakari, C., Sharma, I., Anusha, K., Gupta, N., Nair, P., Tripathi, T. and Kumar, A. 2016. Current and novel therapeutic molecules and targets in Alzheimer's disease. *Journal of the Formosan Medical Association*. **115**(1),pp.3–10.

Kyle, R. a, Gertz, M. a, Greipp, P.R., Witzig, T.E., Lust, J. a, Lacy, M.Q. and Therneau, T.M. 1997. A trial of three regimens for primary amyloidosis: colchicine alone, melphalan and prednisone, and melphalan, prednisone, and colchicine. *The New England journal of medicine*. **336**(17),pp.1202–1207.

Larsson, A., Malmström, S. and Westermark, P. 2011. Signs of cross-seeding: aortic medin amyloid as a trigger for protein AA deposition. *Amyloid : the international journal of experimental and clinical investigation : the official journal of the International Society of Amyloidosis*. **18**(4),pp.229–34.

LeVine, H. 1999. Quantification of β-sheet amyloid fibril structures with thioflavin T. *Methods in Enzymology*. **309**,pp.274–284.

Levitt, M.H., Suter, D. and Ernst, R.R. 1986. Spin dynamics and thermodynamics in solid-state NMR cross polarization. *The Journal of Chemical Physics*. **84**(8),p.4243.

Lewis, G.F. 2005. New Insights Into the Regulation of HDL Metabolism and Reverse Cholesterol Transport. *Circulation Research*. **96**(12),pp.1221–1232.

Li, H., Rahimi, F., Sinha, S., Maiti, P. and Bitan, G. 2009. Amyloids and Protein Aggregation – Analytical Methods. *Encyclopedia of Analytical Chemistry*.,pp.1–32.

Lian, L.Y. and Middleton, D.A. 2001. Labelling approaches for protein structural studies by solution state and solid-state NMR. *Progress in NMR Spectroscopy*. **39**,pp.171–190.

Liu, W., Qin, L., Yu, H., Lv, F. and Wang, Y. 2014. Apolipoprotein A-I and adenosine triphosphate-binding cassette transporter A1 expression alleviates lipid accumulation in hepatocytes. *Journal of gastroenterology and hepatology*. **29**(3),pp.614–22.

Luca, S., Heise, H. and Baldus, M. 2003. High-Resolution Solid-State NMR Applied to Polypeptides and Membrane Proteins. *Accounts of Chemical Research*. **36**(11),pp.858–865.

Luckgei, N., Schütz, A.K., Habenstein, B., Bousset, L., Sourigues, Y., Melki, R., Meier,

B.H. and Böckmann, A. 2014. Solid-state NMR sequential assignments of the amyloid core of Sup35pNM. *Biomolecular NMR Assignments*. **8**(2),pp.365–370.

Madine, J., Davies, H. a., Hughes, E. and Middleton, D. a. 2013. Heparin promotes the rapid fibrillization of a peptide with low intrinsic amyloidogenicity. *Biochemistry*. **52**(50),pp.8984–8992.

Madine, J. and Middleton, D. a 2010. Comparison of aggregation enhancement and inhibition as strategies for reducing the cytotoxicity of the aortic amyloid polypeptide medin. *European biophysics journal : EBJ*. **39**(9),pp.1281–8.

Madine, J., Pandya, M.J., Hicks, M.R., Rodger, A., Yates, E.A., Radford, S.E. and Middleton, D.A. 2012. Site-specific identification of an aβ fibril-heparin interaction site by using solid-state NMR spectroscopy. *Angewandte Chemie (International ed. in English)*. **51**(52),pp.13140–43.

Mahley, W., Franceschini, G. and Sirtori, C.R. 1983. Apolipoprotein A-IMilano. Detection of normal A-I in affected subjects and evidence for a cysteine for arginine substitution in the variant A-I . *Journal of Biological Chemistry*. **258**,pp.2508–2513.

Makin, O.S. and Serpell, L. 2005. Structures for amyloid fibrils. *FEBS Journal*. **272**(23),pp.5950–5961.

Mangione, P., Sunde, M., Giorgetti, S., Stoppini, M., Esposito, G., Gianelli, L., Obici, L., Asti, L., Andreola, a, Viglino, P., Merlini, G. and Bellotti, V. 2001. Amyloid fibrils derived from the apolipoprotein A1 Leu174Ser variant contain elements of ordered helical structure. *Protein science : a publication of the Protein Society*. **10**(1),pp.187–199.

Marbella, L.E., Crawford, S.E., Hartmann, M.J. and Millstone, J.E. 2016. Observation of uniform ligand environments and 31P-197Au coupling in phosphine-terminated Au nanoparticles. *Chem. Commun.* **52**,p.

Masuda, M., Suzuki, N., Taniguchi, S., Oikawa, T., Nonaka, T., Iwatsubo, T., Hisanaga, S., Goedert, M. and Hasegawa, M. 2006. Small molecule inhibitors of alpha-synuclein filament assembly. *Biochemistry*. **45**(19),pp.6085–6094.

Matthys, K.E. and Bult, H. 1997. Nitric oxide function in atherosclerosis. *Mediators of inflammation*. **6**,pp.3–21.

Mayer, M.P. 1995. A new set of useful cloning and expression vectors derived from pBlueScript. *Gene*. **163**(1),pp.41–46.

Maynard, C.J., Bush, A.I., Masters, C.L., Cappai, R. and Li, Q. 2005. Metals and amyloid-β in Alzheimer's disease. *International Journal of experimental pathology*. **86**(3),pp.147–159.

McDermott, A.E. 2009. *Structure and dynamics of membrane proteins by magic angle spinning solid-state NMR.*

McGuire, K. a, Davidson, W.S. and Jonas, a 1996. High yield overexpression and characterization of human recombinant proapolipoprotein A-I. *Journal of lipid research*. **37**(7),pp.1519–1528.

McIlvaine, T.. 1921. A buffer solution for colorimetric comparison. *Journal of Biochemistry*. **49**(1),pp.183–186.

McLaurin, J., Franklin, T., Chakrabartty, A. and Fraser, P.E. 1998. Phosphatidylinositol and inositol involvement in Alzheimer amyloid-β fibril growth and arrest. *Journal of molecular biology*. **278**(1),pp.183–194.

Mei, X. and Atkinson, D. 2011. *Crystal structure of C-terminal truncated apolipoprotein A-I reveals the assembly of High Density Lipoprotein (HDL) by dimerization*.

Meier, J.J., Kayed, R., Lin, C.-Y., Gurlo, T., Haataja, L., Jayasinghe, S., Langen, R., Glabe, C.G. and Butler, P.C. 2006. Inhibition of human IAPP fibril formation does not prevent β-cell death: evidence for distinct actions of oligomers and fibrils of human IAPP. *American journal of physiology. Endocrinology and metabolism*. **291**(6),pp.E1317-24.

Meng, F., Marek, P., Potter, K.J., Verchere, C.B. and Raleigh, D.P. 2008. Rifampicin does not prevent amyloid fibril formation by human islet amyloid polypeptide but does inhibit fibril thioflavin-T interactions: implications for mechanistic studies of β-cell death. *Biochemistry*. **47**(22),pp.6016–6024.

Miles, A.J. and Wallace, B.A. 2006. Synchrotron radiation circular dichroism spectroscopy of proteins and applications in structural and functional genomics. *Chemical Society reviews*. **35**(1),pp.39–51.

Minnich, A., Collet, X., Roghani, A., Cladaras, C., Hamilton, R.L., Fielding, C.J. and Zannis, V.I. 1992. Site-Directed Mutagenesis and Structure-Function Analysis of the Human Apolipoprotein A-I. *The Journal of biological chemistry*.

267,pp.16553–16560.

Mlynarik, V. 2016. Introduction to nuclear magnetic resonance. *Analytical Biochemitry*.

Monti, D.M., Arciello, A. and Piccoli, R. 2011. Amyloidoses associated to apolipoprotein A-I: The intriguing case of a natively unfolded protein fragment. *Febs Journal*. **278**,p.125.

Morris, G. 1980. Sensitivity enhancement in nitrogen-15 NMR: polarization transfer using the INEPT pulse sequence. *Journal of the American Chemical Society*. **102**(1),pp.428–429.

Morris, V.K., Linser, R., Wilde, K.L., Duff, A.P., Sunde, M. and Kwan, A.H. 2012. Solid-state NMR spectroscopy of functional amyloid from a fungal hydrophobin: A well-ordered β-sheet core amidst structural heterogeneity. *Angewandte Chemie - International Edition*. **51**(50),pp.12621–12625.

Mucchiano, G.I., Häggqvist, B., Sletten, K. and Westermark, P. 2001. Apolipoprotein A-1-derived amyloid in atherosclerotic plaques of the human aorta. *The Journal of pathology*. **193**(2000),pp.270–275.

Mucchiano, G.I., Jonasson, L., Häggqvist, B., Einarsson, E. and Westermark, P. 2001. Apolipoprotein A-I-derived amyloid in atherosclerosis. Its association with plasma levels of apolipoprotein A-I and cholesterol. *American journal of clinical pathology*. **115**(2),pp.298–303.

Nagao, K., Hata, M., Tanaka, K., Takechi, Y., Nguyen, D., Dhanasekaran, P., Lund-Katz, S., Phillips, M.C. and Saito, H. 2014. The roles of C-terminal helices of human apolipoprotein A-I in formation of high-density lipoprotein particles. *Biochimica et biophysica acta*. **1841**(1),pp.80–7.

Nagao, T., Komine, Y., Soga, S., Meguro, S., Hase, T., Tanaka, Y. and Tokimitsu, I. 2005. Ingestion of a tea rich in catechins leads to a reduction in body fat and malondialdehyde-modified LDL in men. *American Journal of Clinical Nutrition*. **81**(1),pp.122–129.

Naiki, H., Hashimoto, N., Suzuki, S., Kimura, H., Nakakuki, K. and Gejyo, F. 1997. Establishment of a kinetic model of dialysis-related amyloid fibril extension in vitro. *Amyloid International Journal Of Experimental And Clinical Investigation*. **4**(4),pp.223–232.

Nakajima, H., Nishitsuji, K., Kawashima, H., Kuwabara, K., Mikawa, S., Uchimura,

K., Akaji, K., Kashiwada, Y., Kobayashi, N., Saito, H. and Sakashita, N. 2016. The polyphenol (-)-epigallocatechin-3-gallate prevents apoA-IIowa amyloidosis in vitro and protects human embryonic kidney 293 cells against amyloid cytotoxicity. *Amyloid*. **23**(1),pp.17–25.

Näslund, J., Haroutunian, V., Mohs, R., Davis, K.L., Davies, P., Greengard, P. and Buxbaum, J.D. 2000. Correlation between elevated levels of amyloid beta-peptide in the brain and cognitive decline. *The journal of the American Medical Association*. **283**(12),pp.1571–1577.

Necula, M., Chirita, C.N. and Kuret, J. 2003. Rapid Anionic Micelle-mediated -Synuclein Fibrillization in Vitro. *Journal of Biological Chemistry*. **278**(47),pp.46674–46680.

Nelson, R., Sawaya, M.R., Balbirnie, M., Madsen, A.Ø., Riekel, C., Grothe, R. and Eisenberg, D. 2005. Structure of the cross-β spine of amyloid-like fibrils. *Nature cell biology*. **435**(7043),pp.773–778.

Nielsen, L., Khurana, R., Coats, A., Frokjaer, S., Brange, J., Vyas, S., Uversky, V.N. and Fink, A.L. 2001. Effect of Environmental Factors on the Kinetics of Insulin Fibril Formation. *Biochemistry*. **40**(20),pp.6036–6046.

Nowacka, A., Bongartz, N.A., Ollila, O.H.S., Nylander, T. and Topgaard, D. 2013. Signal intensities in 1H-13C CP and INEPT MAS NMR of liquid crystals. *Journal of Magnetic Resonance*. **230**,pp.165–175.

Obici, L., Franceschini, G., Calabresi, L., Giorgetti, S., Stoppini, M., Merlini, G. and Bellotti, V. 2006. Structure, function and amyloidogenic propensity of apolipoprotein A-I. *Amyloid*. **13**(4),pp.1–15.

Oda, M.N., Bielicki, J.K., Berger, T. and Forte, T.M. 2001. Cysteine substitutions in apolipoprotein A-I primary structure modulate paraoxonase activity. *Biochemistry*. **40**(6),pp.1710–1718.

Oda, M.N., Forte, T.M., Ryan, R.O. and Voss, J.C. 2003. The C-terminal domain of apolipoprotein A-I contains a lipid-sensitive conformational trigger. *Nature structural biology*. **10**(6),pp.455–60.

Olson, R.E. 1998. Discovery of the lipoproteins, their role in fat transport and their significance as risk factors. *The Journal of nutrition*. **128**(2 Suppl),p.439S–443S.

Oram, J.F. and Vaughan, A.M. 2006. ATP-Binding Cassette Cholesterol

Transporters and Cardiovascular Disease. *Circulation Research*. **99**(10),pp.1031–1043.

Ossoli, A., Simonelli, S., Vitali, C., Franceschini, G. and Calabresi, L. 2015. Role of LCAT in Atherosclerosis. *Journal of atherosclerosis and thrombosis*.,pp.119–127.

Palhano, F.L., Lee, J., Grimster, N.P. and Kelly, J.W. 2013. Toward the molecular mechanism(s) by which EGCG treatment remodels mature amyloid fibrils. *Journal of the American Chemical Society*. **135**(20),pp.7503–7510.

Pandey, K.B. and Rizvi, S.I. 2009. Plant polyphenols as dietary antioxidants in human health and disease. *Oxidative medicine and cellular longevity*. **2**(5),pp.270–8.

Pankhurst, G., Wang, X.L., Wilcken, D.E., Baernthaler, G., Panzenböck, U., Raftery, M. and Stocker, R. 2003. Characterization of specifically oxidized apolipoproteins in mildly oxidized high density lipoprotein. *Journal of lipid research*. **44**(2),pp.349–55.

Papy-Garcia, D., Morin, C., Huynh, M., F, S., Sissoeff, L., Sepuveda-Diaz, J. and Raisman-Vozari, R. 2011. Glycosaminoglycans, protein aggregation and neurodegeneration. *Current Protein and Peptide Sciecne*. **12**(3),pp.258–268.

Paravastu, A.K., Leapman, R.D., Yau, W. and Tycko, R. 2008. Molecular structural basis for polymorphism in Alzheimer ’s amyloid fibrils. *Proceedings of the National Academy of Sciences*. **105**(47).

Paravastu, A.K., Qahwash, I., Leapman, R.D., Meredith, S.C. and Tycko, R. 2009. Seeded growth of β-amyloid fibrils from Alzheimer’s brain-derived fibrils produces a distinct fibril structure. *Proceedings of the National Academy of Sciences of the United States of America*. **106**(18),pp.7443–7448.

Perrin, R.J., Fagan, A.M. and Holtzman, D.M. 2009. Multimodal techniques for diagnosis and prognosis of Alzheimer’s disease. *Nature*. **461**(7266),pp.916–922.

Petkova, A.T., Buntkowsky, G., Dyda, F., Leapman, R.D., Yau, W.M. and Tycko, R. 2004. Solid state NMR reveals a pH-dependent antiparallel β-sheet registry in fibrils formed by a β-amyloid peptide. *Journal of Molecular Biology*. **335**(1),pp.247–260.

Petkova, A.T., Ishii, Y., Balbach, J.J., Antzutkin, O.N., Leapman, D., Delaglio, F.,

Tycko, R., Petkova, A.T., Ishii, Y., Balbach, J.J., Oleg, N.A., Leapman, R.D. and Delaglio, F. 2002. A Structural Model for Alzheimer ' s β-Amyloid Fibrils Based on Experimental Constraints from Solid State NMR. *Proc Natl Acad Sci U S A*. **99**(26),pp.16742–16747.

Petkova, A.T., Yau, W. and Tycko, R. 2006. Experimental Constraints on Quaternary Structure in Alzheimer's β-Amyloid. *Biochemistry*. **45**,pp.498–512.

Petrlova, J., Bhattacherjee, A., Boomsma, W., Wallin, S., Lagerstedt, J.O. and Irbäck, A. 2014. Conformational and aggregation properties of the 1-93 fragment of apolipoprotein A-I. *Protein Science*. **23**(11),pp.1559–1571.

Pickhardt, M., Gazova, Z., Von Bergen, M., Khlistunova, I., Wang, Y., Hascher, A., Mandelkow, E.M., Biernat, J. and Mandelkow, E. 2005. Anthraquinones inhibit tau aggregation and dissolve Alzheimer's paired helical filaments in vitro and in cells. *Journal of Biological Chemistry*. **280**(5),pp.3628–3635.

Pickhardt, M., Larbig, G., Khlistunova, I., Coksezen, A., Meyer, B., Mandelkow, E.M., Schmidt, B. and Mandelkow, E. 2007. Phenylthiazolyl-hydrazide and its derivatives are potent inhibitors of tau aggregation and toxicity in vitro and in cells. *Biochemistry*. **46**(35),pp.10016–10023.

Pines, A., Gibby, M.G. and Waugh, J.S. 1973. Proton-enhanced NMR of dilute spins in solids. *The Journal of Chemical Physics*. **59**(1973),pp.569–590.

Podrabsky, J.E., Carpenter, J.F. and Hand, S.C. 2001. Survival of water stress in annual fish embryos: dehydration avoidance and egg envelope amyloid fibers. *American Journal of Physiology. Regulatory, Integrative and Comparative Physiology*. **280**(1),pp.R123–R131.

Prinz, W. a. 2007. Non-vesicular sterol transport in cells. *Progress in Lipid Research*. **46**(6),pp.297–314.

Puchtler, H., Sweat, F. and Levine, M. 1962. On the Binding of Congo Red By Amyloid. *Journal of Histochemistry & Cytochemistry*. **10**(3),pp.355–364.

Rabi, I., Zacharias, J., Millman, S. and Kusch, P. 1938. A new method of measuring nuclear magnetic moments. *Physical Review*. **53**(4),pp.318–318.

Radford, S.E. 2000. Protein folding: progress made and promises ahead. *Experimental Techniques*. **4**(December),pp.611–618.

Raimondi, S., Guglielmi, F., Giorgetti, S., Gaetano, S. Di, Arciello, A., Monti, D.M.,

Relini, A., Nichino, D., Doglia, S.M., Natalello, A., Pucci, P., Mangione, P., Obici, L., Merlini, G., Stoppini, M., Robustelli, P., Tartaglia, G.G., Vendruscolo, M., Dobson, C.M., Piccoli, R. and Bellotti, V. 2011. Effects of the known pathogenic mutations on the aggregation pathway of the amyloidogenic peptide of apolipoprotein A-I. *Journal of Molecular Biology*. **407**(3),pp.465–476.

Ramella, N.A., Schinella, G.R., Ferreira, S.T., Prieto, E.D., Vela, M.E., R??os, J.L., Tricerri, M.A. and Rimoldi, O.J. 2012. Human Apolipoprotein A-I Natural Variants: Molecular Mechanisms Underlying Amyloidogenic Propensity. *PLoS ONE*. **7**(8).

Ramella, N. a, Rimoldi, O.J., Prieto, E.D., Schinella, G.R., Sanchez, S. a, Jaureguiberry, M.S., Vela, M.E., Ferreira, S.T. and Tricerri, M.A. 2011. Human apolipoprotein A-I-derived amyloid: its association with atherosclerosis. *PloS one*. **6**(7),p.e22532.

Ross, R. 1999a. Atherosclaerosis an inflammatory disease. *The New England Journal of Medicine*. **340**(2),pp.115–126.

Ross, R. 1999b. Pathogenesis of Atherosclerosis Atherosclerosis is an inflammatory disease. *American Heart Journal*. **138**(5),pp.419–420.

Ross, R. 1993. The pathogenesis of atherosclerosis: a perspective for the 1990s. *Nature*. **362**(6423),pp.801–9.

Rosú, S. a., Rimoldi, O.J., Prieto, E.D., Curto, L.M., Delfino, J.M., Ramella, N. a. and Tricerri, M.A. 2015. Amyloidogenic Propensity of a Natural Variant of Human Apolipoprotein A-I: Stability and Interaction with Ligands. *Plos One*. **10**(5),p.e0124946.

Rudelle, S., Ferruzzi, M.G., Cristiani, I., Moulin, J., Mace, K., Ferruzzi, M.G., Cristiani, I. and Moulin, J. 2007. Effect of a Thermogenic Beverage on 24-Hour Energy Metabolism in Humans. . **15**(2),pp.349–355.

Ryan, R.O., Forte, T.M. and Oda, M.N. 2003. Optimized bacterial expression of human apolipoprotein A-I. *Protein Expression and Purification*. **27**(1),pp.98–103.

Sabaté, R., Lascu, I. and Saupe, S.J. 2008. On the binding of Thioflavin-T to HET-s amyloid fibrils assembled at pH 2. *Journal of Structural Biology*. **162**(3),pp.387–396.

Sackewitz, M., Scheidt, H.A., Lodderstedt, G., Schierhorn, A., Schwarz, E. and Huster, D. 2008. Structural and dynamical characterization of fibrils from a disease-associated alanine expansion domain using proteolysis and solid-state NMR spectroscopy. *Journal of the American Chemical Society*. **130**(23),pp.7172–7173.

Saito, H., Dhanasekaran, P., Nguyen, D., Holvoet, P., Lund-Katz, S. and Phillips, M.C. 2003. Domain structure and lipid interaction in human apolipoproteins A-I and E, a general model. *Journal of Biological Chemistry*. **278**(26),pp.23227–23232.

Serio, T.R., Cashikar, A.G., Kowal, A.S., Sawicki, G.J., Moslehi, J.J., Serpell, L., Arnsdorf, M.F. and Lindquist, S.L. 2000. Nucleated Conformational Conversion and the Replication of Conformational Information by a Prion Determinant. *Science*. **289**(5483),pp.1317–1321.

Serpell, L. 2000. Alzheimer ' s amyloid fibrils : structure and assembly. *Biochimica et Biophysica Acta*. **1502**,pp.16–30.

Serpell, L., Blake, C. and Fraser, P. 2000. Molecular structure of a fibrillar Alzheimer's A beta fragment. *Biochemistry*. **39**(43),pp.13269–13275.

Serpell, L., Sunde, M., Benson, M.D., Tennent, G.A., Pepys, M.B. and Fraser, P.E. 2000. The protofilament substructure of amyloid fibrils. *Journal of Molecular Biology*. **300**(5),pp.1033–1039.

Serpell, L., Sunde, M. and Blake, C. 1997. The molecular basis of amyloidosis. *Cellular and molecular life sciences : CMLS*. **53**(11–12),pp.871–887.

Sharpe, C.R., Sidoli, A., Shelley, C.S., Lucero, M.A., Shoulders, C.C. and Baralle, F.E. 1984. Human apolipoproteins AI, AII, CII and CIII. cDNA sequences and mRNA abundance. *Nucleic Acids Research*. **12**(9),pp.3917–3932.

Sigalov, A.B. and Stern, L.J. 2001. Oxidation of methionine residues affects the structure and stability of apolipoprotein A-I in reconstituted high density lipoprotein particles. *Chemistry and Physics of Lipids*. **113**(1–2),pp.133–146.

Siligardi, G., Panaretou, B., Meyerc, P., Singh, S., Woolfson, D.N., Piper, P.W., Pearl, L.H. and Prodromou, C. 2002. Regulation of Hsp90 ATPase activity by the Co-chaperone Cdc37p/p50 cdc37. *Journal of Biological Chemistry*. **277**(23),pp.20151–20159.

Sipe, J.D., Benson, M.D., Buxbaum, J.N., Ikeda, S.-I., Merlini, G., Saraiva, M.J.M. and

Westermark, P. 2012. Amyloid fibril protein nomenclature: 2012 recommendations from the nomenclature committee of the international society of amyloidosis. *Amyloid : the international journal of experimental and clinical investigation : the official journal of the International Society of Amyloidosis*. **17**(3–4),pp.101–4.

Sipe, J.D., Benson, M.D., Buxbaum, J.N., Ikeda, S., Merlini, G., Saraiva, M.J.M. and Westermark, P. 2014. Nomenclature 2014: Amyloid fibril proteins and clinical classification of the amyloidosis. *Amyloid*. **21**(4),pp.221–224.

Sipe, J.D. and Cohen, A.S. 2000. Review: History of the Amyloid Fibril. *Journal of Structural Biology*. **130**(2–3),pp.88–98.

Smith, J.F., Knowles, T.P.J., Dobson, C.M., Macphee, C.E. and Welland, M.E. 2006. Characterization of the nanoscale properties of individual amyloid fibrils. *Proceedings of the National Academy of Sciences of the United States of America*. **103**(43),pp.15806–15811.

Soriaga, A.B., Sangwan, S., Macdonald, R., Sawaya, M.R. and Eisenberg, D. 2015. Crystal Structures of IAPP Amyloidogenic Segments Reveal a Novel Packing Motif of Out-of-Register β Sheets. *The Journal of Physical Chemistry B*.,p.acs.jpcb.5b09981.

Soto, C., Sigurdsson, E.., Morelli, L., Asok Kumar, R., Castano, E. and Blas, F. 1998. β-sheet breaker peptides inhibit fibrillogenesis in a rat brain model of amyloidosis: implications for alzheimers therapy. *Group*. **4**(7),pp.623–6.

Soto, C., Sigurdsson, E.., Morelli, L., Asok Kumar, R., Castano, E. and Frangione, B. 1998. β sheet breaker peptides inhibit fibrillogenesis in a rat brain model of amyloisosis: implications for alzheimers therapy. *Nature medicine*. **4**(7),pp.822–826.

Souillac, P.O., Uversky, V.N., Millett, I.S., Khurana, R., Doniach, S. and Fink, A.L. 2002. Elucidation of the Molecular Mechanism during the Early Events in Immunoglobulin Light Chain Amyloid Fibrillation: Evidence for an off-pathway oligomer at acidic pH. *Journal of Biological Chemistry*. **277**(15),pp.12666–12679.

Soutar, A.K. 1992. Apolipoprotein Al mutation Arg-60 causes autosomal dominant amyloidosis . *Proc. natn. Acad. Sci. U.S.A.* . **89**(August),pp.7389–7393.

Sreerama, N. and Woody, R.W. 2000. Estimation of protein secondary structure from circular dichroism spectra: comparison of CONTIN, SELCON, and CDSSTR methods with an expanded reference set. *Analytical biochemistry*. **287**(2),pp.252–260.

Srinivasan, R., Jones, E.M., Liu, K., Ghiso, J., Marchant, R.E. and Zagorski, M.G. 2003. pH-Dependent Amyloid and Protofibril Formation by the ABri Peptide of Familial British Dementia. *Journal of Molecular Biology*. **333**(5),pp.1003–1023.

Stefani, M. 2007. Generic Cell Dysfunction in Neurodegenerative Disorders: Role of Surfaces in Early Protein Misfolding, Aggregation, and Aggregate Cytotoxicity. *The Neuroscientist*. **13**(5),pp.519–531.

Stein, O. and Stein, Y. 1999. Atheroprotective mechanisms of HDL. *Atherosclerosis*. **144**(2),pp.285–301.

Stewart, K.L., Hughes, E., Yates, E.A., Akien, G.R., Huang, T.Y., Lima, M.A., Rudd, T.R., Guerrini, M., Hung, S.C., Radford, S.E. and Middleton, D.A. 2016. Atomic Details of the Interactions of Glycosaminoglycans with Amyloid-β Fibrils. *Journal of the American Chemical Society*. **138**(27),pp.8328–8331.

Takegoshi, K., Nakamura, S. and Terao, T. 2001. C± 1 H dipolar-assisted rotational resonance in magic-angle spinning NMR. *Chemical Physics Letters*. **344**(August),pp.631–637.

Tate, S., Ren, X., Sivashanmugam, A., Chen, B., Li, C., Yang, Y., Neville, T., Hoyt, D., Jerome, W.G., Sparks, D., Li, Q., Wang, J., Magnetic, H.F., Facility, R. and Northwest, P. 2006. NMR structural studies of human apolipoprotein A-I at the lipid-free and HDL-associated states: A progress report. *Functional and Structural Biology on the Lipo-network*. **661**(2),pp.65–93.

Teoh, C.L., Griffin, M.D.W. and Howlett, G.J. 2011. Apolipoproteins and amyloid fibril formation in atherosclerosis. *Protein and Cell*. **2**(2),pp.116–127.

Thijssen, M.A. and Mensink, R.P. 2005. Fatty acids and atherosclerotic risk. *Handbook of experimental pharmacology*. (170),pp.165–94.

Tjernberg, L.O., Näslund, J., Lindqvist, F., Johansson, J., Karlström, a R., Thyberg, J., Terenius, L. and Nordstedt, C. 1996. Arrest of β-amyloid fibril formation by a pentapeptide ligand. *The Journal of biological chemistry*. **271**(15),pp.8545–8548.

Touchette, J.C., Williams, L.L., Ajit, D., Gallazzi, F. and Nichols, M.R. 2010. Probing the amyloid-β(1-40) fibril environment with substituted tryptophan residues. *Archives of Biochemistry and Biophysics*. **494**(2),pp.192–197.

Toyama, B.H. and Weissman, J.S. 2011. Amyloid structure: conformational diversity and consequences. *Annual review of biochemistry*. **80**(6),.557–85.

Tuttle, M.D., Comellas, G., Nieuwkoop, A.J., Covell, D.J., Berthold, D.A., Kloepper, K.D., Courtney, J.M., Kim, J.K., Barclay, A.M., Kendall, A., Wan, W., Stubbs, G., Schwieters, C.D., Lee, V.M.Y., George, J.M. and Rienstra, C.M. 2016. Solid-state NMR structure of a pathogenic fibril of full-length human α-synuclein. *Nature Structural & Molecular Biology*. **23**(February),pp.1–9.

Tycko, R. 2006. Molecular structure of amyloid fibrils: insights from solid-state NMR. *Quarterly reviews of biophysics*. **39**(1),pp.1–55.

Tycko, R. 2011. Solid-State NMR Studies of Amyloid Fibril Structure. *Annual Review of Physical Chemistry*. **62**(1),pp.279–299.

Uversky, V.N. 2010. Mysterious oligomerization of the amyloidogenic proteins. *FEBS Journal*. **277**(14),pp.2940–2953.

Veeman, W.S. 1997. Nuclear magnetic resonance, a simple introduction to the principles and applications. *Geoderma*. **80**,pp.225–242.

Vigushin D.M, Gough, J., Allan, D., Alguacil, A., Penner, B., Pettigrew, N.M., Quinonez, G., Bernstein, K., Soutar, A.K., Hawkins, P.N., Pepys, M.B., Booth, S.. and Booth, D.. 1994. Familial nephropathic systemic amyloidosis caused by apolipoprotein AI variant Arg26. *Quarterly Journal of Medicine*. (June 1992),pp.149–154.

Vivian, J.T. and Callis, P.R. 2001. Mechanisms of tryptophan fluorescence shifts in proteins. *Biophysical journal*. **80**(5),pp.2093–2109.

Walsh, D.M., Klyubin, I., Fadeeva, J. V, Rowan, M.J. and Selkoe, D.J. 2002. Amyloid-β oligomers: their production, toxicity and therapeutic inhibition. *Biochemical Society transactions*. **30**(4),pp.552–557.

Walsh, D.M., Lomakin, A., Benedek, G.B., Condron, M.M. and Teplow, D.B. 1997. Amyloid -Protein Fibrillogenesis: Detection of a protofibrillar intermediate. *Journal of Biological Chemistry*. **272**(35),pp.22364–22372.

Wang, G., Sparrow, J.T. and Cushley, R.J. 1997. The helix-hinge-helix structural motif in human apolipoprotein A-I determined by NMR spectroscopy.

Biochemistry. **36**(44),pp.13657–66.

Wang, G., Treleaven, W.D. and Cushley, R.J. 1996. Conformation of human serum apolipoprotein A-I (166-185) in the presence of sodium dodecyl sulfate or dodecylphosphocholine by H-NMR and CD. Evidence for specific peptide-SDS interactions. *Biochimica et Biophysica Acta*. **1301**,pp.174–184.

Wang, H. and Raleigh, D.P. 2014. General amyloid inhibitors? A critical examination of the inhibition of IAPP amyloid formation by inositol stereoisomers. *PLoS ONE*. **9**(9).

Wang, S.H., Liu, F.F., Dong, X.Y. and Sun, Y. 2010. Thermodynamic analysis of the molecular interactions between amyloid β-peptide 42 and (–)-epigallocatechin-3-gallate. *The journal of physical chemistry. B*. **114**(35),pp.11576–11583.

Wang, X., Sato, R., Brown, M.S., Hua, X. and Goldstein, J.L. 1994. SREBP-1, a membrane-bound transcription factor released by sterol-regulated proteolysis. *Cell*. **77**(1),pp.53–62.

Wang, Y. and Jardetzky, O. 2002. Probability-based protein secondary structure identification using combined NMR chemical-shift data. *Protein Science*. **11**(4),pp.852–861.

Whitehouse, P., Price, D. and RG, S. 1982. Alzheimer's disease and senile dementia, loss of neirons in the basal forebrain. *Science*. **215**,pp.1237–1239.

Whitmore, L. and Wallace, B.A. 2008. Protein secondary structure analyses from circular dichroism spectroscopy: Methods and reference databases. *Biopolymers*. **89**(5),pp.392–400.

Wink, D.J. 1989. Spin-Lattice Relaxation Times in H NMR spectroscopy. *J. Chem. Edu.* **66**,pp.810–813.

Wolfe, L.S., Calabrese, M.F., Nath, A., Blaho, D. V, Miranker, A.D. and Xiong, Y. 2010. Protein-induced photophysical changes to the amyloid indicator dye thioflavin T. *Proceedings of the National Academy of Sciences of the United States of America*. **107**(39),pp.16863–16868.

Wolfram, S. 2007. Effects of green tea and EGCG on cardiovascular and metabolic health. *Journal of the American College of Nutrition*. **26**(4),p.373S–388S.

Wolfram, S., Wang, Y. and Thielecke, F. 2006. Anti-obesity effects of green tea: From bedside to bench. *Molecular Nutrition and Food Research*.

50(2),pp.176–187.

Won, S.-M., Park, Y.-H., Kim, H.-J., Park, K.-M. and Lee, W.-J. 2006. Catechins inhibit angiotensin II-induced vascular smooth muscle cell proliferation via mitogen-activated protein kinase pathway. *Experimental & molecular medicine*. **38**(5),pp.525–34.

Wong, Y.Q., Binger, K.J., Howlett, G.J. and Griffin, M.D.W. 2012. Identification of an amyloid fibril forming peptide comprising residues 46-59 of apolipoprotein A-I. *FEBS Letters*. **586**(13),pp.1754–1758.

Wong, Y.Q., Binger, K.J., Howlett, G.J. and Griffin, M.D.W. 2010. Methionine oxidation induces amyloid fibril formation by full-length apolipoprotein A-I. *Proceedings of the National Academy of Sciences of the United States of America*. **107**(5),pp.1977–82.

Wood, S.J., Wetzel, R., Martin, J.D. and Hurle, M.R. 1995. Prolines and amyloidogenicity in fragments of the Alzheimer's peptide β/A4. *Biochemistry*. **34**(3),pp.724–730.

Wu, Z., Gogonea, V., Lee, X., Wagner, M.A., Li, X.M., Huang, Y., Undurti, A., May, R.P., Haertlein, M., Moulin, M., Gutsche, I., Zaccai, G., DiDonato, J.A. and Hazen, S.L. 2009. *Double superhelix model of high density lipoprotein*.

Wuthrich, K. 2001. The way to NMR structures of proteins. *Nature Structural & Molecular Biology*. **8**(11),pp.923–925.

Wuthrick, K. 1990. Protein structure determination in Solution by NMR Spectroscopy. *BIological Chemistry*. **265**(36),pp.22059–22062.

Xue, W., Homans, S.W. and Radford, S.E. 2008. Systematic analysis of nucleation-dependent polymerization reveals new insights into the mechanism of amyloid self-assembly. *Proceedings of the National Academy of Sciences of the United States of America*. **105**(26),pp.8926–31.

Zhang, M., Li, L., Xie, W., Wu, J., Yao, F. and Tan, Y. 2016. Apolipoprotein A-1 binding protein promotes macrophage cholesterol ef fl ux by facilitating apolipoprotein A-1 binding to ABCA1 and preventing ABCA1 degradation. *Atherosclerosis*. **248**,pp.149–159.

Zhang, R., Mroue, K.H. and Ramamoorthy, A. 2016. Hybridizing cross-polarization with NOE or refocused-INEPT enhances the sensitivity of MAS NMR spectroscopy. *Journal of Magnetic Resonance*. **266**,pp.59–66.

Appendix 1

pBluescript K+ plasmid Map

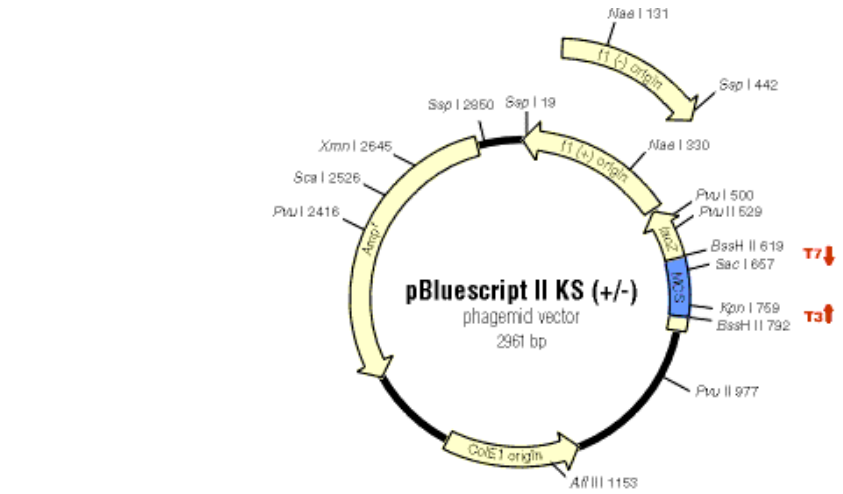

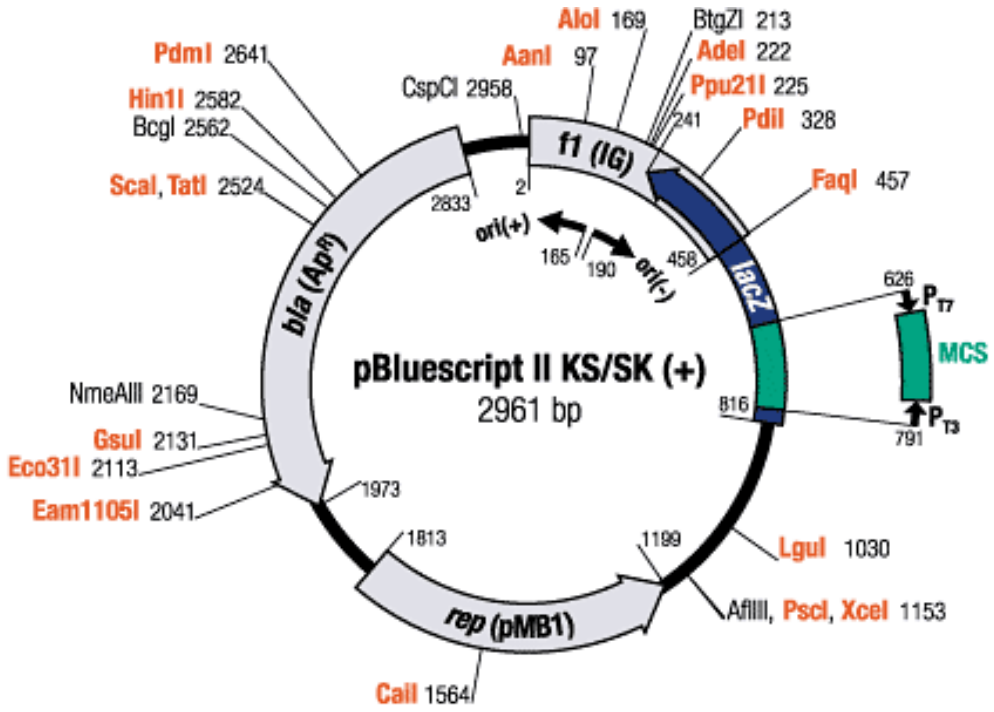

Appendix 2

Site-directed ligase independent mutagenesis (SLIM) primers

Mutated triplicates are highlighted in bold with the individual changed nucleotide/s highlighted in red.

L44STOP

Forward Long Primer

TTG AAC **TAG** AAG CTG CTG GAC AAC TGG GAC AGC GTG ACG T

Forward Short

GAC AAC TGG GAC AGC GTG ACG T

Reverse Long Primer

CAG CAG CTT **CTA** GTT CAA TTG TTT GCC CAA GGC GGA TCC T

Reverse Short

TTG TTT GCC CAA GGC GGA TCC T

L90P

Forward Long Primer

AGC AAG GAT **CCG** GAG GAG GTG AAG GCC AAG GTG CAG CCG TAC C

Forward Short Primer

GTG AAG GCC AAG GTG CAG CCG TAC C

Reverse Long Primer

CTC CTC **CGG** ATC CTT GCT CAT CTC CTG GCG CAG GCC CTC T

Reverse Short Primer

CAT CTC CTG GCG CAG GCC CTC T

K96C

Forward Long Primer

GTG AAG GCC **TGC** GTG CAG CCG TAC CTG GAC GAC TTC CAG A

Forward Short Primer

CCG TAC CTG GAC GAC TTC CAG A

Reverse Long Primer

CTG CAC **GCA** GGC CTT CAC CTC CTC CAG ATC CTT GCT CAT C

Reverse Short Primer

CTC CTC CAG ATC CTT GCT CAT C

R173C

Forward Long Primer

CTG CGC CAG **TGC** TTA GCG GCG CGC CTT GAG GCT CTC AAG G

Forward Short Primer

GCG CGC CTT GAG GCT CTC AAG G

Reverse Long Primer

CGC TAA **GCA** CTG GCG CAG CTC GTC GCT GTA CGG CGC CAG A

Reverse Short Primer

CTC GTC GCT GTA CGG CGC CAG A

Appendix 3

Gene Sequencing of apoA-I Mutants

The sequence in brackets contains the expressed fusion peptide, consisting of the hexa-histidine tag (green), the linker region (orange) and apoA-I mutant sequence (black) with mutants underlined. The formic acid cleavage site is shown as "|" and indistinguishable amino acids are shown as blue "X"s.

ApoA-I E2D

I G R P Q R F P S R N N F V Stop L Stop (**E G D I H M H H H H H H G L V P R G S I D D | P P Q S P W D R V K D L A T V Y V D V L K D S G R D Y V S Q F E G S A L G K Q L N L K L L D N W D S V T S T F S K L R E Q L G P V T Q E F W D N L E K E T E G L R Q E M S K D L E E V K A K V Q P Y L D D F Q K K W Q E E M E L Y R Q K V E P L R A E L Q E G A R Q K L H E L Q E K L S P L G E E M R D R A R A H V D A L R T H L A P Y S D E L R Q R L A A R L E A L K E N G G A R L A E Y H A K A T E H L S T L S E K A K P A L E D L R Q G L L P V L E S F K V S F L S A L E E Y T K K L N T Q Stop**) S A L E L V D L R P H S S T T T T T T E I R L L T K

ApoA-I G26R

K X X X X L X X G X X H **M H H H H H H** I E G X **D X | X X X S P W D R V K D X X T V Y V D V L K D S R R D Y V S Q F E G S A L G K Q L N L K L L D N W D S V T S T F S K L R E Q L G P V T Q E F W D N L E K E T E G L R Q E M S K D L E E V K A K V Q P Y L D D F Q K K W Q E E M E L Y R Q K V E P L R A E L Q E G A R Q K L H E L Q E K L S P L G E E M R D R A R A H V D A L R T H L A P Y S D E L R Q R L A A R L E A L K E N G G A R L A E Y H A K A T E H L S T L S E K A K P A L E D L R Q G L L P V L E S F K V S F L S A L E E Y T K K L N T Q Stop**) G A L E L V D L R P H S S T T T T T T E I R L L T K P

ApoA-I L44Stop

X X X X X X X F C L L Stop (**E G D I H M H H H H H H G L V P R G S I D D P P Q S P W D R V K D L A T V Y V D V L K D S G R D Y V S Q F E G S A L G K Q L N Stop**) K L L D N W D S V T S T F S K L R E Q L G P V T Q E F W D N L E K E T E G L R Q E M S K D L E E V K A K V Q P Y L D D F Q K K W Q E E M E L Y R Q K V E P L R A E L Q E G A R Q K L H E L Q E K L S P L G E E M R D R A R A H V D A L R T H L A P Y S D E L R Q R L A A R L E A L K E N G G A R L A E Y H A K A T E H L S T L S E X A K P A L E D L R Q G L L P V L E S F K V S F L S A L E E Y T K K L N T Q Stop S A L E L V D L R P H S S T T T T T T E I R L L T K P E R K L X W L L P P L X N N Stop

ApoA-I L90P

X X X X X X F C L L Stop (**E G D I H M H H H H H H G L V P R G S I D D | P P Q S P W D R V K D L A T V Y V D V L K D S G R D Y V S Q F E G S A L G K Q L N L K L L D N W D S V T S T F S K L R E Q L G P V T Q E F W D N L E K E T E G L R Q E M S K D P E E V K A K V Q P Y L D D F Q K K W Q E E M E L Y R Q K V E P L R A E L Q E G A R Q K L H E L Q E K L S P L G E E M R D R A R A H V D A L R T H L A P Y S D E L R Q R L A A R L E A L K E N G G A R L A E Y H A K A T E H L S T L S E K A K P A L E X L R Q X L L P V L E S F K V S F L S A L E E Y T K K L N T Q Stop**) S A L E L V D L R P H S S T T T T T T E I R L L T K P E R K L S W L L P P L S N N Stop H N P L G X L N G S W X G F F A E R R N

ApoA-I K96C

X X X X X F C L L Stop (**E G D I H M H H H H H H G L V P R G S I D D | P P Q S P W D R V K D L A T V Y V D V L K D S G R D Y V S Q F E G S A L G K Q L N L K L L D N W D S V T S T F S K L R E Q L G P V T Q E F W D N L E K E T E G L R Q E M S K D L E E V K A C V Q P Y L D D F Q K K W Q E E M E L Y R Q K V E P L R A E L Q E G A R Q K L H E L Q E K L S P L G E E M R D R A R A H V D A L R T H L A P Y S D E L R Q R L A A R L E A L K E N G G A R L A E Y H A K A T E H L S T L S E K A K P A L E D L R Q G L L P V L E S F K V S F L S A L E E Y T K K L N T Q Stop**) S A L E L V D L R P H S S T T T T T T E I R L L T K P E R K L S W L L P P L X I T S I T P W G L Stop T G X E G F F A E R X T I S X I X R Met G R X X X R R I K R

ApoA-I R173C

X X X X X X X X X X C X X Stop (**E G D I H M H H H H H H G L V P R G S I D D | P P Q S P W D R V K D L A T V Y V D V L K D S G R D Y V S Q F E G S A L G K Q L N L K L L D N W D S V T S T F S K L R E Q L G P V T Q E F W D N L E K E T E G L R Q E M S K D L E E V K A K V Q P Y L D D F Q K K W Q E E M E L Y R Q K V E P L R A E L Q E G A R Q K L H E L Q E K L S P L G E E M R D R A R A H V D A L R T H L A P Y S D E L R Q C L A A R L E A L K E N G G A R L A E Y H A K A T E H L S T L S E K A K P A L E D L R Q G L L P V L E S F K V S F L S A L E E Y T K K L N T Q Stop**) S A L E L V D L R P H S S T T T T T T X I R L L T K P E X K L X W L L P P L X N N Stop H X P W G S K R V L R G F L L K X N Y I P D W X X X X R X Stop R R I Stop R X G X X X X R X X D

Appendix 4

Fittings for the calculation of rates of fluorescence increase between the F_I and F_T points. Data from this is incorporated into Figures 4.7, 4.8 and 4.10 for A, B and C respectively.

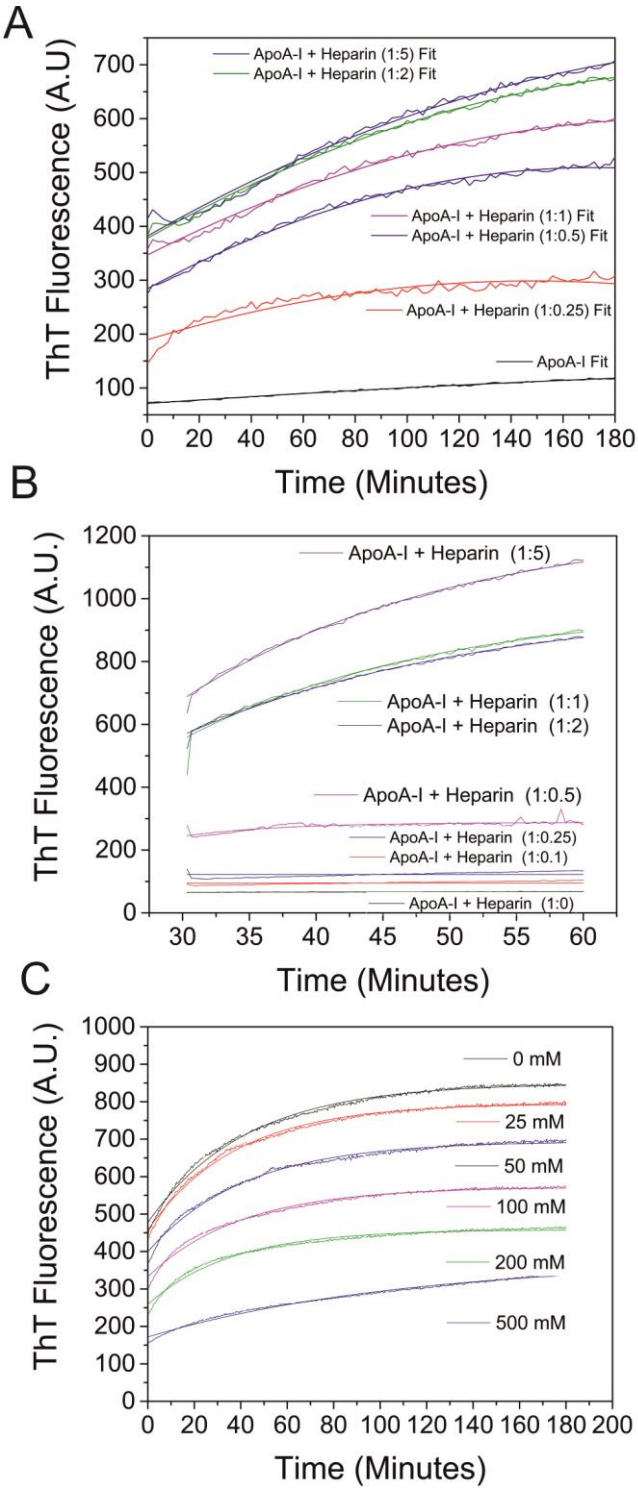

Appendix 5

Cerilliant
Analytical Reference Standards
a SIGMA-ALDRICH company

Certified Reference Material - Certificate of Analysis

Cerilliant Quality
ISO GUIDE 34
ISO/IEC 17025
ISO 13485
ISO 15194
ISO 9001
GMP/GLP

Product Name:	**Green Tea Catechin Mix**
Catalog Number:	**G-016**
Solution Lot:	FN09081401
Expiration Date:	February 2016
Solvent:	80::20 Acetonitrile::Water with 5% 1M HCl (degassed)
Volume per Ampoule:	Not less than 1 mL
Storage:	Store Unopened in Freezer.
Shipping:	Ship Cold. See Stability Section.
Intended Use:	For R&D/ analytical purposes only. Not suitable for human or animal consumption. For qualitative or quantitative applications.
Safety:	Danger. See Safety Data Sheet.

- Expiration Date has been established through real time stability studies.
- Ampules are overfilled to ensure a minimum 1 mL volume. We advise laboratories to quantitively transfer measured volumes of this standard solution before diluting to the desired concentration.
- For quantitative applications, the minimum sample size for intended use is 1 µL.

Component	Certified Concentration
(-)-Epigallocatechin 3-gallate	100.1 ± 0.5 µg/mL
(+)-Catechin	100.0 ± 0.5 µg/mL [1]
(-)-Epicatechin	100.0 ± 0.5 µg/mL [1]
(-)-Epicatechin 3-gallate	100.0 ± 0.5 µg/mL [1]
(-)-Gallocatechin	100.1 ± 0.5 µg/mL [1]
(-)-Gallocatechin 3-gallate	99.9 ± 0.5 µg/mL [1]
(-)-Catechin 3-gallate	100.0 ± 0.5 µg/mL
Caffeine	100.0 ± 0.5 µg/mL

- Uncertainty of the concentration is expressed as an expanded uncertainty in accordance with ISO 17025 and Guide 34 at the approximate 95% confidence interval using a coverage factor of k = 2 and has been calculated by statistical analysis of our production system and incorporates uncertainty of the purity factor, material density, homogeneity of the ampouled standard, and balance and weighing technique. Uncertainty terms for verification and stability are excluded.
- This standard is prepared gravimetrically and mass results are reported on the conventional basis for weighing in air. Concentration is calculated based on: the actual measured mass; Purity Factor of the analyte(s); measured mass of the solution; and the density of the pure diluent at 20°C.
- Concentration is corrected for chromatographic purity, residual water, residual solvents and residual inorganics.
- The Certified Concentration represents the True Value and is expressed in terms of concentration per volume of solution with stated uncertainty at µg/mL. We recommend the Certified Concentration be used for all calculations and dilutions.

[1] Concentration has been corrected using vendor supplied data for residual solvents and residual organics. Cerilliant has not analytically verified this data. Inaccuracies in concentration may exist.

Cerilliant certifies that this standard meets the specifications stated in this certificate and warrants this product to meet the stated acceptance criteria through the expiration/retest date when stored unopened as recommended. Product should be used shortly after opening to avoid concentration changes due to evaporation. Warranty does not apply to ampoules stored after opening.

ACLASS ACCREDITED REFERENCE MATERIAL PRODUCER

Darron Ellsworth, Quality Assurance Manager

October 12, 2015
Date

Cerilliant Corporation 811 Paloma Drive, Suite A, Round Rock, TX 78665 800-848-7837 / 512-238-9974

Traceability

- Gravimetrically prepared using qualified balances calibrated semi-annually by Mettler Toledo using NIST traceable weights. Calibration verification performed weekly and prior to each use utilizing NIST traceable weights. Each balance has been assigned a minimum weighing by Mettler Toledo taking into consideration the balance and installed environmental conditions to ensure weighing complies with USP tolerances of no more than 0.1% relative error.
- Weigh tapes provide traceability to SI units of measure.
- Balances and NIST traceable weights calibrated by ISO 17025 accredited vendors.
- Concentration is verified against an independently prepared calibrator gravimetrically prepared using balances calibrated to NIST.
- In addition, each neat material utilized has been identified and thoroughly characterized by an ISO 17025 accredited laboratory. Spectral data is provided on subsequent pages of the COA.

Standard Solution Assay Parameters

Analysis Method: HPLC/UV
Column: Ascentis ES Cyano 3 µm, 4.6 x 100 mm
Mobile Phase: A: Acetonitrile
B: 5::95 Acetonitrile::Water with 0.2% Acetic acid

Gradient Program:

Time (mins)	%A	%B
0.0	5	95
5.0	25	75
5.1	5	95

Flow Rate: 1.5 mL/min
Wavelength: 278 nm

Calibration Curve

Calibration Curve: Linear Regression
Number of Points: 1

Solution Standard Verification and Homogeneity

Compound	Verified Concentration µg/mL	Acceptance Criteria	%RSD - Homogeneity %	Acceptance Criteria
(-)-Epigallocatechin 3-gallate	97.6	± 10%	3.8	≤ 5%
(+)-Catechin	101.2	± 10%	1.4	≤ 5%
(-)-Epicatechin	99.5	± 10%	0.4	≤ 5%
(-)-Epicatechin 3-gallate	99.7	± 10%	0.5	≤ 5%
(-)-Gallocatechin	96.6	± 10%	4.0	≤ 5%
(-)-Gallocatechin 3-gallate	98.7	± 10%	1.7	≤ 5%
(-)-Catechin 3-gallate	99.9	± 10%	0.7	≤ 5%
Caffeine	100.4	± 10%	0.5	≤ 5%

- The Verified Concentration and acceptance criteria incorporate variability of the analytical method and technique. We recommend the Certified Concentration be used for performing calculations and dilutions.
- Concentration is verified through comparison of multiple ampules to an independently prepared calibrator and reported as the average.
- Homogeneity is ensured through rigorous production process controls statistically analyzed to evaluate risk and verified by analysis. The %RSD of samples pulled from across the lot demonstrate homogeneity.
- Product is compared to prior lot and meets acceptance criteria of ± 10%.

Solution Standard Analysis

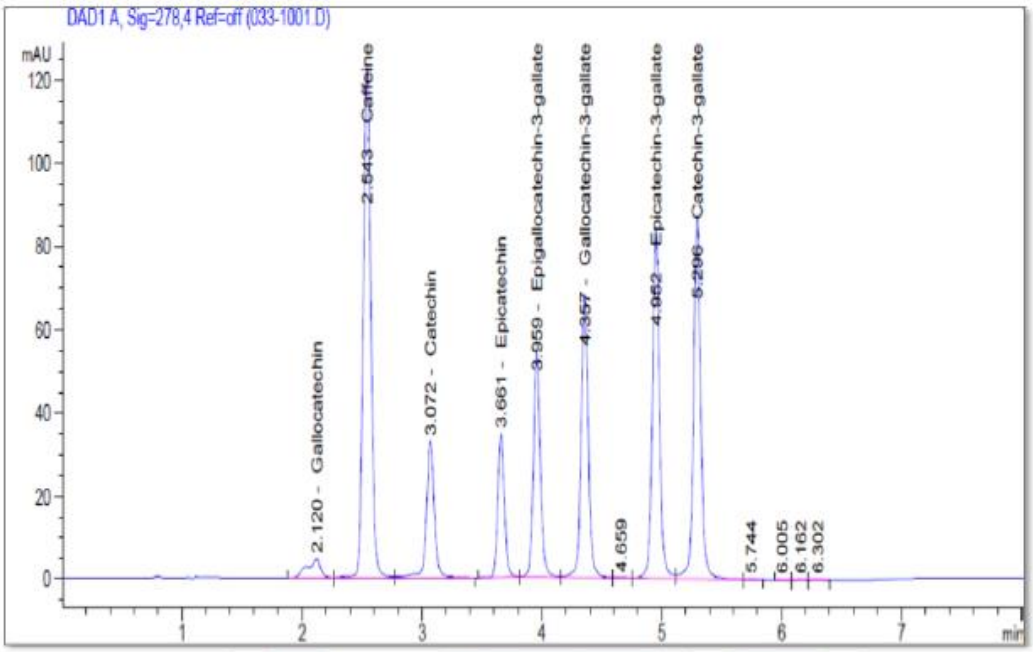

Neat Material Data

Compound	Lot Number	CAS Number	Chemical Formula	Molecular Weight	Identity Confirmed By
(-)-Epigallocatechin 3-gallate	PN072911-01	989-51-5	$C_{22}H_{18}O_{11}$	458.37	LC/MS
(+)-Catechin	PN072911-02	154-23-4	$C_{15}H_{14}O_6$	290.27	LC/MS
(-)-Epicatechin	PN072911-03	490-46-0	$C_{15}H_{14}O_6$	290.27	LC/MS
(-)-Epicatechin 3-gallate	PN072911-04	1257-08-5	$C_{22}H_{18}O_{10}$	442.37	LC/MS
(-)-Gallocatechin	PN072911-05	3371-27-5	$C_{15}H_{14}O_7$	306.27	LC/MS
(-)-Gallocatechin 3-gallate	PN072911-06	4233-96-9	$C_{22}H_{18}O_{11}$	458.37	LC/MS
(-)-Catechin 3-gallate	PN072911-07	130405-40-2	$C_{22}H_{18}O_{10}$	442.37	LC/MS
Caffeine	PN031008-01	58-08-2	$C_8H_{10}N_4O_2$	194.19	GC/MS

Compound	Chromatographic Purity	Residual Solvent	Residual Water	Residual Inorganics	Purity Factor
(-)-Epigallocatechin 3-gallate	99.36%	None Detected	3.69%	< 0.2%	95.69%
(+)-Catechin	99.27%	< 0.05%	5.05%	< 0.1%	94.26%
(-)-Epicatechin	98.06%	< 0.05%	BQL	< 0.1%	98.06%
(-)-Epicatechin 3-gallate	99.54%	< 0.05%	0.69%	< 0.1%	98.85%
(-)-Gallocatechin	99.60%	0.10%	9.39%	< 0.1%	90.15%
(-)-Gallocatechin 3-gallate	99.67%	NA	4.07%	< 0.1%	95.62%
(-)-Catechin 3-gallate	95.01%	13.41%	2.04%	0.50%	79.65%
Caffeine	99.87%	None Detected	Not Detected	< 0.2%	99.95%

- Neat Materials obtained from Phytolab GmbH. Caffeine obtained from Sigma Aldrich.
- Phytolab certification of neat materials includes identity, purity, residual solvent, residual water and residual inorganic content. Residual solvent and residual inorganic values may be obtained from vendor supplied COA.
- Identity, chromatographic purity and residual water values were certified by Cerilliant. Residual solvent values may be independently certified by Cerilliant or obtained from vendor COA.
- Purity Factor = [(100 - wt% residual solvent - wt% residual water - wt% residual inorganics) x Chromatographic Purity/100].
- Purity factor does not include adjustment for chiral and/or isotopic purity.